

INFRASTRUCTURE MONITORING USING SATELLITE IMAGERY AND COMPUTER VISION

**Doctoral Dissertation by
Michele Gazzea**

Thesis submitted for
the degree of Philosophiae Doctor (PhD)
in

Computer Science:
Software Engineering, Sensor Networks and Engineering Computing



Department of Computer Science,
Electrical Engineering and Mathematical Sciences
Faculty of Technology, Environmental and Social Sciences
Western Norway University of Applied Sciences

April 10, 2024

©Michele Gazzea, 2024

The material in this report is covered by copyright law.

Series of dissertation submitted to
the Faculty of Technology, Environmental and Social Sciences,
Western Norway University of Applied Sciences.

ISBN: 978-82-8461-086-3

Author: Michele Gazzea

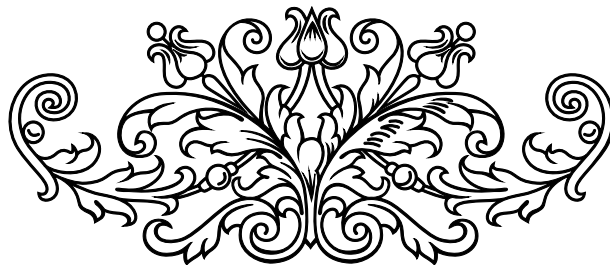
Title: Infrastructure Monitoring using Satellite Imagery and Computer
Vision

Printed production:

Molvik Grafisk / Western Norway University of Applied Sciences

Bergen, Norway, 2024

TO MY PARENTS, FAMILY, AND FRIENDS
for their love, support, advice, and encouragement



PREFACE

The author of this thesis has been employed as a Ph.D. research fellow in the Data Science and Artificial Intelligence Research Group at the Department of Computer Science, Electrical Engineering, and Mathematical Sciences at Western Norway University of Applied Sciences. The author has been enrolled in the Ph.D. program in Computer Science: Software Engineering, Sensor Networks and Engineering Computing, with a specialization on data science and artificial intelligence.

The research presented in this thesis has been accomplished in cooperation with the Department of Civil Engineering at the Florida State University (FSU), Florida, United States. The research has also been supported by the European Space Agency within the GridEyeS project (<https://business.esa.int/projects/grideyes>).

The thesis is organized in two parts. Part I offers an introductory overview of the research area for this thesis, establishing the foundational theories in remote sensing and computer vision. It places the research focus of this thesis within the context of current advancements by reviewing relevant works. Part II consists of five journal papers, four published (Paper A, B, D, and E) and one currently under review (Paper C).

- Paper A** M. Gazzea, M. Pacevicius, D. O. Dammann, A. Saprionova, T. M. Lunde and R. Arghandeh, "Automated Power Lines Vegetation Monitoring Using High-Resolution Satellite Imagery," in *IEEE Transactions on Power Delivery*, vol. 37, no. 1, pp. 308-316, Feb. 2022, doi:10.1109/TPWRD.2021.3059307.
- Paper B** M. Gazzea, L. M. Kristensen, F. Pirotti, E. E. Ozguven and R. Arghandeh, "Tree Species Classification Using High-Resolution Satellite Imagery and Weakly Supervised Learning," in *IEEE Transactions on Geoscience and Remote Sensing*, vol. 60, pp. 1-11, 2022, Art no. 4414311, doi:10.1109/TGRS.2022.3210275.
- Paper C** M. Gazzea and R. Arghandeh, "ASPIRE-V:Artificial Intelligence and Space-based Monitoring for Power Lines Risk Evaluation against Vegetation," submitted to *IEEE Transactions on Power Delivery*, 2024.
- Paper D** M. Gazzea, A. Karaer, M. Ghorbanzadeh, N. Balafkan, T. Abichou, E.E. Ozguven and R. Arghandeh, "Automated Satellite-Based Assessment of Hurricane Impacts on Roadways," in *IEEE Transactions on Industrial Informatics*, vol. 18, no. 3, pp. 2110-2119, March 2022, doi:10.1109/TII.2021.3082906.
- Paper E** M., Gazzea, A., Karaer, M., Ghorbanzadeh, E. E., Ozguven, and R., Arghandeh, (2023). "Roadway Vulnerability Assessment against Hurricanes Using Satellite Images". *Transportation Research Record*, 2677(3), 1453-1464, doi:10.1177/03611981221124593

ACKNOWLEDGMENTS

Embarking on my Ph.D. journey over four years ago marked the beginning of an extraordinary chapter in my life. Despite the challenges and obstacles, when reflecting on my experiences, I consistently affirm that the difficulties were overshadowed by my enjoyment and fulfillment. The decision to pursue this path is one I would eagerly make again. This journey, however, would not have been possible without the remarkable individuals I encountered along the way, whose presence made all the difference.

I want to express my deepest gratitude to my supervisors, Reza and Lars, for their invaluable guidance, patience, and immense kindness. From day one to the final stretch of my PhD, you were a constant source of support. A special thank you to Reza. You were not just a supervisor, but a mentor in the truest sense. You constantly encouraged me to develop a critical mindset, to lead, provide feedback, and offered advice and guidance that extended well beyond academic boundaries. You always strived to foster a supportive and collaborative environment among us, emphasizing teamwork and mutual respect.

I must also express my sincere appreciation to the staff at the FIN-IDER, particularly Håvard, Kristin, and Pål, for always being approachable and helpful.

My experience with the fantastic Cizlab research group has been immensely rewarding, contributing significantly to my professional growth and personal development. A heartfelt thank you goes out to each member and friend in the group – Mojtaba, Amir, Abdul, Mira, Mehak, Lukas and Simon for their invaluable support, engaging discussions, and wonderful companionship. I'm also profoundly grateful to all the individuals and organizations who played a role in supporting our projects and research efforts. Special gratitude is directed to Eren, Alican, Mahyar in Florida, and Nozhan, for our insightful and productive conversations about the Florida use case. I'm thankful for the continued connection we maintain beyond work-related matters. My appreciation also extends to everyone at StormGeo and eSmartSystems for their invaluable support during the GridEyeS project. Furthermore, I'd like to acknowledge Andreas and Charlotte from Kongsberg Satellite for their expertise and useful discussions, Monique and Ivanka from the Fraunhofer Institute for Telecommunications for leading the FG-AI4NDM project, and Planet for their assistance with satellite products.

A huge thanks to the best office-mates and friends one could ever ask for. You've made not only the office but also the life outside of it a truly wonderful environment. Lena, my awesome deskmate, sports buddy, and extraordinary psychotherapist. Your constant encouragement has been a guiding light, pushing me to always do better. The conversations and laughs we've shared are memories I'll cherish forever. Aurora, my charming "Norwegian grandma" and cooking partner. You've brought warmth and joy into my days with your enthusiasm in always planning wonderfully fun activities, creating a sense of home and community, and sharing the Norwegian traditions, turning ordinary days into memorable gatherings. My heartfelt thanks go to Tim, Gerard, Hunter, Haakon, Marianne, Fatemeh, and Jacqueline. Your readiness to join in on adventures, your endless supply of jokes, and your constant presence have been a beacon of joy and happiness, more than words can express. I love you all!

I would like to extend my gratitude to all other Ph.D. colleagues. To Justus, organizing bike trips with you was always a blast. And to Nazerke, Håkon, Thanh, Keila, Guy, Md, Ulisses, Ivan, and Daniel, I am immensely grateful for the countless entertaining and intriguing discussions we shared during our lunch and coffee breaks in Fabrikkgaten. I also want to give a special thanks to my former Ph.D. colleagues - Suresh, Salah, Amin, Satiesh, Frikk, Patrick, Anton, Mahmood, Faustin, Sebastian, Angela, and Alejandro - for your support and guidance, especially during my early months. Within HVL, my gratitude extends to Håvard and Adrian for their fantastic work with the climbing and skiing group, activities which I have thoroughly enjoyed.

I want to extend my thanks to some special people for their support and presence in Bergen. I'm incredibly thankful to Sarah for always organizing and inviting me to extreme cabin trips and thrilling adventures. Also, my gratitude extends to Kristina, Anne-lea, Eugenio, Ekaterina, Omes, Mattia, Ermes, Tamara and Cosimo for your friendship and the moments we've shared and to my flatmates, in particular Hanne, Marcus, Vetle, Maria, and Rebecca.

The initial phase of adjusting to a new city was made easier thanks to my first friends in Bergen, Susanne and Cecilia, and the 'Dutch gang': Mathijs, Bo, Kirsten, and Bran. I cherish the memories of our fun times partying and traveling across Norway.

Even though I've been abroad for many years, I've been fortunate to have the support of my amazing friends back in Italy: Gian luca, Davide, Edoardo, Raffaele, Silvia G., Silvia B., Paola, Elena, Alessandro, Giulia, Antonella, Claudia, Fabio and Sara. Every trip back to Italy for holidays was made so much more special because of you all. Your presence in my life, even from a distance, has been a source of comfort and joy.

Lastly, but most importantly, a huge thanks to my family: my dad Pietro, my mum Dana, and my sister Elena. Your unwavering support throughout these years has been the foundation of everything I've achieved. I am endlessly grateful for your love, encouragement, and belief in me.

ABSTRACT

Infrastructures like roadways and power lines are essential to our society's economy and quality of life, yet they are vulnerable to the environment and severe weather. Trees falling on power lines or obstructing roadways are typical examples of how such vulnerabilities can affect society.

These situations highlight the need for effective and efficient monitoring of infrastructure. Traditional monitoring methods, like ground patrols and visual inspections, are resource-intensive, particularly in vegetation management. These methods are costly, time-consuming, and pose safety risks and environmental concerns. Moreover, the difficulty of monitoring infrastructure is exacerbated by the extensive scale of these networks, especially power lines and roadways, which often span hundreds or even thousands of kilometers. Consequently, the infrequency of inspections often leads to reliance on outdated data, which can hinder the process of making timely and effective decisions.

High-resolution satellite imagery offers a more efficient, cost-effective, and environmentally friendly alternative to traditional methods, providing frequent and comprehensive coverage. This approach enables proactive infrastructure monitoring, improving situational awareness and facilitating prompt action.

This research is centered on developing methodologies and algorithms within the fields of computer vision and earth observation using the most recent remote sensing technologies for infrastructure monitoring. Such methodologies are designed for analyzing satellite imagery to characterize vegetation, detect changes, assess risks, and offer current updates on the condition of infrastructure systems. It covers two main areas: monitoring power line infrastructure to characterize vegetation encroachment and ensure operational integrity and monitoring roadways in natural disaster management. By utilizing satellite imagery, the research aims to offer more timely, cost-effective, and comprehensive monitoring, significantly improving traditional methods and enhancing infrastructure resilience.

SAMMENDRAG

Infrastrukturer som veier og kraftlinjer er essensielle for samfunnet, men er sårbare for miljøet og ekstrem vær. Trær som faller ned på strømlinjer eller blokkerer veier er typiske eksempler på hvordan slike sårbarheter kan påvirke samfunnet.

Disse situasjonene understreker behovet for effektiv overvåking av infrastruktur. Tradisjonelle overvåkningsmetoder, som bakkepatruljer og visuelle inspeksjoner, er ressursintensive, spesielt innen vegetasjonsforvaltning. Metodene er kostbare, tidkrevende, utgjør sikkerhetsrisikoer og påvirker miljøet. I tillegg økes vanskeligheten med å overvåke infrastrukturen av det omfattende omfanget av disse nettverkene, spesielt kraftlinjer og veier, som ofte strekker seg over hundrede- og tusenvis av kilometer. Følgelig fører sjeldenheten av inspeksjoner ofte til beslutninger basert på foreldede data, noe som kan hindre prosessen med å ta rettidige og effektive beslutninger.

Høyoppløselig satellittbilder tilbyr et mer ressurs, kostnadseffektivt og miljøvennlig alternativ til tradisjonelle metoder, og gir hyppig og omfattende dekning. Denne tilnærmingen muliggjør proaktiv overvåking av infrastruktur, forbedrer situasjonsbildet og letter rask handling.

Forskningen setter fokus på å utvikle metoder og algoritmer innen feltene for datamaskinsyn og jordobservasjon ved hjelp av de nyeste fjernmålingsteknologiene for infrastruktureovervåking.

Slike metoder er designet for å analysere satellittbilder for å karakterisere vegetasjon, oppdage endringer, vurdere risikoer og tilby oppdatert informasjon om tilstanden til infrastrukturens systemer.

Forskningen dekker to hovedområder: overvåking av kraftlinjeinfrastruktur for å karakterisere vegetasjon og sikre operasjonell integritet samt overvåking av veier i forvaltning av naturkatastrofer. Ved å utnytte satellittbilder, muliggjør forskningsresultatene mer rettidig, kostnadseffektiv og dekkende overvåking, noe som betydelig forbedrer tradisjonelle metoder og øker infrastrukturens motstandsdyktighet.

Contents

Preface	i
Acknowledgments	iii
Abstract	v
Sammendrag	vii
I OVERVIEW	1
1 Introduction	3
1.1 Background and motivation	3
1.2 Research questions	5
1.3 Research method and approach	6
1.4 Thesis outline	7
1.4.1 List of papers	9
2 Remote sensing technologies	11
2.1 Satellites	12
2.1.1 Satellite geo-positioning	13
2.1.2 Satellite resolutions	15
2.1.3 Optical satellites	17
2.1.4 Synthetic Aperture Radar satellites	20
2.2 LiDAR	22
3 Computer vision in remote sensing	25
3.1 Basics of computer vision	26
3.2 Image processing methods	28
3.2.1 Satellite image enhancement	28
3.2.2 Spatial feature extraction	29
3.3 Machine learning and deep learning methods	32
3.3.1 Convolutional Neural Networks (CNNs)	37
3.3.2 Convolutional Auto-Encoders (CAEs)	38
3.4 Recent trends in computer vision for remote sensing	41
4 Power line monitoring using satellite images	43
4.1 Vegetation detection	46
4.2 The importance of tree species for power lines	47

4.3	Tree characterization and dynamic risk assessment using satellite images	49
5	Roadways disaster management using satellite images	51
5.1	Post-disaster management: damage assessment and recovery	53
5.2	Pre-disaster management: preparedness and vulnerability analysis . .	54
6	Conclusions and future works	57
6.1	Research questions revisited	57
6.2	Contributions	59
6.2.1	Theoretical contributions to remote sensing and computer vision	60
6.2.2	Practical contributions to the use of satellites for infrastructure monitoring	60
6.3	Future work	60
	Bibliography	63
 II ARTICLES		85
	Paper A: Automated Power Lines Vegetation Monitoring Using High-Resolution Satellite Imagery	87
	Paper B: Tree Species Classification Using High-Resolution Satellite Imagery and Weakly Supervised Learning	99
	Paper C: ASPIRE-V:Artificial Intelligence and Space-based Monitoring for Power Lines Risk Evaluation against Vegetation	113
	Paper D: Automated Satellite-Based Assessment of Hurricane Impacts on Roadways	125
	Paper E: Roadway Vulnerability Assessment against Hurricanes Using Satellite Images	137

Part I

OVERVIEW

*All truths are easy to understand once they are discovered;
the point is to discover them.*

—Galileo Galilei (Astronomer and Physicist) [250]

CHAPTER 1

INTRODUCTION

Infrastructures are the fundamental facilities and systems serving a country, city, or area necessary for its economy to function. Roadways, power lines, and communications networks are key examples of such infrastructure, enabling and facilitating essential services like the distribution of electricity, transportation of goods and people, and the exchange of services, forming the backbone of modern civilization.

1.1 Background and motivation

Most infrastructures are geographically and spatially extensive, covering hundreds or even thousands of kilometers, frequently traversing challenging terrains or inaccessible areas such as mountains and fjords. In addition to this, they are often exposed to harsh nature and extreme weather events that can pose a threat to the integrity of the infrastructure. The impacts of climate change have further increased these risks, leading to more frequent and intense extreme weather phenomena [252]. This escalating trend underscores the growing vulnerability of infrastructure to environmental challenges. Because of its importance in society, infrastructure disruptions and outages can directly affect people's life. For instance, trees in proximity to infrastructure can cause operational interruptions, falling and toppling over during severe weather conditions [82]. This can result in trees entangling with electrical lines or blocking transportation routes. In Norway, more than 80% of all power outages are due to a combination of vegetation and weather events [210].

Such incidents can also serve as a catalyst for severe wildfires, which in dry areas can expand quickly, leading to extensive damage and service cessation [28]. The financial repercussions of these events are significant, encompassing not only the direct costs of damage but also those incurred from the necessary repair and recovery processes [205]. Disaster management and response is another critical aspect that comes into play during extreme weather events like hurricanes, where fallen trees can lead to substantial difficulties for local communities. Emergency response teams need to swiftly gather data on the scope and intensity of hurricane-induced damage in order to enhance the effectiveness of the recovery operations that follow such natural catastrophes [117], [76].

Consequently, entities responsible for managing infrastructure assets (such as electricity providers, governmental agencies, and local authorities) are compelled to invest significant resources in the surveillance and monitoring of these infrastructures.

Introduction

In Europe and the US, vegetation management constitutes approximately 35% of the total operational expenditures for utilities, amounting to a cost ranging from 100 to 1500 Euros per kilometer of power line per year, depending on technological factors, geographic location, and the extent of the network [203]. Established methods involve deploying ground crews for visual inspections of the infrastructure network and, at times, utilizing drones or helicopter flights for aerial assessments [154].

In managing the electric grid, operators usually establish a clearance zone along the power lines, typically clearing a swath of land on each side, within which they remove trees to prevent encroachment on the lines. Figure 1.1 shows an example of a transmission power line right of way. Recently, new approaches consist of replacing and replanting potentially hazardous trees with species that are inherently smaller or have slower growth rates, maintaining biodiversity [52]. Therefore, vegetation asset teams can also benefit from knowing the tree species along the lines, enhancing this way the effectiveness of vegetation management strategies.



Fig. 1.1: Transmission tower and relative power line corridor in a forested area. Image from [179].

Despite their necessity, traditional methods of monitoring are not without drawbacks. Manual surveys and visual inspections are labor-intensive, expensive, and potentially dangerous, especially during or in the aftermath of events such as hurricanes where emergency responders may encounter unstable structures or precarious trees that pose additional safety risks. Traditional methods also contribute to environmental pollution through CO₂ emissions during patrols, whether by vehicle or aircraft. It has been estimated that monitoring a 33,000 km stretch of infrastructure using helicopters results in the emission of approximately 165 tonnes of CO₂. This significant carbon footprint reflects the fuel consumption and inefficiency associated with helicopter patrols, especially over extended distances [188]. Given the scale of the infrastructure, inspections are conducted at intervals rather than on a continuous basis, sometimes with several years between assessments [70]. Similarly, tree species databases are often created from field investigations or reference datasets that are typically low in resolution or contain noisy data [68]. As a result, the availability of updated information is infrequent, and the decision-making may not align with the rapid pace at which certain risks, such as vegetation overgrowth, can emerge.

Recently, the advent of more cost-effective satellite launches and the deployment of more sophisticated sensors have revolutionized the potential of using satellite imagery for infrastructure monitoring. The affordability and quality of satellite imagery has significantly improved, and satellite services now offer high-resolution images with frequent updates and comprehensive coverage. Comparative analysis indicates that satellite imagery can be up to 60% more economical compared to images obtained from helicopters and drones [177]. This technology paves the way for a more efficient

approach to monitor potential vegetation encroachment near power lines, as satellites can provide regular, wide-ranging surveillance without the high costs, time investment, and carbon emissions associated with traditional methods. Satellite monitoring of the same 33,000 km line considered before is estimated to result in only about 4.25 tonnes of CO₂ emissions [188]. This drastic reduction is attributed to the satellite's ability to cover vast areas without the direct fuel consumption. The increase coverage and cost efficiency can shift the infrastructure monitoring paradigm from the current cycle-based and reactive protocols to a more proactive approach. By doing so, there would be enhanced and more frequent situational awareness regarding the status of the infrastructure, allowing for timely interventions before issues escalate.

1.2 Research questions

Taking into account the challenges and limitations of traditional infrastructure monitoring methods, leveraging satellite imagery presents a promising avenue for enhancing efficiency in this domain. Despite this potential, it is however impractical and inefficient to manually analyze satellite images and observing infrastructure lines on computer screens. The sheer volume and frequency of the satellite data necessitate the creation of automated processes. These processes are crucial for effectively providing valuable insights from the multitude of imagery, transforming raw data into useful intelligence and decision-making tools without the need for exhaustive manual effort.

The research detailed within this thesis aims to explore how, upon the acquisition of satellite imagery, to effectively monitor the infrastructure networks. The focus is on developing methodologies and algorithms that can analyze satellite images to identify potential physical threats from the surrounding environment, detect changes, assess risks, and provide timely updates about the condition of critical infrastructure. The trajectory of the research undertaken in this thesis is dual, concentrating on two pivotal areas. One direction is the monitoring of power line infrastructure, developing specialized techniques and tools for the surveillance and maintenance of vegetation along power transmission and distribution networks, ensuring their operational integrity and resilience. The second direction is the roadways monitoring and disaster management, especially resulting from natural disasters and extreme weather conditions, with the goal of mitigating the impacts of severe weather events, enhancing the preparedness and responsiveness of communities and infrastructure systems to such unpredictable challenges.

For each of these two directions, research questions, and associated sub research questions have been identified and explored as follows:

- **RQ 1:** How to achieve a better situational awareness of the vegetation status along power lines using satellites?
 - RQ1.1: *How to assess the risk of vegetation near power lines using high-resolution optical satellite images?*
 - RQ1.2: *How to improve the quality of forests inventory databases and classify tree species?*

Introduction

- RQ1.3: *How to characterize trees near infrastructure lines and estimate their vulnerability with respect to weather?*
- **RQ2:** How satellite imagery can help in roadways management against natural disaster?
 - RQ2.1: *How to detect fallen trees on roadways after a hurricane with limited data?*
 - RQ2.2: *How to characterize vegetation-induced roadways vulnerability and enhance infrastructure resilience?*

1.3 Research method and approach

The research in this thesis has been divided into two directions, each targeting one of the two main research questions listed in Section 1.2. This structured approach encompasses two distinct projects, each developed through collaborative efforts with various partners over the course of the Ph.D. research period. These two projects are:

1. **Power line monitoring.** This research has been established by the GridEyeS project [55], supported by the European Space Agency (ESA) with technical collaboration from the industry partners, namely StormGeo [4] and eSmart Systems [2]. The project focuses on the characterization and assessment of vegetation along power lines to prevent service disruptions and maintain the reliability of the electrical grid. Additionally, the project involves collaboration with Linja [3], which plays a pivotal role as an electric utility end user, providing practical insights and real-world applications for the research outcomes.
2. **Roadway management against natural disasters.** The research investigates strategies and methods for managing and mitigating the damage caused by extreme weather events, in particular hurricanes, with an emphasis on preparedness, rapid response and recovery. This project (called internally DisasterView) has been initiated as a collaboration between the Western Norway University of Applied Sciences, Florida State University (FSU), and the City of Tallahassee, capital of Florida. Additional support and collaboration is provided by the United Nations’s Focus Group on AI for Natural Disaster Management [234].

Figure 1.2 presents the overarching research approach and the associated activities that form the backbone of this study, acting as both a roadmap and a visual guide that captures the essence of the research conducted in this thesis. It graphically lays out the research domains we have explored, marking out the specific questions that each attached paper seeks to answer. The initial stage is characterized by a selection process of the specific use case, task, and objectives, which are fundamental in directing the course of the study. State-of-the-art methodologies and tools from the fields of remote sensing and computer vision analysis provide the theoretical foundations upon which tailored methodologies are built and then applied to the specific study area. Following this, there is an acquisition of satellite imagery to the area under study. The selection of these images is critical, with their quality and quantity being directly influenced by the nature and demands of the task at hand. Additionally, when deemed

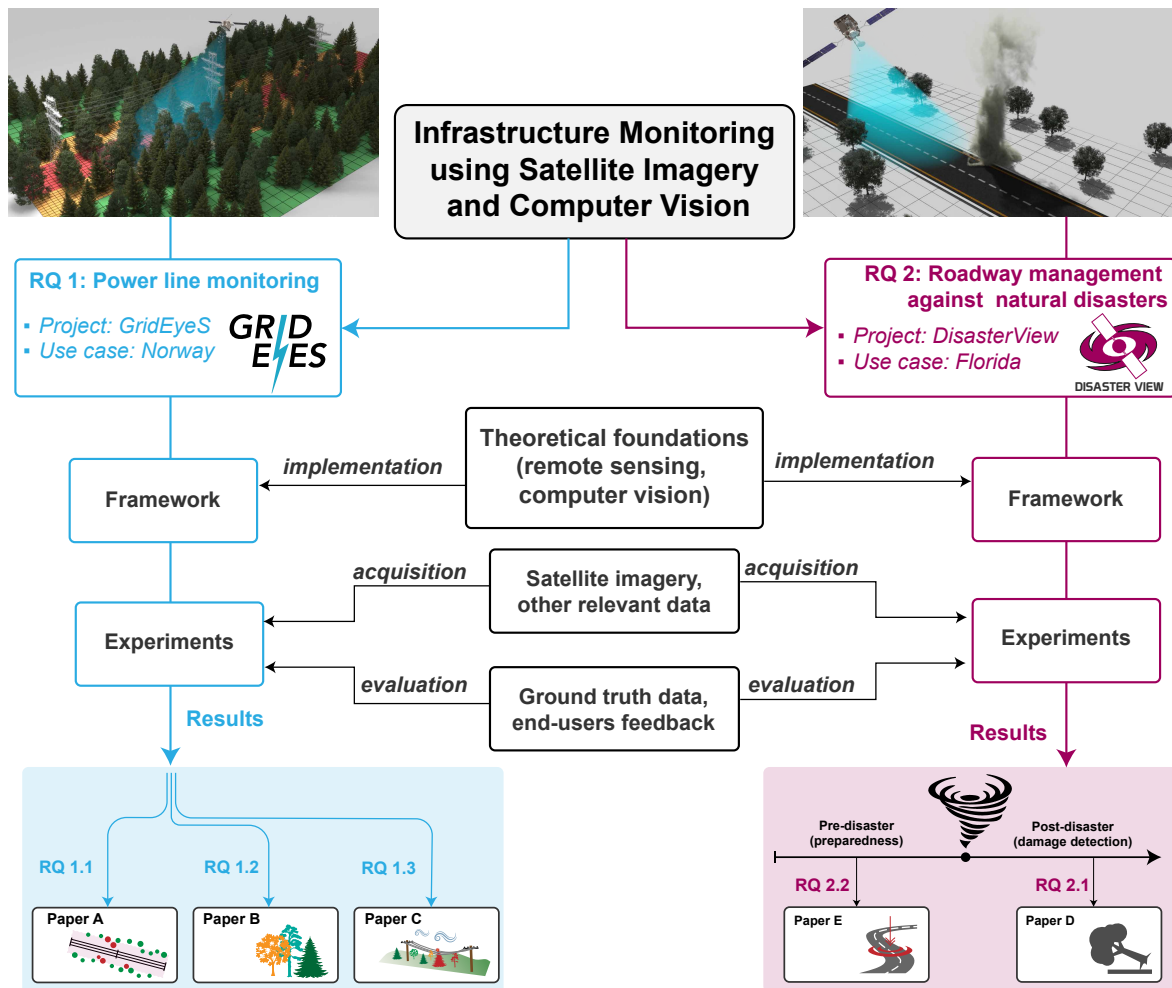


Fig. 1.2: Road-map delineating the scope of research in this thesis. It organizes the study of this Ph.D. thesis into two principal categories: power line monitoring, and roadways management against natural disasters. Within each of these two categories, targeted research questions are formulated and systematically addressed in the respective papers. Further details on Paper A-E are provided in Chapter 4 and Chapter 5.

necessary, supplementary data are gathered. To validate the robustness and accuracy of our research findings, we conduct a series of experiments. Validation processes involves the use of ground truth data, which typically encompasses high-resolution aerial photographs, LiDAR point cloud data, as well as inputs and feedback from domain experts, end-users, and partners of the projects. This multi-faceted approach to validation ensures that our findings are not only theoretically sound but also practically relevant and reliable.

Each research direction with relative research questions and corresponding papers are further discussed in details in Chapter 4 and 5, respectively.

1.4 Thesis outline

The thesis is structured in two parts: Part I provides an overview of the research field of this thesis. It lays out the theoretical groundwork in remote sensing and computer

Introduction

vision and places the research within the current state-of-the-art through a review of related work. Part II comprises the papers that are attached to this thesis and represent its principal contributions. Part I is divided into the following chapters:

2. REMOTE SENSING TECHNOLOGIES: This chapter serves as an introductory overview of the fundamental remote sensing technologies that form the basis of the research presented in this thesis, with particular focus on satellite imagery. The chapter covers the various types of satellite sensors, including optical, radar, and LiDAR, and delves into the different aspects of satellite imagery such as spatial, spectral, and temporal resolution.

3. COMPUTER VISION IN REMOTE SENSING: This chapter focuses on the application of computer vision techniques in remote sensing. It begins with an exploration of traditional image processing methods, discussing how these techniques are used to enhance and extract meaningful information from remote sensing data. The chapter then transitions to more recent advancements in the field, focusing on how machine learning and deep learning have revolutionized computer vision, particularly in the context of remote sensing. Topics include the evolution and impact of machine learning algorithms, the application of models like convolutional neural networks, autoencoders, and the most recent research trends in computer vision.

4. POWER LINES MONITORING USING SATELLITE IMAGES: In this chapter, we delve into the contributions of this thesis within monitoring of power lines using remote sensing techniques, specifically through the analysis of satellite imagery. The chapter systematically introduces the three research papers. Each paper is examined and linked to the specific research question it addresses. The emphasis is on showcasing the approaches and findings that enhance the effectiveness of satellite-based monitoring systems for power line infrastructure.

5. ROADWAYS DISASTER MANAGEMENT USING SATELLITE IMAGES: This chapter is dedicated to exploring the contributions of this thesis to the management of roadways, particularly in the context of disaster scenarios, through the application of remote sensing technologies. Similar to the Chapter 4, it provides an introduction of each research paper pertaining to this area. The focus is on illustrating how satellite imagery and remote sensing methods can be used to enhance the resilience and management of roadway infrastructure with respect to natural disasters and other disruptive events.

6. CONCLUSION AND FUTURE WORKS: In this concluding chapter, we revisit the research questions posed at the outset of this thesis to provide a cohesive summary of the contributions made throughout the research. The chapter synthesizes the key findings, insights, and advancements achieved in the areas of power lines monitoring and roadways disaster management using remote sensing technologies. Additionally, this chapter outlines potential future directions for research in these areas. It identifies gaps in the current knowledge, suggests areas where further investigation could yield

significant benefits, and proposes new methodologies or approaches that could be explored.

1.4.1 List of papers

Part II consists of four published journal papers and one submitted journal paper, as listed in Table 1.1:

Table 1.1: List of publications included in Part II. The symbol '*' denotes papers currently under review.

Paper	Year	Journal
Paper A: Automated power lines vegetation monitoring using high-resolution satellite imagery [70]	2021	IEEE Transactions on Power Delivery
Paper B: Tree species classification using high-resolution satellite imagery and weakly supervised learning [68]	2022	IEEE Transactions on Geoscience and Remote Sensing
Paper C*: ASPIRE-V: Artificial Intelligence and Space-based Monitoring for Power Lines Risk Evaluation against Vegetation	2024	IEEE Transactions on Power Delivery
Paper D: Automated satellite-based assessment of hurricane impacts on roadways [66]	2022	IEEE Transactions on Industrial Informatics
Paper E: Roadway vulnerability assessment against hurricanes using satellite images [67]	2023	SAGE Transportation Research Record

The papers included in this thesis (Table 1.1) encompass a variety of studies and advancements in the domain of infrastructure monitoring. Nevertheless, throughout the duration of Ph.D. project, other significant papers have been published in the same field. These papers offer additional insights and represent further progress in the area. However, they have not been incorporated into this thesis. This exclusion is due to the necessity of selecting only the most relevant papers specifically aligned with the theme of infrastructure monitoring, while also maintaining a manageable number of papers. Below is a list of the papers published during this Ph.D. that are not included in this thesis.

- [65] Gazzea, M., Aalhus, S., Kristensen, L. M., Ozguven, E. E. and Arghandeh, R., "Automated 3D Vegetation Detection Along Power Lines using Monocular Satellite Imagery and Deep Learning," 2021 IEEE International Geoscience and Remote Sensing Symposium IGARSS, Brussels, Belgium, 2021, pp. 3721-3724, doi:10.1109/IGARSS47720.2021.9554938.
- [71] Gazzea, M., Solheim, A. and Arghandeh, R., High-resolution mapping of forest structure from integrated SAR and optical images using an enhanced U-net method, Science of Remote Sensing, 2023, 8, doi:10.1016/j.srs.2023.100093.

Introduction

- [69] Gazzea, M., Miraki, A., Alisan, O., Kuglitsch, M. M., Pelivan, I., Ozguven, E. E. and Arghandeh, R., Traffic monitoring system design considering multi-hazard disaster risks. *Sci Rep* 13, pp. 4883, 2023. doi:[10.1038/s41598-023-32086-6](https://doi.org/10.1038/s41598-023-32086-6)
- [72] Gazzea, M., Sommervold, O., and Arghandeh, R., "MARU-Net: Multiscale Attention Gated Residual U-Net With Contrastive Loss for SAR-Optical Image Matching," in *IEEE Journal of Selected Topics in Applied Earth Observations and Remote Sensing*, vol. 16, pp. 4891-4899, 2023, doi:[10.1109/JSTARS.2023.3277550](https://doi.org/10.1109/JSTARS.2023.3277550).

Moreover, the collaborative efforts within the GridEyeS project and with Florida State University have resulted in the publication of additional papers. My contribution as a co-author in these works has further broadened the scope and impact of our research. These papers are listed as follows:

- [180] M. Pacevicius, D. O. Dammann, M. Gazzea and A. Saprionova, "Heterogeneous Data-merging Platform for Improved Risk Management in Power Grids," 2021 Annual Reliability and Maintainability Symposium (RAMS), Orlando, FL, USA, 2021, pp. 1-7, doi: [10.1109/RAMS48097.2021.9605796](https://doi.org/10.1109/RAMS48097.2021.9605796)
- [117] A. Karaer, M. Chen, M. Gazzea, M. Ghorbanzadeh, T. Abichou, R. Arghandeh, E. E. Ozguven, "Remote sensing-based comparative damage assessment of historical storms and hurricanes in Northwestern Florida", *International Journal of Disaster Risk Reduction*, 2022, (72), doi:[10.1016/j.ijdr.2022.102857](https://doi.org/10.1016/j.ijdr.2022.102857)
- [208] Sommervold O., Gazzea M., Arghandeh R. "A Survey on SAR and Optical Satellite Image Registration". *Remote Sensing*. 2023; 15(3):850. doi:[10.3390/rs15030850](https://doi.org/10.3390/rs15030850)
- [118] Karaer A., Balafkan N., Gazzea M., Arghandeh R., Ozguven E.E. "Analyzing COVID-19 Impacts on Vehicle Travels and Daily Nitrogen Dioxide (NO₂) Levels among Florida Counties". *Energies*. 2020; 13(22):6044. doi:[/10.3390/en13226044](https://doi.org/10.3390/en13226044)

It's tiny out there...it's inconsequential. It's ironic that we had come to study the Moon and it was really discovering the Earth.

— William Anders (Apollo 8 Astronaut) [249]

CHAPTER 2

REMOTE SENSING TECHNOLOGIES

Remote sensing is a scientific discipline focused on collecting both quantitative and qualitative information about an environment from afar, utilizing electromagnetic radiation [167]. The term usually refers to employing satellite or aircraft-based sensor technologies to identify and classify objects on the Earth's surface. Remote sensing is used in an extremely wide range of fields, including geophysics and geography (terrain mapping and tectonic movements) [44, 165], hydrology (monitoring of water levels in rivers and lakes) [166, 184], ecology (monitoring biodiversity) [39, 199], meteorology (weather forecasting) [102], environmental monitoring (tracking deforestation, desertification) [135, 192, 207], oceanography (measuring sea surface temperatures, currents, and marine ecosystems) [16, 17], and glaciology (study glaciers and ice caps, tracking changes related to climate dynamics) [32, 83]. Beyond these scientific fields, remote sensing has vital roles in other various sectors such as military and intelligence (reconnaissance, surveillance) [186], disaster management (damage assessment post-natural disasters and planning evacuation routes) [66, 67, 117], and industrial applications (detection of gas leaks and monitoring of infrastructure integrity) [197]. Remote sensing technologies have evolved to serve these diverse needs through a variety of platforms and sensor types, each tailored to capture different data types – from thermal imagery for heat detection to multispectral imagery [270]. The versatility of remote sensing makes it a crucial component in the toolkit of many professions, enabling a deeper understanding of the Earth and its processes.

There are two main types of sensors in remote sensing technologies: active and passive sensors. Active sensors emit their own signal, such as a laser or radar wave, and measure the characteristics of the signal after it bounces back from the target such as change in energy, direction, and signal properties. The returned signal provides valuable data regarding the object's properties, such as its distance, shape, and material composition. LiDAR (Light Detection and Ranging) and radar systems are prime examples of active remote sensing devices [224]. Unlike active sensors, passive sensors do not emit their own signal. Instead, they detect energy that is reflected or emitted by the object's surface. Passive sensors include a wide array of camera-based optical sensors, such as those on optical satellites, drones, and even the human eye. These sensors depend entirely on external sources of light to capture images, which is in most cases sunlight.

Below we provide an introductory overview of the primary remote sensing technologies utilized in this PhD research, with a specific focus on satellite imagery.

2.1 Satellites

A satellite is an object that orbits around the Earth. The historic milestone of launching the first artificial satellite was achieved by the Soviet Union with Sputnik 1 on October 4, 1957. Since then, the number of satellites in space has grown exponentially. As of the end of June 2023, the number of satellites in orbit has reached 11,330. This number is obtained from the Index of Objects Launched into Outer Space, a registry maintained by the United Nations Office for Outer Space Affairs (UNOOSA) [61], which keeps a comprehensive record of all man-made objects in space. Most Earth observation satellites are positioned in low Earth orbit (LEO) to capture high-resolution data, which is crucial for detailed analysis and application. However, some satellites are placed in geostationary orbit (GEO), which allows them to provide consistent, uninterrupted coverage of specific areas of the Earth [130]. These Earth observation satellites are equipped with an array of different sensors, making them one of the most versatile and valuable instruments for monitoring and studying our planet [270]. Figure 2.1 shows an illustration of a satellite scanning the Earth surface.

Space satellites take advantage of outer space's near perfect vacuum to observe objects in a wide range of the electromagnetic spectrum. Figure 2.2 illustrates the electromagnetic (EM) spectrum, categorizing it by wavelength, denoted as λ . The spectrum encompasses a wide range of wavelengths, extending from radio waves, which have wavelengths in the order of meters or even larger, to gamma rays, with extremely short wavelengths of 10^{-12} meters or less. It is important to remember that, for an electromagnetic wave, the wavelength λ and frequency f are inversely related through the constant speed of light c as described by the equation $c = \lambda f$. This fundamental relationship allows space satellites to be designed with specific sensors that can detect various portions of the EM spectrum.

The Earth's atmosphere acts as a selective barrier to different wavelengths of electromagnetic radiation, a phenomenon known as atmospheric opacity [157]. Certain wavelengths are able to penetrate the atmosphere, while others are absorbed, heavily attenuated or scattered by it. High-energy radiation such as the majority of ultraviolet rays, X-rays, and gamma rays are largely blocked by the atmospheric layers. This protective filtering is crucial as these types of radiation are ionizing, carrying enough energy to detach electrons from atoms or molecules, which can damage living tissue and have detrimental effects on life on Earth. Additionally, parts of the microwave spectrum and long radio waves are also impeded by the atmosphere. Consequently, satellites in orbit around Earth must operate within specific frequency ranges that can pass through the atmospheric barrier unobstructed. For Earth observation satellites,

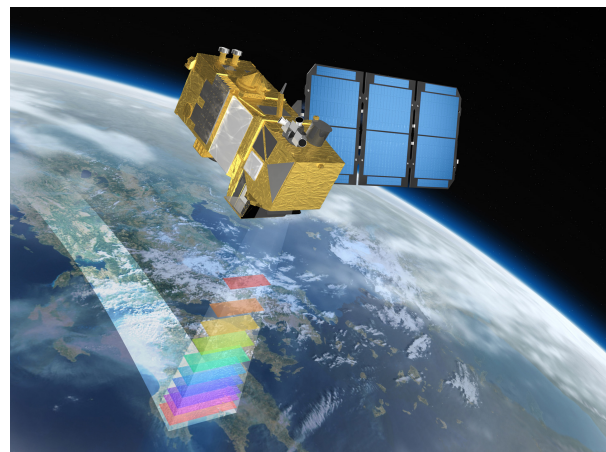


Fig. 2.1: Illustrative image of an Earth observation satellite from the Sentinel-2 mission. Image from European Space Agency (ESA) [56].

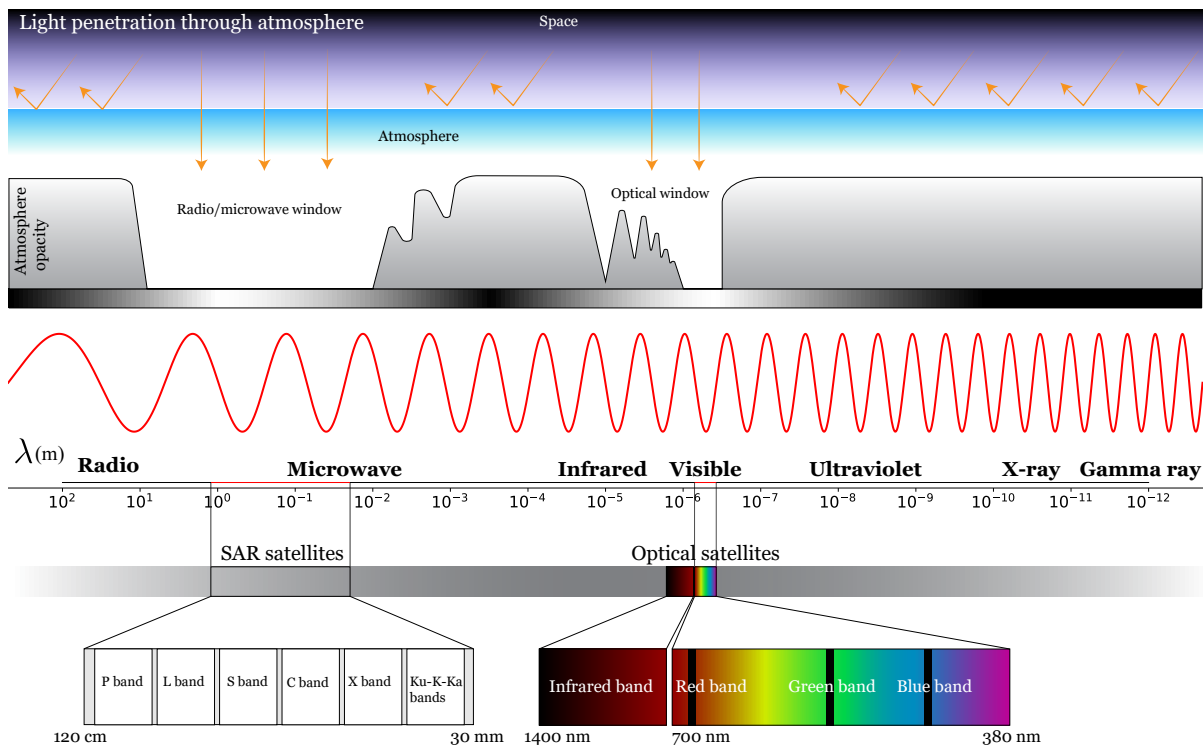


Fig. 2.2: Complete electromagnetic spectrum. Different wavelengths λ have different penetration capabilities through the atmosphere, therefore only certain wavelengths (or frequencies) can be used for space-based remote sensing. The most common intervals are in the visible and infrared band (optical satellites) and the microwaves (SAR satellites).

the most commonly utilized portions of the electromagnetic spectrum fall within the bands of visible light and infrared. Optical satellites make use of these frequencies to capture detailed images of the planet's surface in the wavelengths visible to the human eye, as well as in the infrared range, which can provide information about heat and vegetation health among other things. Synthetic Aperture Radar (SAR) satellites, on the other hand, operate using a band of the microwave spectrum that can penetrate clouds and provide imagery irrespective of the time or weather conditions. These capabilities make SAR imagery particularly valuable for Earth observation applications, including topography, agriculture, and disaster management. Detailed discussions regarding the technical distinctions and applications of optical and SAR satellite imagery can be found in Section 2.1.3 and Section 2.1.4 of this thesis, respectively.

2.1.1 Satellite geo-positioning

Irrespective of the satellite type, the end product of a satellite acquisition is a georeferenced image. This is essentially a raster-based image composed of pixels, each encoded with geographic location data that allows the image to be mapped accurately onto real-world coordinates [217].

The process of obtaining these images from satellites orbiting Earth at high velocities involves intricate steps to ensure precise georeferencing. This is crucial for Earth observation tasks that demand high accuracy, particularly when dealing with detailed

observations at smaller scales. The processing steps required to achieve such accuracy is tailored to the specific characteristics of the satellite's sensors as well as the details of its orbital path and speed. In their orbits, satellites are often not positioned to capture images directly downwards (known as the nadir view). Instead, they collect imagery at an angle. This off-nadir angle, or shooting angle, is a critical consideration. A higher elevation angle (which corresponds to a lower off-nadir angle) is typically desirable, particularly in regions with significant topographical variation or tall structures, to reduce the distortion effect on buildings, known as the "building lean" [23]. However, this preference can conflict with the goal of minimizing the time it takes for the satellite to revisit and capture imagery of the same area again.

Consequently, acquired satellite images require geometric corrections, commonly referred to as orthorectification (Figure 2.3) [11, 137]. This process transforms raw satellite imagery into an orthophoto, a geometrically corrected image that can reliably represent true distances and features on Earth's surface. This is because orthophotos are adjusted for potential distortions due to topographic relief as well as the camera's lens, and the tilt during image capture. The result is a highly accurate depiction of the Earth's surface that can be used for a multitude of applications, from mapping and surveying to detailed environmental monitoring. To carry out the orthorectification of a satellite image, a Digital Elevation Model

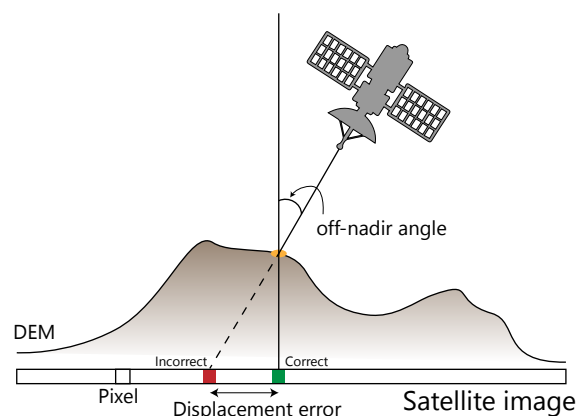


Fig. 2.3: The orthorectification is the process to corrected satellite images with respect to the acquisition conditions such as viewing geometry, platform attitude, Earth rotation and of the relief effects (parallax).

(DEM) is employed in tandem with rational polynomial coefficients (RPCs) [223], which are provided by the satellite operator. The RPCs are derived from the satellite sensor's data and encode detailed information about the sensor's orientation in relation to the Earth's surface, both horizontally and vertically. These coefficients are essential for the accurate modeling of the image's geometry and for ensuring that each pixel is correctly aligned with its geographical position on the Earth's surface. The DEM provides the necessary topographic information to adjust for elevation differences, which is crucial for reducing geometric distortions in the image. In instances where the initial geolocation accuracy of the satellite imagery does not satisfy the specific requirements of a project, the RPCs can be fine-tuned. This refinement is achieved by incorporating additional ground control points (GCPs), which are precise geographic locations on the Earth's surface that have been identified in the satellite image. By matching these known points with their corresponding locations in the image, the RPCs can be recalibrated to enhance the positional accuracy of the orthorectified output. This step is often necessary when the project necessitates a very high level of precision in the geo-referencing of the satellite imagery. Typical elevation angles are of 60 degrees (30-degree off-nadir angles). Higher off-nadir angles are often favored when the objective is to capture views from multiple angles to create stereo images

[107]. Stereo imaging involves taking two or more photographs from different points to produce a three-dimensional effect when they are viewed together. This technique is particularly useful in remote sensing for creating digital elevation models which can accurately represent the Earth's surface in three dimensions, providing valuable data for topographical mapping, urban planning, and geological surveys [134, 222].

2.1.2 Satellite resolutions

When utilizing satellite imagery for various applications, resolution is a crucial factor to consider, and it encompasses several different aspects, each of which is significant depending on the specific task and cost constraints. The primary types of resolution in satellite imagery are summarized below.

SPATIAL RESOLUTION: Spatial resolution (Figure 2.4) is the smallest object that can be detected on the ground by the satellite sensor, and is essentially determining the detail visible in the satellite images. From a practical point of view, it refers to the pixel size of an image represented in a raster format, which ultimately dictates the level of detail observable in the image. Higher spatial resolution provides more detailed images, which is essential for applications like detailed mapping, surveillance, and detailed environmental studies.

The choice of the required spatial resolution is often a trade-off between the level of detail required and the cost. Higher resolution images typically require more advanced sensors and more data storage and processing capacity.

RADIOMETRIC RESOLUTION: Radiometric resolution (Figure 2.5) defines a sensor's ability to differentiate between levels of signal intensity, essentially measuring the sensitivity of the sensor to the magnitude of the electromagnetic energy. A higher radiometric resolution means that the sensor can distinguish subtler differences in energy, which translates to a greater variety of intensity levels in an image. This is typically expressed in bits. For example, an 8-bit sensor can distinguish $2^8 = 256$ levels, while a 14-bit sensor can distinguish $2^{14} = 16,384$ levels.

SPECTRAL RESOLUTION: Spectral resolution refers to a sensor's ability to distinguish between different wavelengths of the continuous electromagnetic spectrum. Because spectral resolution is particularly important for optical sensors, more information is provided in Section 2.1.3.

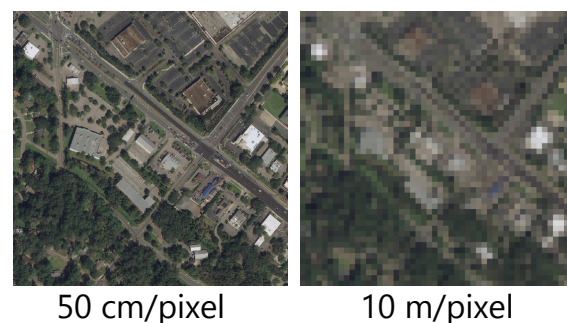


Fig. 2.4: Spatial resolution is the physical dimension of each pixel. The smaller the pixel size, the greater the details of the image.

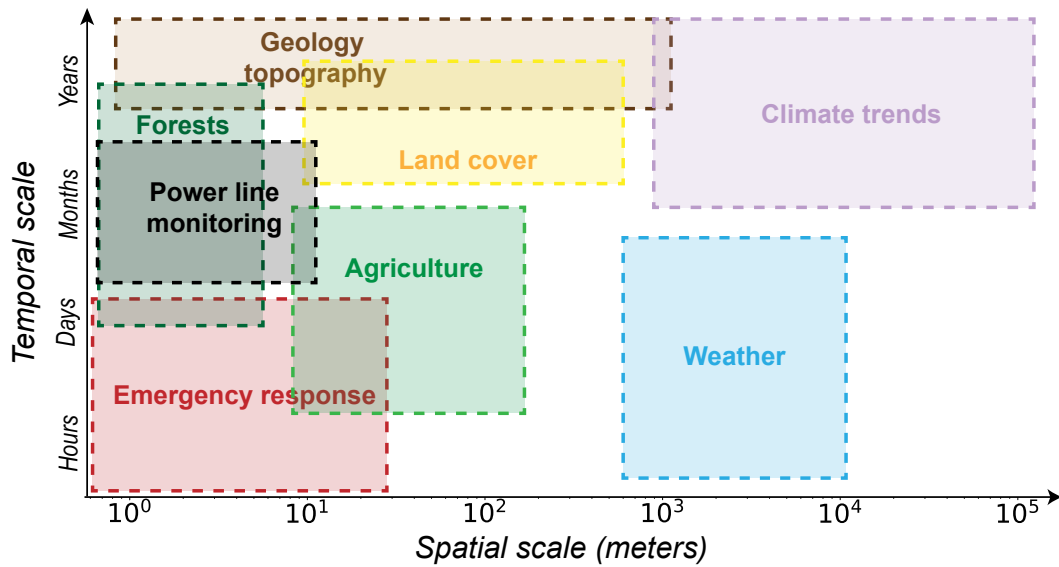


Fig. 2.6: The diagram illustrates the importance of selecting the necessary spatial and temporal resolutions based on different remote sensing applications.

TEMPORAL RESOLUTION: Temporal resolution refers to the frequency at which a satellite captures imagery of the same location. It is a critical factor in monitoring environmental changes, urban development, deforestation or agricultural progress. High temporal resolution is vital for time-sensitive studies, allowing for frequent observations to track rapid changes or for accumulating data to create composite images that minimize the effects of cloud cover or seasonal variability. Picking the right spatial and temporal resolution heavily depend on the application, and the need for up-to-date information versus the costs associated with more frequent image captures (Figure 2.6).

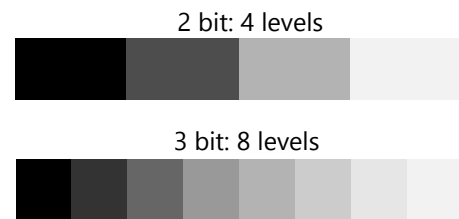


Fig. 2.5: Radiometric resolution is determined by the number of bits used to define each pixel. The larger the bit depth, the higher the number of tones can be represented.

Choosing the appropriate spatial and temporal resolution is crucial and should be tailored to the specific needs of the application at hand. For example, monitoring climate trends or geological topography typically necessitate a long-term approach, where data is gathered and analyzed over several years to identify gradual changes and trends. The temporal resolution may be lower, with images acquired on a monthly or yearly basis, while spatial resolution needs might vary depending on the scale of geological features or climate phenomena being studied. Emergency response situations in contrast require rapid data acquisition with a high temporal resolution, as decisions must be made within hours or days at maximum. In these cases, the latest imagery is essential to assess situations such as natural disasters, where changes occur quickly and updated information is critical for effective response. When monitoring forests, a higher spatial resolution, within sub-meter to tens meters, is typically needed to detect and analyze changes such as deforestation or forest health. This allows for the

identification of individual trees or small-scale changes in forest canopy. For land cover and agriculture applications, the spatial resolution can be lower because the features of interest, such as fields or land cover types, tend to be larger and do not require fine detail to be effectively monitored. However, a moderate level of spatial resolution is still important to distinguish between different types of land use and to monitor agricultural practices. In essence, high temporal resolution is vital when changes over time are rapid and require immediate attention, while high spatial resolution is crucial when the focus is on small-scale features. The key is to balance the resolution requirements with the specific objectives of the study or project to ensure that the data collected is both relevant and useful.

2.1.3 Optical satellites

Optical satellites, a subset of remote sensing spacecraft, utilize sensors that operate within the optical window of the electromagnetic spectrum, encompassing the visible and infrared bands. The majority of these satellites are passive, relying on sunlight reflected off the Earth's surface and atmosphere to capture images. This passive operation means that they require less power, which translates to lower operational costs [156]. The reliance on solar illumination does, however, impose certain limitations on optical satellites. They are generally unable to gather data at night due to the absence of sunlight. Furthermore, their effectiveness is compromised by cloud cover, which can obstruct the view of the Earth's surface, often necessitating multiple imaging attempts to acquire a clear picture of a given location.

MULTISPECTRAL IMAGERY: One of the remarkable capabilities of optical satellites is their ability to detect not only the visible spectrum but also wavelengths beyond human vision. Spectral resolution refers to the number and width of spectral bands that a sensor can discriminate (Figure 2.7).

A higher number of spectral bands allows the sensor to capture a more detailed spectral signature of the observed objects or materials. Similarly, narrower bands provide more precise spectral information. Standard cameras typically capture images in three primary bands corresponding to the colors red, green, and blue (RGB), which are combined to create a full-color image as perceived by the human eye. Satellites with multispectral capabilities, however, can detect a broader range of the electromagnetic spectrum. These multispectral satellites are equipped with sensors that can capture more than the basic RGB bands. They might include additional bands such as the near-infrared (NIR) band, which is just beyond what the human eye can see and is crucial for analyzing vegetation health, among other applications [212]. More advanced multispectral satellites can carry sensors that capture up to ten or twelve different bands. These can include varying levels of the infrared spectrum like the short-wave infrared (SWIR), medium-wave infrared (MWIR), and long-wave infrared (LWIR). Each of these bands can be used to identify different materials or conditions on the Earth's surface, such as moisture content, heat signatures, and geological compositions [26, 34, 247]. The spectral resolution of a satellite sensor thus significantly enhances the types of environmental analysis and remote sensing applications that can be conducted

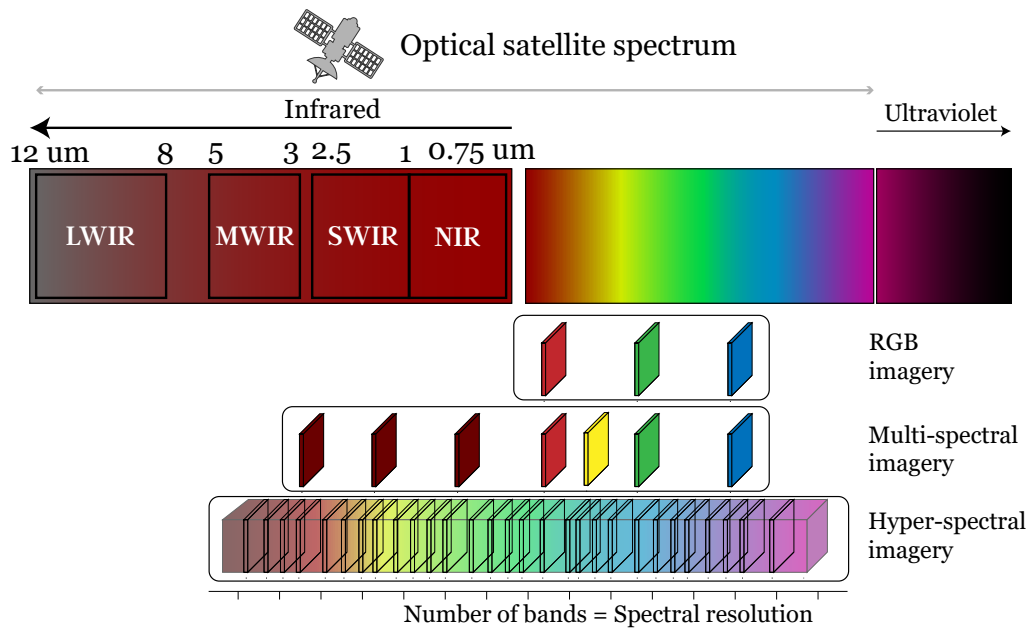


Fig. 2.7: Spectral resolution describes the ability of a sensor to define wavelength intervals. Most of sensors (standard cameras and the human eye) captures only three bands: Red, Green and Blue. Multispectral images can have from four to twelve bands, including infrared bands. Hyperspectral can have hundreds of bands.

HYPER SPECTRAL IMAGERY: Hyperspectral imaging is concerned with images spreading across an extensive range of the electromagnetic spectrum. Hyperspectral sensors can detect dozens, if not hundreds, of narrow spectral bands [33, 131]. Unlike multispectral imaging, which captures discrete bands within wider spectral ranges, hyperspectral imaging provides an almost continuous spectral signature for each pixel in the image. The ability to capture such a detailed spectral resolution makes hyperspectral imaging particularly valuable for applications requiring detailed object identification, chemical composition analysis, and subtle differentiation of materials [62]. This includes fields like mineralogy, agriculture and environmental monitoring [146, 213]. Available satellite are the PROBA-1 from ESA, EO-1 from NASA, and PRISMA from the Italian Space Agency (ASI). They contain between 200 and 250 spectral bands, with a resolution of 30 meters per pixel. However, given the limited spatial resolution, they are challenging to use for small scale applications like infrastructure monitoring.

PANSHARPENING: Multispectral satellite sensors typically include a panchromatic band, which is a single band capturing a broad range of wavelengths, often spanning several hundred nanometers. The panchromatic band is designed to have a wide bandwidth, which allows it to gather more light, resulting in a higher signal-to-noise ratio. This capability enables the panchromatic band to provide imagery at a finer spatial resolution compared to the narrower spectral bands of multispectral data. However, because it encompasses a broad spectrum of light, the panchromatic band does not retain specific color or spectral information about the targets, it only measures their apparent brightness in a form of grayscale image.

Pansharpening is a technique used to fuse the high-resolution detail of the panchro-

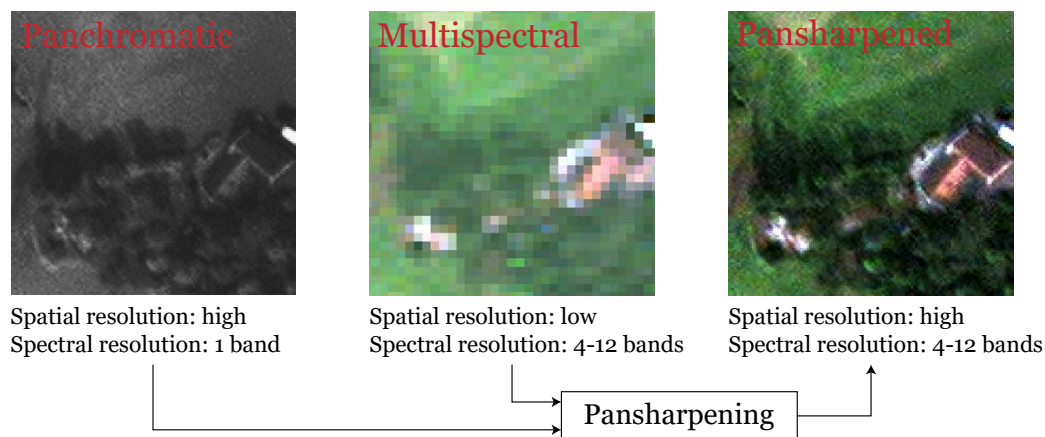


Fig. 2.8: Pansharpening is the technique used to fuse a panchromatic image (high spatial resolution, but single band) with a multispectral image (high spectral resolution, but lower spatial resolution).

matic image with the color and spectral information from the multispectral bands, which often have lower spatial resolution. Figure 2.8 shows an example of the pansharpening procedure on a sample satellite image. This process enhances the spatial resolution of the multispectral image, producing a single high-resolution color image that combines the best qualities of both data types. Pansharpening algorithms take advantage of the spatial detail contained in the panchromatic image and apply it to the multispectral image, effectively "sharpening" the multispectral data while preserving its valuable spectral properties. A review of the different pansharpening methods can be found in [159].

SPECTRAL INDICES: The capability to capture images in multiple spectral bands enables the computation of several spectral indices that are invaluable in remote sensing applications [265]. One of the most widely known indices is the Normalized Difference Vegetation Index (NDVI), which is particularly effective in identifying and assessing the health and vitality of vegetation [6].

The NDVI takes advantage of the fact that healthy vegetation absorbs most of the visible light (particularly the red wavelength) and reflects a large portion of the near-infrared light (700nm to 1000nm). By using the red (RED) and near-infrared (NIR) bands, the NDVI equation is formulated to highlight the density and health of plant life in a given area. The calculation of NDVI is expressed by the equation:

$$\text{NDVI} = \frac{\text{NIR} - \text{RED}}{\text{NIR} + \text{RED}} \quad (2.1)$$

where NIR is the reflectance value in the near-infrared band and RED in the red part of the spectrum. NDVI values range from -1 to 1, where higher values correspond to greater density and health of plant life (Figure 2.9). NDVI has been used in many applications of remote sensing [96], including change detection [147] and vegetation time-series analysis [139].

Besides NDVI, several other spectral indices has been developed to extract information about water content [150], soil moisture [80], and snow coverage [48]. Additionally,

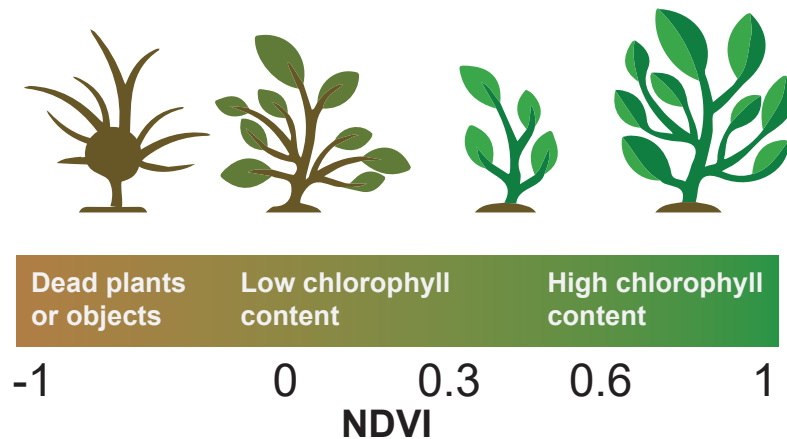


Fig. 2.9: The Normalized Difference Vegetation Index (NDVI) is one of the most used spectral index to assess vegetation status. It is a number between -1 and 1 that has high correlation with the chlorophyll content of vegetation.

satellites are equipped with specialized instruments designed to measure various biogeophysical parameters of the Earth. For example, certain satellites within the European Space Agency’s Sentinel program are tasked with specific observational roles. ESA Sentinel-3 is particularly focused on acquiring data related to Earth’s oceans, marine ecosystems, water quality and pollution. ESA Sentinel-4 and Sentinel-5 are dedicated to the observation of the atmosphere, detecting and measuring the concentration of various atmospheric chemicals such as ozone, atmospheric water vapour content and aerosols, and pollutants as nitrogen dioxide, sulfur dioxide and formaldehyde.

AVAILABILITY Table 2.1 enlists some of the most common multispectral satellites available. The Sentinel satellites [57] are operated by the European Space Agency (ESA), and the products are open access via the Copernicus Access Hub [54].

2.1.4 Synthetic Aperture Radar satellites

Synthetic Aperture Radar (SAR) satellites represent a distinct category of Earth observation technology, utilizing a different segment of the electromagnetic spectrum compared to optical satellites. SAR systems operate primarily within the microwave band, which, as depicted in Figure 2.2, is capable of penetrating the Earth’s atmosphere [108].

Unlike optical sensors that depend on external light sources such as the sun, SAR systems actively emit microwave signals towards the Earth’s surface and capture the backscattered radiation. This active illumination allows SAR satellites to acquire data day and night, overcoming the limitations of passive sensors which require sunlight. Additionally, the lower frequency, (i.e., longer wavelength) of the microwaves, increases the penetration into snow, water, and vegetation. In fact, the SAR microwaves has the ability to penetrate atmospheric conditions, including clouds, smoke, and even to some extent vegetation and soil. Therefore, SAR can provide high-resolution images in a robust and reliable data stream for continuous Earth monitoring, especially in case of extreme weather events or wildfires [24].

Table 2.1: Comparison of some high and medium multispectral satellites

Satellite System	Provider	Spatial Resolution (Meters)	Wavelength (nm)	Radiometric Resolution	Temporal Resolution
Ikonos	DigitalGlobe	Panchromatic: 0.83 Multispectral: 4	Pan: 526-929 Blue: 445-516 Green: 506-595 Red: 632-698 NIR: 757-853	11-bit	2.9 days at 1m 1.5 days at 1.5m
WorldView-2	DigitalGlobe	Panchromatic: 0.5 Multispectral: 2	Coastal: 400-450 Blue: 450-510 Green: 510-580 Yellow: 585-625 Red: 630-690 Red Edge: 705-745 NIR1: 770-895 NIR2: 860-1,040	11-bit	1.1 days at <1m 3.7 days at 20° off-nadir or less
Pléiades-1A	Astrium	Panchromatic: 0.5 Multispectral: 2	Pan: 470-830 Blue: 430-550 Green: 500-620 Red 590-710 NIR: 740-940	12-bit	1 day
Sentinel-2A	ESA	RGB, NIR: 10 Red-EDGE, SWIR: 20	Blue: 0.490 Green: 0.560 Red: 0.665 Red-Edge: 0.705-0.783 NIR: 0.842 SWIR: 1.610-2.190	12-bit	5 days
PlanetScope Dove-R	Planet	Panchromatic: n/d Multispectral: 3.7-4.2	Coastal: 431 - 452 Blue: 465 - 515 Green I: 513 - 549 Green: 547 - 583 Yellow: 600 - 620 Red: 650 - 680 RedEdge: 697 - 713 NIR: 845 - 885	12-bit	1 day

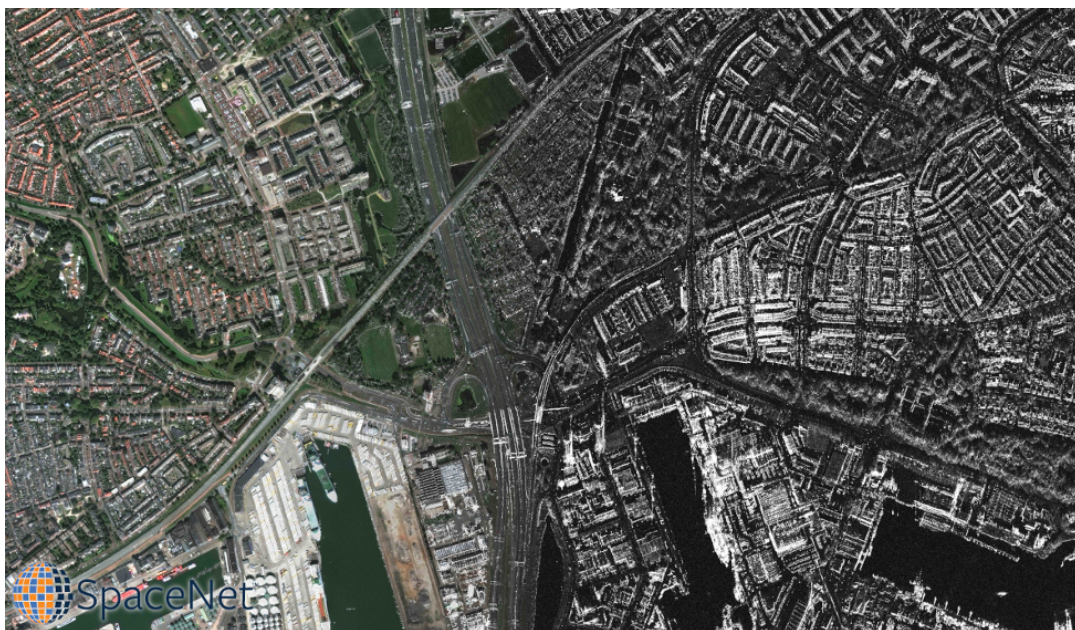


Fig. 2.10: Visual comparison between optical image (left) and SAR image (right). On the left, an optical image displays a rich variety of colors, providing a vivid representation of the Earth's surface. On the right, a SAR image, devoid of color, illustrates structural and textural details through variations in grayscale, highlighting the different imaging capabilities of these two satellite sensor types. Image taken from the SpaceNet Challenge Datasets [209].

However, SAR imagery is generated from the intensity and phase of microwave signals reflected back to the satellite's sensors, and these signals are typically represented in grayscale values. Therefore, unlike optical images, it does not contain any spectral information and the interpretation of SAR images can be challenging. Figure 2.10 shows a visual comparison between an optical and SAR image. SAR images reveal textural and structural features of the Earth's surface rather than color variations [230]. For instance, smooth surfaces like water bodies tend to reflect SAR signals away from the satellite, appearing dark in the image, while rough surfaces like urban areas or forests scatter the signal back, appearing brighter.

L-, C- and X- bands in the microwave spectrum are the most widely employed in SAR instruments, with application in mapping and land cover classification and forest monitoring [225].

Interferometric Synthetic Aperture Radar (InSAR) is an advanced remote sensing technique that involves comparing two SAR images to measure changes in the Earth's surface. These images can be captured simultaneously by sensors mounted on the same satellite platform, known as single-pass interferometry [112]) or they can be acquired during separate orbits at different times, which is referred to as repeat-pass interferometry [206]. The primary application of InSAR is to produce interferograms, complex images that represent phase differences between the two SAR images. These phase differences can be interpreted to detect subtle ground movement, providing crucial data for surface deformation mapping. This capability is instrumental in monitoring geological phenomena such as earthquakes, volcanic activity, and land subsidence. InSAR is also employed to generate high-precision digital elevation models (DEMs), which are detailed 3D representations of terrain elevations [183].

2.2 LiDAR

LiDAR (Light Detection And Ranging) is a technique that involves directing pulsed laser beams towards an object or surface and measuring the time it takes for the reflected light to return to the receiver [241]. This information can be used to reconstruct a precise and three-dimensional shape of objects and surfaces, allowing to examine both natural and human-made environments with accuracy, precision, and flexibility. LiDAR is commonly used to make high-resolution maps, with applications in surveying, geodesy, geomatics [110], archaeology, geography, geology, geomorphology, seismology, forestry [42, 256], as well as robotics. It is utilized for creating digital 3-D models of areas on the Earth's surface, ocean floor, and near coastal zones by altering the wavelength of light. Topographic LiDAR typically uses a near-infrared laser (1064 nm) to map the land, while bathymetric LiDAR uses water-penetrating green light (532 nm) to measure seafloor [141]. Figure 2.11 shows an example of a LiDAR point cloud over the City of Tallahassee, Florida.

While LiDAR technology offers exceptional precision, it comes with significant drawbacks. The equipment and operation of LiDAR technology are relatively expensive. The cost factor can be a significant barrier, especially for extensive or repeated surveys over large geographical areas. LiDAR sensors produce extremely dense point clouds, resulting in vast datasets. These large volumes of data demand substantial storage capacity and robust processing power, which can be costly and technically challenging

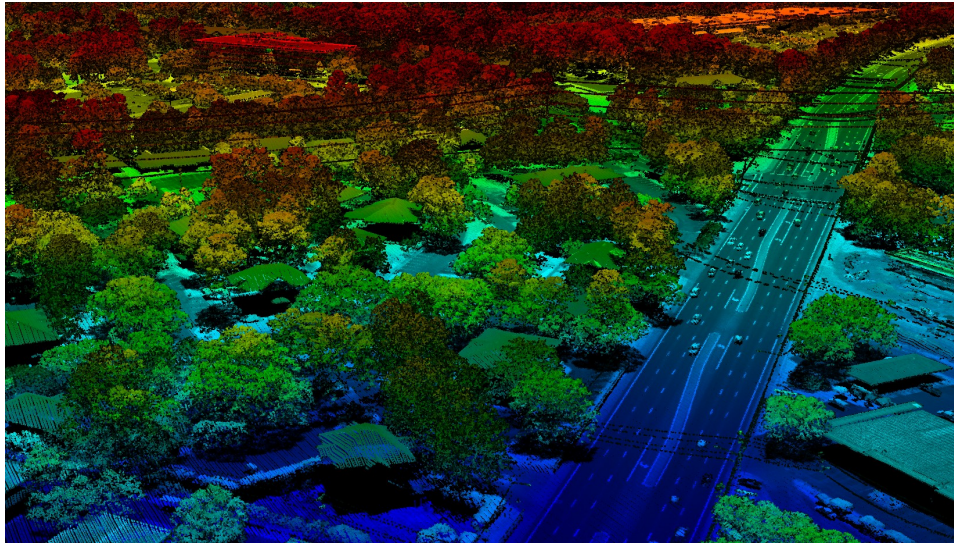


Fig. 2.11: Example of LiDAR point clouds acquired for Tallahassee, Florida. Open Access data available at [136].

to manage [246]. Due to these factors, the practicality of LiDAR for applications that require ongoing or recurrent scanning over extensive regions such as regular infrastructure monitoring is limited. Nonetheless, LiDAR data is invaluable for certain applications. It provides highly accurate elevation data and it serves as an excellent source of ground truth information. This is particularly useful for validating and calibrating other remote sensing data and for training and refining machine learning algorithms.

A computer would deserve to be called intelligent if it could deceive a human into believing that it was human.

—Alan Turing (Mathematician and Computer Scientist) [248]

COMPUTER VISION IN REMOTE SENSING

Computer Vision (CV) is a branch of Artificial Intelligence (AI) that develop methodologies to enable automatic systems with the capability to interpret and comprehend the content of visual inputs, including digital images, videos, and other forms of visual media. Image processing is the foundation of computer vision and involves algorithms and filters for image enhancement (e.g., blurring, sharpening, and denoising), color correction, image compression, geometrical analysis and feature extraction, making them more suitable for further analysis. The focus of computer vision lies in the interpretation and comprehension of the imagery content, emulating human visual perception. Currently, this is increasingly achieved through the integration of traditional image processing techniques with the capabilities of machine learning, deep learning, and pattern recognition [90, 153]. Machine learning offers a collection of methodologies to learn, make predictions or decisions based on data. In the context of computer vision, machine learning algorithms are trained on images to recognize patterns, classify objects, and infer semantic information. These technologies enable the extraction of complex patterns and features from images, facilitating a deeper understanding of visual content (Figure 3.1).

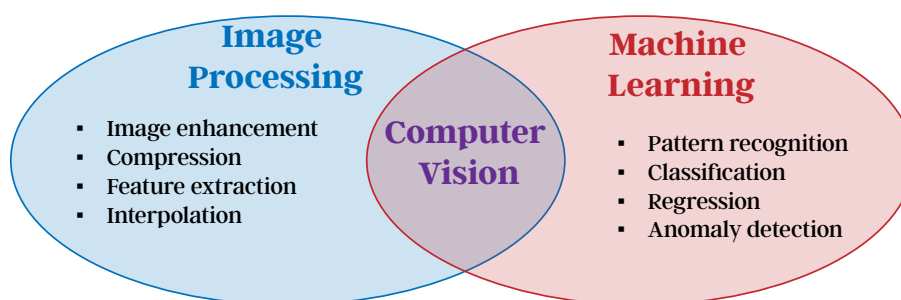


Fig. 3.1: Computer vision sits at the intersection of image processing and machine learning, blending techniques from both disciplines. Image processing encompasses a variety of techniques for processing images to improve their quality or to extract features. Machine learning brings a set of methodologies for making classifications and predictions based on data.

When applied to satellite imagery, the computer vision techniques become powerful tools for addressing the unique challenges presented by large volumes of spatial data. State-of-the-art computer vision techniques, with the ability to learn and

identify features from the environment, can process satellite images with exceptional accuracy and speed [100]. This enables the extraction of valuable insights for various applications, making it possible to rapidly interpret vast datasets that would be impractical to handle manually [221]. This interdisciplinary field is continuously evolving, with advancements in both image processing techniques and machine learning models driving the development of more sophisticated and accurate computer vision applications. The use of AI and computer vision techniques now allows for the handling of challenges in land monitoring in ways that were not feasible or easy to accomplish just a few years ago. [263]. Below we introduce the most common methods used in computer vision to process satellite imagery.

3.1 Basics of computer vision

The minimum input for any computer vision task is an image. In a digital representation, an image is a grid of small units called pixels, each represented by a numerical values that describe the luminance of a certain hue (Figure 3.2).

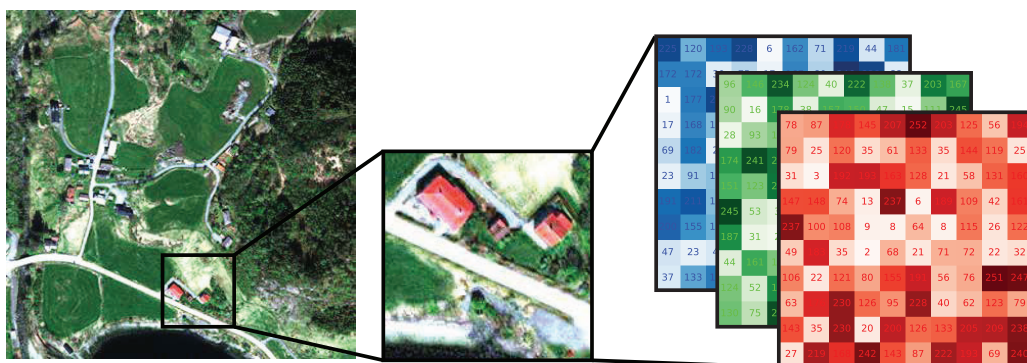


Fig. 3.2: A digital image is a matrix composed of numbers (pixels), each with finite, discrete quantities of numeric representation for its intensity. The numerical range of each pixels depends on the radiometric resolution (Section 2.1.2).

As mentioned in Section 2.1.3, the number of channels depends on the spectral resolution of the satellite image. Most satellite images have at least four channels (Red, Green, Blue and Near-Infrared bands). Computer vision algorithm analyze images by examining the pixel values, identifying certain colors or particular patterns indicative of a specific object category.

When analyzing the content of a remote sensing image, a key task often performed is the classification of its content. Classification involves assigning a discrete label or category to elements within the image to understand and categorize what is being observed. The labeling can occur at different levels of granularity, as shown in Figure 3.3.

1. In scene classification, a single label is assigned to the entire image or scene, characterizing the predominant feature or land use. This type of classification is particularly useful in land use studies where the aim is to differentiate between broad categories such as forests, urban areas, or agricultural land, and to identify

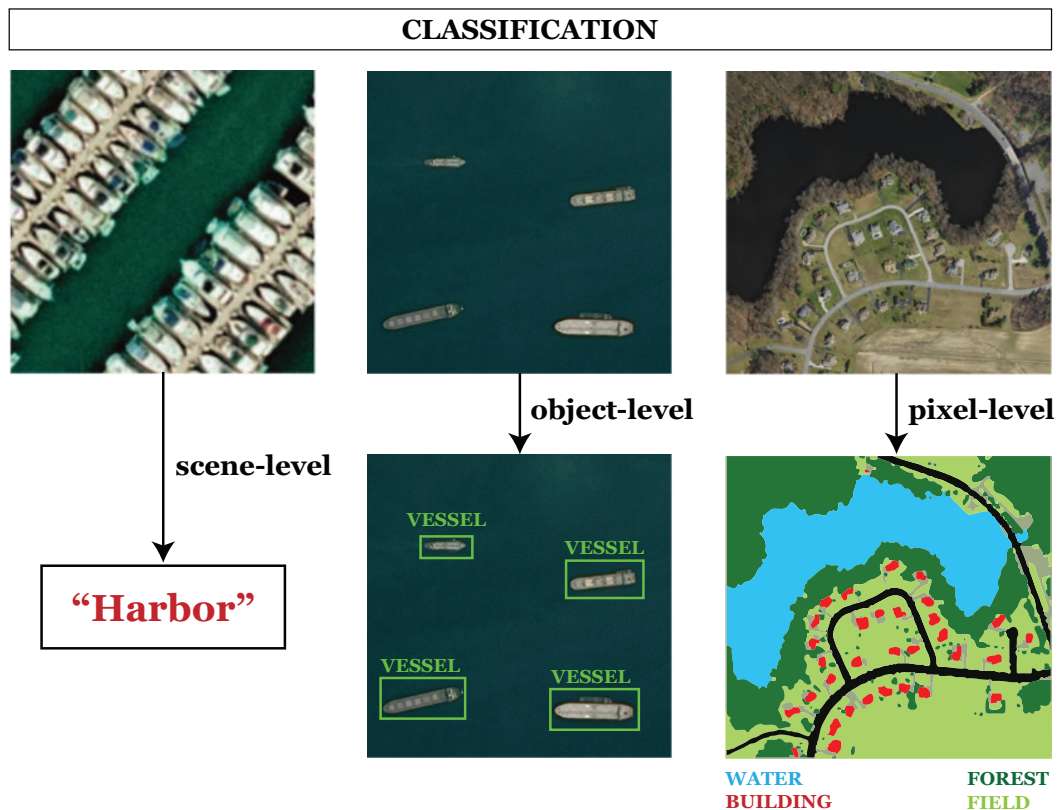


Fig. 3.3: Hierarchies of classification in remote sensing. This image showcases the varying scales at which classification can be applied: from the broad identification of a scene to the detailed segmentation of the image into pixel-level categories.

key locations like harbors or airports. However, scene classification does not provide spatial details and the precise boundaries or locations of specific objects within the scene.

2. Object classification involves identifying and labeling specific objects within an image. Unlike scene classification, object detection provides spatial information about the objects, including their boundaries and locations within the image. This is valuable for tasks such as identifying buildings, vehicles, or other distinct structures in remote sensing imagery.
3. Pixel-wise classification (also referred as image segmentation) is the most fine granularity approach. Each pixel in the image is classified, resulting in a detailed map that shows the exact boundaries and shapes of different features or land covers. Segmentation is crucial for detailed analysis where spatial precision is important, such as delineating agricultural fields, water bodies, or other specific land cover types at the pixel level.

Classification, and especially segmentation, represents a challenge in the domain of remote sensing. The integration of machine learning has significantly advanced these tasks, rendering them more attainable. Conventionally, the process begins with image processing techniques that enhance the image and extract salient features. These features are then input into machine learning models that perform the classification

[201]. With the advent of deep learning, more integrated approaches have become prevalent. Deep learning models, particularly convolutional neural networks (CNNs), are adept at both feature extraction and classification inference within a singular, unified framework. This end-to-end process can learn hierarchical representations of data, automatically determining the most effective features for the task during the training phase, and subsequently applying this knowledge to classify new, unseen data with high levels of accuracy [161]. In the field of remote sensing, the synergy between image processing, machine learning, and deep learning has forged a powerful toolkit for analyzing and interpreting satellite imagery. Below we provide a brief overview of how these tools are commonly utilized.

3.2 Image processing methods

The field of remote sensing has benefited greatly from the development of several tools of image processing and analysis techniques, each designed to extract valuable information from imagery data [19]. In this section, we explore some of the most commonly employed procedures for analyzing and interpreting remote sensing images.

3.2.1 Satellite image enhancement

To facilitate visual interpretation, the visual characteristics of objects within an image can be optimized through various image enhancement techniques. Image enhancement techniques are employed to bolster contrast, accentuate edges, and improving the overall clarity and definition of the image [9]. Additionally, normalizing the images is crucial for achieving consistent and efficient results, particularly when training deep learning models. Normalization processes adjust the images to standardize the pixel intensity distribution, which not only clarifies image details but also promotes a more homogeneous pixel distribution. This step is also essential as it can significantly accelerate the convergence of deep learning algorithms and contribute to the robustness of the model's performance [104].

Histogram normalization is a technique that rescales the pixel values across a specified range, enhancing the image contrast and making the features more distinguishable [127]. The process can be mathematically represented as follows:

$$P_{\text{out}} = (P_{\text{in}} - c) \left(\frac{b - a}{d - c} \right) + a \quad (3.1)$$

where a and b are the lower and upper limit of the resulting range, which typically are zero and one, respectively, and c and d are the lower and upper values of the input range. A simple method for determining c and d is to respectively take the min and max values of the input data. However, this can be problematic in the presence of outliers, as they can disproportionately influence the normalization range. To mitigate this, a more robust strategy is to set c and d at the 2nd and 98th percentiles of the image's pixel value histogram at each band. By doing so, the influence of outliers is reduced, providing a more representative scaling that ensures the main body of the image data is effectively normalized, thereby enhancing overall image quality for subsequent processing and analysis. Figure 3.4 shows visually two RGB images with each band's

pixel distribution and the resulting image after the histogram normalization using the percentile method.

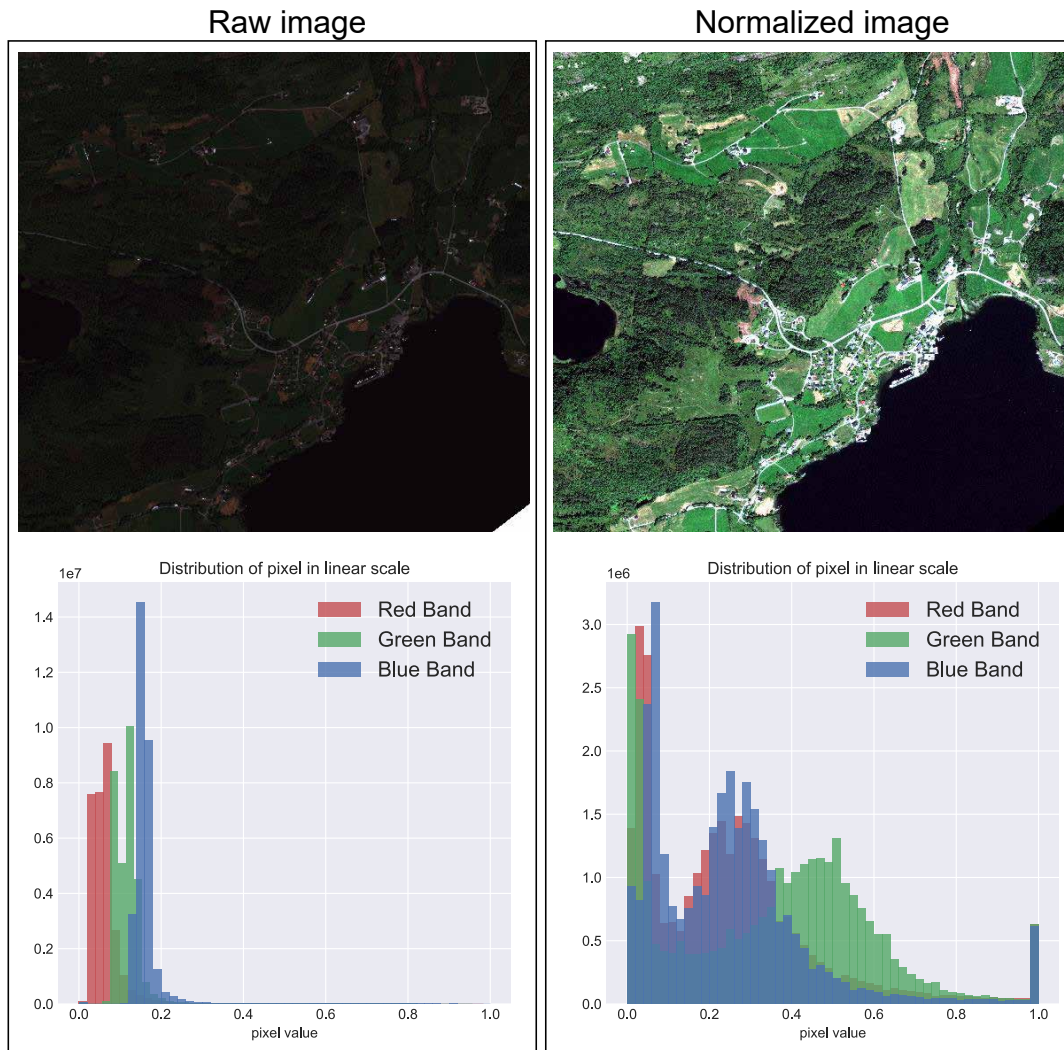


Fig. 3.4: Histogram Normalization on RGB Satellite Imagery. The left part displays the original, raw image, characterized by a pixel intensity distribution in each of the Red, Green, and Blue bands that is heavily left-skewed, where only a minority of pixel values fall above 0.4, resulting in an overall dark and detail-deficient visual. In contrast, the right part exhibits the results of applying percentile-based histogram normalization. This method has stretched the pixel intensity values to a broader range, effectively lightening the image and bringing out more discernible details, thus significantly enhancing the visual clarity and interpretability of the satellite imagery.

3.2.2 Spatial feature extraction

In computer vision, the notion of a 'feature' is fundamental and refers to distinctive elements within an image that are particularly informative or relevant for a given task [89]. The significance of a feature is determined by the extent to which it aids in accomplishing a specific objective, such as identifying an object or categorizing an image. For instance, in facial recognition technology, typical features that hold

importance are identifiable parts of the face such as the eyes, nose, and mouth. These features are key to distinguishing one individual from another and are therefore integral to the recognition process. Similarly, in the domain of image classification, the detection of specific attributes like wheels or roofs may suggest the presence of a vehicle or a building, respectively, within the image. Features can be as simple as edges and corners or as complex as shapes and textures that are distinctive to certain objects or classes. Higher level features encode more complex objects information. Computer vision algorithms often require a detailed understanding of the image, which necessitates considering the contextual, textural, and geometrical properties of features. These algorithms analyze the relationships between neighboring pixels to extract spatial information, which can include the orientation, arrangement, and frequency of patterns within the image.

CONVOLUTIONAL KERNEL: The use of convolutional kernels is one the most common and simple ways to extract low-level features in an image. These kernels, also known as filters, are small, square matrices used to transform an image through a convolution operation. The kernel is applied to the image by sliding it over every pixel and computing a weighted sum of the pixel values within its footprint. Certain kernels are designed to blur an image, averaging out the pixel values to create a smoother appearance. Others are crafted to sharpen the image, thereby enhancing the contrast between adjacent pixels to make features more distinct. There are also specialized kernels for embossing and for edge detection, which isolates and highlights the boundaries within the image. Despite their simplicity, convolutional kernels are the building blocks of more complex computer vision systems, including those based on Convolutional Neural Networks (CNNs) [47]. In CNNs, kernels are learned from the data itself during the training process, enabling the network to automatically and adaptively extract features that are most useful for the task at hand. The basic principle behind convolutional kernels is illustrated in Figure 3.5.

Convolutional kernels are versatile tools in image processing that, when strategically combined and followed by thresholding techniques, can effectively highlight and extract critical features such as edges (Canny edge detection [37]), corners (Harris corner detection [81]), and other key structural elements within an image. Finally, kernels are used for more advanced feature extractors and descriptors such as the Scale-Invariant Feature Transform (SIFT) [145] and Speeded-Up Robust Feature (SURF) [27].

TEXTURAL OPERATORS: One of the most used methods to spatially analyzing the pixels in an image is the Gray-Level Co-occurrence Matrix (GLCM). The GLCM measures how often pairs of pixel with specific values and in a specified spatial relationship occur in an image. Denoting with L the image radiometric resolution (image depth), then the GLCM is an $L \times L$ matrix where each element in the position (i, j) in the matrix counts the frequency with which a pixel with the value i is adjacent to a pixel with the value j . Figure 3.6 shows graphically the computation of the GLCM matrix. More information is provided in [85]. The GLCM is used for texture analysis in various fields of imaging science, because it can help to identify areas of an image with similar texture or to distinguish different textures within an image.

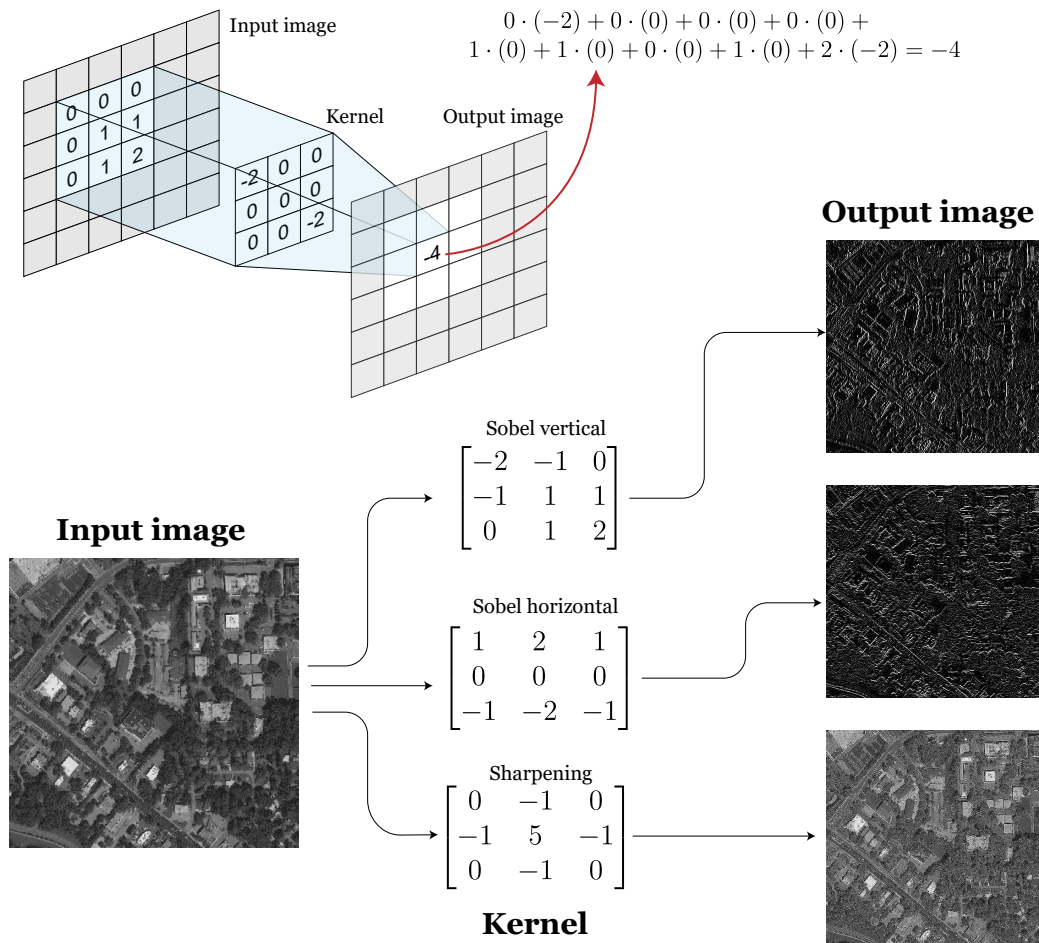


Fig. 3.5: This figure illustrates how the convolution operation is performed and how different kernels transform the input image.

Once a Gray-Level Co-occurrence Matrix (GLCM) has been constructed for an image, a set of statistical measures can be computed from this matrix. These measures are known as Haralick features, or Haralick texture descriptors [87]. They are used to quantify the texture of an image based on the GLCM and are fundamental in the analysis of spatial relationships between pixel intensities. Some of the commonly used Haralick features include contrast, correlation, energy, homogeneity and entropy. These texture operators serve as a bridge between the raw pixel data and higher-level image properties, enabling advanced image processing and interpretation tasks. Texture features can be used further as input to machine learning models to classify images, or part of images. Figure 3.7 shows an example on how such texture operators can help in distinguishing between forest and fields areas.

The GLCM is widely used technique in remote sensing to extract and classify textural patterns from satellite images [129, 162, 219]. Other feature extraction techniques include the Locally Binary Pattern (LBP) [239], and Histogram of Oriented Gradients (HOG) [169].

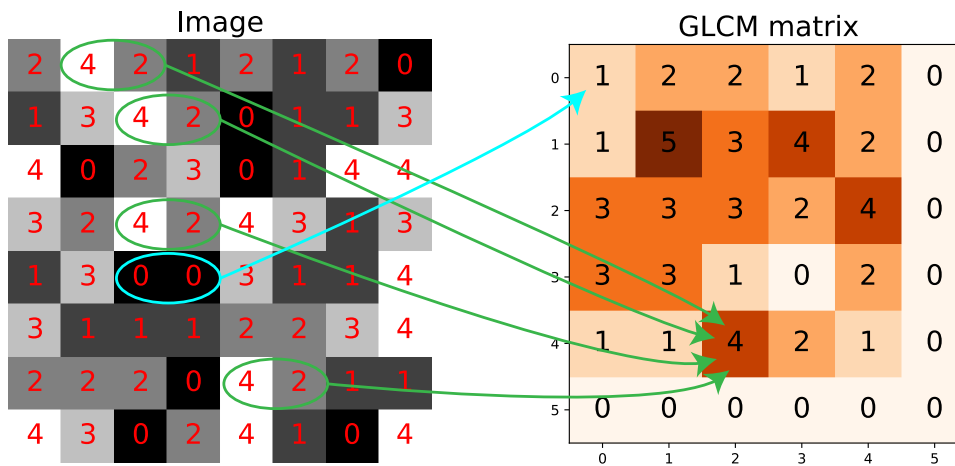


Fig. 3.6: The Gray-Level Co-occurrence Matrix (GLCM) counts the occurrence of pixels in an image. There are three occurrences in the image where a pixel with the intensity value of 4 is adjacent to a pixel with the intensity value of 2. The GLCM will reflect this by placing the value 3 at the position (4,2). This entry in the matrix indicates that this specific pixel intensity relationship occurs three times. Similarly, if the sequence where a pixel with value 0 is adjacent to another pixel with value 0 occurs just once, the GLCM will have the value 1 at the position (0,0).

3.3 Machine learning and deep learning methods

Machine Learning (ML) is a branch of artificial intelligence that focuses on developing systems capable of learning patterns, making predictions based on input data, without explicitly programmed instructions [63].

The core idea of machine learning is about developing algorithms that can learn a specific function or mapping from given input data, and use this mapping on new input data.

The learning process usually entails training a model using a dataset. In this phase, the algorithm iteratively modifies its internal parameters to reduce a certain loss function between its predictions and the expected results. After the model is adequately trained and demonstrates satisfactory performance, it can be utilized to make predictions on new, unseen data.

Machine learning methodologies are commonly categorized based on the paradigm of the learning process they utilize, with each category addressing different types of data and learning objectives. These categories include:

- **Supervised Learning:** In this paradigm, the model is trained using a dataset that includes both input features and corresponding correct outputs (labels) [109]. The model learns to map inputs to outputs, aiming to generalize this mapping to new, unseen data. Supervised learning is further divided into two main types:
 - Classification is used when the output variable is discrete, for example tree species or a land use. Figure 3.3 provided details about the levels of classification in remote sensing.

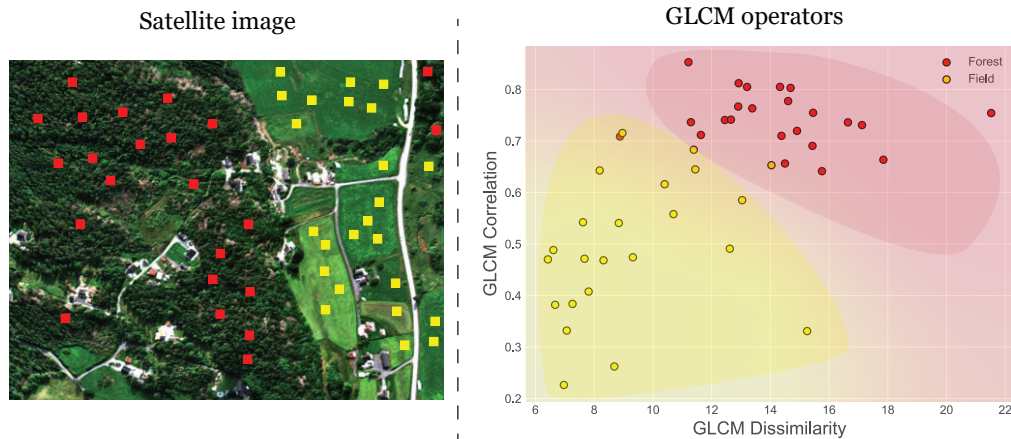


Fig. 3.7: On the left, red and yellow patches represent 10×10 pixel extracted from forested (red) and field (yellow) areas within a satellite image. On the right, we calculate the GLCM for each patch and derive the correlation and dissimilarity Haralick features. When plotted on a scatter plot, the correlation and dissimilarity values allow for a clear distinction between forest and field areas, demonstrating the efficacy of texture analysis in classifying different land cover types.

- Regression applies when the output variable is a continuous value, for example the height of a tree, the size of a glacier, or forecast wind speed.
- **Unsupervised Learning:** This approach involves training models on data that does not have labeled outcomes [15, 63]. The model tries to learn the structure and patterns inherent in the data. Common applications of unsupervised learning include:
 - Clustering: grouping data points into subsets or clusters
 - Anomaly Detection: identifying outlier data points that do not conform to the general pattern of the data.
 - Density Estimation: determining the distribution of data within the input space.
- **Semi-supervised and Weakly-supervised Learning:** hybrid approaches are developed when training examples have very limited, missing, noisy or unreliable labels [236, 260]. Unlabeled data, when used in conjunction with a small amount of labeled data, can produce a considerable improvement in learning accuracy.

FEATURE ENGINEERING: Machine learning algorithms often perform poorly when dealing directly with raw data, such as unprocessed images or datasets containing excessive or redundant information. To address this, the process of feature engineering becomes crucial. Feature engineering involves transforming the data into a format that is more suitable and effective for machine learning algorithms. In the context of image data, feature extraction means converting images into numerical values or derived metrics that capture the essential characteristics of the images [189]. The goal is to reduce the complexity of the raw data while retaining its informative aspects. The selection

of relevant features often requires domain knowledge and expertise from experts in the remote sensing domain (e.g., agronomists, forest engineers, oceanographers, and climatologists) to identify which characteristics of the data are most relevant to the problem being addressed. Indeed, when dealing with raw images, particularly in the context of remote sensing and computer vision, the extraction and combination of various derived features into a feature vector is a critical step for effective image analysis. For instance, spectral index calculation (2.1.3), filtering, color histograms, texture descriptors, edge statistics (3.2) or additional derived information (geometric properties, color histograms, edge features) can be consolidated into a comprehensive feature vector. The vector serves as a condensed representation of the image's most informative attributes. This feature vector is then used as the input for a classifier. Machine learning classifiers, trained to recognize patterns within these feature vectors, can effectively categorize the images based on the extracted features. This approach allows for a more nuanced and accurate classification than would be possible using raw pixel values alone, as it leverages the underlying information content of the images more directly and efficiently.

MACHINE LEARNING ALGORITHMS: There exist several machine learning algorithms, suited for both regression and classifications tasks. An overview of the different methods can be found in [195]. Although several machine learning models exist, they all operate under the same principle. Once the feature input is provided, machine learning models divide the feature space into distinct regions, commonly referred to as decision regions. This process is at the center of how these models make predictions or classifications. The feature space is a multidimensional space where each dimension represents a feature in the dataset. For instance, in a two-dimensional feature space, each point can be represented in \mathbb{R}^2 . The decision regions are the areas within the feature space where all points are predicted to belong to the same class. The goal of a machine learning model is to determine the boundaries of these regions based on the training data it has been fed. When a new data point (or feature vector) is input into the model, the model assigns it to one of these regions, and thus to a specific class, based on where it falls in the feature space. The effectiveness of a machine learning model in making accurate predictions or classifications largely depends on how well it can learn and define these decision regions and boundaries from the training data. A well-designed feature selection process simplifies the task of accurately dividing the feature space into meaningful decision regions.

Figure 3.8 illustrates the process of classifying land use in a satellite image, specifically distinguishing between forests and farmlands, through a simple machine learning pipeline. The effectiveness of this classification heavily relies on the number and quality of features used, underscoring the significance of the feature engineering process. In this example, the classification is based on just two simple features: average color and a single texture operator. However, for more complex scenarios, such as multi-class classification or images with diverse content, a broader set of features is generally required to achieve accurate results.

A potential practical challenge is dealing with an excessively large number of features, many of which might not significantly contribute to the predictive power of the model. To address this challenge, techniques such as feature selection and dimensionality

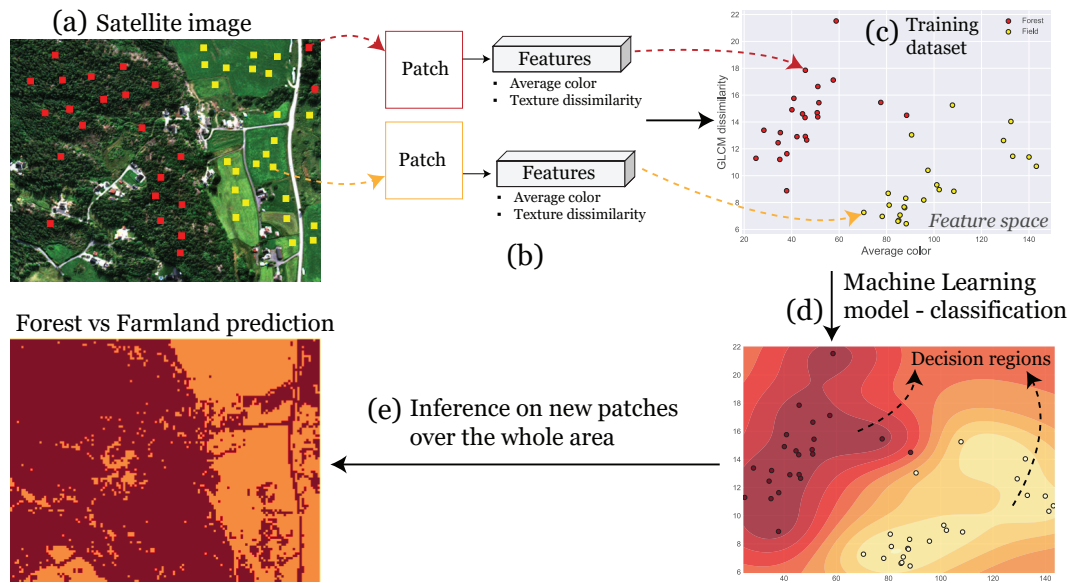


Fig. 3.8: Process of classifying land use in a satellite image with a classic machine learning pipeline. (a): Similarly to Figure 3.7, red and yellow patches represent 10×10 pixel extracted from forested (red) and field (yellow) areas within a satellite image. (b): feature extraction process where each patch is converted into a feature vector, incorporating metrics like average color across bands and Haralick texture dissimilarity score. (c): illustrates the feature space, formed by the aggregate of all feature vectors from the extracted patches (training dataset). (d) A machine learning model (in this example a Support Vector Machine) is trained to divide the feature space into decision regions. (e): demonstrates the application of this model: feature vectors are calculated for arbitrary patches in the image, and the model assigns a corresponding label (forest or field) based on its learned decision regions.

reduction are employed. This include techniques like Principal Component Analysis (PCA) [121] to transform the feature space to a lower dimension, and reducing the number of features while retaining most of the original data's variability and information [229]. These methods help in building more efficient, effective, and interpretable models.

The most common ML methods used in remote sensing are Support Vector Machines (SVM) [164],[181], Random Forests (RF) [29], [215], AdaBoost [259], Gradient Boosting (XGBoost) [7] and Artificial Neural Networks (ANNs) [152].

DEEP LEARNING: Deep learning is a subset of machine learning that employs artificial neural networks with multiple hidden layers to approximate a complex function, which is where the term "deep" originates. Deep learning models can process raw data directly and autonomously extract relevant features, a process traditionally handled by manual feature engineering in classical machine learning approaches.

Each layer comprises a certain number of neurons, where each neuron typically performs a simple transformation (i.e., a weighted sum followed by a non-linear activation). Information passes through these layers sequentially, allowing the network to build increasingly abstract representations of the data. Deep learning models are highly flexible and can be applied to a wide range of tasks, including speech recognition

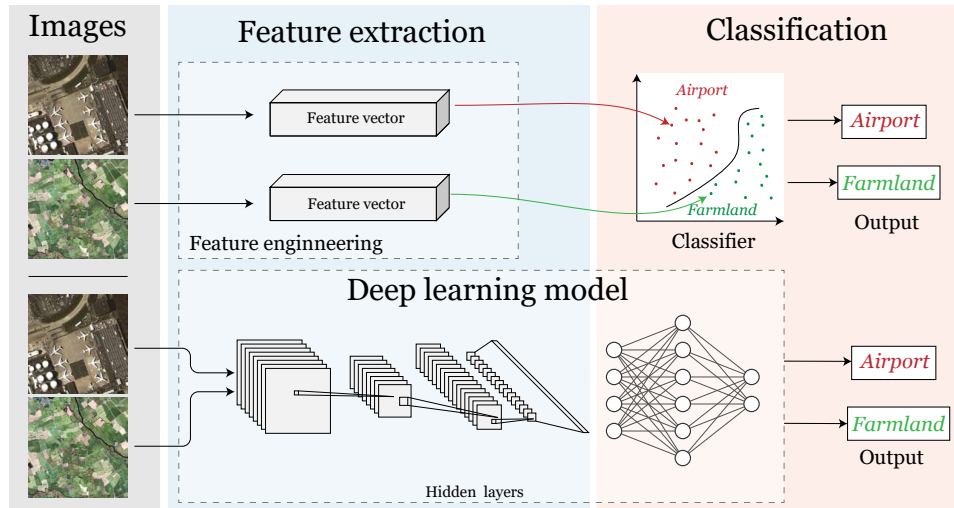


Fig. 3.9: In traditional machine learning approaches, a significant part of the process involves feature engineering — the manual extraction and selection of relevant features from raw data. These features are then used as input for a machine learning model to perform tasks like classification or prediction. In contrast, deep learning models streamline this process by integrating both feature extraction and inference within a single model framework. As data passes through the successive layers of a deep neural network, the model automatically learns to extract and represent features. After the feature extraction, the same deep learning model continues to process these learned features to make predictions or decisions based on them. This end-to-end processing capability allows for a seamless flow from raw input to final output.

[191], natural language processing [132], and complex decision-making tasks [204]. Deep learning is nowadays heavily used for image classification and segmentation [161, 243]. However, deep learning models typically require large amounts of training data to perform well. The more data they are trained on, the better they become at extracting features and making accurate predictions or classifications [163]. Figure 3.9 shows the main difference between machine learning and deep learning.

However, there is a trade-off between the flexibility and effectiveness of deep learning models and their interpretability, which is well-acknowledged challenge in the field [18]. This issue is often referred to as the "black box" problem in machine learning.

In traditional machine learning approaches with manual feature engineering process, the nature and significance of each feature are well-understood and explicitly defined by the data scientist. For instance, in the satellite image classification example (referenced in Figure 3.8), features like color and texture are selected and engineered with a clear understanding of their relevance and representation. In contrast, deep learning models, especially those with multiple hidden layers, autonomously identify and process features in a way that is not always interpretable. The features extracted by these models, particularly in the deeper layers, often do not correspond to intuitive or easily understandable characteristics. While these features may be highly effective for the task at hand, understanding exactly what they represent and how they contribute to the final decision or prediction can be challenging. This lack of transparency can be a significant issue, especially in applications where understanding the decision-making process is crucial, such as in medical diagnosis or autonomous driving. It raises

concerns about accountability and trust in the models, particularly in scenarios where decisions need to be justified or explained. Efforts to address this challenge include the development of techniques in the field of explainable AI (XAI), which aims to make the workings of complex models more transparent and their decisions more interpretable. These efforts involve creating models that are both accurate and interpretable, or developing methods to explain the decisions of existing complex models. We discuss this further in Section 3.4.

Two of the most prevalent types of deep learning models are Recurrent Neural Networks (RNNs) [93] and Convolutional Neural Networks (CNNs), each particularly suited to specific types of data and tasks. RNNs are designed to process sequential data, making them highly effective for tasks involving time series analysis. CNNs are particularly well-suited for analyzing imagery. Given the focus on computer vision in this context, CNNs are particularly relevant for this thesis and they are further described below.

3.3.1 Convolutional Neural Networks (CNNs)

Convolutional Neural Networks (CNNs) is a class of deep neural networks specifically designed for processing data that has a grid-like structure, such as images [47, 140]. The architecture of a typical CNN includes several key components:

- **Convolutional Layers:** As in the traditional image processing methods described in 3.2.2, convolutional layers in CNNs use filters to extract features from the input images. These filters, or kernels, slide over the image and perform element-wise multiplications followed by a summation. In the initial layers of a CNN, the filters typically detect simple patterns like edges and textures. As the data progresses through the network, subsequent convolutional layers combine these simple patterns to detect more complex features. Compared to the traditional filters however, these filters are learnable during the training process.
- **Pooling Layers:** These layers are used to reduce the spatial dimensions (width and height) of the feature maps obtained from the convolutional layers. Pooling helps in decreasing the computational load and the number of parameters.

Figure 3.10 illustrates two influential deep learning models, each serving distinct purposes in computer vision.

The first model, VGG16, achieved notable success in the ImageNet Large Scale Visual Recognition Challenge (ILSVRC) in 2014 [194] setting a benchmark for image classification tasks. VGG16's architecture is particularly effective in classifying images into predefined categories [190, 262] and it is often fine-tuned for different applications using transfer learning techniques [218]. However, the VGG16 model, like other image classification architectures, is not inherently suited for segmentation tasks, as it tends to lose spatial information which is crucial for pixel-level labeling (refer to Figure 3.3.) To address segmentation challenges, architectures such as Fully Convolutional Networks (FCNs) have been developed [143]. FCNs are designed for semantic segmentation and are characterized by their use of only locally connected layers like convolution, pooling, and upsampling, while removing dense layers. This enables them to maintain spatial

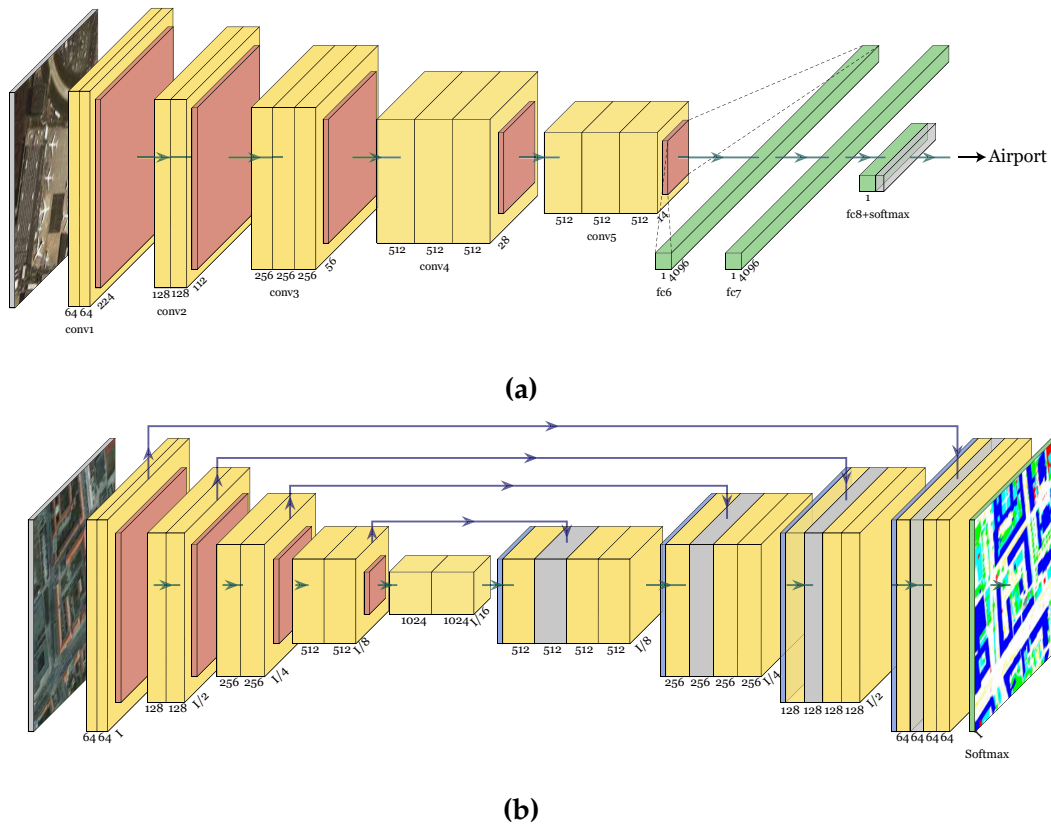


Fig. 3.10: Two popular deep learning architectures for computer vision tasks. (a): VGG16 for image classification. (b): UNet for image segmentation. Legend: convolution operation (yellow), pooling (red), up-sampling (blue), dense layers (green), concatenation (gray)

information. One of the most used example of FCNs is UNet, initially conceived for biomedical image segmentation [193]. UNet stands out with its unique architecture that includes a contracting path for context capture and a symmetric expanding path for detailed localization. This structure facilitates precise segmentation across various fields within computer vision, including remote sensing. The versatility and effectiveness of the UNet architecture have led to its widespread adoption and adaptation in a multitude of segmentation tasks in remote sensing [149, 214, 261]. Throughout this thesis, modified versions of the UNet architecture have been extensively utilized. The original UNet model, known for its efficiency in image segmentation, has been adapted and customized to suit the specific requirements of the tasks and different datasets addressed in our research.

3.3.2 Convolutional Auto-Encoders (CAEs)

Convolutional Auto-Encoders (CAEs) [41] is another class of deep learning models. They are a subset of CNNs that employs a similar toolkit of convolutional kernels and pooling layers. CAEs however operate in an unsupervised manner, eliminating the need for labeled data. Figure 3.11 shows the general architecture of a CAE.

An input image being is fed into the encoder part of the network. The encoder is

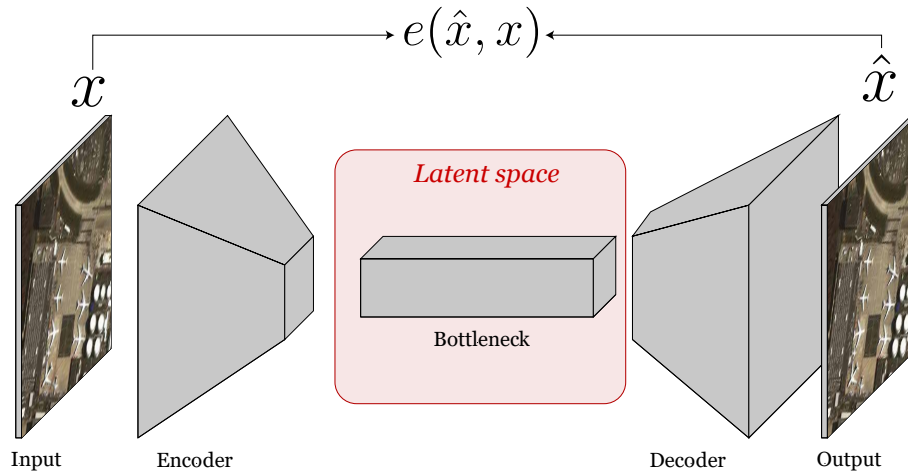


Fig. 3.11: Architecture of a Convolutional Auto-Encoder (CAE).

typically composed of a series of convolutional and pooling layers, as those found in Fully Convolutional Networks (FCNs) in 3.3.1. These layers progressively downsample the image, mapping its content into a compact, encoded representation in a lower-dimensional latent space called bottleneck. Following encoding, the network transitions to the decoder phase. The decoder aims to reconstruct the original image from the encoded representation. This involves a series of layers that gradually upsample the encoded representation back to the original image size. The training objective of a CAE is to minimize the reconstruction error $e(\cdot)$, which is the difference between the input image x and its reconstructed output \hat{x} .

The latent space is generally set smaller than the input dimensionality. Therefore there is an inherent loss of information, leading to imperfect reconstruction and the network has to compress the data. This constraint forces the CAE to learn and retain only the most salient and relevant features of the input in its encoded representation. Consequently, CAEs are effective tools for feature extraction and dimensionality reduction, capturing the important content of the input [30, 158]. However, as discussed in Section 3.3, because autoencoder is a type of deep learning models, the extracted features can be difficult to understand and interpret.

Figure 3.12 demonstrates the application of a convolutional autoencoder in extracting features from the EuroSAT dataset [92], a collection of 27,000 labeled 64×64 images from the Sentinel-2 satellite, aimed at land use and land cover classification.

In this example, each image from the dataset is processed through an autoencoder, which encodes the image into a 1024-dimensional feature vector. These high-dimensional vectors encapsulate the essential characteristics of the images, capturing meaningful patterns relevant to land use and land cover types. To visualize such feature vectors the t-distributed Stochastic Neighbor Embedding (t-SNE) technique [235] is used to map them in a more interpretable two-dimensional space (i.e., plane). The t-SNE is a powerful nonlinear dimensionality reduction method that maps high-dimensional data to a lower-dimensional space (in this case, \mathbb{R}^2), ensuring that similar objects in the high-dimensional space are placed close together in the reduced space, while dissimilar objects are placed far apart. Each point in the plane corresponds to the encoded representation of an image, and these points are color-coded according

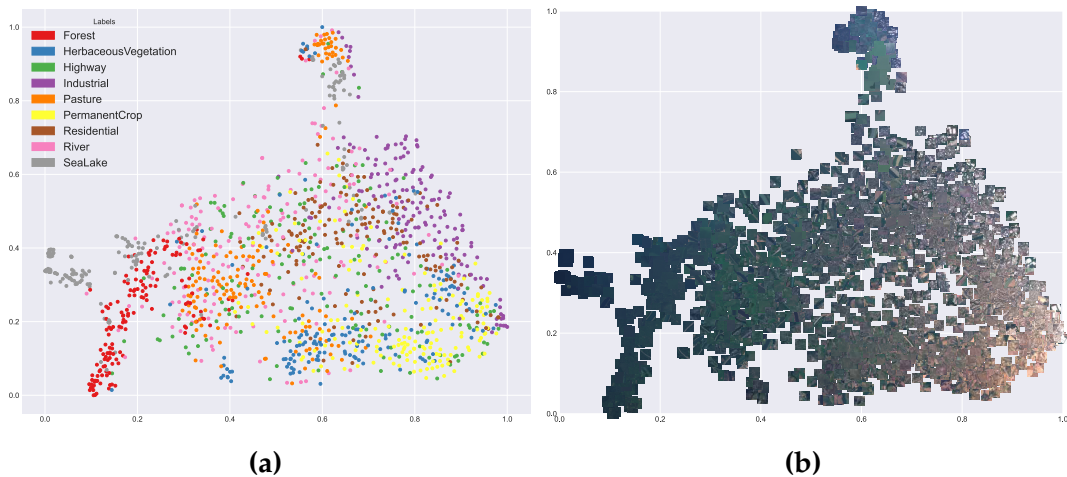


Fig. 3.12: This figure illustrates the process of encoding satellite images from the EuroSAT dataset [92] into a 1024-dimensional feature space using a convolutional autoencoder. The feature vectors are projected onto a two-dimensional plane using t-distributed Stochastic Neighbor Embedding (t-SNE), facilitating a visual representation in \mathbb{R}^2 . (a): Each point represents the encoded features of an image, with the points color-coded according to the various land cover and land use categories defined in the EuroSAT dataset. (b): To enhance interpretability, actual images from the dataset are placed at their corresponding locations in the latent feature space.

to the various land use and cover categories defined in the EuroSAT dataset, such as forests, rivers, highways, and so forth. As a result, similar images in the feature space are located near each other in the t-SNE plot. Clusters of points representing forests, pastures, and lakes are situated in closer proximity to each other, suggesting a higher degree of similarity in their encoded features. In contrast, categories like permanent crops or residential areas are noticeably distanced from these natural land cover types, indicating distinct feature characteristics as perceived by the autoencoder. Furthermore, the class 'highway' is uniformly spread across the feature space. This observation aligns well with the real-world understanding that highways traverse through diverse types of land use. Unlike more homogeneous categories like forests or lakes, highways can cut across urban areas, fields, forests, and various other landscapes.

Convolutional autoencoders have recently gained prominence in the field of remote sensing due to their effectiveness in feature extraction through unsupervised learning. They have demonstrated their versatility and efficiency in several key areas such as unsupervised change detection [148], [53], semantic segmentation [144], and building extraction [185]. This thesis also extensively utilizes convolutional autoencoders to extract features from satellite images, as presented in Part II.

Variational Autoencoders (VAEs) are a specialized type of autoencoder that introduce a probabilistic approach to encoding data. Unlike traditional autoencoders, which learn a deterministic function to compress the input data into a latent (bottleneck) space and then reconstruct it, VAEs model the latent space using probability distributions, typically Gaussian [20]. In VAEs, the encoder does not output fixed values for the encoded representation of the input data. Instead, it produces parameters (mean and variance) of a probability distribution (typically the Gaussian distribution), repre-

senting the data in the latent space. Due to the probabilistic nature and regularization of the latent space, VAEs are considered generative models, as they can generate new data that is similar to the training data [49, 95].

3.4 Recent trends in computer vision for remote sensing

Recently, deep learning has seen significant advancements within the fields of computer vision and remote sensing. Convolutional Neural Networks have emerged as a core technology driving numerous applications in these fields. However, alongside this growth, there is a burgeoning interest in enhancing the interpretability of machine learning models, evolving training paradigms, and exploring novel model architectures.

As previously discussed, deep neural networks, despite being at the forefront of various remote sensing tasks, often operate as "black boxes". Unlike traditional methods where feature vectors are manually engineered and their significance is well-understood, the features learned by deep learning models can be abstract and not easily interpretable in physical or intuitive terms. To address this, recent developments in the field have focused on methods that enhance model transparency and offer insights into the decision-making process. Techniques such as Grad-CAM (Gradient-weighted Class Activation Mapping) [198] and LIME (Local Interpretable Model-agnostic Explanations) [10] have been developed. These methods aim to highlight which pixels or regions of an image are most influential in the model's predictions and improve transparency of the decision-making process. These interpretability techniques are now being applied in the context of remote sensing as well [74, 113].

Another recent research direction is the adoption of federated learning paradigms, particularly in applications involving sensitive or private remote sensing data. Federated learning involves training a machine learning model across distributed databases without exchanging them. One of the primary advantages of federated learning is its ability to maintain the confidentiality of individual datasets. Each client in the federated network trains a model locally with their own data and only shares model updates (e.g., gradients or parameters), preserving data privacy. Despite the decentralized training, the shared knowledge from all clients is aggregated to improve the overall model performance. Recent advancements in federated learning techniques specifically tailored for remote sensing are explored in various studies, such as those by Zhu et al., 2023 [269], Byktas et al., 2023 [36], and Zhang et al., 2023 [267].

In 2017, Vaswani et al. [237] introduced a novel architecture called Transformer, which marked a significant milestone in the field of Natural Language Processing (NLP). The core innovation of the Transformer is its self-attention mechanism, which enables the model to weigh the significance of different parts of the input data (like words in a sentence) relative to each other. This mechanism allows the Transformer to understand long-range dependencies within the data, a critical feature for handling sequences like sentences where context and order are essential. Some of the most well-known language models, such as Google BERT [46] and the GPT-based models (like OpenAI Chat-GPT), are built on the Transformer architecture. These models have achieved state-of-the-art performance in a range of NLP tasks

In 2020, the concept of Transformers was extended to the field of computer vision by Dosovitskiy et al. [50] with the introduction of Vision Transformer (ViT). The ViT

model adapts the Transformer architecture for image processing by treating images not as a grid of pixels but as a sequence of patches, similar to how words in a sentence are treated in NLP. This approach marked a significant departure from traditional convolutional models in computer vision, as ViT is free of convolutional layers. Recent developments of transformers used in computer vision are presented in [86]. Motivated by the recent advances in computer vision, researchers in the the remote sensing field have explored te use of vision transformers for a wide array of tasks. A complete survey covering recent transformer-based methods using very optical and synthetic aperture radar (SAR) imagery is provided at [14].

In 2023, researchers from Meta, inspired by large language models, have introduced Segment Anything Model (SAM) [122]. SAM represents a groundbreaking approach in image segmentation, particularly with its capability for zero-shot segmentation. This innovative model is trained only on labeled data from certain known (seen) categories, but is still able to extend its segmentation capabilities to categories that it has never seen during training. Building on this advancement, in 2023 Osco et al. [178], adapted SAM for remote sensing imagery. Recent works make uses of SAM and existing remote sensing datasets to develop pipelines for generating new large-scale segmentation datasets [242, 257].

Every leaf of the tree becomes a page of the book, once the heart is opened and it has learned to read.

— Saadi (13th's century Persian poet) [251]

CHAPTER 4

POWER LINE MONITORING USING SATELLITE IMAGES

Power transmission lines, responsible for transporting high-voltage electricity over long distances from power plants, stretch over 7 million kilometers globally. These transmission lines feed into a more extensive network of distribution lines, spanning over 72 million kilometers, which carry lower-voltage electricity directly to consumers [58]. These transmission and distribution lines constitute the backbone of the global electric power market. This market is valued at approximately 151.99 billion USD and is projected to grow at a Compound Annual Growth Rate (CAGR) of 6.4% from 2023 to 2030, indicating a substantial expansion in the coming years [211].

The global network of power lines is expected to undergo a significant expansion to accommodate the increasing customer demand. In tandem with this growth, the development of super grids and the rising integration of renewable energy sources are anticipated to drive the deployment of even longer-distance grid systems. This expansion of the grid network will add layers of complexity to the tasks of grid monitoring and maintenance. Due to this increased complexity and scale, there is a growing need for new, automated methods for conducting essential monitoring tasks along power lines. Traditional, manual approaches will become impractical or too costly as the grid expands and diversifies over a large scale. Therefore, the future of grid management must rely heavily on innovative solutions that can offer efficient, low-cost monitoring and maintenance to keep pace with the evolving demands of the global power grid infrastructure.

In recent years, there has been a notable shift towards the adoption of advanced remote sensing methods for power line inspection, leveraging technologies such as LiDAR and Unmanned Aerial Vehicles (UAVs) [111, 154, 160, 200]. UAV and LiDAR inspections greatly reduce inspectors' work and improve the efficiency of power line monitoring. However, this shift to more technologically advanced methods also introduces new challenges, primarily related to data management and operational costs. One of the main issues with both UAV and LiDAR inspections is the generation of a substantial amount of data [142]. While these methods provide detailed and high-resolution imagery, the sheer volume of data produced can be overwhelming. Processing, analyzing, and storing this data require significant computational resources and can be time-consuming, posing a challenge in terms of data management efficiency. Furthermore, despite their advantages, UAV and LiDAR inspections are not without cost implications. The acquisition and operation of these technologies can be expensive,

and their coverage can sometimes be limited. UAVs, for instance, may have restrictions in terms of flight duration and range, while LiDAR systems are limited by their deployment and operational requirements. These limitations can affect the overall cost-effectiveness and the extent to which these technologies can be deployed for large-scale power line monitoring.

Space technologies, particularly satellite imagery, hold significant potential in enhancing the efficiency of power line monitoring at a lower cost. According to [173], the market for satellite-based earth observation (EO) predicts that annual revenues from Big Data analytics utilizing satellite imagery will hit approximately \$1.3 billion by 2026 (Figure 4.1).

Satellite imagery can offer wide-area coverage and frequent updates at lower costs than UAVs or other imagery sources. This approach not only enhances the reliability and efficiency of power distribution, but also reduces the operational costs and environmental impact associated with traditional ground-based or aerial monitoring methods. Indeed, while satellite imagery offers significant advantages in terms of scalability and broad-

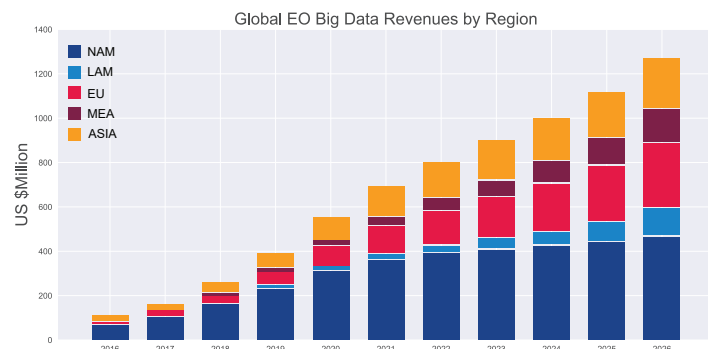


Fig. 4.1: Satellite-based earth observation market forecast by region. Source: [173].

area coverage for power infrastructure monitoring, there are tradeoffs, particularly in terms of spatial accuracy and detail. This limitation necessitates a balanced approach that combines the strengths of both satellite-based monitoring and traditional visual inspections. Visual inspections remain crucial for detailed assessment of specific power line components such as insulators or the status of power poles, which typically require a high level of detail to evaluate effectively. Due to spatial resolution constraints, such components may not be visible in satellite images. Therefore, ground-based or close-range aerial inspections continue to play an essential role in comprehensive infrastructure assessments, providing the level of detail necessary for evaluating these critical elements [170]. However, satellite imagery proves highly beneficial for general monitoring of power line corridors and rights of way. It enables utilities to maintain situational awareness over vast areas with greater efficiency and at a lower cost compared to traditional methods. Satellite imagery has been recently used for different power lines inspection tasks such as identifying the transmission towers and relative corridors [116], assessing direct damages to power lines due to landslides [88], and estimate fire ignition points on transmission line [268].

The European Space Agency (ESA) has been actively supporting the development of various initiatives that leverage satellite technologies for energy sector applications. One of these initiatives is the GridEyeS project [55] (introduced in Section 1.3), which initialized the research presented in this PhD thesis. In the subsequent sections, we review and associate our research questions with our contributions, demonstrating how we have addressed these questions through our published papers.

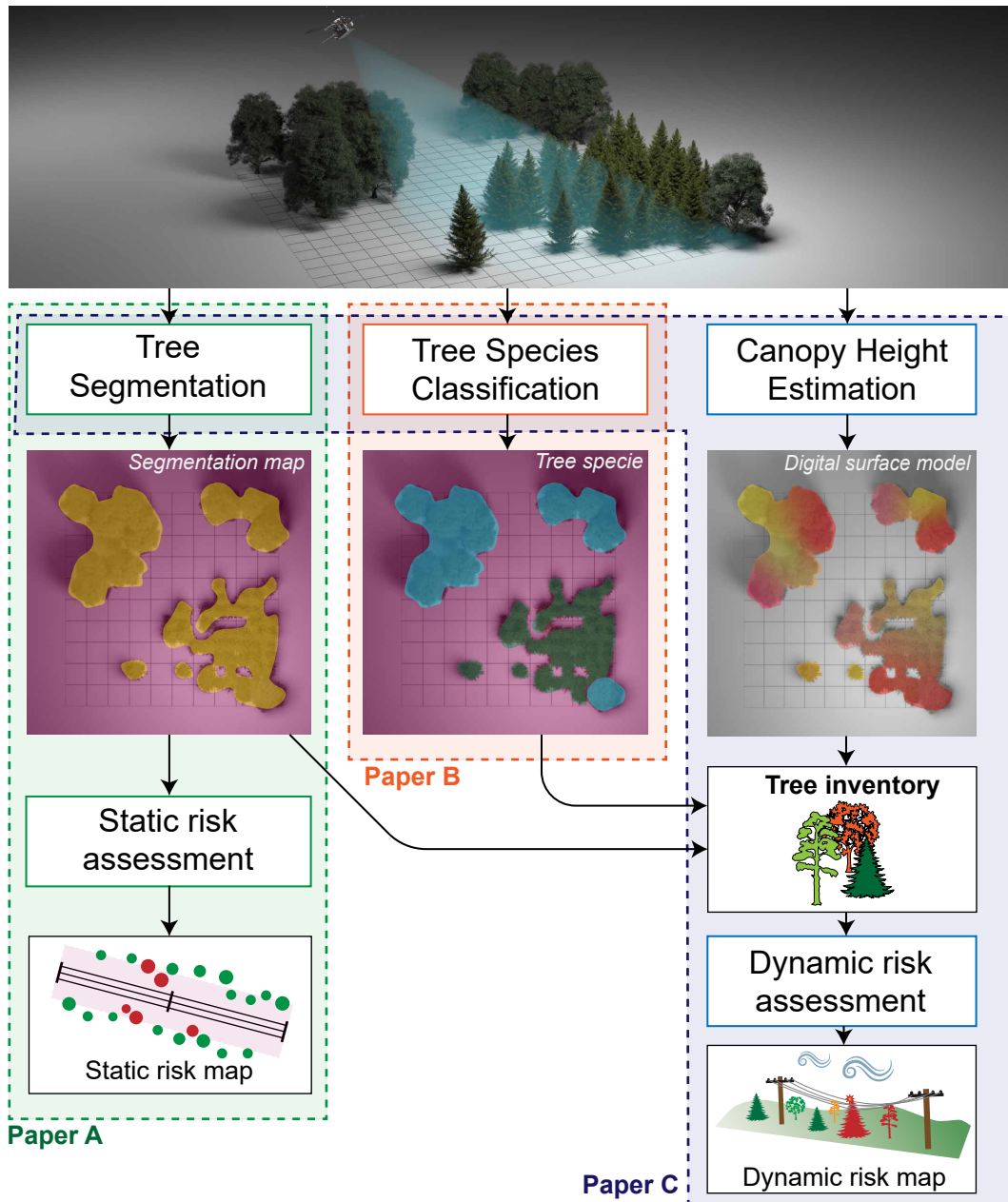


Fig. 4.2: Overview of our research on power line monitoring.

OVERVIEW AND ROAD-MAP OF THE PHD RESEARCH ON POWER LINE MONITORING Figure 4.2 provides an overview of the research papers attached to this thesis focusing on power line monitoring. Each paper in this collection is dedicated to exploring a specific task related to this area of study.

- Paper A started our research on this topic. It is centered on detecting trees along power lines and developing a risk map. Such risk map is created based on the proximity and distance of trees from the power lines, aiming to identify potential hazards that these trees might pose.
- Paper B delves into the classification of tree species. It focuses on refining available tree species databases, enhancing the accuracy and reliability of species identification.

- Paper C combines and integrates the results from our different past works, in particular Paper A [70], Paper B [68] and [65], to characterize comprehensively trees along power lines. Moreover, it estimates the tree vulnerability to the power lines under varying conditions, particularly considering the impact of environmental factors such as weather.

The code of our framework for power line monitoring is available on GitHub [64].

4.1 Vegetation detection

Vegetation, particularly when interacting with strong winds and other extreme weather events, has been identified as a primary contributor to power outages, as supported by various studies and reports [12, 82]. This issue was further substantiated through extensive surveys conducted with numerous companies and end-users during the GridEyeS project [3, 210]. Diverse stakeholders underline the importance of an effective vegetation management as a critical component in maintaining the integrity of power networks (see Figure 4.3). Effective vegetation management involves regularly assessing the growth and proximity of trees and other plants by setting a clearance zone along power lines and their right-of-ways. After surveys, the vegetation management teams consider appropriate actions such as trimming, removal or replacing trees with less-dangerous trees, to mitigate risks on the infrastructure.

Given this insight, the project emphasized monitoring and managing vegetation encroachment along power lines. Vegetation growing too close to power lines poses a substantial risk, as it can lead to disruptions in service during extreme weather conditions.

Several studies have explored the use of stereo pairs of satellite images for identifying trees along power lines, demonstrating the potential of this approach in vegetation management near power infrastructure, [13, 124, 255]. However, obtaining stereo pairs that are accurately aligned and suitable for creating precise 3D models can be technically challenging. Furthermore, the process of capturing and processing stereo satellite imagery can be costly. This cost factor becomes particularly significant when monitoring extensive power line networks, making it less feasible for widespread, routine applications [79].

Vegetation detection using single images is a topic that has gathered considerable attention, especially in the contexts of forest management and urban and agricultural area monitoring. Traditional image processing tools have been effectively employed for vegetation detection, as evidenced by several studies, [97, 98, 126, 182]. These approaches, however, tend to be most effective in environments where trees are easily distinguishable, such as areas with low-density vegetation or in orchards where trees are regularly spaced. This is not typically the case for the areas surrounding power lines'



Fig. 4.3: A tree fallen onto the power line in Innlandet, Norway, in 2021. Credits: NRK [172].

4.2 The importance of tree species for power lines

rights of way (ROW), where vegetation can be denser and more randomly distributed, posing challenges for traditional methods. Machine learning, when integrated with vegetation indices and other relevant features, has also been utilized effectively for vegetation detection. By combining these indices with other features and employing machine learning techniques, researchers have developed more sophisticated and accurate methods for vegetation detection [21, 151, 227]. In recent years, Convolutional Neural Networks (CNNs) have emerged as a dominant methodology in various fields, including vegetation detection, classification and segmentation [120, 138]. For instance, [22] proposed a semantic segmentation-based deep learning method to classify vegetation using RGB images. Similarly, segmentation models like the U-Net architecture have been used to analyze high-resolution satellite images for forest mapping [128, 151, 240]. However, a significant limitation of deep learning methods, particularly in remote sensing applications, is their reliance on large labeled datasets for training, which can be scarce and expensive to acquire for satellite imagery [245].

While various methodologies have been explored for vegetation detection, specific focus on assessing the risk posed by vegetation encroachment in relation to power lines has been limited in previous works. Our paper, titled "*Automated Power Lines Vegetation Monitoring Using High-Resolution Satellite Imagery (Paper A)*" [70], and published in the IEEE Transactions of Power Delivery journal addresses this gap. It answers the first research question: "RQ 1-1: How to assess the risk of vegetation near power lines using high-resolution optical satellite images?" by proposing a semi-supervised approach for vegetation detection near power lines. We investigate spatial features (such as the ones presented in Section 3.2.2) and train a machine learning classifier to perform a pixel-level segmentation of trees. The output is further combined with an unsupervised segmentation technique based on deep learning. Vegetation in the vicinity of power lines is identified, and a risk index is formulated based on the density and proximity of the vegetation to the power lines. The key output of this study is a risk map that pinpoints vegetation-related threats along power lines. This map can be a valuable tool for electric utility companies, providing them with updated situational awareness that is crucial for effective vegetation management. The outcomes from satellite images exhibited a high degree of correlation with the existing LiDAR survey data, which served as the ground truth for our use case area. Additionally, in the paper, we offer practical insights for electric utilities regarding the utilization of satellite images for power line monitoring.

The complete paper is attached in Chapter A.

4.2 The importance of tree species for power lines

In the initial phase of the GridEyeS project, our focus was primarily on assessing the risk posed by vegetation to power lines. Building on this foundation, we expanded our research to include also the identification of tree species. The importance of having a detailed inventory of tree species extends across various fields such as ecology and conservation [254], wildlife habitat mapping [105], sustainable land use management [25], and urban planning [133].

However, power line operator teams can also benefit from tree species inventories by significantly enhancing the effectiveness of vegetation management strategies. Different

tree species have varying growth rates, sizes, and branching patterns, which can affect how they interact with power lines. By identifying the species, operators can tailor their tree trimming and cutting plans more effectively. For instance, faster-growing species might require more frequent maintenance, while certain species might have characteristics that pose higher risks to power lines during extreme weather events [264]. Additionally, recently, there has been a shift towards more environmentally friendly vegetation management practices in the context of power line maintenance. Rather than indiscriminately clearing all vegetation within the rights of way of power lines, a more conservative approach is being adopted. New strategies focus on selectively replacing certain tree species with others, aiming to balance the need for safety and reliability in power transmission with the goals of maintaining biodiversity and sustainability [176, 228]. Thus, the extension of our research to include tree species identification not only broadens its applicability across various environmental and urban planning contexts, but also provides a critical tool for power line operators to optimize their vegetation management practices while contributing positively to environmental conservation.

Conventional methods for tree species identification rely heavily on field surveys, which are labor-intensive and time-consuming. These surveys often involve research groups physically collecting samples and recording data using GPS devices, a process that can be complex and slow. Remote sensing technology, particularly Airborne Laser Scanning (ALS) tools [59, 115] plays a vital role in tree species classification. Airborne vehicles can provide detailed data over small areas. Still, their use is limited for systematic data acquisition over larger areas (greater than 1000 hectares), as they are not considered stable or efficient platforms for extensive forest inventories [226].

Satellite imagery, combined with advancements in computer vision, offers an alternative approach. Machine learning techniques such as decision trees, random forests, support vector machines, and neural networks have become increasingly popular for estimating tree species using satellite images [45, 60, 103]. Convolutional neural networks (CNNs), more recently, have shown high accuracy in tree species classification. In [101], the authors compared various neural network architectures for detecting dominant forest species. In [40], the authors used WorldView-3 imagery and a Res-UNet deep-learning model for individual tree species classification.

However, a significant challenge in these studies is the acquisition of reliable labels, which often come from field investigations or existing reference datasets that may be of low resolution or contain noisy data. The quality of these labels is crucial, as machine learning models are highly sensitive to the accuracy of their training data. Inaccurate or noisy labels can lead to a decline in the model's generalization performance, as the model might memorize incorrect labels and thereby degrade its performance on unseen data [171]. This highlights the need for high-quality, reliable data in the development of machine learning models for tree species classification using satellite imagery.

To illustrate the complexities involved in typical tree species inventories, especially in high-resolution applications like infrastructure monitoring, Figure 4.4 shows an example from the Norwegian tree species reference dataset [175].

This example highlights several challenges commonly encountered in reference datasets for tree species. Some trees that are visible in the satellite imagery are not included in the dataset. This incomplete coverage can lead to gaps in the data.

4.3 Tree characterization and dynamic risk assessment using satellite images

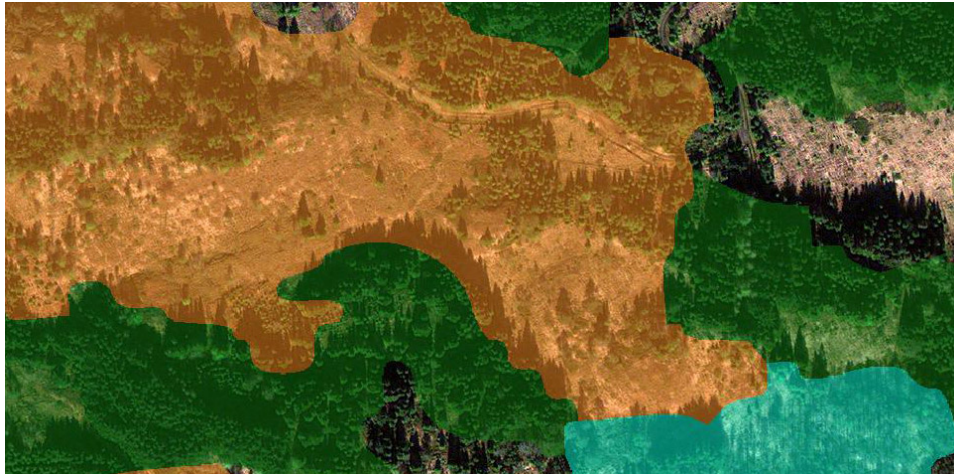


Fig. 4.4: Challenges in a typical tree species reference dataset. Tree species inventory databases often exclude certain trees and have imprecise boundaries between different forest areas. Spruces (green), pines (blue), and deciduous trees (orange).

Moreover, the dataset often features boundaries between different forest stands that are chunky and imprecise. These challenges pose significant difficulties for conventional supervised classification procedures, which typically involve extracting patches from satellite images and the tree dataset and using them to train a model. The inaccuracies and imprecisions in the dataset can hinder the model's ability to learn effectively, resulting in poor performance and unreliable outcomes. This underscores the need for improved methodologies and datasets for tree species classification.

To answer the second research question, "*RQ 1.2: How to improve the quality of forests inventory databases and classify tree species?*" we wrote the paper titled "*Tree species classification using high-resolution satellite imagery and weakly supervised learning (Paper B)*" [68], published in the IEEE Transactions on Geoscience and Remote Sensing journal. The study introduces an innovative automated approach designed to enhance the accuracy and detail of tree species datasets using single high-resolution satellite images. This method not only refines existing tree species datasets but also enables classification at an almost individual tree level. The paper presents a solution that significantly improves the quality of available forest inventories by addressing some of the key challenges typically associated with tree species classification, such as incomplete coverage, imprecise boundaries, and coarse-level labeling. By employing weakly supervised learning techniques, the approach efficiently overcomes the limitations of conventional supervised segmentation methods, which often struggle with the imperfections and inconsistencies present in standard reference datasets.

The complete paper is attached in Chapter B.

4.3 Tree characterization and dynamic risk assessment using satellite images

Building on our initial research into vegetation-related risks to power lines, as detailed in Section 4.1, our work has progressed towards a new, more comprehensive approach.

We have expanded our focus beyond the presence and proximity of trees near power lines, aiming to comprehensively characterize the trees in these areas with as much detail as possible.

Existing literature includes several vegetation monitoring tools designed for forestry and arboriculture, such as ForestGALES [5] and TREEFALL [84]. These models aim to assess the vulnerability of trees with respect to environmental factors such as weather. However, these models typically rely on pre-collected tree data, including location, species, and physical characteristics, which are often gathered through field surveys or ground inspections. The challenge lies in the high costs and logistical complexities of monitoring expansive infrastructure networks, leading to infrequent data updates and a potential mismatch between real-time vegetation growth and the data used for management decisions. Estimating critical information from satellite imagery offers a cost-effective and efficient way to obtain up-to-date data. Utilizing satellite technology enables the frequent collection of information, which is especially advantageous in scenarios where regular monitoring is necessary but difficult or expensive to conduct through traditional means. We have advanced our research by integrating the analysis from Paper A, which focused on detecting trees and developing a risk map along power lines, with the tree species classification explored in Paper B. Building upon these foundations, we have investigated estimating canopy height models from single satellite images. This approach aligns with methodologies highlighted in existing literature, such as those by [35, 75, 99], as well as our methodology presented in [65]. We employ a regression machine learning model to estimate the height of tree canopies directly from satellite imagery. Combining tree detection, species classification, and canopy height estimation offers a multidimensional approach to vegetation analysis using satellite data.

To address the third research question: "RQ 1.3: *How to characterize trees near infrastructure lines and estimate their vulnerability with respect to weather?*", we have recently developed a new paper titled: "***ASPIRE-V: Artificial Intelligence and Space-based Monitoring for Power Lines Risk Evaluation against Vegetation (Paper C)***", currently under review process in the IEEE Transactions of Power Delivery journal. This paper represents a pivotal advancement in our research, introducing a methodology for the dynamic assessment of risks posed by vegetation to power lines. Our approach leverages high-resolution satellite images to estimate crucial tree parameters, such as tree crown position, canopy height, distance to power lines, and species type. It also incorporates wind data, providing a dynamic and predictive element to risk assessment by simulating the susceptibility of trees to falling due to wind impact and potentially colliding with the power line.

The complete paper is attached in Chapter C.

ROADWAYS DISASTER MANAGEMENT USING SATELLITE IMAGES

Natural disasters have a devastating impact on human life, property, and the environment. Between 2005 and 2015, these catastrophic events affected approximately 1.5 billion people worldwide in various ways. The toll included the loss of 700,000 lives, 1.4 million injuries, and the displacement of 23 million people who were rendered homeless. The majority of these natural disasters were found to be hydrometeorological in origin, meaning they were related to water (floods), weather (hurricanes), and other climate phenomena [234].

These events also significantly affect infrastructure, leading to consequences such as power outages [231], roadways blockages [125], and service disruptions [238]. In light of these impacts and the increasing challenges posed by climate change, it is crucial that infrastructure networks, including electrical and transportation systems, are designed for resilience. This means they should be capable of withstanding natural disasters like floods, earthquakes, or wildfires, ensuring their continued operation and rapid recovery [94, 232, 233].

Remote sensing technologies, especially satellite imagery, combined with the recent advancements in artificial intelligence, have the potential to significantly bolster efforts in disaster management, relief, and early warning systems. Despite these capabilities, AI is not currently a standard element in the operational procedures for managing natural disasters. This indicates a gap between AI's potential applications and its actual integration into disaster management strategies. Therefore, the second direction of this Ph.D. research, as illustrated in Figure 1.2, centers on utilizing satellite imagery to enhance disaster management practices. We established a collaboration between the Florida State University, the City of Tallahassee, Florida, and the United Nation's Focus Group on AI for Natural Disaster Management (FG-AI4NDM) [234] to address this second direction, specifically



Fig. 5.1: Picture of a tree blocking a road in Florida due to Hurricane Irma in 2017. Image from [220].

Roadways disaster management using satellite images

targeting hurricanes as the primary natural disaster, with an emphasis on their impact on roadways. This research direction has been divided into two distinct scenarios:

- *Post-Hurricane Scenario:* The objective is to analyze the aftermath of a hurricane. The focus is on detecting changes and damages through satellite imagery for fast damage assessment and efficient recovery efforts. This approach is crucial for quick response and recovery of affected areas.
- *Pre-Hurricane Scenario:* In this case, the emphasis shifts to the period before a hurricane strikes. Since no physical damages have occurred yet, the goal is to identify vulnerabilities in infrastructure. By pinpointing these potential weak spots, resources and attention can be allocated more effectively to mitigate the impact of the impending hurricane.

This dual approach underscores the versatility of satellite imagery in both proactive and reactive disaster management strategies, aiming to minimize the impact of hurricanes on infrastructural systems. Each scenario is further described and related to our research in Section 5.1 and Section 5.2.

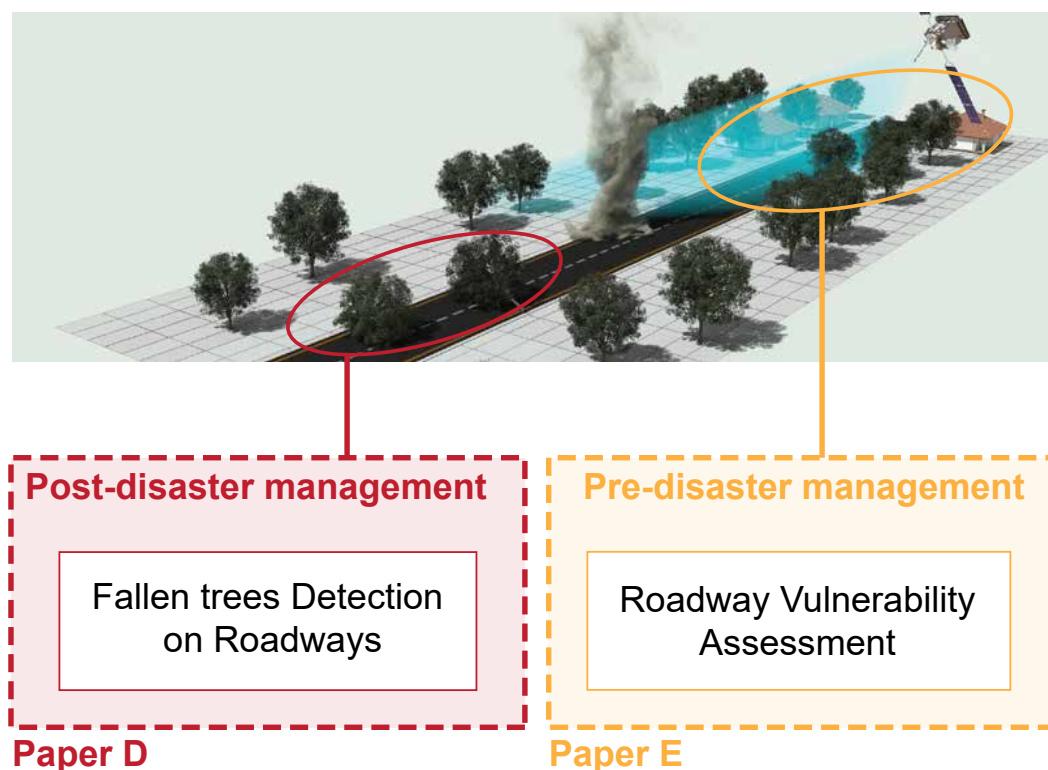


Fig. 5.2: Overview of our PhD research on disaster management.

OVERVIEW AND ROAD-MAP OF THE PHD RESEARCH ON DISASTER MANAGEMENT Figure 5.2 serves as an overview of the research papers included in this thesis and focusing on disaster management. Each paper in this collection is dedicated to exploring a specific task related to this area of study. Specifically:

- Paper D is dedicated to the detection of fallen trees along roadways following hurricanes. It proposes a methodology for identifying and assessing such incidents to aid in prompt and efficient disaster response.
- Paper E deals with the pre-hurricane assessment of roadways. It evaluates the vulnerability of roadways, taking into account factors such as exposure to vegetation, the roadway network, and the potential impact on the population.

5.1 Post-disaster management: damage assessment and recovery

Assessing damage is critical following catastrophic events such as hurricanes, earthquakes, or tsunamis. Given the benefits of satellite imagery already outlined in this thesis – namely scalability, cost efficiency, and extensive coverage – remote sensing has increasingly been adopted for damage assessment purposes. For instance, recently, remote sensing techniques have been used for damage assessment following earthquakes [43], floods [187], building damages [216, 253], and hurricanes [31, 155]. Hurricanes particularly inflict substantial damage in the United States, with the subtropical regions of Florida, Alabama, and Louisiana often bearing the brunt. The U.S. ranks among the top five countries most affected by natural disasters. From 1980 to 2019, the estimated cost of damages from such disasters in the U.S. has reached approximately \$1.75 trillion [174].

In recent times, machine learning techniques have been introduced for detecting hurricane-induced damages using satellite imagery, providing an efficient and accurate approach to assess the extent of damage from such natural disasters [38, 119, 123, 258]. One significant limitation of supervised machine learning models, like those used for damage assessment, is their heavy reliance on scarce and costly manually labeled data. Moreover, it's essential to have accurate, noise-free labels to train these models effectively. For instance, obtaining extensive datasets with several images of damage or covering the same area before and after a disaster is particularly challenging in damage assessment scenarios. In addition to these challenges, supervised models generally offer less scalability. They often require retraining for deployment in different geographical areas [168].

In real-world remote sensing applications, unsupervised machine learning methods often present more practical options [202]. Unlike supervised techniques, unsupervised approaches in image processing automatically extract features for tasks like image segmentation or change analysis. This methodology is particularly beneficial as it does not require the labor-intensive and costly process of labeling data. Key examples of these unsupervised approaches include the use of algorithms for unsupervised change detection and autoencoders as discussed in [114, 266].

As part of our research on damage assessment for infrastructure, we focused on identifying fallen trees that obstruct roadways after hurricanes. Utilizing high-resolution satellite imagery captured before and after a hurricane, we developed a change detection method to pinpoint areas where trees have fallen onto roads. In this regard, to answer the research question *RQ 2.1: How to detect fallen trees on roadways after a hurricane with limited data?*, we contributed with the paper titled *Automated Satellite-Based Assessment of Hurricane Impacts on Roadways (Paper D)* [66], published in

the IEEE Transactions on Industrial Informatics journal. The paper presents a novel approach for detecting fallen trees on roadways following hurricanes, leveraging the strengths of advanced machine learning techniques in remote sensing. Our approach requires a limited number of labeled satellite images for trees in their normal state and no labeled data for fallen trees. Effectively, it operates as an unsupervised method in the context of fallen trees, enhancing resilience against the common issue of noisy or inaccurate labels in satellite imagery and remote sensing.

The complete paper is attached in Chapter [D](#).

5.2 Pre-disaster management: preparedness and vulnerability analysis

Pre-disaster assessments involve analyzing an area before an event (e.g., a hurricane) to evaluate vulnerabilities and enhance prevention and resilience. The general methodology involves assessing the current state of infrastructure and identifying areas more susceptible to hurricane damage. Factors like infrastructure age, design, and location relative to predicted hurricane paths are usually considered. By identifying these vulnerabilities, preventative measures can be taken to reinforce infrastructure, and emergency response plans can be tailored to anticipate areas of greatest need. This approach aims to mitigate the impact of hurricanes on infrastructure, potentially saving resources and lives [51].

Current research primarily focuses on statistical methods to recognize spatial patterns of potential outages and their correlation with demographic and socioeconomic factors, as seen in [78] and [77]. Another emerging approach in vulnerability analysis is analyzing the network topology [106]. This is done using graph mathematical tools such as centrality [196] and percolation theory [8]. Moreover, traffic flow is integrated to analyze the performance loss of road networks, or in general, any other transportation system, in case of a failure [69, 91, 244]. However, vegetation, a significant contributor to roadway blockages during severe weather, is often overlooked in calculating road vulnerability.

We bridge the gap between vegetation detection and network topology analysis with our paper *Roadway Vulnerability Assessment against Hurricanes Using Satellite Images* [67], published in the SAGE Transportation Research journal. The paper addresses the research question *RQ 2.2: How to identify potential vulnerabilities in roadways before a hurricane strikes?*. The work proposes a new framework for rapid, scalable, and cost-effective assessment of roadway vulnerabilities using high-resolution satellite imagery. Our approach involves assessing the risk posed to roadways by surrounding vegetation. This is achieved by evaluating tree characteristics from satellite images, such as their height, distance to the road, health status, and density. We have created a vulnerability index that combines this data on vegetation exposure with the importance of each road. The potential impact of road closures on the transportation network, including factors such as disruption to mobility and the number of buildings affected, determines the road's importance. This method enables the creation of a detailed, road-specific vulnerability map for the entire network, which can be prepared ahead of a hurricane. Such a map can significantly improve city and state agencies'

5.2 Pre-disaster management: preparedness and vulnerability analysis

planning and response strategies.

The full details of our method and findings are presented in Chapter [E](#) of our thesis.

CONCLUSIONS AND FUTURE WORKS

This chapter summarizes the main research topic. Section 6.1 revisits the research questions, providing an overview of how they have been addressed throughout this thesis. Section 6.2 highlights the major contributions and advancements of this Ph.D. study. Finally, Section 6.3 presents potential research efforts, suggesting directions for continued exploration and development in the area.

The primary objective of this study has been to explore the application of high-resolution satellite imagery in infrastructure monitoring, an area traditionally dependent on manual surveys, ground patrols, aerial images, helicopters, and historical datasets. However, these standard methods have significant disadvantages: they are expensive, time-consuming, and, as a result, not regularly performed. This often results in the reliance on outdated or limited situational awareness regarding monitoring infrastructure.

Additionally, the challenge is elevated by the vast spatial extent of infrastructure networks, particularly power lines and roadways, which can stretch across hundreds or even thousands of kilometers. The use of satellite imagery for monitoring offers a promising solution to these challenges. It presents a more cost-effective and scalable alternative, capable of covering extensive areas more efficiently. This approach can significantly enhance the effectiveness and timeliness of infrastructure monitoring.

However, while we recognize the significant potential of satellite imagery in infrastructure monitoring, it is important to note that it cannot replace entirely the traditional approaches. Rather, it should be viewed as a complementary tool that enhances conventional monitoring approaches. A more robust, comprehensive, and efficient monitoring system can be established by integrating satellite imagery with standard methods like manual surveys and ground patrols. This combination leverages the strengths of both approaches, offering a more holistic solution to infrastructure monitoring challenges.

6.1 Research questions revisited

Our research was divided into two interconnected use cases: (1) power line monitoring and (2) roadway monitoring in disaster management. A particular emphasis was placed on vegetation-related assessments. This focus stems from the recognition that vegetation, especially when coupled with environmental factors such as weather, is the leading cause of both power outages in power lines and roadway blockages during nat-

Conclusions and future works

ural disasters like hurricanes. By leveraging satellite imagery and artificial intelligence, our research aimed to provide more timely, cost-effective, and comprehensive insights into infrastructure vulnerabilities and damages. The use of satellite data offers a significant improvement over traditional methods, enabling more frequent, wide-scale, and up-to-date monitoring.

In our study, we have identified two primary research questions, each of which is further subdivided into a series of sub-questions focusing on specific tasks.

RQ1: HOW TO ACHIEVE A BETTER SITUATIONAL AWARENESS OF THE VEGETATION STATUS ALONG POWER LINES USING SATELLITES? The first research question addresses specific gaps in the field of power line monitoring through satellite imagery. To tackle these gaps more effectively, we have divided RQ1 into three distinct sub-questions.

RQ1.1: *How to assess the risk of vegetation near power lines using high-resolution optical satellite images?* Vegetation is a leading factor in power outages. Although numerous methods for vegetation detection have been explored, the focus on evaluating the risk posed by vegetation encroachment near power lines remains underrepresented in existing research. We propose an approach for vegetation detection that combines spatial features, a machine learning classifier and an unsupervised segmentation technique based on deep learning to perform a pixel-level segmentation of trees. Furthermore, we develop a risk index along power lines, pinpointing areas where vegetation encroaches the corridor. This index is an important tool for identifying potential hazards and minimizing the risk of power outages due to vegetation interference.

RQ1.2: *How to improve the quality of forests inventory databases and classify tree species?* Power line operators can significantly improve vegetation management by utilizing tree species inventories. Different tree species vary in growth rates, sizes, and branching patterns, affecting their interaction with power lines. Also, recently, there has been a shift towards environmentally conscious vegetation management in power line maintenance. Knowing the species allows operators to customize their maintenance strategies, such as adjusting the trimming frequency for faster-growing species and selectively replacing certain tree species to ensure safety and reliability in power transmission while preserving biodiversity and sustainability. Existing tree species inventories frequently suffer from being scarce and lacking in detail. To address this, we have developed a method to improve the precision and granularity of tree species datasets using single high-resolution satellite images. This technique improves upon current tree species datasets and facilitates classification at a near-individual tree level.

RQ1.3: *How to characterize trees near infrastructure lines and estimate their vulnerability with respect to weather?* Expanding upon our studies on vegetation-related risk to power lines (RQ1.1) and our investigations into tree species classification (RQ1.2), our research has evolved to characterize the trees along power lines more comprehensively. Our focus extends beyond assessing the proximity and density of trees near the power lines. In our risk assessment calculations, we also incorporate additional parameters like canopy height and meteorological data to estimate tree vulnerability.

RQ2: HOW SATELLITE IMAGERY CAN HELP IN ROADWAYS MANAGEMENT AGAINST NATURAL DISASTER? The second research question tackles the challenges in roadway monitoring with respect to disaster management. In particular, we have established collaborations with multiple partners in Florida, leading us to select hurricanes as our focus of study. Our work encompasses both pre-disaster and post-disaster management phases.

RQ2.1: *How to detect fallen trees on roadways after a hurricane with limited data?* Addressing this question, we tackle the issue in damage assessment scenarios where acquiring extensive remote sensing images after a disaster is notably challenging. This scarcity of post-disaster data often hinders the effectiveness and generalizability of traditional supervised machine learning models. To address this challenge, we introduce a novel solution for detecting fallen trees on roadways in the aftermath of hurricanes. Our method utilizes two satellite images – one taken before the hurricane and another captured after it. In practice, this method works as an unsupervised approach when applied to the context of fallen trees.

RQ2.2: *How to characterize vegetation-induced roadways vulnerability and enhance infrastructure resilience?* Pre-disaster assessments involve analyzing an area before an event, like a hurricane, occurs to evaluate vulnerabilities, aiming for enhanced prevention and resilience. In most of the works in literature, the vegetation status is often ignored or merely considered. We bridge the gap by including the vegetation status (height, distance to the road, health status, and density) estimated from satellite images on top of the traditional roadway network analysis.

Table 6.1 presents an overview of the research questions, linking them with the respective research papers.

Table 6.1: Overview of the research questions and the research papers addressing them. The symbol '*' denotes papers currently under review.

RQ	Sub RQ	Research focus	Addressed in
RQ1	1.1	Tree risk assessment along power lines	Paper A [70], Paper C [*]
	1.2	Tree species classification and database refinements	Paper B [68]
	1.3	Tree characterization and weather risk assessment along power lines	Paper C [*]
RQ2	2.1	Detection of fallen trees along roadways after hurricanes	Paper D [66]
	2.2	Roadways vulnerability assessment before hurricanes	Paper E [67]

6.2 Contributions

The key contributions of this thesis are twofold, encompassing both theoretical advancements in remote sensing and computer vision, and practical applications in the use of satellite technology for infrastructure monitoring. These contributions are further detailed below.

6.2.1 Theoretical contributions to remote sensing and computer vision

Our work contributes to computer vision and remote sensing by developing approaches specifically tailored to address challenges associated with incomplete or limited data. In pursuit of this, we have designed and implemented customized semi-supervised and weakly-supervised methods, as exemplified in our research presented in Paper B [68] and Paper D [66]. These innovative approaches are particularly focused on maximizing the effectiveness of data analysis under data-constrained scenarios.

6.2.2 Practical contributions to the use of satellites for infrastructure monitoring

Our research has also made practical contributions toward enhancing the awareness and application of satellite imagery in infrastructure monitoring. Following the publication of Paper A and Paper C, our findings were recognized and included in the European Space Agency's market trend report [58]. This acknowledgment led to the extension of the GridEyeS project into a new phase, where we are now tasked with deploying it in real-world electric utility settings. Additionally, through our research presented in Paper D and Paper E, we have actively contributed to the United Nations Group on AI for Natural Disaster Management [234] in advancing the use of AI technologies in the field of disaster management. This progression signifies our work's tangible impact and relevance in advancing satellite-based monitoring solutions in the infrastructure sector.

6.3 Future work

Our research has laid the groundwork for utilizing satellite imagery in infrastructure monitoring, covering various topics in this field with both theoretical and practical implications. Nonetheless, there are promising new avenues worth exploring further.

Our studies predominantly employed multispectral optical satellite images, but Synthetic Aperture Radar (SAR) satellites present an exciting new frontier in earth observation, particularly for infrastructure monitoring. SAR's significance is amplified in the context of damage assessment following extreme weather events [73]. Obtaining cloud-free images quickly is often crucial for emergency response, and this is where optical images can fall short. SAR's weather-independent capabilities could provide a new level of robust analysis. While our research has delved into SAR applications with some published papers, such as SAR-optical image matching [72] and forest characterization [71], we have yet to apply SAR technology to infrastructure monitoring tasks. Exploring the integration of SAR in infrastructure monitoring represents a compelling and potentially fruitful research direction. This study area is currently being pursued by other Ph.D. candidates in our research group, the Connectivity, Information and Intelligence Lab [1].

Investigating the latest advancements in computer vision, such as the "Segment-Anything" approach in remote sensing [178], is a prospective area for future exploration. These cutting-edge techniques, which emerged late in 2023, were beyond the scope of this thesis due to their recent development. They represent a promising method

for processing images from a variety of geographical contexts and for generating new samples and datasets thanks to their zero-shot learning capabilities. Their adaptability and applicability to remote sensing data analysis make them a promising avenue for further research.

Incorporating additional parameters into the risk calculation index presented in Paper C could significantly enhance its comprehensiveness and accuracy. Integrating more sophisticated weather and climate models and considering the effects of terrain, slope, and topography would provide a more nuanced understanding of risk factors. This enrichment of the risk index would allow for a deeper analysis of how various environmental and geographical elements interact and impact the tree-related risk to infrastructure.

Exploring the intersection of recent Large Language Models (LLMs) and remote sensing presents another intriguing research direction. The integration of Natural Language Processing (NLP) with convolutional neural networks could, for instance, enable the formulation of textual queries and the extraction of answers from satellite imagery. This approach would harness the capabilities of both language understanding and visual data analysis, potentially revolutionizing how we interact with and interpret satellite data.

BIBLIOGRAPHY

- [1] Connectivity, Information & Intelligence Lab (CizLab). <https://www.ci2lab.com/>. 6.3
- [2] eSmart Systems. <https://www.esmartsystems.com/>. 1
- [3] Linja AS. <https://www.linja.no/>. 1, 4.1
- [4] StormGeo. <https://www.stormgeo.com/>. 1
- [5] Forestry Commission and Forest Research. ForestGALES. <https://www.forestryresearch.gov.uk/tools-and-resources/fthr/forestgales/>. 4.3
- [6] F. B. A. Bannari, D. Morin and A. R. Huete. A review of vegetation indices. *Remote Sensing Reviews*, 13(1-2):95–120, 1995. 2.1.3
- [7] F. Abdul Gafoor, M. R. Al-Shehhi, C.-S. Cho, and H. Ghedira. Gradient boosting and linear regression for estimating coastal bathymetry based on sentinel-2 images. *Remote Sensing*, 14(19):5037, Oct. 2022. 3.3
- [8] B. Abdulla and B. Birgisson. Characterization of vulnerability of road networks to random and nonrandom disruptions using network percolation approach. *Journal of Computing in Civil Engineering*, 35, 10 2020. 5.2
- [9] R. Ablin, C. H. Sulochana, and G. Prabin. An investigation in satellite images based on image enhancement techniques. *European Journal of Remote Sensing*, 53:86 – 94, 2019. 3.2.1
- [10] P. S. R. Aditya and M. Pal. Local interpretable model agnostic shap explanations for machine learning models. *ArXiv*, abs/2210.04533, 2022. 3.4
- [11] M. A. Aguilar, M. del Mar Saldaña, and F. J. Aguilar. Assessing geometric accuracy of the orthorectification process from geoeye-1 and worldview-2 panchromatic images. *International Journal of Applied Earth Observation and Geoinformation*, 21:427–435, 2013. 2.1.1
- [12] J. Ahmad, A. Malik, L. Xia, and N. Ashikin. Vegetation encroachment monitoring for transmission lines right-of-ways: A survey. *Electric Power Systems Research*, 95:339–352, 2013. 4.1
- [13] J. Ahmad, A. S. Malik, and L. Xia. Vegetation monitoring for high-voltage transmission line corridors using satellite stereo images. In *2011 National Postgraduate Conference*, pages 1–5, 2011. 4.1
- [14] A. A. Aleissaee, A. Kumar, R. M. Anwer, S. Khan, H. Cholakkal, G.-S. Xia, and F. S. Khan. Transformers in remote sensing: A survey. *Remote Sensing*, 15(7):1860, 2023. 3.4

BIBLIOGRAPHY

- [15] M. Alloghani, D. Al-Jumeily, J. Mustafina, A. Hussain, and A. J. Aljaaf. *A Systematic Review on Supervised and Unsupervised Machine Learning Algorithms for Data Science*, pages 3–21. Springer International Publishing, Cham, 2020. [3.3](#)
- [16] M. Amani, A. Ghorbanian, M. Asgarimehr, B. Yekkehkhany, A. Moghimi, S. Jin, A. Naboureh, F. Mohseni, S. Mahdavi, and N. F. Layegh. Remote sensing systems for ocean: A review (part 1: Passive systems). *IEEE Journal of Selected Topics in Applied Earth Observations and Remote Sensing*, 15:210–234, 2022. [2](#)
- [17] M. Amani, F. Mohseni, N. F. Layegh, M. E. Nazari, F. Fatolazadeh, A. Salehi, S. A. Ahmadi, H. Ebrahimi, A. Ghorbanian, S. Jin, S. Mahdavi, and A. Moghimi. Remote sensing systems for ocean: A review (part 2: Active systems). *IEEE Journal of Selected Topics in Applied Earth Observations and Remote Sensing*, 15:1421–1453, 2022. [2](#)
- [18] P. P. Angelov, E. A. Soares, R. Jiang, N. I. Arnold, and P. M. Atkinson. Explainable artificial intelligence: an analytical review. *Wiley Interdisciplinary Reviews: Data Mining and Knowledge Discovery*, 11, 2021. [3.3](#)
- [19] A. Asokan, A. Jude, M. Ciobanu, A. M. Gabor, N. Antoanela, and J. D. Image processing techniques for analysis of satellite images for historical maps classification—an overview. *Applied Sciences*, 10:4207, 06 2020. [3.2](#)
- [20] A. Asperti, D. Evangelista, and E. Loli Piccolomini. A survey on variational autoencoders from a green ai perspective. *SN Computer Science*, 2(4):301, 2021. [3.3.2](#)
- [21] B. Ayhan, K. Chiman, B. Bence, K. Liyun, L. Yan, P. Daniel, L. Jiang, S. Dimitrios, and M. Vlachos. Vegetation detection using deep learning and conventional methods. *Remote Sensing*, 12(15):2502, 2020. [4.1](#)
- [22] B. Ayhan and C. Kwan. Tree, shrub, and grass classification using only rgb images. *Remote. Sens.*, 12:1333, 2020. [4.1](#)
- [23] F. Ayoub, S. Leprince, R. Binet, K. W. Lewis, O. Aharonson, and J.-P. Avouac. Influence of camera distortions on satellite image registration and change detection applications. In *IGARSS 2008 - 2008 IEEE International Geoscience and Remote Sensing Symposium*, volume 2, pages II–1072–II–1075, 2008. [2.1.1](#)
- [24] Y. Ban, P. Zhang, A. Nascetti, A. Bevington, and M. Wulder. Near real-time wildfire progression monitoring with sentinel-1 sar time series and deep learning. *Scientific Reports*, 10, 01 2020. [2.1.4](#)
- [25] A. Barbati, P. Corona, and M. Marchetti. A forest typology for monitoring sustainable forest management: The case of european forest types. *Plant Biosystems - An International Journal Dealing with all Aspects of Plant Biology*, 141:103 – 93, 2007. [4.2](#)
- [26] E. Barreira, R. Almeida, and J. Delgado. Infrared thermography for assessing moisture related phenomena in building components. *Construction and Building Materials*, 110:251–269, 2016. [2.1.3](#)

- [27] H. Bay, T. Tuytelaars, and L. Van Gool. Surf: Speeded up robust features. In A. Leonardis, H. Bischof, and A. Pinz, editors, *Computer Vision – ECCV 2006*, pages 404–417, Berlin, Heidelberg, 2006. Springer Berlin Heidelberg. 3.2.2
- [28] BBC News. PG&E to stand trial over deadly California wildfire . <https://www.bbc.com/news/world-us-canada-64505596>, 2020. 1.1
- [29] M. Belgiu and L. Drăguț. Random forest in remote sensing: A review of applications and future directions. *ISPRS Journal of Photogrammetry and Remote Sensing*, 114:24–31, 2016. 3.3
- [30] Y. Bengio, A. C. Courville, and P. Vincent. Representation learning: A review and new perspectives. *IEEE Transactions on Pattern Analysis and Machine Intelligence*, 35:1798–1828, 2012. 3.3.2
- [31] P. Berezina and D. Liu. Hurricane damage assessment using coupled convolutional neural networks: a case study of hurricane michael. *Geomatics, Natural Hazards and Risk*, 13(1):414–431, 2022. 5.1
- [32] A. Bhattacharya, T. Bolch, K. Mukherjee, T. Pieczonka, J. Kropacek, and M. F. Buchroithner. Overall recession and mass budget of gangotri glacier, garhwal himalayas, from 1965 to 2015 using remote sensing data. *Journal of Glaciology*, 62:1115 – 1133, 2016. 2
- [33] J. M. Bioucas-Dias, A. Plaza, G. Camps-Valls, P. Scheunders, N. Nasrabadi, and J. Chanussot. Hyperspectral remote sensing data analysis and future challenges. *IEEE Geoscience and Remote Sensing Magazine*, 1(2):6–36, 2013. 2.1.3
- [34] D. Bratanu, I. Nedelcu, and M. Datcu. Interactive spectral band discovery for exploratory visual analysis of satellite images. *IEEE Journal of Selected Topics in Applied Earth Observations and Remote Sensing*, 5(1):207–224, 2012. 2.1.3
- [35] I. L. Bretas, D. S. M. Valente, T. F. de Oliveira, D. B. Montagner, V. P. B. Euclides, and F. H. M. Chizzotti. Canopy height and biomass prediction in mombaça guinea grass pastures using satellite imagery and machine learning. *Precision Agriculture*, 24:1638–1662, 2023. 4.3
- [36] B. Büyüktas, G. Sumbul, and B. Demir. Learning across decentralized multi-modal remote sensing archives with federated learning. *IGARSS 2023 - 2023 IEEE International Geoscience and Remote Sensing Symposium*, pages 4966–4969, 2023. 3.4
- [37] J. F. Canny. A computational approach to edge detection. *IEEE Transactions on Pattern Analysis and Machine Intelligence*, PAMI-8:679–698, 1986. 3.2.2
- [38] Q. D. Cao and Y. Choe. Building damage annotation on post-hurricane satellite imagery based on convolutional neural networks. *Natural Hazards*, pages 1–20, 2020. 5.1

BIBLIOGRAPHY

- [39] J. Cavender-Bares, F. D. Schneider, M. J. Santos, A. Armstrong, A. Carnaval, K. M. Dahlin, L. Fatoyinbo, G. C. Hurtt, D. Schimel, P. A. Townsend, S. L. Ustin, Z. Wang, and A. M. Wilson. Integrating remote sensing with ecology and evolution to advance biodiversity conservation. *Nature Ecology & Evolution*, 6(13):506–519, 2022. [2](#)
- [40] C. Chen, L. Jing, H. Li, and Y. Tang. A new individual tree species classification method based on the resu-net model. *Forests*, 12(9):1202, Sep 2021. [4.2](#)
- [41] S. Chen and W. Guo. Auto-encoders in deep learning—a review with new perspectives. *Mathematics*, 11(8):1777, 2023. [3.3.2](#)
- [42] N. C. Coops, P. Tompalski, T. R. Goodbody, M. Queinnec, J. E. Luther, D. K. Bolton, J. C. White, M. A. Wulder, O. R. van Lier, and T. Hermosilla. Modelling lidar-derived estimates of forest attributes over space and time: A review of approaches and future trends. *Remote Sensing of Environment*, 260:112477, 2021. [2.2](#)
- [43] F. Dell’Acqua and P. Gamba. Remote sensing and earthquake damage assessment: Experiences, limits, and perspectives. *Proceedings of the IEEE*, 100(10):2876–2890, 2012. [5.1](#)
- [44] J. A. M. Demattê, L. Ramirez-Lopez, R. Rizzo, M. R. Nanni, P. R. Fiorio, C. T. Fongaro, L. G. M. Neto, J. L. Safanelli, and P. P. D. S. Barros. Remote Sensing from Ground to Space Platforms Associated with Terrain Attributes as a Hybrid Strategy on the Development of a Pedological Map. *Remote Sensing*, 8(10):826, 2016. [2](#)
- [45] M. Deur, M. Gasparovic, and I. Balenović. Tree species classification in mixed deciduous forests using very high spatial resolution satellite imagery and machine learning methods. *Remote Sensing*, 12:3926, 11 2020. [4.2](#)
- [46] J. Devlin, M.-W. Chang, K. Lee, and K. Toutanova. Bert: Pre-training of deep bidirectional transformers for language understanding. In *North American Chapter of the Association for Computational Linguistics*, 2019. [3.4](#)
- [47] A. Dhillon and G. K. Verma. Convolutional neural network: a review of models, methodologies and applications to object detection. *Progress in Artificial Intelligence*, 9:85–112, 2020. [3.2.2](#), [3.3.1](#)
- [48] A. Dixit, A. Goswami, and S. Jain. Development and evaluation of a new “snow water index (swi)” for accurate snow cover delineation. *Remote Sensing*, 11(23):2774, Nov. 2019. [2.1.3](#)
- [49] C. Doersch. Tutorial on variational autoencoders. *ArXiv*, abs/1606.05908, 2016. [3.3.2](#)
- [50] A. Dosovitskiy, L. Beyer, A. Kolesnikov, D. Weissenborn, X. Zhai, T. Unterthiner, M. Dehghani, M. Minderer, G. Heigold, S. Gelly, J. Uszkoreit, and N. Houlsby. An image is worth 16x16 words: Transformers for image recognition at scale. *ArXiv*, abs/2010.11929, 2020. [3.4](#)

- [51] M. A. Dulebenets, J. Pasha, O. F. Abioye, M. Kavooosi, E. E. Ozguven, R. Moses, W. R. Boot, and T. Sando. Exact and heuristic solution algorithms for efficient emergency evacuation in areas with vulnerable populations. *International Journal of Disaster Risk Reduction*, 39:101114, 2019. 5.2
- [52] Electrical Safety Authority - Government of Ontario. Planting under or around powerlines & electrical equipment. https://esasafe.com/assets/files/esasafe/pdf/Electrical_Safety_Products/Guidelines/Tree-Planting%20AODA%20Final%20Tagged.pdf. [Online]. 1.1
- [53] M. M. Elkholy, M. Mostafa, D. ElSayad, H. M. Ebeid, and M. F. Tolba. Convolutional autoencoder for remote sensing change detection. In A. A. Gad, D. Elfiky, A. Negm, and S. Elbeih, editors, *Applications of Remote Sensing and GIS Based on an Innovative Vision*, pages 223–232, Cham, 2023. Springer Nature Switzerland. 3.3.2
- [54] European Space Agency (ESA). Copernicus Open Access Hub. <https://scihub.copernicus.eu/>. 2.1.3
- [55] European Space Agency (ESA). GridEyeS Project. <https://business.esa.int/projects/grideyes>. 1, 4
- [56] European Space Agency (ESA). Sentinel-2. https://www.esa.int/Applications/Observing_the_Earth/Copernicus/Sentinel-2. 2.1
- [57] European Space Agency (ESA). The Sentinel missions. https://www.esa.int/Applications/Observing_the_Earth/Copernicus/The_Sentinel_missions. 2.1.3
- [58] European Space Agency (ESA). Transmission and distribution of electrical power - market trends. <https://commercialisation.esa.int/2023/08/transmission-and-distribution-of-electrical-power/>. 4, 6.2.2
- [59] F. E. Fassnacht, H. Latifi, K. Stereńczak, A. Modzelewska, M. Lefsky, L. T. Waser, C. Straub, and A. Ghosh. Review of studies on tree species classification from remotely sensed data. *Remote Sensing of Environment*, 186:64–87, 2016. 4.2
- [60] M. P. Ferreira, F. H. Wagner, L. E. Aragão, Y. E. Shimabukuro, and C. R. de Souza Filho. Tree species classification in tropical forests using visible to shortwave infrared worldview-3 images and texture analysis. *ISPRS Journal of Photogrammetry and Remote Sensing*, 149:119–131, 2019. 4.2
- [61] U. N. O. for Outer Space Affairs (UNOOSA). United nations register of objects launched into outer space. <https://www.unoosa.org/oosa/en/spaceobjectregister/index.html>, 2023. 2.1
- [62] L. S. Galvão, A. R. Formaggio, E. G. Couto, and D. A. Roberts. Relationships between the mineralogical and chemical composition of tropical soils and topography from hyperspectral remote sensing data. *ISPRS Journal of Photogrammetry and Remote Sensing*, 63(2):259–271, 2008. 2.1.3

BIBLIOGRAPHY

- [63] J. Gareth, W. Daniela, H. Trevor, T. Robert, and J. Taylor. *An introduction to statistical learning with applications in Python*. Springer, 2023. 3.3
- [64] M. Gazzea. ASPIRE-V. https://github.com/Ci2Lab/Michele_ASPIREv. 4
- [65] M. Gazzea, S. Aalhus, L. M. Kristensen, E. E. Ozguven, and R. Arghandeh. Automated 3d vegetation detection along power lines using monocular satellite imagery and deep learning. In *2021 IEEE International Geoscience and Remote Sensing Symposium IGARSS*, pages 3721–3724, 2021. 1.4.1, 4, 4.3
- [66] M. Gazzea, A. Karaer, M. Ghorbanzadeh, N. Balafkan, T. Abichou, E. E. Ozguven, and R. Arghandeh. Automated satellite-based assessment of hurricane impacts on roadways. *IEEE Transactions on Industrial Informatics*, 18(3):2110–2119, 2022. 1.1, 2, 5.1, 6.1, 6.2.1
- [67] M. Gazzea, A. Karaer, M. Ghorbanzadeh, E. E. Ozguven, and R. Arghandeh. Roadway vulnerability assessment against hurricanes using satellite images. *Transportation Research Record*, 2677(3):1453–1464, 2023. 1.1, 2, 5.2, 6.1
- [68] M. Gazzea, L. M. Kristensen, F. Pirotti, E. E. Ozguven, and R. Arghandeh. Tree species classification using high-resolution satellite imagery and weakly supervised learning. *IEEE Transactions on Geoscience and Remote Sensing*, 60:1–11, 2022. 1.1, 1.1, 4, 4.2, 6.1, 6.2.1, B, D
- [69] M. Gazzea, A. Miraki, O. Alisan, M. M. Kuglitsch, I. Pelivan, E. E. Ozguven, and R. Arghandeh. Traffic monitoring system design considering multi-hazard disaster risks. *Scientific Reports*, 13:4883, 2023. 1.4.1, 5.2
- [70] M. Gazzea, M. Pacevicius, D. O. Dammann, A. Saprionova, T. M. Lunde, and R. Arghandeh. Automated power lines vegetation monitoring using high-resolution satellite imagery. *IEEE Transactions on Power Delivery*, 37(1):308–316, 2022. 1.1, 1.1, 4, 4.1, 6.1, A
- [71] M. Gazzea, A. Solheim, and R. Arghandeh. High-resolution mapping of forest structure from integrated sar and optical images using an enhanced u-net method. *Science of Remote Sensing*, 8:100093, 2023. 1.4.1, 6.3
- [72] M. Gazzea, O. Sommervold, and R. Arghandeh. Maru-net: Multiscale attention gated residual u-net with contrastive loss for sar-optical image matching. *IEEE Journal of Selected Topics in Applied Earth Observations and Remote Sensing*, 16:4891–4899, 2023. 1.4.1, 6.3
- [73] P. Ge, H. Gokon, and K. Meguro. A review on synthetic aperture radar-based building damage assessment in disasters. *Remote Sensing of Environment*, 240:111693, 2020. 6.3
- [74] C. M. Gevaert. Explainable ai for earth observation: A review including societal and regulatory perspectives. *International Journal of Applied Earth Observation and Geoinformation*, 112:102869, 2022. 3.4

- [75] P. Ghamisi and N. Yokoya. Img2dsm: Height simulation from single imagery using conditional generative adversarial net. *IEEE Geoscience and Remote Sensing Letters*, 15(5):794–798, 2018. 4.3
- [76] M. Ghorbanzadeh, M. Koloushani, E. E. Ozguven, A. Vanli, and R. Arghandeh. City transportation network vulnerability to disasters: the case of hurricane hermine in florida. *Environmental Hazards*, 21:199 – 217, 2021. 1.1
- [77] M. Ghorbanzadeh, M. Koloushani, E. E. Ozguven, A. Vanli, and R. Arghandeh. City transportation network vulnerability to disasters: the case of hurricane hermine in florida. *Environmental Hazards*, 21(3):199–217, 2022. 5.2
- [78] M. Ghorbanzadeh, M. Koloushani, M. B. Ulak, E. E. Ozguven, and R. A. Jouneghani. Statistical and spatial analysis of hurricane-induced roadway closures and power outages. *Energies*, 13(5):1098, Mar 2020. 5.2
- [79] G. Goldbergs, S. Maier, S. Levick, and A. Edwards. Limitations of high resolution satellite stereo imagery for estimating canopy height in australian tropical savannas. *Int. J. Appl. Earth Obs. Geoinformation*, 75:83–95, 2019. 4.1
- [80] C. Graham, J. M. Girkin, and C. J. Bourgenot. Spectral index selection method for remote moisture sensing under challenging illumination conditions. *Scientific Reports*, 12, 2022. 2.1.3
- [81] L. Gueguen and M. Pesaresi. Multi scale harris corner detector based on differential morphological decomposition. *Pattern Recognit. Lett.*, 32:1714–1719, 2011. 3.2.2
- [82] H. Gugel, S. Ekisheva, M. Lauby, and F. Tafreshi. Vegetation-related outages on transmission lines in north america. In *2018 IEEE Power and Energy Society General Meeting (PESGM)*, 2018. 1.1, 4.1
- [83] D. Gui, R. Lei, X. Pang, J. K. Hutchings, G. Zuo, and M. Zhai. Validation of remote-sensing products of sea-ice motion: a case study in the western arctic ocean. *Journal of Glaciology*, 66:807 – 821, 2020. 2
- [84] D. Gullick, G. Blackburn, J. Whyatt, P. Vopenka, J. Murray, and J. Abbatt. Tree risk evaluation environment for failure and limb loss (treefall): An integrated model for quantifying the risk of tree failure from local to regional scales. *Computers, Environment and Urban Systems*, 75:217–228, 2019. 4.3
- [85] M. Hall-Beyer. GLCM Texture: A Tutorial. <https://prism.ucalgary.ca/item/s/8833a1fc-5efb-4b9b-93a6-ac4ff268091c>, 2017. Online. 3.2.2
- [86] K. Han, Y. Wang, H. Chen, X. Chen, J. Guo, Z. Liu, Y. Tang, A. Xiao, C. Xu, Y. Xu, Z. Yang, Y. Zhang, and D. Tao. A survey on vision transformer. *IEEE Transactions on Pattern Analysis and Machine Intelligence*, 45(1):87–110, 2023. 3.4
- [87] R. M. Haralick, K. Shanmugam, and I. Dinstein. Textural features for image classification. *IEEE Transactions on Systems, Man, and Cybernetics*, SMC-3(6):610–621, 1973. 3.2.2

BIBLIOGRAPHY

- [88] F. M. E. Haroun, S. N. M. Deros, and N. M. Din. Detection and monitoring of power line corridor from satellite imagery using retinanet and k-mean clustering. *IEEE Access*, 9:116720–116730, 2021. [4](#)
- [89] M. Hassaballah, A. A. Abdelmgeid, and H. A. Alshazly. *Image Features Detection, Description and Matching*, pages 11–45. Springer International Publishing, Cham, 2016. [3.2.2](#)
- [90] M. Hassaballah and A. I. Awad. *Deep Learning in Computer Vision: Principles and Applications*. 03 2020. [3](#)
- [91] Z. He, K. Navneet, W. van Dam, and P. Van Mieghem. Robustness assessment of multimodal freight transport networks. *Reliability Engineering & System Safety*, 207:107315, 2021. [5.2](#)
- [92] P. Helber, B. Bischke, A. Dengel, and D. Borth. Eurosat: A novel dataset and deep learning benchmark for land use and land cover classification. *IEEE Journal of Selected Topics in Applied Earth Observations and Remote Sensing*, 2019. [3.3.2](#), [3.12](#)
- [93] H. Hewamalage, C. Bergmeir, and K. Bandara. Recurrent neural networks for time series forecasting: Current status and future directions. *International Journal of Forecasting*, 37(1):388–427, 2021. [3.3](#)
- [94] E. Hossain, S. Roy, N. Mohammad, N. Nawar, and D. R. Dipta. Metrics and enhancement strategies for grid resilience and reliability during natural disasters. *Applied Energy*, 290:116709, 2021. [5](#)
- [95] X. Hou, L. Shen, K. Sun, and G. Qiu. Deep feature consistent variational autoencoder. In *2017 IEEE Winter Conference on Applications of Computer Vision (WACV)*, pages 1133–1141, 2017. [3.3.2](#)
- [96] S. Huang, L. Tang, J. P. Hupy, Y. Wang, and G. Shao. A commentary review on the use of normalized difference vegetation index (ndvi) in the era of popular remote sensing. *Journal of Forestry Research*, 32:1–6. [2.1.3](#)
- [97] X. Huang, C. Shi, and S. C. Liew. Tree crown detection and delineation using optical satellite imagery. In *IGARSS 2018 - 2018 IEEE International Geoscience and Remote Sensing Symposium*, pages 2944–2947, 2018. [4.1](#)
- [98] L. Häme, J. Norppa, P. Salovaara, and J. Pylvänäinen. Power line monitoring using optical satellite data. In *CIREN Workshop 2016*, pages 1–4, 2016. [4.1](#)
- [99] S. Illarionova, D. Shadrin, V. Ignatiev, S. Shayakhmetov, A. Trekin, and I. Oseledets. Estimation of the canopy height model from multispectral satellite imagery with convolutional neural networks. *IEEE Access*, 10:34116–34132, 2022. [4.3](#)
- [100] S. Illarionova, D. Shadrin, P. Tregubova, V. Ignatiev, A. Efimov, I. Oseledets, and E. Burnaev. A survey of computer vision techniques for forest characterization and carbon monitoring tasks. *Remote Sensing*, 14(7):5861, 2022. [3](#)

- [101] S. Illarionova, A. Trekin, V. Ignatiev, and I. Oseledets. Neural-based hierarchical approach for detailed dominant forest species classification by multispectral satellite imagery. *IEEE Journal of Selected Topics in Applied Earth Observations and Remote Sensing*, 14:1810–1820, 2021. 4.2
- [102] S. D. Ilčev. *Satellite Remote Sensing in Meteorology*. Springer Nature, 2018. 2
- [103] M. Immitzer, C. Atzberger, and T. Koukal. Tree species classification with random forest using very high spatial resolution 8-band worldview-2 satellite data. *Remote Sensing*, 4(9):2661–2693, Sep 2012. 4.2
- [104] S. Ioffe and C. Szegedy. Batch normalization: Accelerating deep network training by reducing internal covariate shift. In *Proceedings of the 32nd International Conference on International Conference on Machine Learning - Volume 37, ICML'15*, page 448–456. JMLR.org, 2015. 3.2.1
- [105] G. Jansson and P. Angelstam. Threshold levels of habitat composition for the presence of the long-tailed tit (*aegithalos caudatus*) in a boreal landscape. *Landscape Ecology*, 14:283–290, 2004. 4.2
- [106] E. Jenelius and L.-G. Mattsson. Road network vulnerability analysis: Conceptualization, implementation and application. *Computers, Environment and Urban Systems*, 49:136–147, 2015. 5.2
- [107] J. Jeong, C. Yang, and T. Kim. Geo-positioning accuracy using multiple-satellite images: Ikonos, quickbird, and kompsat-2 stereo images. *Remote Sensing*, 7(4):4549–4564, 2015. 2.1.1
- [108] Jet Propulsion Laboratory (JPL-NASA). SAR Overview. <https://nisar.jpl.nasa.gov/mission/get-to-know-sar/overview/>. 2.1.4
- [109] T. Jiang, J. L. Gradus, and A. J. Rosellini. Supervised machine learning: A brief primer. *Behavior Therapy*, 51(5):675–687, 2020. 3.3
- [110] L. Jones and P. Hobbs. The application of terrestrial lidar for geohazard mapping, monitoring and modelling in the british geological survey. *Remote Sensing*, 13(3):395, 2021. 2.2
- [111] J. Jung, E. Che, M. J. Olsen, and K. C. Shafer. Automated and efficient powerline extraction from laser scanning data using a voxel-based subsampling with hierarchical approach. *ISPRS Journal of Photogrammetry and Remote Sensing*, 163:343–361, 2020. 4
- [112] M.-H. Ka, P. E. Shimkin, A. I. Baskakov, and M. I. Babokin. A new single-pass sar interferometry technique with a single-antenna for terrain height measurements. *Remote Sensing*, 11(9):1070, May 2019. 2.1.4
- [113] I. Kakogeorgiou and K. Karantzalos. Evaluating explainable artificial intelligence methods for multi-label deep learning classification tasks in remote sensing. *International Journal of Applied Earth Observation and Geoinformation*, 103:102520, 2021. 3.4

BIBLIOGRAPHY

- [114] E. Kalinicheva, J. Sublime, and M. Trocan. Neural network autoencoder for change detection in satellite image time series. In *2018 25th IEEE International Conference on Electronics, Circuits and Systems (ICECS)*, pages 641–642, 2018. [5.1](#)
- [115] A. Kamińska, M. Lisiewicz, and K. Stereńczak. Single tree classification using multi-temporal als data and cir imagery in mixed old-growth forest in poland. *Remote Sensing*, 13(24):5101, Dec 2021. [4.2](#)
- [116] W. Kang and Y. Kim. Extraction of landslide-related factors near power transmission facilities using high-resolution satellite images. In *IGARSS 2023 - 2023 IEEE International Geoscience and Remote Sensing Symposium*, pages 2477–2480, 2023. [4](#)
- [117] A. Karaer, M. Chen, M. Gazzea, M. Ghorbanzadeh, T. Abichou, R. Arghandeh, and E. E. Ozguven. Remote sensing-based comparative damage assessment of historical storms and hurricanes in northwestern florida. *International Journal of Disaster Risk Reduction*, 72:102857, 2022. [1.1](#), [1.4.1](#), [2](#)
- [118] N. B. M. G. R. A. Karaer, Alican and E. E. Ozguven. Analyzing covid-19 impacts on vehicle travels and daily nitrogen dioxide (no2) levels among florida counties, 2020. [1.4.1](#)
- [119] S. Kaur, S. Gupta, S. Singh, D. Koundal, and A. Zaguia. Convolutional neural network based hurricane damage detection using satellite images. *Soft Comput*, 09 2021. [5.1](#)
- [120] R. Kemker, C. Salvaggio, and C. Kanan. Algorithms for semantic segmentation of multispectral remote sensing imagery using deep learning. *Isprs Journal of Photogrammetry and Remote Sensing*, 145:60–77, 2018. [4.1](#)
- [121] F. Kherif and A. Latypova. Chapter 12 - principal component analysis. In *Machine Learning*, pages 209–225. Academic Press, 2020. [3.3](#)
- [122] A. Kirillov, E. Mintun, N. Ravi, H. Mao, C. Rolland, L. Gustafson, T. Xiao, S. Whitehead, A. C. Berg, W.-Y. Lo, P. Dollár, and R. B. Girshick. Segment anything. *ArXiv*, abs/2304.02643, 2023. [3.4](#)
- [123] D. E. Kislov and K. Korznikov. Automatic windthrow detection using very-high-resolution satellite imagery and deep learning. *Remote. Sens.*, 12:1145, 2020. [5.1](#)
- [124] Y. Kobayashi, G. G. Karady, G. T. Heydt, and R. G. Olsen. The utilization of satellite images to identify trees endangering transmission lines. *IEEE Transactions on Power Delivery*, 24(3):1703–1709, 2009. [4.1](#)
- [125] A. Kocatepe, M. Ulak, G. Kakareko, E. Ozguven, S. Jung, and R. Arghandeh. Measuring the accessibility of critical facilities in the presence of hurricane-related roadway closures and an approach for predicting future roadway disruptions. *Natural Hazards*, 95, 02 2019. [5](#)

- [126] Y. Kokubu, S. Hara, and A. Tani. Mapping seasonal tree canopy cover and leaf area using worldview-2/3 satellite imagery: A megacity-scale case study in tokyo urban area. *Remote Sensing*, 12(9):1505, May 2020. 4.1
- [127] N. S. P. Kong. A literature review on histogram equalization and its variations for digital image enhancement. *International journal of innovation, management and technology*, 2013. 3.2.1
- [128] K. Korznikov, D. Kislov, J. Altman, J. Dolezal, A. Vozmishcheva, and P. Krestov. Using u-net-like deep convolutional neural networks for precise tree recognition in very high resolution rgb (red, green, blue) satellite images. *Forests*, 12:66, 01 2021. 4.1
- [129] P. Kupidura. The comparison of different methods of texture analysis for their efficacy for land use classification in satellite imagery. *Remote Sensing*, 11(10):1233, May 2019. 3.2.2
- [130] T. V. La and C. Messenger. Convective system observations by leo and geo satellites in combination. *IEEE Journal of Selected Topics in Applied Earth Observations and Remote Sensing*, 14:11814–11823, 2021. 2.1
- [131] D. Landgrebe. Hyperspectral image data analysis. *IEEE Signal Processing Magazine*, 19(1):17–28, 2002. 2.1.3
- [132] P. Lavanya and E. Sasikala. Deep learning techniques on text classification using natural language processing (nlp) in social healthcare network: A comprehensive survey. In *2021 3rd International Conference on Signal Processing and Communication (ICPSC)*, pages 603–609, 2021. 3.3
- [133] A. M. Lechner, G. M. Foody, and D. S. Boyd. Applications in remote sensing to forest ecology and management. *One Earth*, 2(5):405–412, 2020. 4.2
- [134] H.-Y. Lee, T. Kim, W. Park, and H. K. Lee. Extraction of digital elevation models from satellite stereo images through stereo matching based on epipolarity and scene geometry. *Image and Vision Computing*, 21(9):789–796, 2003. 2.1.1
- [135] S.-H. Lee, K.-J. Han, K. A. Lee, K. Lee, K.-Y. Oh, and M.-J. Lee. Classification of landscape affected by deforestation using high-resolution remote sensing data and deep-learning techniques. *Remote. Sens.*, 12:3372, 2020. 2
- [136] Leon County, Florida. 2018 TLCGIS LiDAR dataset. <https://noaa-nos-coastal-lidar-pds.s3.amazonaws.com/laz/geoid18/9115/index.html>. 2.11
- [137] S. Leprince, S. Barbot, F. Ayoub, and J.-P. Avouac. Automatic and precise orthorectification, coregistration, and subpixel correlation of satellite images, application to ground deformation measurements. *IEEE Transactions on Geoscience and Remote Sensing*, 45(6):1529–1558, 2007. 2.1.1
- [138] S. Li, W. Song, L. Fang, Y. Chen, P. Ghamisi, and J. Benediktsson. Deep learning for hyperspectral image classification: An overview. *IEEE Transactions on Geoscience and Remote Sensing*, 57:6690–6709, 2019. 4.1

BIBLIOGRAPHY

- [139] S. Li, L. Xu, Y. Jing, H. Yin, X. Li, and X. Guan. High-quality vegetation index product generation: A review of ndvi time series reconstruction techniques. *International Journal of Applied Earth Observation and Geoinformation*, 105:102640, 2021. [2.1.3](#)
- [140] Z. Li, F. Liu, W. Yang, S. Peng, and J. Zhou. A survey of convolutional neural networks: Analysis, applications, and prospects. *IEEE Transactions on Neural Networks and Learning Systems*, 33(12):6999–7019, 2022. [3.3.1](#)
- [141] Q. Liu, D. Liu, X. Zhu, Y. Zhou, C. Le, Z. Mao, J. Bai, D. Bi, P. Chen, W. Chen, and C. Liu. Optimum wavelength of spaceborne oceanic lidar in penetration depth. *Journal of Quantitative Spectroscopy and Radiative Transfer*, 256:107310, 2020. [2.2](#)
- [142] X. Liu, X. Miao, H. Jiang, and J. Chen. Data analysis in visual power line inspection: An in-depth review of deep learning for component detection and fault diagnosis. *Annual Reviews in Control*, 50:253–277, 2020. [4](#)
- [143] J. Long, E. Shelhamer, and T. Darrell. Fully convolutional networks for semantic segmentation. In *Proceedings of the IEEE Conference on Computer Vision and Pattern Recognition (CVPR)*, June 2015. [3.3.1](#)
- [144] R. M. Lotfy, M. Khalifa, and M. A.-M. Salem. Autoencoder models optimization for remote sensing image semantic segmentation. In *2022 International Conference on Microelectronics (ICM)*, pages 241–245, 2022. [3.3.2](#)
- [145] D. Lowe. Object recognition from local scale-invariant features. In *Proceedings of the Seventh IEEE International Conference on Computer Vision*, volume 2, pages 1150–1157 vol.2, 1999. [3.2.2](#)
- [146] B. Lu, P. D. Dao, J. Liu, Y. He, and J. Shang. Recent advances of hyperspectral imaging technology and applications in agriculture. *Remote. Sens.*, 12:2659, 2020. [2.1.3](#)
- [147] R. Lunetta, J. Knight, and J. Ediriwickrema. Land-cover characterization and change detection using multitemporal modis ndvi data. In *International Workshop on the Analysis of Multi-Temporal Remote Sensing Images, 2005.*, pages 191–194, 2005. [2.1.3](#)
- [148] L. T. Luppino, M. A. Hansen, M. Kampffmeyer, F. M. Bianchi, G. Moser, R. Jenssen, and S. N. Anfinsen. Code-aligned autoencoders for unsupervised change detection in multimodal remote sensing images. *IEEE Transactions on Neural Networks and Learning Systems*, pages 1–13, 2022. [3.3.2](#)
- [149] Z. Lv, H. Huang, L. Gao, J. A. Benediktsson, M. Zhao, and C. Shi. Simple multiscale unet for change detection with heterogeneous remote sensing images. *IEEE Geoscience and Remote Sensing Letters*, 19:1–5, 2022. [3.3.1](#)
- [150] S. Ma, Y. Zhou, P. H. Gowda, J. Dong, G. Zhang, V. G. Kakani, P. Wagle, L. Chen, K. C. Flynn, and W. Jiang. Application of the water-related spectral reflectance indices: A review. *Ecological Indicators*, 98:68–79, 2019. [2.1.3](#)

- [151] F. Mahdi Elsiddig Haroun, S. Mohamad Deros, Z. Baharuddin, and N. Din. Detection of vegetation encroachment in power transmission line corridor from satellite imagery using support vector machine: A features analysis approach. *Energies*, 14, 06 2021. [4.1](#)
- [152] N. A. Mahmon and N. Ya'acob. A review on classification of satellite image using artificial neural network (ann). In *2014 IEEE 5th Control and System Graduate Research Colloquium*, pages 153–157, 2014. [3.3](#)
- [153] N. O. Mahony, S. Campbell, A. Carvalho, S. Harapanahalli, G. A. Velasco-Hernández, L. Krpalkova, D. Riordan, and J. Walsh. Deep learning vs. traditional computer vision. *ArXiv*, abs/1910.13796, 2019. [3](#)
- [154] L. Matikainen, M. Lehtomäki, E. Ahokas, J. Hyyppä, M. Karjalainen, A. Jaakkola, A. Kukko, and T. Heinonen. Remote sensing methods for power line corridor surveys. *Isprs Journal of Photogrammetry and Remote Sensing*, 119:10–31, 2016. [1.1](#), [4](#)
- [155] M. J. McCarthy, B. Jessen, M. J. Barry, M. Figueroa, J. McIntosh, T. Murray, J. Schmid, and F. E. Muller-Karger. Mapping hurricane damage: A comparative analysis of satellite monitoring methods. *International Journal of Applied Earth Observation and Geoinformation*, 91:102134, 2020. [5.1](#)
- [156] G. A. McCue, J. G. Williams, and J. M. Morford. Optical characteristics of artificial satellites. *Planetary and Space Science*, 19(8):851–868, 1971. [2.1.3](#)
- [157] M. L. Meeks. Atmospheric emission and opacity at millimeter wavelengths due to oxygen. *Journal of Geophysical Research (1896-1977)*, 66(11):3749–3757, 1961. [2.1](#)
- [158] Q. Meng, D. Catchpoole, D. Skillicom, and P. J. Kennedy. Relational autoencoder for feature extraction. In *2017 International Joint Conference on Neural Networks (IJCNN)*, pages 364–371, 2017. [3.3.2](#)
- [159] X. Meng, H. Shen, H. Li, L. Zhang, and R. Fu. Review of the pansharpening methods for remote sensing images based on the idea of meta-analysis: Practical discussion and challenges. *Inf. Fusion*, 46:102–113, 2019. [2.1.3](#)
- [160] S. J. Mills, M. P. Gerardo Castro, Z. Li, J. Cai, R. Hayward, L. Mejias, and R. A. Walker. Evaluation of aerial remote sensing techniques for vegetation management in power-line corridors. *IEEE Transactions on Geoscience and Remote Sensing*, 48(9):3379–3390, 2010. [4](#)
- [161] S. Minaee, Y. Boykov, F. Porikli, A. Plaza, N. Kehtarnavaz, and D. Terzopoulos. Image segmentation using deep learning: A survey. *IEEE Transactions on Pattern Analysis and Machine Intelligence*, 44(7):3523–3542, 2022. [3.1](#), [3.3](#)
- [162] P. Mohammadpour, D. X. Viegas, and C. Viegas. Vegetation mapping with random forest using sentinel 2 and glcm texture feature—a case study for lousã region, portugal. *Remote Sensing*, 14(18):4585, Sept. 2022. [3.2.2](#)

BIBLIOGRAPHY

- [163] A. J. Moshayedi, A. S. Roy, A. Kolahdooz, and Y. Shuxin. Deep learning application pros and cons over algorithm deep learning application pros and cons over algorithm. *EAI Endorsed Transactions on AI and Robotics*, 1(1), 2 2022. 3.3
- [164] G. Mountrakis, J. Im, and C. Ogole. Support vector machines in remote sensing: A review. *ISPRS Journal of Photogrammetry and Remote Sensing*, 66(3):247–259, 2011. 3.3
- [165] V. Mulder, S. de Bruin, M. Schaepman, and T. Mayr. The use of remote sensing in soil and terrain mapping — a review. *Geoderma*, 162(1):1–19, 2011. 2
- [166] O. Munyaneza, U. G. Wali, S. Uhlenbrook, S. Maskey, and M. J. Mlotha. Water level monitoring using radar remote sensing data: Application to lake kivu, central africa. *Physics and Chemistry of the Earth, Parts A/B/C*, 34(13):722–728, 2009. 9th WaterNet/WARFSA/GWP-SA Symposium: Water and Sustainable Development for Improved Livelihoods. 2
- [167] National Oceanic and Atmospheric Administration (NOAA). What is remote sensing?). <https://oceanservice.noaa.gov/facts/remotesensing.html>. 2
- [168] F. Nex, D. Duarte, F. G. Tonolo, and N. Kerle. Structural building damage detection with deep learning: Assessment of a state-of-the-art cnn in operational conditions. *Remote Sensing*, 11(23):2765, Nov 2019. 5.1
- [169] T. Ngobeni and R. Ajoodha. Satellite image classification using hog and daisy feature descriptors. In *2022 International Conference on Electrical, Computer, Communications and Mechatronics Engineering (ICECCME)*, 2022. 3.2.2
- [170] V. N. Nguyen, R. Jenssen, and D. Roverso. Automatic autonomous vision-based power line inspection: A review of current status and the potential role of deep learning. *International Journal of Electrical Power & Energy Systems*, 99:107–120, 2018. 4
- [171] N. Nigam, T. Dutta, and H. P. Gupta. Impact of noisy labels in learning techniques: A survey. In M. L. Kolhe, S. Tiwari, M. C. Trivedi, and K. K. Mishra, editors, *Advances in Data and Information Sciences*, pages 403–411, Singapore, 2020. Springer Singapore. 4.2
- [172] NRK. Kunstig intelligens kan hindra straubrot. <https://www.nrk.no/vestland/kunstig-intelligens-kan-hindra-straumbrot-1.16333843>. 4.3
- [173] NSR. Earth observation: analytics-as-a-service. <https://www.nsr.com/earth-observation-analytics-as-a-service/>. 4, 4.1
- [174] N. Oceanic and A. A. (NOAA). Hurricane costs. <https://coast.noaa.gov/states/fast-facts/hurricane-costs.html>. 5.1
- [175] N. I. of Bioeconomy Research (NIBIO). https://kilden.nibio.no/?lang=nb&topic=arealinformasjon&X=7195706.12&Y=284337.75&zoom=0.050089679614182224&bgLayer=graatone_cache. Online. 4.2

- [176] K. Oki, M. Soga, T. Amano, and S. Koike. Power line corridors in conifer plantations as important habitats for butterflies. *Journal of Insect Conservation*, 25, 12 2021. 4.2
- [177] H. O. Ørka and M. Hauglin. Use of remote sensing for mapping of non-native conifer species. <https://www.miljodirektoratet.no/globalassets/publikasjoner/m490/m490.pdf>, 2016. [Online]. 1.1
- [178] L. P. Osco, Q. Wu, E. L. de Lemos, W. N. Gonçalves, A. P. M. Ramos, J. Li, and J. Marcato. The segment anything model (sam) for remote sensing applications: From zero to one shot. *International Journal of Applied Earth Observation and Geoinformation*, 124:103540, 2023. 3.4, 6.3
- [179] Overstory. Rethinking vegetation management on electric utility corridors — combining ai & satellite data. <https://www.overstory.com/blog/rethinking-g-vegetation-management-on-electric-utility-corridors-combining-ai-satellite-data>. 1.1
- [180] M. Pacevicius, D. O. Dammann, M. Gazzea, and A. Saprionova. Heterogeneous data-merging platform for improved risk management in power grids. In *2021 Annual Reliability and Maintainability Symposium (RAMS)*, pages 1–7, 2021. 1.4.1
- [181] M. Pal and P. M. Mather. Support vector machines for classification in remote sensing. *International Journal of Remote Sensing*, 26(5):1007–1011, 2005. 3.3
- [182] Z. Pan. Urban vegetation type analysis method based on high resolution satellite images. In *2016 International Conference on Smart City and Systems Engineering (ICSCSE)*, pages 613–616, 2016. 4.1
- [183] A. Pepe and F. Calò. A review of interferometric synthetic aperture radar (insar) multi-track approaches for the retrieval of earth’s surface displacements. *Applied Sciences*, 7(12):1264, Dec. 2017. 2.1.4
- [184] C. Pipitone, A. Maltese, G. Dardanelli, M. L. Brutto, and G. L. Loggia. Monitoring water surface and level of a reservoir using different remote sensing approaches and comparison with dam displacements evaluated via gnss. *Remote. Sens.*, 10:71, 2018. 2
- [185] E. Protopapadakis, A. Doulamis, N. Doulamis, and E. Maltezos. Stacked autoencoders driven by semi-supervised learning for building extraction from near infrared remote sensing imagery. *Remote Sensing*, page 371, 2021. 3.3.2
- [186] P. Qin, Y. Cai, J. Liu, P. Fan, and M. Sun. Multilayer feature extraction network for military ship detection from high-resolution optical remote sensing images. *IEEE Journal of Selected Topics in Applied Earth Observations and Remote Sensing*, 14:11058–11069, 2021. 2
- [187] M. Rahman and L. Di. A systematic review on case studies of remote-sensing-based flood crop loss assessment. *Agriculture*, 10:131, 04 2020. 5.1

BIBLIOGRAPHY

- [188] Railway-News. How green is satellite monitoring? let's do the math. <https://railway-news.com/how-green-is-satellite-monitoring-lets-do-the-math/>, 2022. [Online]. 1.1
- [189] B. Rasti, D. Hong, R. Hang, P. Ghamisi, X. Kang, J. Chanussot, and J. A. Benediksson. Feature extraction for hyperspectral imagery: The evolution from shallow to deep: Overview and toolbox. *IEEE Geoscience and Remote Sensing Magazine*, 8(4):60–88, 2020. 3.3
- [190] M. Rezaee, Y. Zhang, R. Mishra, F. Tong, and H. Tong. Using a vgg-16 network for individual tree species detection with an object-based approach. In *2018 10th IAPR Workshop on Pattern Recognition in Remote Sensing (PRRS)*, pages 1–7, 2018. 3.3.1
- [191] A. Rista and A. Kadriu. Automatic speech recognition: A comprehensive survey. *SEEU Review*, 15:86–112, 12 2020. 3.3
- [192] D. Rivera-Marin, J. Dash, and B. Ogutu. The use of remote sensing for desertification studies: A review. *Journal of Arid Environments*, 206:104829, 2022. 2
- [193] O. Ronneberger, P. Fischer, and T. Brox. U-net: Convolutional networks for biomedical image segmentation. In *Medical Image Computing and Computer-Assisted Intervention – MICCAI 2015*, pages 234–241. Springer International Publishing, 2015. 3.3.1
- [194] O. Russakovsky, J. Deng, H. Su, J. Krause, S. Satheesh, S. Ma, Z. Huang, A. Karpathy, A. Khosla, M. Bernstein, A. C. Berg, and L. Fei-Fei. ImageNet Large Scale Visual Recognition Challenge. *International Journal of Computer Vision (IJCV)*, 115(3):211–252, 2015. 3.3.1
- [195] I. H. Sarker. Machine learning: Algorithms, real-world applications and research directions. *Sn Computer Science*, 2, 2021. 3.3
- [196] A. Saxena and S. Iyengar. Centrality measures in complex networks: A survey. *ArXiv*, abs/2011.07190, 2020. 5.2
- [197] O. Schneising, M. Buchwitz, M. Reuter, S. Vanselow, H. Bovensmann, and J. P. Burrows. Remote sensing of methane leakage from natural gas and petroleum systems revisited. *Atmospheric Chemistry and Physics*, 2020. 2
- [198] R. R. Selvaraju, A. Das, R. Vedantam, M. Cogswell, D. Parikh, and D. Batra. Grad-cam: Visual explanations from deep networks via gradient-based localization. *International Journal of Computer Vision*, 128:336 – 359, 2016. 3.4
- [199] C. Senf. Seeing the system from above: The use and potential of remote sensing for studying ecosystem dynamics. *Ecosystems*, 25, 09 2022. 2
- [200] H. Shakhathreh, A. H. Sawalmeh, A. Al-Fuqaha, Z. Dou, E. Almaita, I. Khalil, N. S. Othman, A. Khreishah, and M. Guizani. Unmanned aerial vehicles (uavs): A

- survey on civil applications and key research challenges. *IEEE Access*, 7:48572–48634, 2019. 4
- [201] M. Sheykhoumoussa, M. Mahdianpari, H. Ghanbari, F. Mohammadimanesh, P. Ghamisi, and S. Homayouni. Support vector machine versus random forest for remote sensing image classification: A meta-analysis and systematic review. *IEEE Journal of Selected Topics in Applied Earth Observations and Remote Sensing*, 13:6308–6325, 2020. 3.1
- [202] W. Shi, M. Zhang, R. Zhang, S. Chen, and Z. Zhan. Change detection based on artificial intelligence: State-of-the-art and challenges. *Remote Sensing*, 12(10):1688, May 2020. 5.1
- [203] T. A. Short. *Electric Power Distribution Handbook*. CRC Press, 2014. Chapter 3. Overhead Line Performance. 1.1
- [204] Y. R. Shrestha, V. Krishna, and G. von Krogh. Augmenting organizational decision-making with deep learning algorithms: Principles, promises, and challenges. *Journal of Business Research*, 123:588–603, 2021. 3.3
- [205] M. Shuai, W. Chengzhi, Y. Shiwen, G. Hao, Y. Jufang, and H. Hui. Review on economic loss assessment of power outages. *Procedia Computer Science*, 130:1158–1163, 2018. The 9th International Conference on Ambient Systems, Networks and Technologies (ANT 2018) / The 8th International Conference on Sustainable Energy Information Technology (SEIT-2018) / Affiliated Workshops. 1.1
- [206] F. Sica, A. Pulella, M. Nannini, M. Pinheiro, and P. Rizzoli. Repeat-pass sar interferometry for land cover classification: A methodology using sentinel-1 short-time-series. *Remote Sensing of Environment*, 232:111277, 2019. 2.1.4
- [207] J. V. Solórzano, J. F. Mas, J. A. Gallardo-Cruz, Y. Gao, and A. Fernández-Montes de Oca. Deforestation detection using a spatio-temporal deep learning approach with synthetic aperture radar and multispectral images. *ISPRS Journal of Photogrammetry and Remote Sensing*, 199:87–101, 2023. 2
- [208] M. G. Sommervold, Oscar and R. Arghandeh. A survey on sar and optical satellite image registration, 2023. 1.4.1
- [209] SpaceNet. SpaceNet Challenge Datasets). <https://spacenet.ai/datasets/>. 2.10
- [210] Statnett. Årsrapporter fra Feilanalyse. <https://www.statnett.no/for-aktorer-i-kraftbransjen/systemansvaret/arsrapporter-fra-feilanalyse/>. 1.1, 4.1
- [211] Straits Research. Global power transmission and distribution (t&d) equipment market worth usd 265.63 billion by 2031. <https://straitsresearch.com/press-release/global-power-transmission-and-distribution-equipment-market-outlook>. 4
- [212] B. Stuart. *Infrared Spectroscopy*. John Wiley & Sons, Ltd, 2005. 2.1.3

BIBLIOGRAPHY

- [213] M. B. Stuart, A. J. S. McGonigle, and J. R. Willmott. Hyperspectral imaging in environmental monitoring: A review of recent developments and technological advances in compact field deployable systems. *Sensors (Basel, Switzerland)*, 19, 2019. [2.1.3](#)
- [214] Y. Sun, F. Bi, Y. Gao, L. Chen, and S. Feng. A multi-attention unet for semantic segmentation in remote sensing images. *Symmetry*, 14:906, 2022. [3.3.1](#)
- [215] J. Svoboda, P. Štych, J. Laštovička, D. Paluba, and N. Kobliuk. Random forest classification of land use, land-use change and forestry (lulucf) using sentinel-2 data—a case study of czechia. *Remote Sensing*, 14(5):1189, Feb. 2022. [3.3](#)
- [216] V. T. M. J., van den Homberg M., and L. J. Multi-hazard and spatial transferability of a cnn for automated building damage assessment. *Remote Sensing*, 17:2839, 12 2020. [5.1](#)
- [217] S. Tang, B. Wu, and Q. Zhu. Combined adjustment of multi-resolution satellite imagery for improved geo-positioning accuracy. *ISPRS Journal of Photogrammetry and Remote Sensing*, 114:125–136, 2016. [2.1.1](#)
- [218] J. Tao, Y. Gu, J. Sun, Y. Bie, and H. Wang. Research on vgg16 convolutional neural network feature classification algorithm based on transfer learning. In *2021 2nd China International SAR Symposium (CISS)*, pages 1–3, 2021. [3.3.1](#)
- [219] B. Tavus. Glcm features for learning flooded vegetation from sentinel-1 and sentinel-2 data. *The International Archives of the Photogrammetry, Remote Sensing and Spatial Information Sciences*, 2023. [3.2.2](#)
- [220] The New York Times. Irma swiftly lays claim to florida’s sea of trees. <https://www.nytimes.com/2017/09/11/us/miami-orlando-tampa.html>, 2017. [5.1](#)
- [221] H. Tian, T. Wang, Y. Liu, X. Qiao, and Y. Li. Computer vision technology in agricultural automation—a review. *Information Processing in Agriculture*, 7(1):1–19, 2020. [3](#)
- [222] J. Tian, S. Cui, and P. Reinartz. Building change detection based on satellite stereo imagery and digital surface models. *IEEE Transactions on Geoscience and Remote Sensing*, 52(1):406–417, 2014. [2.1.1](#)
- [223] X. Tong, S. Liu, and Q. Weng. Bias-corrected rational polynomial coefficients for high accuracy geo-positioning of quickbird stereo imagery. *ISPRS Journal of Photogrammetry and Remote Sensing*, 65(2):218–226, 2010. [2.1.1](#)
- [224] C. Toth and G. Józków. Remote sensing platforms and sensors: A survey. *ISPRS Journal of Photogrammetry and Remote Sensing*, 115:22–36, 2016. Theme issue ‘State-of-the-art in photogrammetry, remote sensing and spatial information science’. [2](#)
- [225] A. Tsokas, M. Rysz, P. M. Pardalos, and K. Dipple. SAR data applications in earth observation: An overview. *Expert Systems with Applications*, 205:117342, 2022. [2.1.4](#)

- [226] S. Tuominen, A. Balazs, H. Saari, I. Pölönen, J. Sarkeala, and R. Viitala. Unmanned aerial system imagery and photogrammetric canopy height data in area-based estimation of forest variables. *Silva Fennica*, 49:1348, 2015. 4.2
- [227] U. C. Turhal. Vegetation detection using vegetation indices algorithm supported by statistical machine learning. *Environ Monit Assess*, 194:826, 2022. 4.1
- [228] L. Twerd, A. Sobieraj-Betlińska, and P. Szefer. Roads, railways, and power lines: Are they crucial for bees in urban woodlands? *Urban Forestry & Urban Greening*, 61:127120, 2021. 4.2
- [229] M. P. Uddin, M. A. Mamun, and M. A. Hossain. Pca-based feature reduction for hyperspectral remote sensing image classification. *IETE Technical Review*, 38:377–396, 2020. 3.3
- [230] F. T. Ulaby, F. Kouyate, B. Brisco, and T. H. L. Williams. Textural information in sar images. *IEEE Transactions on Geoscience and Remote Sensing*, GE-24(2):235–245, 1986. 2.1.4
- [231] M. Ulak, A. Kocatepe, L. Sriram, E. Ozguven, and R. Arghandeh. Assessment of the hurricane-induced power outages from a demographic, socioeconomic, and transportation perspective. *Natural Hazards*, 92, 07 2018. 5
- [232] M. B. Ulak, L. M. Konila Sriram, A. Kocatepe, E. E. Ozguven, and R. Arghandeh. Resilience characterization for multilayer infrastructure networks. *IEEE Intelligent Transportation Systems Magazine*, 14(4):121–132, 2022. 5
- [233] M. B. Ulak, A. Yazici, E. E. Ozguven, A. Vanli, and R. Arghandeh. Power resilience assessment from physical and socio-demographic perspectives. In *2019 4th International Conference on System Reliability and Safety (ICSRS)*, pages 421–428, 2019. 5
- [234] United Nations’ International Telecommunication Union. Focus Group on AI for Natural Disaster Management (FG-AI4NDM). <https://www.itu.int/en/ITU-T/focusgroups/ai4ndm/Pages/default.aspx>. 2, 5, 5, 6.2.2
- [235] L. van der Maaten and G. E. Hinton. Visualizing data using t-sne. *Journal of Machine Learning Research*, 9:2579–2605, 2008. 3.3.2
- [236] van Engelen and J. E. A survey on semi-supervised learning. *Machine Learning*, 109:373–440, 2020. 3.3
- [237] A. Vaswani, N. M. Shazeer, N. Parmar, J. Uszkoreit, L. Jones, A. N. Gomez, L. Kaiser, and I. Polosukhin. Attention is all you need. In *Neural Information Processing Systems*, 2017. 3.4
- [238] J. Verschuur, E. Koks, and J. Hall. Port disruptions due to natural disasters: Insights into port and logistics resilience. *Transportation Research Part D: Transport and Environment*, 85:102393, 2020. 5

BIBLIOGRAPHY

- [239] T. Vigneshl and K. K. Thyagarajan. Local binary pattern texture feature for satellite imagery classification. In *2014 International Conference on Science Engineering and Management Research (ICSEMR)*, pages 1–6, 2014. [3.2.2](#)
- [240] F. Wagner, A. Sánchez, Y. Tarabalka, R. G. Lotte, M. P. Ferreira, M. P. Aïdar, E. Gloor, O. Phillips, and L. Aragão. Using the u-net convolutional network to map forest types and disturbance in the atlantic rainforest with very high resolution images. *Remote Sensing in Ecology and Conservation*, 5:360–375, 2019. [4.1](#)
- [241] U. Wandinger. *Introduction to Lidar*, pages 1–18. Springer New York, New York, NY, 2005. [2.2](#)
- [242] D. Wang, J. Zhang, B. Du, D. Tao, and L. Zhang. Scaling-up remote sensing segmentation dataset with segment anything model. *ArXiv*, abs/2305.02034, 2023. [3.4](#)
- [243] P. Wang, E. Fan, and P. Wang. Comparative analysis of image classification algorithms based on traditional machine learning and deep learning. *Pattern Recognition Letters*, 141:61–67, 2021. [3.3](#)
- [244] S. Wang, C. Chen, J. Zhang, X. Gu, and X. Huang. Vulnerability assessment of urban road traffic systems based on traffic flow. *International Journal of Critical Infrastructure Protection*, 38:100536, 2022. [5.2](#)
- [245] S. Wang, W. Chen, S. Xie, G. Azzari, and D. Lobell. Weakly supervised deep learning for segmentation of remote sensing imagery. *Remote Sensing*, 12:207, 01 2020. [4.1](#)
- [246] Z. Wang and M. Menenti. Challenges and opportunities in lidar remote sensing. *Frontiers in Remote Sensing*, 2:641723, 03 2021. [2.2](#)
- [247] K. Watson. Geologic applications of thermal infrared images. *Proceedings of the IEEE*, 63(1):128–137, 1975. [2.1.3](#)
- [248] Wikipedia contributors. Alan turing — Wikipedia. https://no.wikipedia.org/w/index.php?title=Alan_Turing&oldid=23911908, 2023. [2.2](#)
- [249] Wikipedia contributors. William Anders — Wikipedia. https://en.wikipedia.org/w/index.php?title=William_Anders&oldid=1191195866, 2023. [1.4.1](#)
- [250] Wikipedia contributors. Galileo Galilei. https://en.wikipedia.org/w/index.php?title=Galileo_Galilei&oldid=1197580793, 2024. [I](#)
- [251] Wikipedia contributors. Saadi Shirazi — Wikipedia. https://en.wikipedia.org/w/index.php?title=Saadi_Shirazi&oldid=1198015829, 2024. [3.4](#)
- [252] R. M. Wise, T. Capon, B. B. Lin, and M. Stafford-Smith. Pragmatic cost–benefit analysis for infrastructure resilience. *Nature Climate Change*, 12:881–883, 2022. [1.1](#)

- [253] C. Wu, F. Zhang, J. Xia, Y. Xu, G. Li, J. Xie, Z. Du, and R. Liu. Building damage detection using u-net with attention mechanism from pre- and post-disaster remote sensing datasets. *Remote Sensing*, 13:905, 02 2021. [5.1](#)
- [254] M. A. Wulder, R. J. Hall, N. C. Coops, and S. E. Franklin. High Spatial Resolution Remotely Sensed Data for Ecosystem Characterization. *BioScience*, 54(6):511–521, 06 2004. [4.2](#)
- [255] C. Xiao, R. Qin, X. Huang, and J. Li. Individual tree detection from multi-view satellite images. In *IGARSS 2018 - 2018 IEEE International Geoscience and Remote Sensing Symposium*, pages 3967–3970, 2018. [4.1](#)
- [256] D. Xu, H. Wang, W. Xu, Z. Luan, and X. Xu. Lidar applications to estimate forest biomass at individual tree scale: Opportunities, challenges and future perspectives. *Forests*, 12(5):550, 2021. [2.2](#)
- [257] Z. Yan, J. Li, X. Li, R. Zhou, W. Zhang, Y. Feng, W. Diao, K. Fu, and X. Sun. Ringmo-sam: A foundation model for segment anything in multimodal remote-sensing images. *IEEE Transactions on Geoscience and Remote Sensing*, 61:1–16, 2023. [3.4](#)
- [258] B. Yang, S. Wang, Y. Zhou, F. tao Wang, Q. Hu, Y. Chang, and Q. Zhao. Extraction of road blockage information for the jiuzhaigou earthquake based on a convolution neural network and very-high-resolution satellite images. *Earth Science Informatics*, 13:115–127, 2019. [5.1](#)
- [259] L. Yang, X. Wu, E. Praun, and X. Ma. Tree detection from aerial imagery. In *Proceedings of the 17th ACM SIGSPATIAL International Conference on Advances in Geographic Information Systems, GIS '09*, page 131–137, New York, NY, USA, 2009. Association for Computing Machinery. [3.3](#)
- [260] X. Yang, Z. Song, I. King, and Z. Xu. A survey on deep semi-supervised learning. *IEEE Transactions on Knowledge and Data Engineering*, 35(9):8934–8954, 2023. [3.3](#)
- [261] H. Ye, S. Liu, K. Jin, and H. Cheng. Ct-unet: An improved neural network based on u-net for building segmentation in remote sensing images. In *2020 25th International Conference on Pattern Recognition (ICPR)*, pages 166–172, 2021. [3.3.1](#)
- [262] M. Ye, N. Ruiwen, Z. Chang, G. He, H. Tianli, L. Shijun, S. Yu, Z. Tong, and G. Ying. A lightweight model of vgg-16 for remote sensing image classification. *IEEE Journal of Selected Topics in Applied Earth Observations and Remote Sensing*, 14:6916–6922, 2021. [3.3.1](#)
- [263] L. Yolyan. Computer vision applications for smart cities using remote sensing data: Review. *Bulletin of Yerevan University G: Economics*, 13(3 (39)):67–75, 2022. [3](#)
- [264] H. Zeng, H. Peltola, A. Talkkari, A. Venäläinen, H. Strandman, S. Kellomäki, and K. Wang. Influence of clear-cutting on the risk of wind damage at forest edges. *Forest Ecology and Management*, 203(1):77–88, 2004. [4.2](#)

BIBLIOGRAPHY

- [265] L. Zeng, B. D. Wardlow, D. Xiang, S. Hu, and D. Li. A review of vegetation phenological metrics extraction using time-series, multispectral satellite data. *Remote Sensing of Environment*, 237:111511, 2020. [2.1.3](#)
- [266] P. Zhang, M. Gong, H. Zhang, J. Liu, and Y. Ban. Unsupervised difference representation learning for detecting multiple types of changes in multitemporal remote sensing images. *IEEE Transactions on Geoscience and Remote Sensing*, 57(4):2277–2289, 2019. [5.1](#)
- [267] X. Zhang, B. Zhang, W. Yu, and X. Kang. Federated deep learning with prototype matching for object extraction from very-high-resolution remote sensing images. *IEEE Transactions on Geoscience and Remote Sensing*, 61:1–16, 2023. [3.4](#)
- [268] F. Zhou, Y. Ma, and H. Wang. Research on transmission line fire monitoring technology based on remote sensing satellite data. In *2020 International Conference on Urban Engineering and Management Science (ICUEMS)*, pages 314–317, 2020. [4](#)
- [269] J. Zhu, J. Wu, A. K. Bashir, Q. Pan, and W. Yang. Privacy-preserving federated learning of remote sensing image classification with dishonest majority. *IEEE Journal of Selected Topics in Applied Earth Observations and Remote Sensing*, 16:4685–4698, 2023. [3.4](#)
- [270] L. Zhu, J. Suomalainen, J. Liu, J. Hyypä, H. Kaartinen, and H. Haggren. A review: Remote sensing sensors. In R. B. Rustamov, S. Hasanova, and M. H. Zeynalova, editors, *Multi-purposeful Application of Geospatial Data*, Rijeka, 2017. IntechOpen. [2](#), [2.1](#)

Part II

ARTICLES



AUTOMATED POWER LINES VEGETATION MONITORING USING HIGH-RESOLUTION SATELLITE IMAGERY

Gazzea M., Pacevicius M., Dammann D. O., Sapronova A., Lunde T. M. and Arghandeh R.

In IEEE Transactions on Power Delivery, vol. 37, no. 1, pp. 308-316, 2022, doi:
[10.1109/TPWRD.2021.3059307](https://doi.org/10.1109/TPWRD.2021.3059307)

©2024 IEEE. Reprinted, with permission, from [70]

Automated Power Lines Vegetation Monitoring using High-Resolution Satellite Imagery

Michele Gazzea , *Member, IEEE*, Michael Pacevicius, Dyre Oliver Dammann, Alla Saprionova, Torleif Markussen Lunde, and Reza Arghandeh , *Senior Member, IEEE*

Abstract—Vegetation Management is a significant preventive maintenance expense in many power transmission and distribution companies. Traditional Vegetation Management operational practices have proven ineffective and are rapidly becoming obsolete due to the lack of frequent inspection of vegetation and environmental states. The rise of satellite imagery data and machine learning provides an opportunity to close the loop with continuous data-driven vegetation monitoring. This paper proposes an automated framework for monitoring vegetation along power lines using high-resolution satellite imagery and a semi-supervised machine learning algorithm. The proposed satellite-based vegetation monitoring framework aims to reduce the cost and time of power line monitoring by partially replacing ground patrols and helicopter or drone inspection with satellite data analytics. It is implemented and demonstrated for a power distribution system operator (DSO) in the west of Norway. For further assessment, the satellite-based algorithm outcomes are compared with LiDAR survey data collected by helicopters. The results show the potential of the solution for reducing the monitoring costs for electric utilities.

Index Terms—Satellite imagery, Vegetation management, Power systems, Electric grid monitoring, Semi-supervised segmentation

I. INTRODUCTION

POWER transmission and distribution networks spread across countries and pass through forests, over various terrain, and cities on their journey to electricity consumers. Whenever vegetation interferes with power lines, it brings safety, economic, and environmental risks. Vegetation, combined with severe weather conditions, is the predominant reason for outages in power systems that put millions of people in darkness and bring billions of dollars in economic damage [1]. In areas with severe drought, vegetation encroachment in power lines' right-of-way (ROW) can cause massive wildfires with high fatality rate [2], [3]. Vegetation monitoring and management is becoming ever more important in the wake

This work is supported by the European Space Agency (ESA) through the GridEyeS project (No. 4000127831/19/NL/MM/ra).

M. Gazzea and R. Arghandeh are with the Department of Computer Science and Electrical Engineering at the Western Norway University of Applied Sciences, Bergen 5063, Norway. E-mail: (michele.gazzea@hvl.no, reza.arghandeh@hvl.no).

M. Pacevicius is with the Department of Mechanical and Industrial Engineering at the Norwegian University of Science and Technology, Trondheim, Norway and with eSmart Systems, Halden, Norway. E-mail: (michael.pacevicius@esmartsystems.com).

D. O. Dammann is with the University of Alaska Fairbanks. E-mail: (dodammann@alaska.edu)

A. Saprionova is with StormGeo company, Bergen, Norway E-mail: (Alla.Saprionova@stormgeo.com).

T. M. Lunde is with the Faculty of medicine at the University of Bergen, Norway. E-mail: (torleif.lunde@uib.no).

of climate change and the increasing frequency and duration of extreme weather events [4].

Utilities traditionally take a time-based approach with a fixed cycle to vegetation monitoring by sending ground-based patrol for visual line inspection and flying helicopters or drones for optical and LiDAR surveys of the power lines. Due to the vast size of service territories, the length of power lines, and the line inspection costs, vegetation monitoring's typical cycle varies between one to ten years for different electric utilities [5]. For example, the US electrical grid has more than 200,000 miles of high-voltage transmission lines and 5.5 million miles of local distribution lines [6].

Existing literature on vegetation monitoring mostly uses LiDAR surveys performed by helicopters or drones [7], [8]. LiDAR data provide an accurate 3D representation of an environment. However, LiDAR data acquisition and processing are extremely pricey and time-consuming. If LiDAR-based line monitoring is performed for a large transmission or distribution company, it is often done infrequently at an interval of once every 5 to 10 years to scan the whole service area [9].

In recent years, the drop in launching costs and the growing number of satellites and mini-satellites in orbit with high-quality sensors has significantly reduced the cost of satellite imagery [10]. Commercial satellite providers can offer high-resolution images (0.25 or 0.5 meters/pixel) with frequent revisiting time that covers most of the world. Consequently, it brings the opportunity to combine scale, frequency, and cost efficiency to enhance situational awareness regarding vegetation encroachment in power lines' right-of-way using high-resolution satellite imagery [11], [12]. Therefore, vegetation management can be changed from traditional time-based monitoring to risk-based monitoring.

Some studies [13], [14], [15] made use of multispectral stereo pairs of satellite images for each specific area to identify trees along power lines. However, stereo images are challenging to capture and are costly for large scale areas [16]. This paper proposes a machine learning-based algorithm for vegetation detection using a single satellite image, which is more cost-effective.

Vegetation detection from single monocular images is also a well-studied topic, particularly in the forest management of agriculture and urban areas using classic image processing tools for vegetation detection [17], [18], [19], [20]. However, such approaches have been developed to work well where trees are easily distinguishable, i.e., in low-density vegetation areas [21] or when the trees are regularly spaced from each other in orchards, which is not the case in the vast majority of power

lines' ROW [22].

Nowadays, Convolution Neural Networks (CNNs), have become the leading machine learning methodology in many fields due to their effectiveness at extracting feature representations from images for classification and segmentation purposes [23], [24]. For example, [25] proposed a semantic segmentation-based deep learning method to classify vegetation (tree, shrub, and grass) using only RGB images. In a similar work, [26] used a U-Net architecture for analyzing high-resolution satellite images to map forests. However, deep learning methods are generally supervised approaches and need massive labeled datasets for the training, which is extremely scant and expensive for satellite imagery and remote sensing applications. Weakly-supervised methods are, in general, more practical [27].

This paper proposes a framework to monitor vegetation proximity to power lines using high-resolution satellite images. From a methodological point of view, it is a semi-supervised approach for vegetation detection that is a combination of a deep unsupervised architecture and a supervised machine learning algorithm. Being unsupervised, the first layer of the proposed framework does not need any training data and takes advantage of deep learning to capture meaningful patterns in satellite images automatically. Nevertheless, it lacks the semantic information about the physical meaning of the different clusters. On the other hand, the second supervised layer contains the semantic knowledge of the vegetation patterns in a satellite image, and it can be trained with minimal training data. The proposed approach's outcome is a geolocation map for vegetation-related threats along power lines that provides updated situational awareness to vegetation management teams in electric utilities. The vegetation threat map is based on the density and proximity of vegetation encroachment in power lines' right-of-way. The proposed framework is implemented and validated in a vegetation management system for a power distribution company in the western part of Norway. The vegetation detection results from satellite images showed high matching with the available LiDAR survey data which has been used as the ground truth for the use case area.

II. USE CASE AND DATA DESCRIPTION

The study has been performed in collaboration with a power distribution system operator (DSO) located in the western part of Norway. The study area is a 22kV sub-transmission network in a rural region that includes fields, sparse and dense forests, and water streams. Power lines' right-of-way is 20 meters on each side which forms a 40 meter corridor (see Fig. 1). Different datasets relative to the study area have been acquired as further described in the following.

A. Satellite imagery

Two commercial high-resolution multispectral satellite images were used for the study area. The first is a Worldview-2 8-channel image provided by Maxar and acquired in May 2018. The second is a Pleiades-1 4-channel image provided by Airbus and acquired in September 2017, (see Fig. 2). Both images contain separate channels ranging from visible to near-infrared with a 0.5 meter/pixel spatial resolution.



Fig. 1: Study area located on the western coast of Norway



(a)



(b)

Fig. 2: RGB satellite image for the study area. The figure highlights the regional power line (red) and sub-regional power line (green).

B. LiDAR point clouds

We also use LiDAR data in our study as a benchmark to validate our satellite-based vegetation detection. The available LiDAR data are grouped into different categories (vegetation, buildings, roads, stones, poles), see Fig. 3.

The heights of 22kV overhead lines in the study area in the western part of Norway are at a minimum of 7.8 meters with an average of 10.8 meters. Trees should have at least a 2.0 m distance to the conductors considering the catenary curvature of wires [28], [29]. In this study, we used LiDAR data provided by our electric utility partner as the ground truth for trees' location in the vicinity of power lines' right-of-way. However, the acquisition time for the available LiDAR data

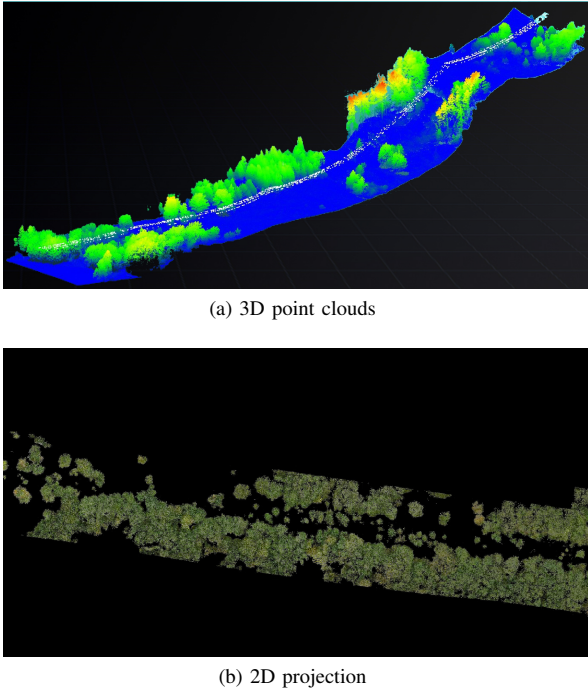


Fig. 3: Examples of LiDAR data used in the study

(Sep 2019) is different from the satellite imagery data we have (Sep 2017 and May 2018) for the study area. To resolve the time difference among data from LiDAR and both satellite images, we assume that trees with a height higher than 2.5 meters in 2019, as observed in LiDAR data, are probably older than two years old based on growth rate of trees in this region. Therefore, the trees taller than 2.5 meters in 2019 are observable in satellite images from 2018 and 2017 at the same location along the power lines' ROW.

III. METHODOLOGY

The satellite image is analyzed using the proposed algorithm, within a sliding window covering the power line right-of-way. In this study, we use windows of 40 by 40 meters (80×80 pixels). The algorithm sweeps the whole length of the electric power line in the study area.

Then, a segmentation map is created to show whether each pixel is a part of a tree or not. The proposed machine learning framework for satellite image processing is an ensemble of two different algorithms to enhance the overall performance. The first one is a supervised segmentation approach based on hand-crafted features, while the second one is a fully unsupervised algorithm developed for image segmentation tasks [30]. The output of the proposed machine learning framework is used for mapping vegetation risk along the power lines. Different blocks of our proposed framework, as shown in Fig. 4, are explained as follows.

A. Data Pre-processing Block

To develop a learning algorithm for tree detection, we need to have labeled data for training and testing. Such labeled data are a collection of binary images (for example "1" for tree and

"0" for non-tree) that include the ground truth with the correct location of trees. In this paper, we create the first labeled dataset with the open-source raster graphics editor GIMP. A second set of labeled data is created automatically using LiDAR point-clouds for the same region. The 3D point clouds are projected in 2D at Nadir and converted into gray-scale. The resultant gray-scale binary image is smoothed through a dilation operation (using a 3×3 kernel).

The satellite image that we use is ortho-rectified and pan-sharpened [31]. Ortho-rectification enables the correction of potential defaults that exist due to satellite tilt or terrain distortions in cases where the satellite on-board sensor is not pointing directly at the Nadir direction. Pan-sharpening, on the other hand, increases the natively low-resolution parts of a multispectral image by combining them with the higher resolution panchromatic pixels. The image is in GeoTiff format, which includes geo-references for each pixel, allowing for proper location in real-world coordinates.

B. Supervised Image Segmentation Block

Specific features are extracted at pixel-level, directly from the multi-channel images, and grouped into a vector associated with each pixel. A machine learning classifier [32] is then trained. In this paper, we use spectral features, texture features, and a Gaussian kernel as follows:

1) *Spectral Features*: First, we extract the pixel values coming from the different bands of a multispectral satellite image. Furthermore, we use the Normalized Difference Vegetation Index (NDVI) [33] to recognize vegetation. NDVI is a commonly used tool in remote sensing for vegetation detection and defined as:

$$NDVI = \frac{\rho_{nir} - \rho_{red}}{\rho_{nir} + \rho_{red}} \quad (1)$$

where ρ_{red} and ρ_{nir} stand for the spectral reflectance measurements acquired in the red (visible) and near-infrared regions, respectively.

2) *Texture Features*: Texture patterns are useful in identifying objects that may appear very similar to each other in an image from a color-based perspective (for example, trees and green fields). We convolute the gray-scale image obtained from the RGB components with a set of filter banks composed by Gabor filters to generate pixel responses at different scales and orientations [34].

As additional texture information, we also use the Gray Level Co-Occurrence Matrix (GLCM) [35]. From such a matrix, specific texture operators [36] can be extracted. Although a large number of operators exist, most of them are correlated, as explained in [37]. Therefore, we decided to use only contrast and correlation operators.

3) *Gaussian Kernels*: The next feature we use in this study is a Gaussian kernel. The Gaussian kernel (with variance equal to 1) is convolved with a gray-scale image derived from the RGB components. Such a kernel acts as a low-pass filter leading to a slightly blurred image. The Gaussian low pass filters are becoming more common in image processing to cancel the noise [38].

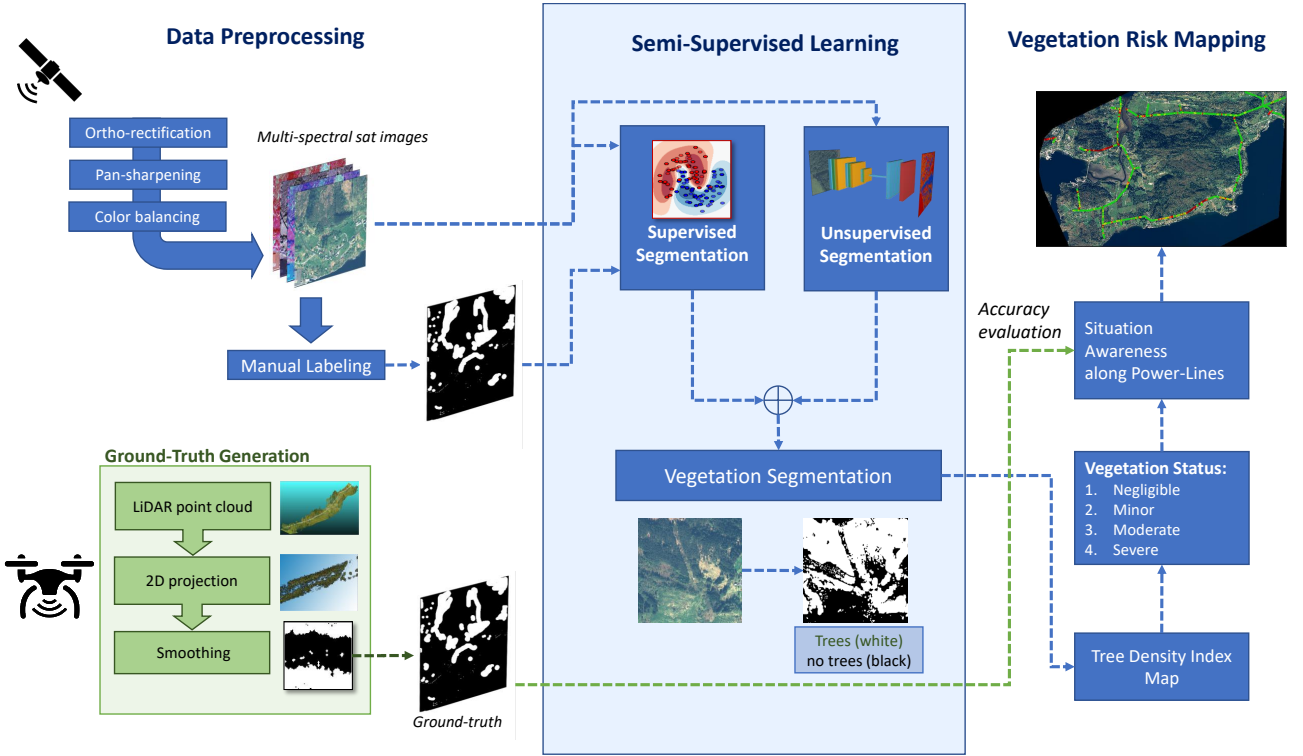


Fig. 4: Overview of the proposed vegetation monitoring framework

4) *Supervised Machine Learning Algorithm for Vegetation Segmentation*: The computed features values are stacked into a vector and we use the AdaBoost ensemble technique [39] to train a classifier. Such a classifier will assign a probability of being part of a tree, P_{tree} , to each pixel in the image. Finally, we use an energy minimization algorithm solved via graph cuts [40] to turn the probabilistic map into a binary segmentation map.

C. Unsupervised Image Segmentation Block

The unsupervised segmentation block is composed of a fully convolutional neural network (FCN) [41] to extract features and a superpixel refinement process [42] for self-training of the model. Fig. 5 illustrates the architecture of this network.

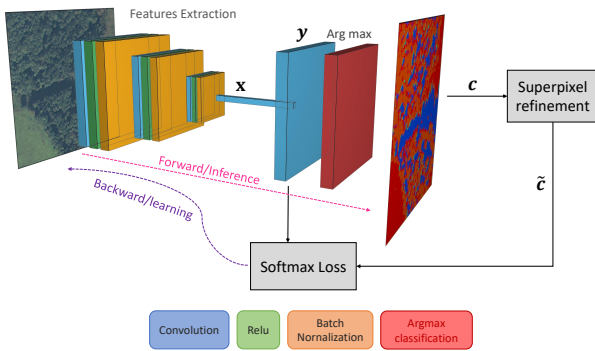


Fig. 5: Diagram of the unsupervised segmentation block

We compute the feature map x from the image I through M (equal to 4 in our study) convolutional blocks consisting

each of a 2D convolution with a 3×3 kernel, a *relu* activation function, and a batch normalization step. Then, a response map is calculated through an additional convolution as $y = W_c x + b_c$ where W_c, b_c are, respectively, the weights and biases of the last convolutional layer. Finally, we obtain the cluster label c for each pixel by selecting the dimension along the vector y that has the maximum value.

In image segmentation, the clusters of image pixels should be spatially continuous. Therefore, we first extract K fine superpixels from the image. Then, we force all the pixels in each superpixel to have the same cluster label \tilde{c} , defined as the most frequent cluster in each superpixel.

The self-training procedure is done solving two sub-problems alternately: a forward process of the network followed by the superpixel refinement and a back-propagation process based on stochastic gradient descent with a learning rate of 0.01. The loss function is calculated as the cross-entropy between the network response y and \tilde{c} . Algorithm 1 shows the pseudo-code of such an approach.

D. Combination Strategy

The aforementioned fully unsupervised approach can segment the image into different clusters. A cluster is a group of pixels sharing common properties (color, texture pattern, etc). However, the algorithm lacks the semantic knowledge about the physical meaning of different clusters available in an image. On the other hand, the supervised model has been specifically trained to recognize trees. Therefore, we combine the output of the supervised block presented in subsection III-B with the output of the unsupervised block of subsection

Algorithm 1 Unsupervised image segmentation

Input: Image I
Output: Segmented image S
 $(W_m, b_m, W_c, b_c) \leftarrow \text{InitializeWeights}()$
 $S_k \leftarrow \text{GetSuperPixels}(I)$
for $t = 1$ to N iterations **do**
 $\mathbf{x} \leftarrow \text{getFeatures}(I; W_m, b_m)|_{m=1}^M$
 $\mathbf{y} \leftarrow \text{forwardStep}(\mathbf{x}; W_c, b_c)$
 $c \leftarrow \arg \max\{y\}$
for $k=1$ to K **do**
 $c_{max} \leftarrow \arg \max c, \quad \forall c \in S_k$
 $\tilde{c} \leftarrow c_{max}, \quad \forall \text{pixel} \in S_k$
end for
 $\mathcal{L} \leftarrow \text{CrossEntropyLoss}(\mathbf{y}, \tilde{c})$
 $(W_m, b_m, W_c, b_c) \leftarrow \text{Update}(\mathcal{L})$
end for

III-C. In this way it is possible to understand whether a cluster should be considered as "trees" or "non-trees". Algorithm 2 shows how this combination is performed.

Algorithm 2 Combination of the two blocks

Input1: Multi-class segmentation image from the unsupervised block ($\mathbf{U} = \{U_0, U_1, U_2, \dots\}$)
Input2: Binary segmentation image from the supervised block ($\mathbf{S} = \{S_0 = \text{trees}, S_1 = \text{no-trees}\}$)
for each cluster U_i in (\mathbf{U}) **do**
 Check in which class of (\mathbf{S}) the pixels of U_i are mapped into
if most of the pixels are mapped into $S_0 = 0$ **then**
 Assign the pixels of U_i to S_0
end if
if most of the pixels are mapped into S_1 **then**
 Assign the pixels of U_i to $S_1 = 1$
end if
end for

IV. RESULTS AND DISCUSSIONS

To validate the performance of the proposed framework for vegetation detection, we implement it on a 22kV sub-transmission power line in the western part of Norway with 26 km of lines. Two high-resolution satellite images have been used, as explained in subsection II-A. The available LiDAR survey for the same part of lines has been used as the ground truth to cross-validate our satellite-based solution's outcomes.

To start the validation, we test the supervised block to compute the segmentation output accuracy by applying different combinations of features. We use the manually-annotated dataset for the satellite imageries. The training dataset consists of five manually labeled 800x800 pixels images, where a subset of 1.500.000 pixels has been selected to have balanced classes. The validation dataset is made of ten 400x400 pixels images.

We found out that the GLCM texture operator performs better than the Gabor filter. Surprisingly, adding the NDVI lowers the overall accuracy. NDVI is an indicator of the chlorophyll richness, so it can be used to detect vegetation. However, it fails to sufficiently distinguish between trees and grassy fields. Furthermore, trees with small canopies or otherwise sparse foliage might not be adequately detected using NDVI. However, NDVI remains an important vegetation

detection index that may still be helpful in other scenarios with different datasets.

The machine learning algorithm output is a black and white segmented image that shows tree and non-tree in each part of the line, (see the blue-colored zone in the middle of the Fig. 4). For the sake of visualization, Fig. 6 shows a comparison between the manually labeled satellite images and the classifier's output for three image samples. A comparison between the proposed approach's output and LiDAR's ground truth is shown in Fig. 7.

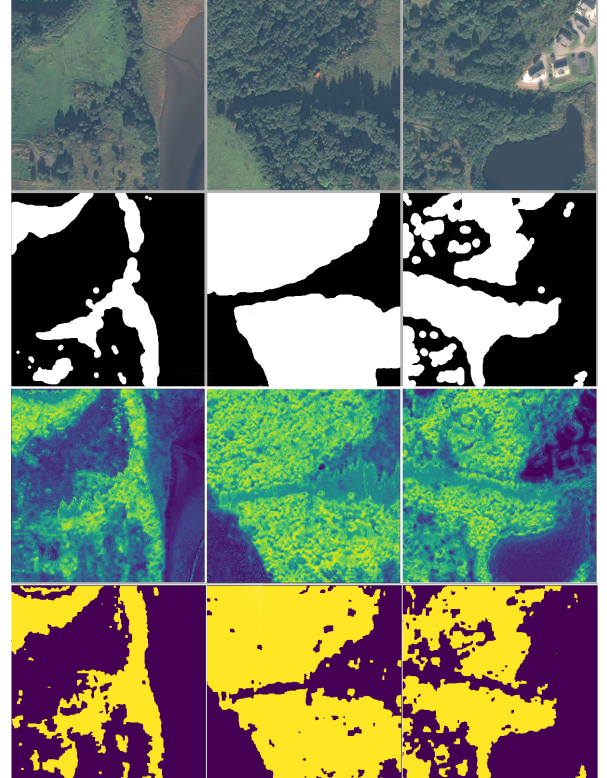


Fig. 6: From top to bottom: RGB image (*first row*), ground truth provided by manual labeling (*second row*), probabilistic map showing P_{tree} for each pixel (*third row*), and segmentation output (*last row*)

We create an easy-to-understand metric, called *Tree Density Index* (TDI), to present and visualize our vegetation detection algorithm's outcome for grid maintenance teams. The proposed metric can be used in mapping vegetation encroachment to power lines right-of-way. The TDI quantifies the presence of trees near power lines, especially the trees that encroach into the lines' ROW.

We multiply the segmented images M with a Gaussian kernel G as a weighting function within the window W , as described in Eq. (2). The weighting function's choice (TDI) is based on the distance of trees to power lines, since trees near power lines pose more risk.

$$TDI = \int_W M \otimes G dw \in (0, 1) \quad (2)$$

The TDI values, in the range of [0,1], are divided into different levels of vegetation status using the following criteria.

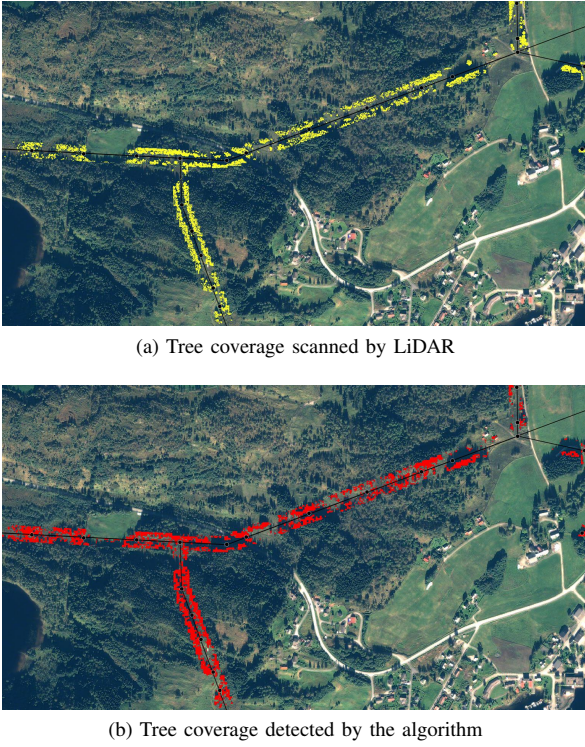


Fig. 7: Example of trees detected along the power grid by (a) LiDAR and (b) the proposed classifier

$$\begin{cases} \text{Level 0 (Negligible):} & TDI \leq 0.2 \\ \text{Level 1 (Minor):} & 0.2 < TDI \leq 0.4 \\ \text{Level 2 (Moderate):} & 0.4 < TDI \leq 0.8 \\ \text{Level 3 (Severe):} & TDI > 0.8 \end{cases} \quad (3)$$

Using the Tree-Density Index from Eq. (2), it is possible to create a heat map showing vegetation density and proximity levels along the power grid. We calculate TDI values for the entirety of the power lines in our study area using the two satellite images and the LiDAR ground truth. Fig. 8 shows an example of the resultant heat map for the study area. The vegetation density heat map shows that most of the line sections are safe (green colored and $TDI < 0.2$). It also shows that our partner electric utility does not need to make an immediate tree trimming action in those areas.

A confusion matrix is then used to show the comparison results for detected trees' location in satellite images and LiDAR data. Fig. 9a and 9b show the confusion matrices for Pleiades-1 and WorldView-2 imagery respectively. The upper-triangular part of each confusion matrix corresponds to locations where the predicted TDI is higher than the true value; it means that we are overestimating the vegetation density. Symmetrically, the lower-triangular part corresponds to areas where the predicted TDI is lower than the real value; in other words, it shows that we are underestimating the vegetation density.

We make the assumption that all locations with TDI values higher than 0.4 can cause a vegetation related threat to power lines. From Eq. (3), values higher than 0.4 cover areas with

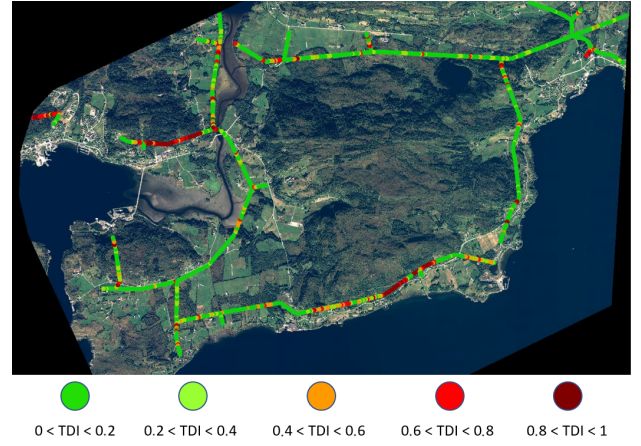


Fig. 8: Heat-map showing areas where there is more vegetation around power lines

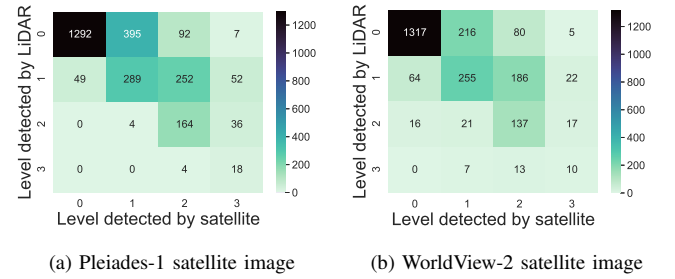


Fig. 9: Confusion matrix from the levelized values of the TDI along the line using the Pleiades-1 and WorldView-2 satellite image

moderate to high vegetation densities, and they need to be monitored carefully for possible tree trimming and cutting actions. In this way, we can compute how well the algorithm detects a vegetation threat. For example, using Pleiades-1 satellite image, the algorithm detects non-threat vegetation zones correctly by 98.2% and it detects the threat vegetation zones by 84.6%.

From Fig. 9, we also see that there are very few cases in which the algorithm underestimates the vegetation level. For example, using Pleiades-1 there are zero cases in which a location detected as *negligible* (level 0) is *severe* (level 3) in reality.

In practice, this means that our algorithm has high confidence in detecting areas with low vegetation density. In other words, the vegetation management team can avoid inspecting areas that the algorithm points to as "safe" (green) or without risky vegetation. Consequently, it brings the vegetation management teams' attention on areas with high vegetation density or with risky vegetation (red). It reduces the power line inspection time and cost accordingly.

V. PRACTICAL CONSIDERATIONS FOR ELECTRIC UTILITIES

The combination of satellite-based data and artificial intelligence gives electric utilities a unique opportunity to modernize tasks that incorporated repetitive observation and inspection,

especially over large areas. This paper introduces a platform for monitoring vegetation encroachment into power lines' right-of-way using high-resolution satellite imagery.

A. On the classic close-up asset monitoring and satellite images

It is worth mentioning that the need for close-up inspection of power line components using ground patrol, helicopters, or drones to check the asset's mechanical and structural health, in addition to vegetation monitoring, remains the same. In reality, classic close-up visual inspections for the whole grid are performed once within a long period (up to 10 years) due to their high costs and time constraints. This infrequent inspection over a long span of time can increase the probability of failures and outages specifically for vegetation-related events considering vegetation growth rates. Therefore, vegetation-related inspections need to be executed more often and in periods between classic close-up asset inspections. Our proposed satellite-based vegetation monitoring approach complements the legacy asset management practice by providing low-cost and frequent situational awareness for vegetation management teams.

Consequently, vegetation management can be changed from traditional time-based ROW inspection (periodic) to risk-based ROW inspection by improving scale, frequency, and cost-efficiency in ROW inspection.

B. On the cost-effectiveness of satellite images for vegetation monitoring

Satellite imagery data is typically more cost-effective than other image capture methods such as helicopter and drone, especially as the inspection area increases [11], [12]. Commercial satellite providers can offer high-resolution images with a high revisiting time covering most of the world. A survey performed in 2015 [43] showed that satellite imagery for a specific region was up to 60 % cheaper than using drone images.

Our study was performed under the GridEyeS project for using satellite imagery for power system operation supported by the European Space Agency [44]. We have surveyed 15 electric utilities in North America and Europe regarding their typical practices and cost of vegetation monitoring during our study. The line inspection cost using helicopters, light airplanes, or drones varies from 60 to 1300 Euros per km of the power line. The higher range of inspection costs belongs to LiDAR scanning technologies. The high cost of power lines' health condition monitoring (including vegetation encroachment monitoring) and the vast size of service territories force utilities to often cover the whole service area with a long periodicity (typically 2 to 10 years) [5]. This leads to sub-optimal revisiting frequency for each section of the line.

The use of high-resolution satellite imagery for vegetation-related inspection costs is generally below 15 Euros, depending on commercial providers. This makes satellite-based solutions economically attractive. The power line in our selected study area is approximately 26 kilometers long. In total, 20 kilometers of the line are in a normal condition regarding

vegetation encroachment into power lines' ROW. Using the proposed platform, the vegetation management team has an option to only focus on the 6 km of the line with a high vegetation level, identifiable with the red color in Fig. 8.

The average cost of line inspection for our partner utility using a helicopter or a drone is 1200 Euros per km, which means an overall $26 \times 1200 = 31200$ Euros in the inspection cost. Limiting vegetation-related inspections to only 6 km of the red zone leads to inspection cost reduction depending on the distribution of red spots across the entire line and the number of helicopter or ground crew maneuvers to cover those spots. This example aims to provide an idea of saving potential for vegetation monitoring rather than a detailed cost-benefit analysis.

C. On the selecting the appropriate satellite images for vegetation monitoring

From a practical point of view, remote sensing applications' accuracy, including vegetation detection, is highly influenced by different aspects.

- A major factor in the quality of vegetation detection is the resolution of the satellite images. In this study, we used 50 cm resolution satellite images, which are one of the best resolution available from commercial providers. For example, there are no-cost to low-cost satellite images with 10 meters resolution from Sentinel satellites under the Copernicus program provided by the European Space Agency [45]. However, such low-resolution images can not provide the level of details needed to detect and measure vegetation's density in the vicinity of power lines. Moreover, the high-resolution satellite images also provide insights on vegetation type, growth rate, vegetation health, environmental impacts, and the quality of trimming activities by using data from multiple satellite images of the same area over time. Figure 10 shows how the different resolution of some available products can dramatically affect the detection quality.

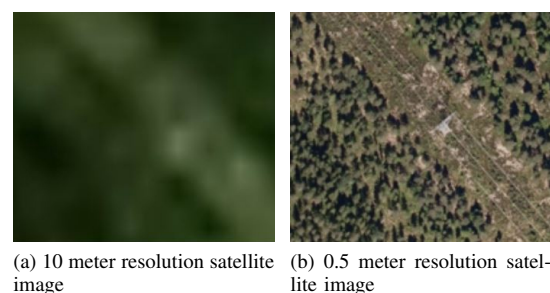


Fig. 10: Visual comparison of the same area from two different popular satellite providers

- Another important aspect is the acquisition date. As shown in the Results section, Pleiades-1 provided slightly better accuracy. A possible explanation is that in early May, trees are not yet completely developed, especially in Norway. Therefore, the algorithm has more difficulties in precisely detecting trees, particularly deciduous ones.

Fig. 11 shows a comparison between two image samples from different seasons. Note that the foliage of some trees are not as fully developed in May compared to the canopy cover in September. It is worth mentioning that there can be periods more suitable for vegetation monitoring. Power companies should prioritize monitoring in specific months rather than in other months (in summer, for example) to generate the best results, taking geographical location and growing seasons into consideration.

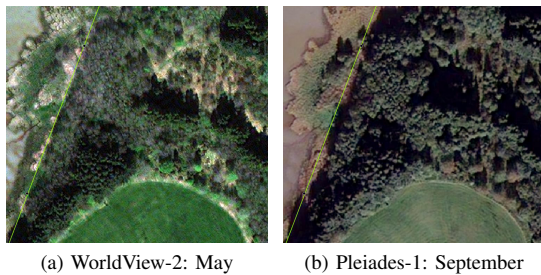


Fig. 11: Visual comparison between two images before and after summer. Note how the canopy of some trees are not fully developed yet in May compared to September

- Cloud coverage is also another factor that affects all remote sensing applications which are based on optical imagery. Prior to our analytics, we tried to pick proper satellite images that have less cloud coverage over the target area. Nowadays, commercial satellite image providers are launching more satellites to orbit using private companies such as Space-X. More satellites in the space means more frequent revisit for any location in the world. Consequently, the recent increase in satellite revisit frequency will make it easier to acquire a cloud-less image for a specific area with a short waiting time.

VI. CONCLUSIONS

This paper presents a framework to monitor vegetation along power lines using high-resolution satellite images and machine learning. Satellite imagery data introduce a new paradigm for power transmission and distribution companies with the potential to reduce the time and cost of ground inspections. We propose a semi-supervised approach that combines a supervised classifier with a deep learning-based unsupervised architecture for image segmentation. This enables the detection of vegetation close to power lines and thus pose a risk to power line infrastructure. The proposed framework has the potential to aid operators of power-line infrastructure with vegetation management. We validated the image segmentation approach for a power grid in western Norway using airborne LiDAR. Initial results indicate that this approach can correctly identify vegetation risk areas with 84% accuracy for this particular area. Areas of no risk are identified correctly in 92% of cases. These initial results demonstrate the potential promise of this satellite-based framework. The future work is toward further improving the detection accuracy.

VII. ACKNOWLEDGMENTS

This work is funded partly by the European Space Agency (ESA) under the Smart Grid Eye, from Space to Sky (GridEyeS) project [44].

REFERENCES

- [1] H. Gugel, S. Eklisheva, M. Lauby, and F. Tafreshi. Vegetation-related outages on transmission lines in north america. In *2018 IEEE Power Energy Society General Meeting (PESGM)*, pages 1–5, 2018.
- [2] Yoshitaka Kumagai, John C. Bliss, Steven E. Daniels, and Matthew S. Carroll. Research on causal attribution of wildfire: An exploratory multiple-methods approach. *Society & Natural Resources*, 17(2):113–127, 2004.
- [3] P. Eavis and I. Penn. California says pg&e power lines caused camp fire that killed 85. <https://www.nytimes.com/2019/05/15/business/pg-e-fire.html?action=click&module=RelatedLinks&pgtype=Article>. 2019-05-15.
- [4] J. Ahmad, A. Malik, L. Xia, and Nadia Ashikin. Vegetation encroachment monitoring for transmission lines right-of-ways: A survey. *Electric Power Systems Research*, 95:339–352, 2013.
- [5] B. Sacks. Ai improves resilience of vegetation management. <https://www.tdworld.com/vegetation-management/article/21131079/ai-improves-resilience-of-vegetation-management>. 2020-05-11.
- [6] J. Weeks. U.s. electrical grid undergoes massive transition to connect to renewables. <https://www.scientificamerican.com/article/what-is-the-smart-grid/>. 2010-04-28.
- [7] Y. Xie, Zongyao Sha, and Mei Yu. Remote sensing imagery in vegetation mapping: a review. *Journal of Plant Ecology*, 1:9–23, 2008.
- [8] Leena Matikainen, M. Lehtomäki, E. Ahokas, J. Hyypä, M. Karjalainen, A. Jaakkola, A. Kukko, and T. Heinonen. Remote sensing methods for power line corridor surveys. *Isprs Journal of Photogrammetry and Remote Sensing*, 119:10–31, 2016.
- [9] R. A. McLaughlin. Extracting transmission lines from airborne lidar data. *IEEE Geoscience and Remote Sensing Letters*, 3(2):222–226, 2006.
- [10] Lake Singh, William Whittecar, Marc DiPrinzio, Jonathan Herman, Matthew Ferringier, and Patrick Reed. Low cost satellite constellations for nearly continuous global coverage. *Nature Communications*, 11, 01 2020.
- [11] Ucs satellite database. <https://www.ucsusa.org/nuclear-weapons/space-weapons/satellite-database>. 2020-08-01.
- [12] H. Jones. The recent large reduction in space launch cost. 2018.
- [13] Y. Kobayashi, G. G. Karady, G. T. Heydt, and R. G. Olsen. The utilization of satellite images to identify trees endangering transmission lines. *IEEE Transactions on Power Delivery*, 24(3):1703–1709, 2009.
- [14] M. Moeller. Monitoring powerline corridors with stereo satellite imagery. 2006.
- [15] C. Xiao, R. Qin, X. Huang, and J. Li. Individual tree detection from multi-view satellite images. In *IGARSS 2018 - 2018 IEEE International Geoscience and Remote Sensing Symposium*, pages 3967–3970, 2018.
- [16] Grigorijs Goldbergs, S. Maier, S. Levick, and Andrew Edwards. Limitations of high resolution satellite stereo imagery for estimating canopy height in australian tropical savannas. *Int. J. Appl. Earth Obs. Geoinformation*, 75:83–95, 2019.
- [17] S. J. Mills, M. P. Gerardo Castro, Z. Li, J. Cai, R. Hayward, L. Mejias, and R. A. Walker. Evaluation of aerial remote sensing techniques for vegetation management in power-line corridors. *IEEE Transactions on Geoscience and Remote Sensing*, 48(9):3379–3390, 2010.
- [18] X. Huang, C. Shi, and S. C. Liew. Tree crown detection and delineation using optical satellite imagery. In *IGARSS 2018 - 2018 IEEE International Geoscience and Remote Sensing Symposium*, pages 2944–2947, 2018.
- [19] Z. Pan. Urban vegetation type analysis method based on high resolution satellite images. In *2016 International Conference on Smart City and Systems Engineering (ICSCSE)*, pages 613–616, 2016.
- [20] L. Häme, J. Norppa, P. Salovaara, and J. Pylvänäinen. Power line monitoring using optical satellite data. In *CIREC Workshop 2016*, pages 1–4, 2016.
- [21] Yutaka Kokubu, Seiichi Hara, and Akira Tani. Mapping seasonal tree canopy cover and leaf area using worldview-2/3 satellite imagery: A megacity-scale case study in tokyo urban area. *Remote Sensing*, 12(9):1505, May 2020.
- [22] Pedro Marques, L. Pádua, Telmo Adão, Jonas Hruska, E. Peres, A. M. Sousa, and J. Sousa. Uav-based automatic detection and monitoring of chestnut trees. *Remote. Sens.*, 11:855, 2019.

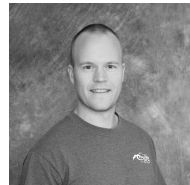
- [23] S. Li, W. Song, Leyuan Fang, Yushi Chen, P. Ghamisi, and J. Benediktsson. Deep learning for hyperspectral image classification: An overview. *IEEE Transactions on Geoscience and Remote Sensing*, 57:6690–6709, 2019.
- [24] Ronald Kemker, C. Salvaggio, and Christopher Kanan. Algorithms for semantic segmentation of multispectral remote sensing imagery using deep learning. *Isprs Journal of Photogrammetry and Remote Sensing*, 145:60–77, 2018.
- [25] B. Ayhan and C. Kwan. Tree, shrub, and grass classification using only rgb images. *Remote. Sens.*, 12:1333, 2020.
- [26] F. Wagner, A. Sánchez, Yuliya Tarabalka, R. G. Lotte, Matheus Pinheiro Ferreira, M. P. Aidar, E. Gloor, O. Phillips, and L. Aragão. Using the u-net convolutional network to map forest types and disturbance in the atlantic rainforest with very high resolution images. *Remote Sensing in Ecology and Conservation*, 5:360–375, 2019.
- [27] Sherrie Wang, William Chen, Sang Xie, George Azzari, and David Lobell. Weakly supervised deep learning for segmentation of remote sensing imagery. *Remote Sensing*, 12:207, 01 2020.
- [28] <https://www.lysenett.no/byggeoggrave/grave-og-arbeide-nar/trefelling-og-beskjaring/>.
- [29] Knut Ove Hillestad. Kraft, ledning og landskap. http://publikasjoner.nve.no/kraftogmiljoe/kraftogmiljoe_08.pdf.
- [30] A. Kanazaki. Unsupervised image segmentation by backpropagation. In *2018 IEEE International Conference on Acoustics, Speech and Signal Processing (ICASSP)*, pages 1543–1547, 2018.
- [31] Snehmami, Akshay Gore, Ashwagosh Ganju, S. Kumar, P. K. Srivastava, and P HariRamR. A comparative analysis of pansharpening techniques on quickbird and worldview-3 images. *Geocarto International*, 32:1268 – 1284, 2017.
- [32] Jerome Friedman Trevor Hastie, Robert Tibshirani. *The Elements of Statistical Learning*. Springer, 2009.
- [33] https://en.wikipedia.org/wiki/Normalized_difference_vegetation_index.
- [34] U. Marmol. Use of gabor filters for texture classification of airborne images and lidar data. *Archiwum Fotogrametrii, Kartografii i Teledetekcji*, 22, 2011.
- [35] Mryka Hall-Beyer. Gcm texture: A tutorial v. 3.0 march 2017, 03 2017.
- [36] R. M. Haralick, K. Shanmugam, and I. Dinstein. Textural features for image classification. *IEEE Transactions on Systems, Man, and Cybernetics*, SMC-3(6):610–621, 1973.
- [37] Mryka Hall-Beyer. Practical guidelines for choosing glm textures to use in landscape classification tasks over a range of moderate spatial scales. *International Journal of Remote Sensing*, 38:1312 – 1338, 2017.
- [38] Pascal Getreuer. A survey of gaussian convolution algorithms. *Image Process. Line*, 3:286–310, 2013.
- [39] R. E. Schapire and Y. Freund. *Boosting: Foundations and Algorithms*. MIT Press, 2012.
- [40] Yuri Boykov and Olga Veksler. Graph cuts in vision and graphics: Theories and applications. In *Handbook of Mathematical Models in Computer Vision*, 2006.
- [41] J. Long, E. Shelhamer, and T. Darrell. Fully convolutional networks for semantic segmentation. In *2015 IEEE Conference on Computer Vision and Pattern Recognition (CVPR)*, pages 3431–3440, 2015.
- [42] Murong Wang, Xiabi Liu, Yixuan Gao, Xiao Ma, and N. Q. Soomro. Superpixel segmentation: A benchmark. *Signal Process. Image Commun.*, 56:28–39, 2017.
- [43] Eyes in the sky: Satellite remote sensing and data analytics for electric utilities. <https://www.epri.com/research/products/000000003002017281,2019-09-10>.
- [44] <https://business.esa.int/projects/grideyes>.
- [45] https://www.esa.int/Applications/Observing_the_Earth/Copernicus.



in Western Norway University of Applied Sciences in Bergen (Norway). His research interests are in data analytics, machine learning, computer vision, and remote sensing applications.



Administration from the Technische Universität Braunschweig (TUBS) in Germany. He worked as a project coordinator and analyst in the Big Data business development department of SAP in Munich, Germany, before joining eSmart Systems back in 2017.



around sea ice system services and emerging needs of Arctic stakeholders. His research is particularly focused on expanding monitoring tools using synthetic aperture radar in support of ice travel and on-ice operations of landfast sea ice.



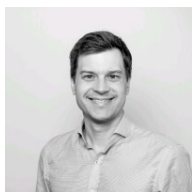
Head of Data Science for the Big Data Analysis Center at the University of Bergen, with responsibility ranging from project management and data science team leading to external project building and customer relationship. From 2019 she is a Lead Data Scientist at the StormGeo company. During her career as Data Scientist, she completed projects within artificial intelligence and machine learning for various industries and public sectors, ranging from medical hospitals and fisheries to oil drilling and insurance companies. Saponova has over 20 scientific publications for the past 10 years.

Michele Gazzea, IEEE Student Member Michele Gazzea received his Bachelor's degree in Information Engineering and his Master's degree in Automation and Control Engineering, both from the University of Padova (Italy). He worked for one year in Cielle.srl in Treviso (Italy) as an R&D engineer studying and designing diagnostic techniques on milling and engraving CNC machines. He worked as a researcher for Electrolux to perform model-based analysis of power consumption in washing machines until he started his new occupation as a Ph.D. student

Michael Pacevicius Michael Pacevicius is an industrial PhD candidate in the RAMS group at NTNU, Norway and works as a researcher in eSmart Systems, a company delivering high-tech IT solutions for power grid related companies. His research activities focus on the development and implementation of dynamic risk analysis methods for large-scale interconnected power systems. He has a MSc. in Operational safety, Risks and Environment from the Université de Technologie de Troyes (UTT) in France and a MSc. in Economics and Business

Dyre Oliver Dammann Dyre Oliver Dammann received the Ph.D. degree in geophysics in 2017 from the University of Alaska Fairbanks, Fairbanks, AK, USA. From 2017-2019 he was a Postdoctoral Researcher in the Department of Earth, Space, and Environment, Chalmers University of Technology, Gothenburg, Sweden. From 2019-2020 he was a Senior Scientist with StormGeo, Bergen, Norway. He is currently a Research Professional at the University of Alaska Fairbanks. His research interests include coastal sea ice properties and processes centered

Alla Saponova Alla Saponova, Ph.D., has experience in artificial intelligence, machine learning, and data analysis. She graduated from Moscow State University, Russia, in 2004 with Ph.D. in Physics and Mathematics with Honored President's Stipend. After completing the postdoctoral program at the University of Bergen, Norway, in 2008, she started to work with artificial intelligence as a Senior Researcher at the Bergen Center for Computational Science affiliated with the University of Bergen, Norway. From 2014 Saponova was appointed as a



Torleif Markussen Lunde Torleif Markussen Lunde is Managing Director of Innovation Centre for Health at the University of Bergen. He has worked in the intersection between industry and research for the last 10 years years and has experience from a leadership positions related to software development, strategy, research, and transformation. Torleif is passionate about technology and people that delivers real impact and solve real-world problems. Holds a PhD in mathematical modelling & big data, climate change, and malaria.



Reza Arghandeh, IEEE Senior Member Dr. Reza Arghandeh is a Full Professor in the Department of Computing, Mathematics, and Physics and Department of Electrical Engineering at the Western Norway University of Applied Sciences (HVL), Norway. He is the Director of Collaborative Intelligent Infrastructure Lab (CI2). He is also a lead data scientist with StormGeo AS. He has been an Assistant Professor in ECE Dept, FSU, USA 2015-2018, and a postdoctoral scholar at EECS Dept, University of California, Berkeley 2013-2015. He was a power

system software designer at Electrical Distribution Design Inc. in Virginia, USA, from 2011 to 2013. His research has been supported by U.S. National Science Foundation, U.S. Department of Energy, the European Space Agency, and the European Commission.





TREE SPECIES CLASSIFICATION USING HIGH-RESOLUTION SATELLITE IMAGERY AND WEAKLY SUPERVISED LEARNING

Gazzea M., Kristensen L. M., Pirotti F., Ozguven E. E. and Arghandeh R.

In IEEE Transactions on Geoscience and Remote Sensing, vol. 60, pp. 1-11, 2022, doi:
[10.1109/TGRS.2022.3210275](https://doi.org/10.1109/TGRS.2022.3210275)

©2024 IEEE. Reprinted, with permission, from [68]

Tree Species Classification Using High-Resolution Satellite Imagery and Weakly-Supervised Learning

Michele Gazzea , Member, IEEE, Lars Michael Kristensen, Francesco Pirotti 
Eren Erman Ozguven , Member, IEEE, and Reza Arghandeh , Senior Member, IEEE

Abstract—Knowing vegetation type in an area is crucial for several applications, including ecology, land use management, and infrastructure risk assessment. In combination with recent advancements in image processing, remote sensing technology has been used to perform fast vegetation type estimation and reduce the need for intensive and time-consuming field-based surveys. This paper proposes a weakly supervised method based on deep learning to estimate tree species relying on multi-spectral high-resolution satellite images. We tested the approach against noisy labels, which often occur in real-world datasets. We validate our approach for a study area in Norway and in Italy using images taken in different periods of the year. Our method significantly enhances the quality of the available forestry inventory dataset.

Index Terms—Remote Sensing, Satellite Imagery, Tree Species Classification, Weakly-Supervised Learning

I. INTRODUCTION

HAVING a spatial tree species inventory is fundamental for a wide range of applications such as ecology and conservation [1], wildlife habitat mapping [2], sustainable land use management [3], urban planning [4], as well as infrastructure monitoring and risk assessment [5], [6]. For example, power lines and roadway maintenance teams can make more effective tree trimming and cutting plans knowing the tree species [7], [8].

Conventional methods for documenting tree species are based on field surveys that are intensive, time-consuming, and often impractical in mountainous or inaccessible areas. However, remote sensing technologies such as optical satellite images, Light Detection and Ranging (LiDAR), and aerial images coming from helicopters or airborne vehicles have been explored over the last few decades to address such challenges. According to the review study conducted in [9], almost all the recent works combine a passive sensor (hyper-spectral or multi-spectral optical sensor) with an active sensor, typically LiDAR. These kinds of sensors are often mounted on airborne vehicles. For example, in [10], the authors used a combination

This work was supported in part by the Research Council of Norway through the Project "Prediction of ignition and spread of wildfires in Scandinavia: from experiments to models (PREWISS)," under Grant 315870 and in part by the Project "Disruptive Technologies for a Resilient Future (INTPART-TRF)" under Grant 309448. (Corresponding author: Michele Gazzea.)

Michele Gazzea, Lars Michael Kristensen, and Reza Arghandeh are with the Department of Computer Science, Electrical Engineering and Mathematical Sciences, Western Norway University of Applied Sciences, 5063, Bergen, Norway. E-mail: (mgaz@hvl.no)

Francesco Pirotti is with CIRGEO, University of Padova, 35020 Legnaro, Italy.

Eren Erman Ozguven is with the Department of Civil and Environmental Engineering, Florida State University, Tallahassee, FL 32310 USA.

of Airborne Laser Scanning (ALS) and color-infrared imagery to classify tree species in a mixed temperate forest in Poland. Airborne vehicles can provide detailed data over small areas, but they are still considered experimental [11] and, according to [12] currently are not considered a stable platform to efficiently acquire systematic data to support forest inventories over large areas (> 1000 ha). Airborne sensors are limited by flight time, large area coverage and high operations costs. For example, LiDAR data is in the range of 62–240€ per km² while aerial imagery is approximately 35–62€ per km² [13].

Nowadays, several commercial satellite providers offer easy-accessible images for any part of the world with a high revisiting time (currently up to 0.25 - 0.5 meters/pixel resolution). Furthermore, the drop in launching costs and the growing number of satellites and mini-satellites in orbit combined with high-quality sensors have reduced the cost of satellite imagery to less than 15€ per km² [13]. Satellite imagery is therefore currently the best trade-off between acquisition price, quality, and revisiting frequency [14].

Remote sensing-based tree species discrimination and classification evolved with methodological developments in the domain of statistical learning. In early studies, parametric approaches have been used (discriminant analysis, maximum likelihood) [15] while non-parametric approaches (decision trees, random forests, support vector machines, and neural networks) have gained more popularity in recent years [16], [17], [18]. Furthermore, the inclusion of texture information, mainly related to crown-internal shadows, foliage properties (size, and branching) provided by the grey-level co-occurrence matrix (GLCM) [19] have been shown to result in improvement in the accuracy [20].

Recently, deep learning has become an effective tool for object detection and classification, especially in remote sensing applications [21]. Among deep learning techniques, convolutional neural networks (CNNs) have demonstrated high classification accuracy for digital images in the computer vision field [22]. Using cascades of learnable convolutional filters, it is possible to exploit the spatial relationship between pixels to provide information regarding the textures and shapes of trees [23]. In [24], the authors compared several neural network architectures using a hierarchical approach to detect dominant species in forests. In [25] the authors used WorldView-3 imagery and a Res-UNet deep-learning model for individual tree species classification. One of the most notable advantages of deep learning compared to other machine learning methods is that deep learning does not require manual feature extraction.

In many current tree species classification works, labels are

obtained via field investigation performed by research groups collecting samples using GPS devices, which is a complex and time-intensive task. Other sources include existing tree reference datasets, which are often low resolution or noisy. However, machine learning models are heavily affected by the quality of data labels. Unreliable or noisy labels severely degrade the generalization performance of such models as they can easily memorize corrupted labels and correspondingly degenerate their generalizations on unseen data [26]. Achieving a good generalization capability in the presence of noisy labels is still a key challenge [27].

This paper proposes an automated approach to detect tree species using single high-resolution satellite images to lower costs and ease of implementation for practical reasons. The main contributions of this paper are two-fold:

- From a methodological point of view, we propose a weakly supervised machine learning approach to improve and refine forest inventory datasets. Our method relies on feature extraction from noisy labels and relabeling the data.
- From a practical point of view, our approach refines the coarse and low resolution tree species maps using one high-resolution satellite image. This process enhances the quality of the available forest inventories at a lower cost in scale in comparison to classic methods (e.g. sending ground-based crew or taking LiDAR or aerial images using helicopters and airplanes).

II. STUDY AREA AND DATA USED

The main study area is a $\approx 25\text{Km}^2$ region located in the Sogn og Fjordane county in Western Norway. We used a high-resolution satellite image from Maxar WorldView-2, acquired in the middle of May 2017. The image has a resolution of 0.5 m/pixel and have been ortho-rectified and pan-sharpened [28] by the provider.

The tree species reference dataset has been provided by the Norwegian Institute of Bioeconomy Research (NIBIO) [29], available and downloadable at [30]. The NIBIO dataset shows the forest distribution over the entire country. The dataset provides information such as the dominant tree species in forest stands. The term *forest stand* in forest inventory instructions defines a contiguous forested area sufficiently uniform in essential characteristics to distinguish it from adjacent communities.

The dominant tree species is defined on the basis of the estimated share of volume in a population as follows:

- *Spruces*: If more than 50% of the trees are characterized as spruces, then the tree type's label is "spruces". The spruce group is mainly composed of Norway spruce (*Picea abies*) but also contains small portions of other spruce species such as Sitka spruce (*Picea sitchensis*).
- *Pines*: If more than 50% of the trees are characterized as pines, then the tree type's label is "pines", specifically Scots pines (*Pinus sylvestris*).
- *Deciduous*: If more than 50% of the trees are characterized as deciduous, then the tree type's label is "deciduous". The deciduous group is dominated by birch species

(*Betula pubescens* and *Betula pendula*) but contains small portions of aspen (*Populus tremula*) and rowan (*Sorbus aucuparia*).

More detailed information on how the dataset has been created and validated can be found in [31].

A second study area has been selected in Italy, in the Dolomites and part of the Veneto region. An image of $\approx 15\text{Km}^2$ in the study area has been acquired from July 2019. The resolution is 0.5 m/px. The tree inventory dataset was acquired from *Regione del Veneto* at [32]. Similarly to the NIBIO dataset, it divides the forest stands of the selected area into three groups: (1) *Spruces*, mainly Norway spruces (*Picea abies*) which are also very common in the Dolomites; (2) Larches (*Larix decidua*) and (3) Deciduous, mainly grey alders (*Alnus incana*) and birches (*Betula pendula*).

The two study areas are shown in Fig. 1.

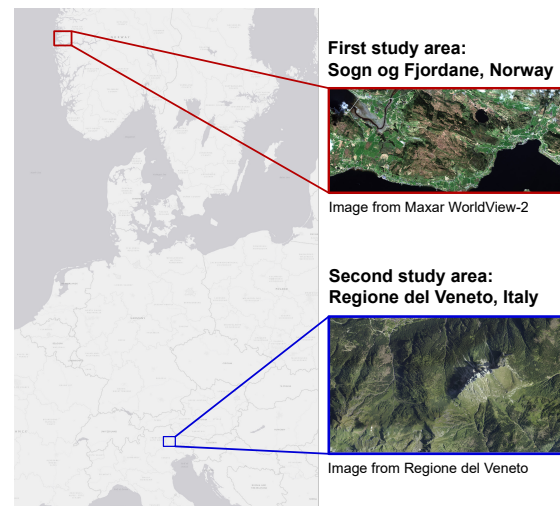


Fig. 1: The two study areas used. The first is located in the Sogn og Fjordane county, Western Norway. The second one is located in the Dolomites, in the Veneto region, Northern Italy.

The tree inventory datasets are raster images with the same geographical extends of the satellite images where each pixel has a discrete value as: 0-no-trees, 1: spruces, 2: pines/larches, 3: deciduous.

III. METHODOLOGY

We propose here a weakly-supervised learning approach that produces a model capable of detecting the different species at almost tree-level from a noisy low-resolution dataset.

To understand the reason and the advantages of such an approach, we first explain some issues present in both of the datasets used for tree species, and which may often be present in other real-world datasets. Fig. 2 shows some issues in the Norwegian tree species reference dataset.

We note, from Fig. 2, that some trees are not covered by the dataset even though they are visible from the satellite imagery. Moreover, the boundaries of the different forest stands are often chunky, tight, and not always precise. Finally, labels are assigned at a coarser level, and hence some regions are marked even though they do not contain any trees. A conventional fully-supervised segmentation procedure (i.e., extracting



Fig. 2: Issues present in a typical tree species reference dataset. Some trees are not covered by the dataset and the boundaries between regions are often not precise.

patches from both the satellite image and the tree dataset and directly training a model) will not handle these issues well and the model will not be able to learn properly. We propose a strategy to overcome these issues showing that we can learn from this dataset and refine it. Specifically, the method has the three-fold advantage: detecting trees, assigning a label to those trees not initially covered by the dataset, and refining the boundaries between classes. The overall pipeline is sketched in Fig. 3 and each block is further described in the following.

A. Data Preprocessing

We first pre-process the multi-spectral satellite images. Pixel values in each band are scaled and stretched to the minimum and maximum value calculated, respectively as the 2% and 98% percentile of the pixel distribution. This leads to higher contrast and better brightness uniformity among different images.

We use the Normalized Difference Vegetation Index (NDVI) as an additional channel in addition to the channels initially present. NDVI is a popular index in remote sensing for vegetation detection and it is defined as [33]:

$$NDVI = \frac{\rho_{nir} - \rho_{red}}{\rho_{nir} + \rho_{red}} \quad (1)$$

where ρ_{red} and ρ_{nir} denote the spectral reflectance measurements acquired in the red (visible) and near-infrared regions, respectively. Green living plants are brighter in the near-infrared band due to chlorophyll's near-infrared high sensitivity. Each channel is then mapped into the same interval $(0, 1)$ to ease the training procedure.

B. Pixel-wise Tree Segmentation Model

We design a tree segmentation algorithm. Given an input image, the corresponding output *treemap* is a single-channel pixel-wise mask. The segmentation model detects and labels the pixels that belong to (or are part of) a tree. We use an encoder-decoder based architecture [34] as a segmentation model. The architecture is composed by a cascade of [16, 32, 64, 128, 256] convolutional layers activated by a *relu* activation function, followed by a batch normalization layer and a Max Pooling layer. The architecture is shown in Fig. 4.

Binary cross entropy \mathcal{L} is used as the loss function for training the network since only two labels are considered (0

for *no-trees* and 1 for *trees*). To train the tree segmentation model, we use a manually created dataset for the considered study areas.

C. Tree Species Relabeling

The tree species reference we use in this study shows the dominant tree species in forest stands. However, it presents several issues (i.e., noisy or missing labels) as we showed in Fig. 2. The first step is to relabel the dataset to reduce the noise. This is because the species boundaries are coarse in the original dataset, and some trees are assigned to the same label as the surrounding trees, even if visually they are different species.

Therefore, we assume that trees from the same species have similar characteristics (features) in a feature space regardless of their assigned label. Furthermore, we assume that in most cases the given tree species inventory dataset S_{map} , provided by the Norwegian and Italian authorities, is correct. In other words, for example, the majority of trees marked as *spruces* are indeed *spruces*. The principle is sketched in Fig. 5. However, there are reservations regarding these assumptions which we discuss in Section V.

The implementation of the principle is divided into three steps.

1) *Random Sample Extraction*: We first multiply element-wise the tree reference dataset S_{map} (i.e., NIBIO dataset) with the *treemask* generated by the tree segmentation model in III-B. We denote the result $S_{map_{treemask}} \equiv S_{map} \otimes treemask$. In this way, fields, bare lands, roads, and any other non-tree elements which are included in the original dataset are filtered out. Afterwards, a defined number N of patches, each of size $s_p \times s_p$, are extracted randomly from the input satellite image, sampled among the three different families (i.e. *spruces*, *pinelarches*, *deciduous*) of $S_{map_{treemask}}$. Each patch P_i , whose dimensions are $s_p \times s_p \times N_{ch}$, is naturally associated (yet not necessarily correct) with the label l taken from $S_{map_{treemask}}$.

$$P_{i=1,2,\dots,N} \rightarrow l \in \{spruces, pinelarches, deciduous\}$$

2) *Feature Extraction*: For each patch P_i , a feature vector \mathcal{F}_i is extracted. Although features can be calculated in several ways, we use and compare two different techniques in this paper.

The first approach is to hand-engineer the features. We create \mathcal{F} as follows. The first components are the mean of each spectral band: $j = 1, 2, \dots, N_{ch}$. In addition, texture signature operators [35] derived from the Gray Level Co-Occurrence Matrix (GLCM) matrix are used. The GLCM can be thought of as a record of how often different combinations of pixel brightness values occur in imagery. While many operators exist, based on the Principal Component Analysis performed in [18], we included the GLCM Variance and Mean over other operators, as they showed the two highest eigenvalues. With this approach, a feature vector is calculated from a generic patch P_i as follows:

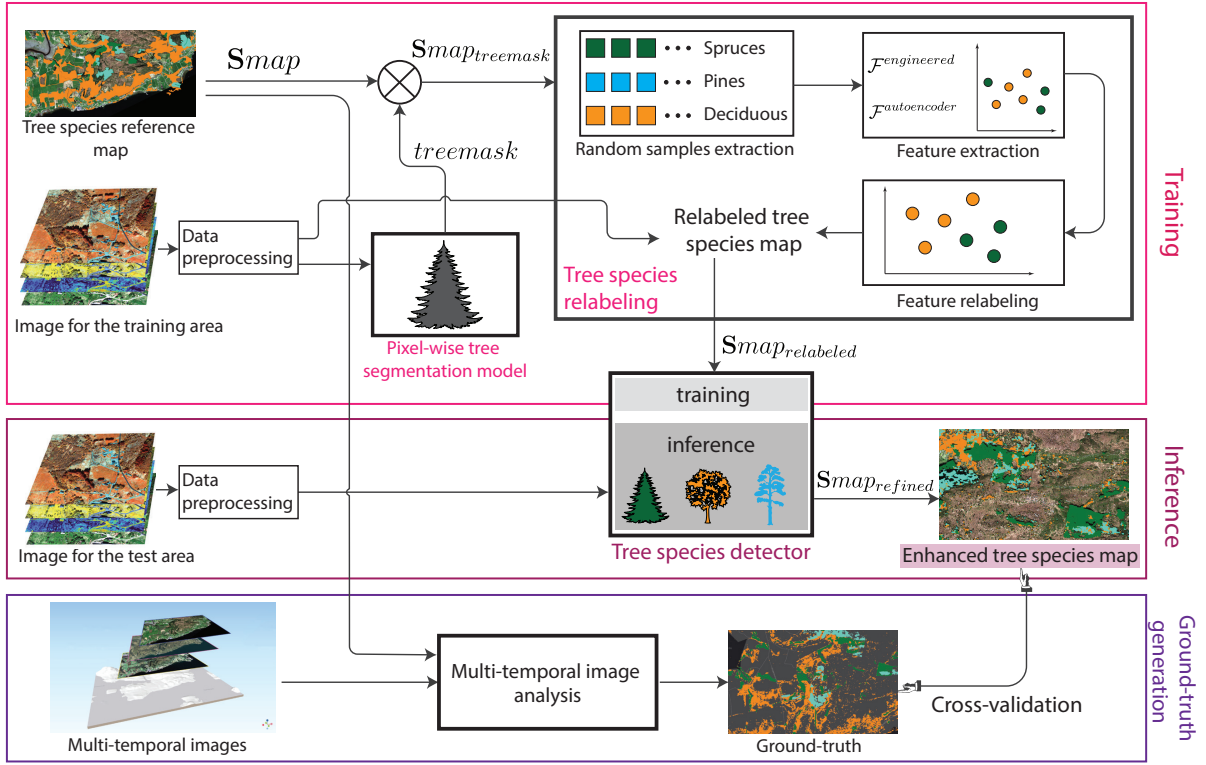


Fig. 3: Overall pipeline of the proposed approach. First, a binary tree segmentation model is trained to detect trees in the map. Random patches are extracted from the considered tree families (here spruces, pines, and deciduous), and for each patch, specific features are calculated. Such features are relabeled based on their position in the feature space. We then relabel the entire map, generating a pre-refined version of the original tree species dataset. The output is used to train a deep learning model. Once the model is trained, it can be used to generate refined versions of the original dataset at tree level and with fuzzy boundaries.

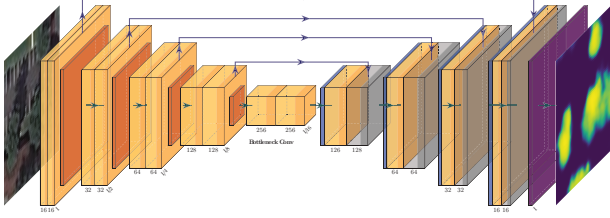


Fig. 4: Architecture used for trees segmentation model. Given a satellite image I as input, the corresponding output is a mask where trees are detected.

$$P_i \rightarrow \mathcal{F}_i^{\text{engineered}} = \begin{bmatrix} \mathbb{E}_{j=1}^{N_{ch}} P_i(:, :, j) \\ \text{Variance}(GLCM) \\ \text{Mean}(GLCM) \end{bmatrix} \quad (2)$$

The second approach is to take advantages of the deep learning capabilities to extract features automatically using convolutional autoencoders [36]. In an autoencoder, an input image x is encoded through an encoder E_θ into a low-dimensional representation z (often denoted as bottleneck layer or code of the auto-encoder) through a cascade of convolutional kernels. The code can then be decoded by a decoder D_ϕ to reconstruct back the original image through up-sampling operations. The autoencoder, and its parameters θ and ϕ , are trained to reconstruct as close as possible x in

terms of the mean square error (MSE). Following this idea, we extract a feature vector \mathcal{F}_i from the flattening of P_i 's low-dimensional encoded representation:

$$P_i \rightarrow \mathcal{F}_i^{\text{autoencoder}} = E_\theta(P_i) \quad (3)$$

In this paper, we used an encoder composed of a cascade of two convolutional layers activated by a *relu* activation function, followed by a batch normalization layer and a Max Pooling layer as shown in Fig. 6. The decoder architecture is symmetric.

3) *Relabeling*: Regardless of the method used for the feature extraction, a feature vector-label dataset $(\cap_{i=1}^N \{\mathcal{F}_i; l_i\})$ is generated, where $\mathcal{F} \in \mathbb{R}^d$. The value d is the dimension of the feature space, which depends on how many features are considered if the first approach is used (hand-engineered features) or on the auto-encoder architecture if the second approach is used instead. Nevertheless, following the idea in Fig. 5, it is expected that trees that belong to different types are mapped into different region of the \mathbb{R}^d space. If it is possible to learn the mapping regions in the d -dimensional space, patches with a wrong label can be relabeled according to their position in the feature space. We refer to the process of assigning to each region of \mathbb{R}^d a label as *semantic embedding*. The assumption that each tree type is distinguishable in the feature space holds, in theory. On the other hand, in practice, the cohesion and separation of each tree type's region in the

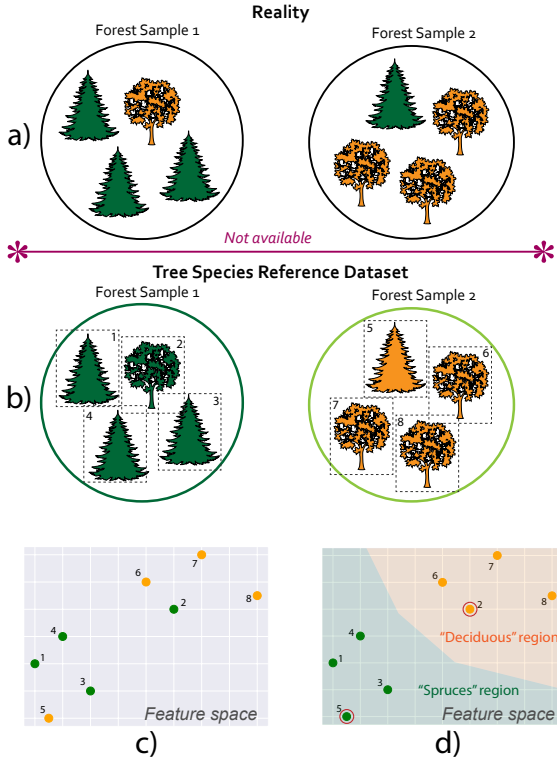


Fig. 5: Principle of the relabeling process. There are two forest stands in the example: (a) the first has three spruces and one deciduous tree, while the second has three deciduous trees and one spruce. However, such information is not available. (b) In the available tree species reference dataset, all the trees in the first group are marked as *spruces* and all the trees in the second group are marked as *deciduous* regardless of their real type. (c) Trees of the same species should have similar characteristics (features) even if they are wrongly assigned different labels if mapped into a feature space. (d) Trees can be relabeled based on the position of their features in the feature space. The image shows a two-dimensional feature space with only spruce and deciduous classes for better visualization.

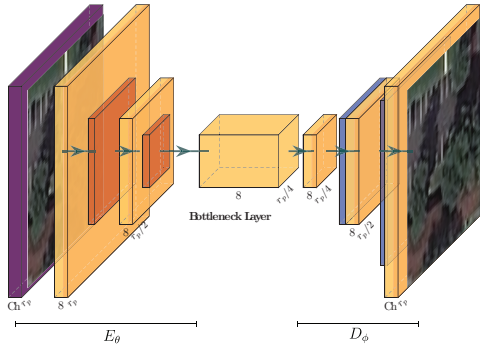


Fig. 6: Architecture used for the auto-encoder. The feature vector \mathcal{F} is extracted from the bottleneck layer.

feature space heavily depends on the “quality” of the feature extracted, which in turn depends on the quality of the input data as well as the power of the feature extraction method used.

We implement the semantic embedding using a majority voting scheme among the points. We first over-cluster the feature space with K clusters using the unsupervised clustering

algorithm Kmeans. Over-clustering means to cluster a space with more clusters than the number of groups the elements in the space belong to (which in our case is three, as the number of the considered tree types). Within each cluster $k = \{1, 2, \dots, K\}$ we compute a score Φ defined as the number of points belonging to each tree type label l as follows:

$$\Phi_k^l = \text{Number of points in cluster } k \text{ with label } l \quad (4)$$

We then assign to the cluster k the label with the highest score among Φ_k^l . Each point in the cluster k is assigned the label l set in the previous step. In this way, features “close” to each other in the feature space have the same label. Finally, patches are extracted sequentially from the whole area and features are calculated based on one of the earlier described methods (engineered or autoencoder-based features). Each patch is relabeled according to the learned semantic embedding and the output is the relabeled map $Smap_{relabelled}$.

D. Tree Species Detector

Compared to the original tree type dataset $Smap$, the relabeled map $Smap_{relabelled}$ has the following advantages: 1) each pixel belonging to a tree has a label, 2) non-trees are excluded from the dataset, 3) trees visually similar have the same label. However, it has been generated patch-wise from the previous step, and therefore it is blocky. We design and train a CNN model to solve this issue. Such a procedure has two advantages. The first is to refine the tree species map $Smap_{relabelled}$ further, making the output smoother. The second one is to create a standalone model. Once it is trained, such model can be used to directly estimate the tree species in the surrounding areas with the same tree species that has been trained on without performing the relabeling process again. The architecture is similar to the one in Fig. 4 with the difference that the task is now a multi-label segmentation where the output is a three-label mask corresponding to spruces, pines/larches, and deciduous trees. The output is $Smap_{refined}$ in Fig. 3.

E. Ground-truth Generation

Finally, $Smap_{refined}$ is compared with the ground-truth. Since the original tree inventory dataset $Smap$ cannot be used for comparison (because of the earlier discussed issues), we generate a ground truth by visual inspection, taking advantage of available acquired multi-temporal images. For the Norwegian use case we got two additional images: one from Airbus Pleiades-1 (4 channels) acquired in September 2018 and another one from the Norwegian program *NorgeIBilder* [37]. The image is a 3-channels image acquired in April 2019. For the Italian use case we acquired two images from Planet, taken in April and October 2021 respectively. Similar to the process done in [18], interpretation was conducted using different imagery compositions of the available images at different times, labeled by forest experts. The generation of such ground truth was a time-intensive yet necessary task. Although a certain degree of uncertainty still exists, the obtained ground truth is more consistent than the original tree inventory. However, our approach is using the original

raw reference dataset $Smap$ and therefore the ground truth generation is not needed for the implementation.

IV. RESULTS & DISCUSSIONS

The proposed pipeline has been implemented in Python using the Keras/Tensorflow [38] libraries for the deep learning part, and the sklearn library [39] for the machine learning part. QGIS [40] has been used to integrate data and results. The testing platform is a computer equipped with an Intel i7 Core 10th Gen processor, 32GB of RAM, and an Nvidia RTX 2080 Super as a GPU.

To validate the overall procedure we divided each study area into two non-overlapping regions A_1 and A_1 of similar size. Area A_1 is used for training and validation. This means that we calculate $Smap_{treemask}$ and $Smap_{relabelled}$ on A_1 . Also, we train the deep-learning model only on area A_1 . Afterward, we tested the trained model in A_2 . The generated map $Smap_{refined}$ is compared with the ground truth. Ground-truth has been created only for the testing region A_2 . To avoid biases, A_1 and A_2 have been selected to have similar tree species distributions. Fig. 7 shows the distribution of pixels as percentages within each tree type group in the two study areas (e.g. Norway and Italy).

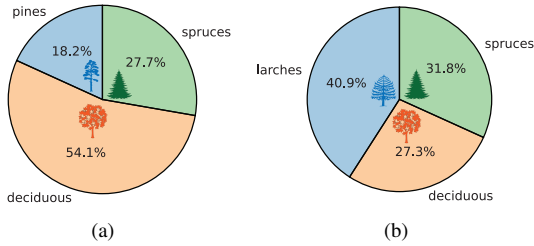


Fig. 7: Distribution of pixels as percentages for: (a) Norwegian study area, (b) Italian study area

We notice that the datasets, as it often happens in practice, are unbalanced. To overcome this issue, we sample the same number of patches per tree group in the *random sample extraction* step, when the patches are extracted to generate the feature space. Hence a balanced dataset is used to create the feature space. Furthermore, when evaluating our final model in the testing area A_2 , we use the F1-score as a metric to compare the different approaches. The F1-score is defined as the harmonic mean of the precision and recall and has been proven to be superior to accuracy when dealing with imbalanced classification problems [41].

A. Tree Segmentation Model

We first trained and tested the tree segmentation model used at the first stage of our methodology. The model is trained using a manually created binary mask of trees in the A_1 region. The dataset is split into a training and a validation set with a 80-20% ratio, and the model described in III-B is trained. The Adam optimizer is used with a learning rate of 10^{-4} . An early stopping callback, which monitors the validation loss, keeps track of the loss, stopping the training to avoid over-fitting.

Fig. 8 shows the accuracy for the validation dataset, whose value stabilizes at $\approx 95\%$.

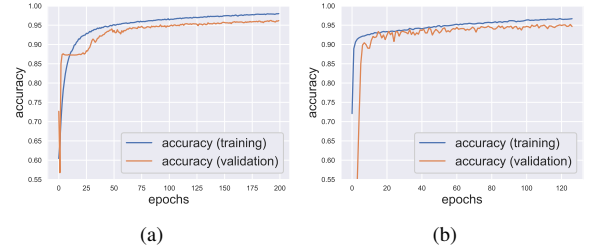


Fig. 8: Training and validation accuracy for (a) Norway and (b) Italy.

Once the model is trained, it can be used to generate the *treemask*. We multiply pixel-wise the original tree species dataset $Smap$ with *treemask* calculated from the trained tree segmentation model to get $Smap_{treemask} = Smap \otimes treemask$, as presented in the methodology section.

B. Relabeling Process

Once $Smap_{treemask}$ is created, randomly sampled patches of fixed size $s_p \times s_p$ are extracted from it. A small patch size makes it difficult to compute useful features out of it due to the lack of contextual information. On the other hand, a too large patch has the risk of incorporating different trees under the same label. We chose a patch size $s_p = 12 \times 12px$, which is equivalent to 6×6 meters given the resolution of our satellite images. A balanced dataset of 2500 patches per tree type (spruces, pines, and deciduous) is extracted from the satellite image. We recall that each patch P has an associated label l derived from $Smap_{treemask}$.

Then, features are extracted using the two methods presented in subsection III-C (i.e. engineered and autoencoder-based). The engineered features are calculated from each patch using Eq. 2. The GLCM matrix is calculated over each extracted patch P . We used the GLCM matrix computed with angles in the set $\{0; \frac{\pi}{2}\}$ and offsets $\{1; 2\}$. Details on the implementation can be found in [42]. The autoencoder in Fig. 6 has been used to extract feature automatically using Eq. 3. For visualization purposes, we make use of the Uniform Manifold Approximation and Projection (UMAP) algorithm [43]. to map the features space \mathbb{R}^d into \mathbb{R}^2 . Fig. 9 shows the UMAP plots of the feature space generated via autoencoder for WorldView-2 (Fig 9a) with labels taken from $Smap_{treemask}$ and the multi-temporal stacked image with labels taken from the ground-truth (Fig. 9b).

We recall that the feature space is a mathematical space where the points are the feature vectors $\mathcal{F} \in \mathbb{R}^d$ extracted from the patches $P_{i=1, \dots, N}$. The UMAP algorithm map the relative position of the points in the higher-dimensional space into \mathbb{R}^2 positions while preserving the pairwise distance relations between points and the global structures. Therefore, the distance between points and the orientation of the clusters do not have a geographical meaning. From the UMAP plots, we observe qualitatively that spruces, in particular, are more detached and separable from deciduous and pines in WorldView-2 imagery.

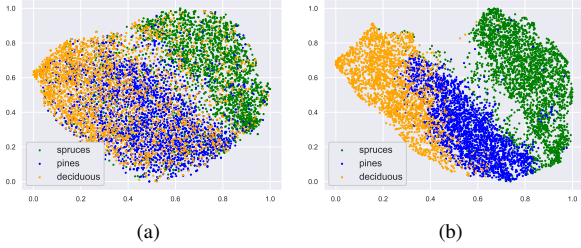


Fig. 9: UMAP plots of the feature space into \mathbb{R}^2 . Feature space generated by the autoencoder from (a) WorldView-2 with labels taken from $\mathbf{Smaptreemask}$, (b) Feature space generated by the auto-encoder from multi-temporal stacked image (WorldView-Pleiades-NorgeBilder) with labels taken from the ground truth.

From Fig. 9b we observe that the feature space generated using all the available images and the labels from the ground-truth provided by III-E is smoother, with each tree type having its own region in the feature space. This supports our assumptions and the idea presented in Fig. 5. We then perform the relabeling process described in the methodology. Points outside their semantic space are considered to have a wrong label and are then relabeled accordingly. We recall that the clustering is performed in the feature space \mathbb{R}^d . Once the semantic embedding has been performed in the feature space, patches of size $s_p \times s_p$ are extracted from the whole A_1 area, and the new learned labels are assigned, generating this way the output $\mathbf{Smaprabeled}$. It is worth mentioning that, besides the relabeling of the existing labels, this procedure also assigns to each tree that was not covered by the original tree reference dataset \mathbf{Smap} a new label.

C. Evaluation of the Inference Process

We train a CNN model using satellite images and the calculated $\mathbf{Smaprabeled}$ from both the engineered features and the autoencoder-based features as a training dataset. Similar to the tree segmentation model’s training, we extract 15000 tiles of 80×80 pixels (equal to 40×40 meters given the resolution of our satellite images), randomly samples within A_1 . We then train a model with the architecture and training parameters of the tree segmentation model. The output is three-channel, corresponding to the three tree types considered. Thus categorical cross-entropy loss function is used. To show the effectiveness of our approach, we test the performances using a CNN trained in a traditional supervised procedure. It consists in training the model using directly the original tree species dataset \mathbf{Smap} , without the relabeling process in our proposed pipeline. In addition, we train the model using $\mathbf{Smaptreemask}$ and the highly-refined ground truth.

1) *Norwegian study area*: First, we use confusion matrices to visualize in particular the classification matches per each category using WorldView-2 image, shown in Fig. 10.

Note how the confusion matrices with a standard approach are far from being diagonal (Fig. 10b). Due to the intrinsic noise of the dataset, a model trained with a traditional procedure (i.e. without relabeling) is incapable of learning, and the performance easily degrades into low performances. In Fig.

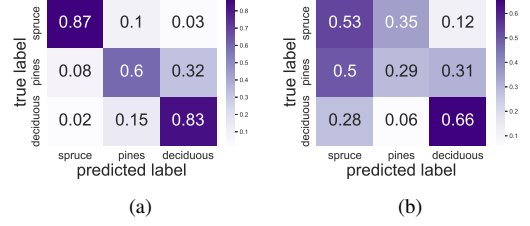


Fig. 10: Normalized confusion matrices (percentages) between predicted and true tree type for WorldView-2 imagery using: (a) our learning procedure and auto-encoder-based features, (b) traditional supervised approach without relabeling.

10a we observe that while spruces and deciduous are correctly identified with high accuracy, pines are more problematic. There is a percentage of pines misclassified as deciduous trees.

Table I provides the F1-score per each class for WorldView-2 using different approaches.

TABLE I: F1-scores for each class using our proposed approach and a traditional training procedure.

	WorldView-2		
	Spruces	Pines	Deciduous
Weakly-supervised + $\mathcal{F}^{\text{engineered}}$	0.799	0.506	0.675
Weakly-supervised + $\mathcal{F}^{\text{autoencoder}}$	0.883	0.648	0.761
Supervised from \mathbf{Smap}	0.458	0.322	0.531
Supervised from $\mathbf{Smaptreemask}$	0.492	0.441	0.586

Learning from $\mathbf{Smaptreemask}$ slightly improves the performances compared to learning directly from \mathbf{Smap} . This is due to the fact that in $\mathbf{Smaptreemask}$ the non-trees elements have been filtered out. However, the coarse boundaries between forest stands are still the same as \mathbf{Smap} and many pixels remain unlabeled. We note how using the relabeling step, before training the model, greatly boosts the performances with an average enhancement of the F1-score of 78% for the WorldView-2 imagery compared to not using our relabeling step. Finally, not surprisingly learning directly from the ground truth leads to the best results (F1-score: 0.915, 0.797, 0.864). However, this is not applicable in practice as the ground truth, which has been created by visual inspection of multi-temporal high resolution images, is not available in general. It is worth mentioning that engineered features are challenging to design. For example, texture operators can be applied to each channel separately or any combination of them. Manually engineering this considerable amount of combinations is impractical. Features extracted from auto-encoders are, by definition, extracted automatically from the network instead.

Finally, in Table II we show the computational running times of the different methods.

TABLE II: Computational running times for the different approaches.

Routine	Running time	
	Training	Inference
Engineered features extraction	—	491 sec
Autoencoder-based feature extraction	28.4 sec	5.3 sec
Tree species detector	36 min	8.2 sec

The high running time of the features extraction method lies in the CPU implementation of the sklearn library. Features

are extracted within a for-loop (which are usually slow in Python), called several times in the main script. On the other hand, auto-encoders are running on GPU using the TensorFlow implementation, making much faster the process of feature extraction. Furthermore, auto-encoders' architecture contain much less parameters (2,323 learnable weights) compared to the segmentation model (1,946,993 learnable weights), making the training procedure much faster.

2) *Italian study area*: For further validation we implement the approach in the another study area located in Italy. Table III provides the resulting F1-scores per each class.

TABLE III: F1-scores for each class using our proposed approach and a traditional training procedure for the Italian use case.

Imagery and Feature Type	F1-score		
	<i>Spruces</i>	<i>Larches</i>	<i>Deciduous</i>
Weakly-supervised + $\mathcal{F}^{\text{engineered}}$	0.381	0.387	0.442
Weakly-supervised + $\mathcal{F}^{\text{autoencoder}}$	0.422	0.450	0.494
Supervised from <i>Smap</i>	0.261	0.266	0.357
Supervised from <i>Smap_{treemask}</i>	0.312	0.304	0.408

We note that our relabeling approach improves the results compared to the traditional approach, confirming the outcomes found in the first use case. Learning directly from the ground truth leads again to the best results (F1-score: 0.531, 0.495, 0.585). However, we also notice that the F1-scores in this case are generally lower than the previous case study. This is due to the fact that the image has been acquired in summer, which is the season that minimizes the seasonality changes between tree species. We provide further discussion in V.

In both cases, our methodology can properly train a model through a two-step relabeling procedure, showing clear benefits compared to traditional approaches without the relabeling step. It can generate a more detailed version of the original tree species dataset. A visual example is shown in Fig. 11.

We note how the generated output is much more refined and semantically more coherent than the original dataset. Our procedure can greatly enhance the quality of available datasets for tree species.

V. PRACTICAL CONSIDERATIONS AND LIMITATIONS

Correctly recognizing tree species from satellite images is a difficult task, especially when available tree inventory are noisy and not precise enough, like in this study. However, there is another consideration. Available imagery might not be sufficient to recognize the different species effectively. To demonstrate this problem, we extracted random patches from the three species, labeled according to the original tree inventory dataset *Smap* and from the ground truth, respectively in the Norwegian study area. We compute and plot the mean (as solid line) and standard deviation (as confidence interval line plot) per channel in Fig. 12.

We observe that in the Norwegian use case (WorldView imagery from May), if we sample from the ground truth (Fig. 12a) each tree specie has a specific spectral curve. On the other hand the spectral curves taken from *Smap* (Fig. 12b) are more mixed. This shows that the ground truth is more consistent than the starting tree species inventory *Smap*. However, we recall that the ground truth is not available in practice in

most of the cases. It is worth mentioning that spectral curves only show pixel intensity in the different spectra but other contextual information (related for instance to texture) that can potentially be use to discriminate between species is missing. This suggests, and confirms several studies [44], that the number of channels available (i.e., the amount of information we can extract from satellite images) and the seasonality plays an important role indeed.

Spruces have been found to be easily identified in Norway. However, compared to spruces, which have large, dark green canopies, pines have more scattered and pruned canopies with little foliage, making them more difficult to distinguish from deciduous trees. The fact that pines are the most problematic type is also confirmed by Fig. 9 where we observe that their features generally lay between the spruces and deciduous' space, making it less separable. In Italy, on the other hand, we found spruces and larches to be less distinguishable. This is because they have nearly the same canopy structure. However, larches are one of the few conifers that lose their needles in the autumn. Therefore, it is desirable to align the time of image acquisition with the phenological cycle of the species under investigation to increase the performance of tree species classification.

As presented in the Methodology section, we use two main assumptions to facilitate our framework development. The first assumption is that trees of the same species share the same position in the feature space. However, there is a possibility that two or more different tree species have similar visual characteristics. Therefore we suggest, in regions where such tree species exist, to combine classic ground-based approaches in addition to satellite surveys. The second assumption is that the majority of trees have the right label in the given tree species inventory data set *Smap*. However, generating tree inventories at national or regional-level is a time-consuming and challenging task which has some uncertainties. In regions where existing tree inventories have low accuracy, it is possible to manually label part of the satellite images by experts on a limited scale.

While the proposed methodology works with any number of images, we were particularly interested in evaluating the method when only one multi-spectral satellite image is used. Acquiring multi-temporal images has some advantages in terms of performance (because more information can be extracted) but also exhibits some potential drawbacks. Multi-temporal high-resolution images can be expensive. In addition, land use can change and large portions of trees can be cut down between two frames, making the analysis more complicated to automate.

Furthermore, hyper-spectral imaging is an option to discriminate even further different types of trees. Hyper-spectral images contain multiple (typically between 64 and 256) continuous narrow bands, providing significant levels of detail, which allow for the distinction of fine spectral variations among tree species [45]. However, the main limitations of such images are the costs, complexity, and their availability in different locations. Recently some hyper-spectral sensors have been launched, including EO-1 from NASA and PROBA-1 from ESA, spanning from 60 to 200 spectral bands with a

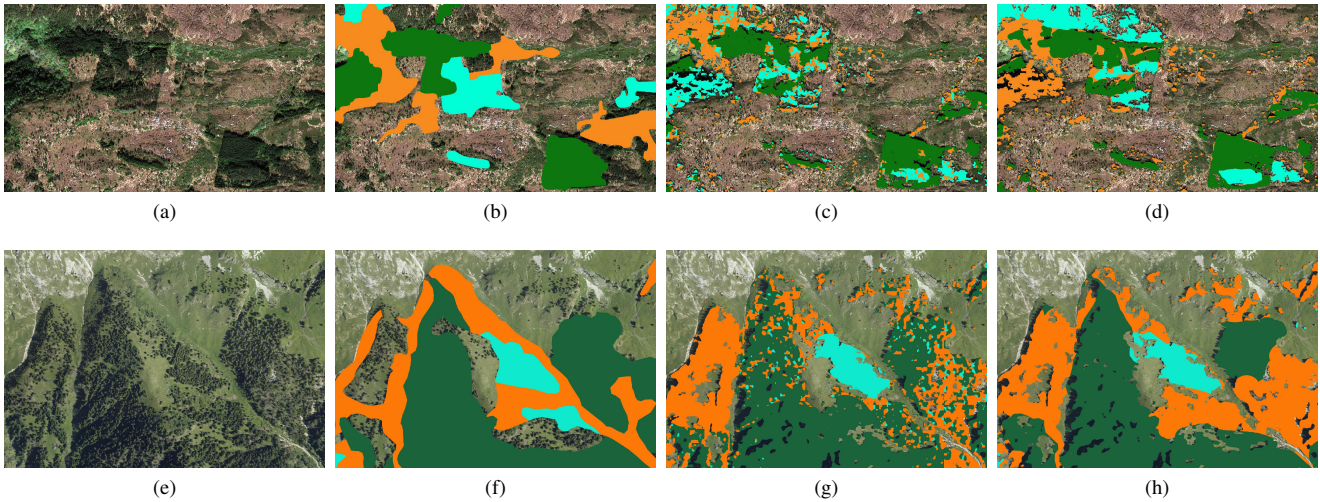
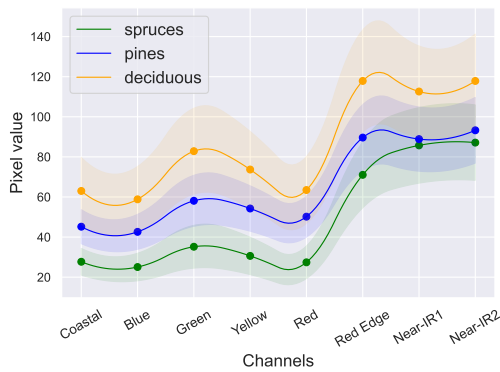
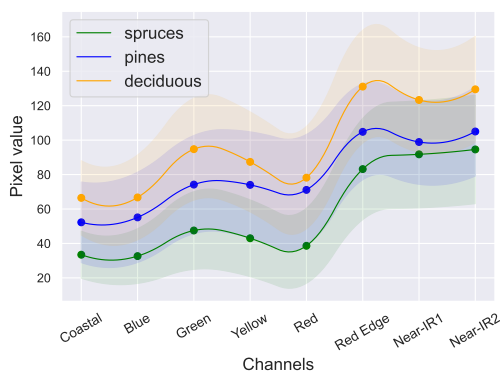


Fig. 11: Sample of the WorldView imagery in Norway (top row) and Italy (bottom row): (a,e) optical image, (b,f) starting tree species dataset $Smap$, (c,g) refined tree species map $Smap_{refined}$, (d,h) Ground-truth. Note the issues present in the original dataset. Despite these, the output generated via our approach can automatically capture new trees and refine better the forest stands. Legend: spruces (green), pines/larches (cyan), deciduous (orange).



(a)



(b)

Fig. 12: Spectral curves per channel with: (a) patches sampled from the ground truth (b) patches sampled from the $Smap$ (NIBIO dataset).

30-meters resolution. To our knowledge, no satellite providers offer high-resolution hyper-spectral images (i.e., 1-meter or less). The current studies on hyper-spectral images are limited to airborne scanning, which faces the challenges introduced in

Section I.

Different available approaches exist, each with specific advantages and disadvantages (quality, data availability, coverage, storage constraints, costs, etc.). We find that our method can serve as a complementary source to the other approaches, providing a high potential for added satellite based observability with minimal costs and high availability.

VI. ACKNOWLEDGMENTS

This work is partly funded by the Research Council of Norway under the project "Prediction of ignition and spread of wildfires in Scandinavia: from experiments to models", project number 315870.

VII. CONCLUSIONS

This paper has proposed a framework to identify tree species using high-resolution satellite images and a noisy reference forestry survey dataset. The proposed methodology relies on feature extraction from samples in the tree reference dataset to learn the characteristic properties of each class. The features are relabeled based on their position in the feature space, and a pre-refined map is generated using an additional tree segmentation model. A deep learning model is then trained with the pre-refined map to further smooth the pre-refined map. The strength of our approach is that refined version of tree species inventories, often available at regional-scales, can be generated automatically from single images as input, making the approach practical and relatively cheap. Multi-temporal images and different case studies have been used for cross-validation. Our evaluation shows that the proposed methodology exhibits clear benefits compared to traditional training procedures. Our method can be helpful as a complementary source, providing a high potential for added observability with minimal costs and high availability for everyone. Future work will be towards improving further the performances, especially with trees with less foliage. In

addition, we plan to improve the methodology by detecting outliers (trees that do not belong to any of the specified species) in the feature space and testing the approach with more tree species.

REFERENCES

- [1] Michael A. Wulder, Ronald J. Hall, Nicholas C. Coops, and Steven E. Franklin. High Spatial Resolution Remotely Sensed Data for Ecosystem Characterization. *BioScience*, 54(6):511–521, 06 2004.
- [2] G. Jansson and P. Angelstam. Threshold levels of habitat composition for the presence of the long-tailed tit (*aegithalos caudatus*) in a boreal landscape. *Landscape Ecology*, 14:283–290, 2004.
- [3] A. Barbati, P. Corona, and M. Marchetti. A forest typology for monitoring sustainable forest management: The case of european forest types. *Plant Biosystems - An International Journal Dealing with all Aspects of Plant Biology*, 141:103 – 93, 2007.
- [4] Alex M. Lechner, Giles M. Foody, and Doreen S. Boyd. Applications in remote sensing to forest ecology and management. *One Earth*, 2(5):405–412, 2020.
- [5] Ryan Klein, Andrew Koeser, Richard Hauer, and Gail Hansen. Risk assessment and risk perception of trees: A review of literature relating to arboriculture and urban forestry. *Arboriculture & Urban Forestry*, 45:26–38, 01 2019.
- [6] Alican Karaer, Mehmet Baran Ulak, Tarek Abichou, Reza Arghandeh, and Eren Erman Ozguven. Post-hurricane vegetative debris assessment using spectral indices derived from satellite imagery. *Transportation Research Record*, 2021.
- [7] Michele Gazzea, Michael Pacevicius, Dyre Oliver Dammann, Alla Sapronova, Torleif Markussen Lunde, and Reza Arghandeh. Automated power lines vegetation monitoring using high-resolution satellite imagery. *IEEE Transactions on Power Delivery*, 37(1):308–316, 2022.
- [8] Michele Gazzea, Alican Karaer, Mahyar Ghorbanzadeh, Nozhan Balafkan, Tarek Abichou, Eren Erman Ozguven, and Reza Arghandeh. Automated satellite-based assessment of hurricane impacts on roadways. *IEEE Transactions on Industrial Informatics*, 18(3):2110–2119, 2022.
- [9] Fabian Ewald Fassnacht, Hooman Latifi, Krzysztof Stereńczak, Aneta Modzelewska, Michael Lefsky, Lars T. Waser, Christoph Straub, and Aniruddha Ghosh. Review of studies on tree species classification from remotely sensed data. *Remote Sensing of Environment*, 186:64–87, 2016.
- [10] Agnieszka Kamińska, Maciej Lisiewicz, and Krzysztof Stereńczak. Single tree classification using multi-temporal als data and cir imagery in mixed old-growth forest in poland. *Remote Sensing*, 13(24):5101, Dec 2021.
- [11] Lina Tang and Guofan Shao. Drone remote sensing for forestry research and practices. *Journal of Forestry Research*, 26:791–797, 2015.
- [12] Sakari Tuominen, Andras Balazs, Heikki Saari, Ilkka Pölonen, Janne Sarkeala, and Risto Viitala. Unmanned aerial system imagery and photogrammetric canopy height data in area-based estimation of forest variables. *Silva Fennica*, 49:1348, 2015.
- [13] Hans Ole Ørka and M. Hauglin. Use of remote sensing for mapping of non-native conifer species. <https://www.miljodirektoratet.no/globalassets/publikasjoner/m490/m490.pdf>, 2016. [Online].
- [14] Michele Gazzea, Alican Karaer, Nozhan Balafkan, Eren Erman Ozguven, and Reza Arghandeh. Post-hurricanes roadway closure detection using satellite imagery and semi-supervised ensemble learning. In *Transportation Research Board 100th Annual Meeting 2021*, number TRBAM-21-00892, 2021.
- [15] Margaret Moore and Marvin Bauer. Classification of forest vegetation in north-central minnesota using landsat multispectral scanner and thematic mapper data. *Forest Science*, 36:330–342, 06 1990.
- [16] Markus Immitzer, Clement Atzberger, and Tatjana Koukal. Tree species classification with random forest using very high spatial resolution 8-band worldview-2 satellite data. *Remote Sensing*, 4(9):2661–2693, Sep 2012.
- [17] M. Dalponte, H. O. Ørka, T. Gobakken, D. Gianelle, and E. Næsset. Tree species classification in boreal forests with hyperspectral data. *IEEE Transactions on Geoscience and Remote Sensing*, 51(5):2632–2645, 2013.
- [18] Martina Deur, Mateo Gasparovic, and Ivan Balenović. Tree species classification in mixed deciduous forests using very high spatial resolution satellite imagery and machine learning methods. *Remote Sensing*, 12:3926, 11 2020.
- [19] Mryka Hall-Beyer. Glcm texture: A tutorial v. 3.0 march 2017. <https://prism.ucalgary.ca/bitstream/handle/1880/51900/texture03> 2017. Online.
- [20] Matheus Pinheiro Ferreira, Fabien Hubert Wagner, Luiz E.O.C. Aragão, Yosio Edemir Shimabukuro, and Carlos Roberto de Souza Filho. Tree species classification in tropical forests using visible to shortwave infrared worldview-3 images and texture analysis. *ISPRS Journal of Photogrammetry and Remote Sensing*, 149:119–131, 2019.
- [21] N. Kussul, M. Lavreniuk, S. Skakun, and A. Shelestov. Deep learning classification of land cover and crop types using remote sensing data. *IEEE Geoscience and Remote Sensing Letters*, 14(5):778–782, 2017.
- [22] Shutao Li, Weiwei Song, Leyuan Fang, Yushi Chen, Pedram Ghamisi, and Jón Atli Benediktsson. Deep learning for hyperspectral image classification: An overview. *IEEE Transactions on Geoscience and Remote Sensing*, 57(9):6690–6709, 2019.
- [23] Masanori Onishi and Takeshi Ise. Explainable identification and mapping of trees using uav rgb image and deep learning. *Scientific Reports*, 11, 01 2021.
- [24] S. Illarionova, A. Trekin, V. Ignatiev, and I. Oseledets. Neural-based hierarchical approach for detailed dominant forest species classification by multispectral satellite imagery. *IEEE Journal of Selected Topics in Applied Earth Observations and Remote Sensing*, 14:1810–1820, 2021.
- [25] Caiyan Chen, Linhai Jing, Hui Li, and Yunwei Tang. A new individual tree species classification method based on the resu-net model. *Forests*, 12(9):1202, Sep 2021.
- [26] Nitika Nigam, Tanima Dutta, and Hari Prabhat Gupta. Impact of noisy labels in learning techniques: A survey. In Mohan L. Kolhe, Shailesh Tiwari, Munesh C. Trivedi, and Krishn K. Mishra, editors, *Advances in Data and Information Sciences*, pages 403–411, Singapore, 2020. Springer Singapore.
- [27] Hwanjun Song, Minseok Kim, Dongmin Park, and J. Lee. Learning from noisy labels with deep neural networks: A survey. *ArXiv*, abs/2007.08199, 2020.
- [28] Kidiyo Kpalma, Miloud Chikr El Mezouar, and Nasreddine Taleb. Recent trends in satellite image pan-sharpening techniques. 1st International Conference on Electrical, Electronic and Computing Engineering, pages 1–10, Vrnjacka Banja, Serbia, 2014.
- [29] Norwegian Institute of Bioeconomy Research (NIBIO). <https://www.nibio.no/en/about-eng>. Online.
- [30] Norwegian Institute of Bioeconomy Research (NIBIO). https://kilden.nibio.no/?lang=nb&topic=arealinformasjon&X=7195706.12&Y=284337.75&zoom=0.050089679614182224&bgLayer=graatone_cache. Online.
- [31] Rasmus Astrup, Johannes Rahlf, Knut Björkelo, Misganu Debella-Gilo, A. K. Gjertsen, and Johannes Breidenbach. Forest information at multiple scales: development, evaluation and application of the norwegian forest resources map sr16. *Scandinavian Journal of Forest Research*, 34:484 – 496, 2019.
- [32] Regione del Veneto. Idt-rv 2.0 – infrastruttura dati territoriali della regione del veneto. <https://idt2.regione.veneto.it/idt/webgis/viewer?webgisId=147>. Online.
- [33] John Wilson Rouse, Robert H. Haas, John A. Schell, and D. W. Deering. Monitoring vegetation systems in the great plains with erts. 1973.
- [34] O. Ronneberger, P. Fischer, and T. Brox. U-net: Convolutional networks for biomedical image segmentation. *ArXiv*, abs/1505.04597, 2015.
- [35] R. M. Haralick, K. Shanmugam, and I. Dinstein. Textural features for image classification. *IEEE Transactions on Systems, Man, and Cybernetics*, SMC-3(6):610–621, 1973.
- [36] Wei Luo, Jun Li, Jian Yang, Wei Xu, and Jian Zhang. Convolutional sparse autoencoders for image classification. *IEEE Transactions on Neural Networks and Learning Systems*, 29(7):3289–3294, 2018.
- [37] Statens vegvesen, Norsk institutt for Bioøkonomi (NIBIO), and Kartverket. Norge i bilder. <https://norgebilder.no/>. Online.
- [38] Francois Chollet et al. Keras, 2015.
- [39] F. Pedregosa, G. Varoquaux, A. Gramfort, V. Michel, B. Thirion, O. Grisel, M. Blondel, P. Prettenhofer, R. Weiss, V. Dubourg, J. Vanderplas, A. Passos, D. Cournapeau, M. Brucher, M. Perrot, and E. Duchesnay. Scikit-learn: Machine learning in Python. *Journal of Machine Learning Research*, 12:2825–2830, 2011.
- [40] QGIS Development Team. *QGIS Geographic Information System*. Open Source Geospatial Foundation, 2009.
- [41] László A. Jeni, Jeffrey F. Cohn, and Fernando De la Torre. Facing imbalanced data—recommendations for the use of performance metrics. *2013 Humaine Association Conference on Affective Computing and Intelligent Interaction*, pages 245–251, 2013.
- [42] Stéfan van der Walt, Johannes L. Schönberger, Juan Nunez-Iglesias, François Boulgogne, Joshua D. Warner, Neil Yager, Emmanuelle Goullart, Tony Yu, and the scikit-image contributors. scikit-image: image processing in Python. *PeerJ*, 2:e453, 6 2014.

- [43] Leland McInnes and John Healy. Umap: Uniform manifold approximation and projection for dimension reduction. *ArXiv*, abs/1802.03426, 2018.
- [44] Philipp Gartner, Michael Forster, and Birgit Kleinschmit. The benefit of synthetically generated rapideye and landsat 8 data fusion time series for riparian forest disturbance monitoring. *Remote Sensing of Environment*, 177:237–247, 2016.
- [45] Laurel Ballanti, Leonhard Blesius, Ellen Hines, and Bill Kruse. Tree species classification using hyperspectral imagery: A comparison of two classifiers. *Remote Sensing*, 8(6):445, May 2016.



Michele Gazzea (IEEE Member) received the bachelor's degree in information engineering and the master's degree in automation and control engineering from the University of Padova, Padua, Italy, in 2014 and 2017, respectively. He is currently pursuing the Ph.D. degree with the Western Norway University of Applied Sciences, Bergen, Norway. He worked as a research and development Engineer with Cielle srl, Zona Artigianale Pero, Italy, designing machine-learning-based diagnostic techniques on

(CNC) machines. His research interests are in data analytics, machine and deep learning, computer vision, and remote-sensing applications.



Lars Michael Kristensen received the Ph.D. degree in computer science from the University of Aarhus, Aarhus, Denmark, in 2000. He is currently a Professor of computer science and software engineering with the Western Norway University of Applied Sciences, Bergen, Norway. Upon the completion of his Ph.D. degree, he worked as a Post-Doctoral Researcher in computer systems engineering with the University of South Australia, Adelaide, SA, Australia and the Australian Defence Science and Technology Organization, Canberra, ACT, Australia.

Following the post-doctoral research position, he obtained a permanent position with the University of Aarhus and was involved in a number of industry-supported research projects within modeling and validation of internet protocols, mobile ad-hoc networks, and sensor networks. He has coauthored the most recent textbook on Coloured Petri Net (CPN) Tools which is one of the most widely used software tools for modeling and validation of concurrent systems.



Francesco Pirotti is an Associate Professor of geomatics with the Department of Land Environment and Agriculture and Forestry, University of Padova, Padua, Italy. His research touches on geospatial frameworks [geodatabases and geographical information system (GIS)], surveying, photogrammetry, and remote sensing for environmental applications. He focuses primarily on methods for processing data from imagery-optical and radar-and lidar/photogrammetric point clouds for understanding forest structure dynamics. He has authored more

than 100 scientific publications and is involved in several academic societies and services.



Eren Erman Ozguven (Member, IEEE) received the Ph.D. degree in civil and environmental engineering from Rutgers University, Piscataway, NJ, USA, in 2012, with a focus on emergency supply transportation operations. He is an Associate Professor with the Department of Civil and Environmental Engineering and the Director of Resilient Infrastructure and Disaster Response (RIDER) Center, Florida A&M University-Florida State University, Tallahassee, FL, USA. His research interests include smart cities, urban mobility, transportation accessibility,

traffic safety and reliability, disaster resilience, and intelligent transportation systems.





Reza Arghandeh (IEEE Senior Member) is a Full Professor with the Department of Computing, Mathematics, and Physics and the Department of Electrical Engineering, Western Norway University of Applied Sciences (HVL), Bergen, Norway. He is the Director of the Collaborative Intelligent Infrastructure Laboratory (CI2), Bergen. He is also a Lead Data Scientist with StormGeo AS, Bergen. He has been an Assistant Professor with the Department of ECE, FSU, Tallahassee, FL, USA, from 2015 to 2018, and a Post-Doctoral Scholar with the Department of EECS, University of California at Berkeley, Berkeley, CA, USA, from 2013 to 2015. His research has been supported by the U.S. National Science Foundation, the U.S. Department of Energy, the European Space Agency, and the European Commission.

ASPIRE-V: ARTIFICIAL INTELLIGENCE AND SPACE-BASED MONITORING FOR POWER LINES RISK EVALUATION AGAINST VEGETATION

Gazzea M., and Arghandeh R.

Submitted to IEEE Transactions on Power Delivery, 2024

ASPIRE-V: Artificial Intelligence and Space-based Monitoring for Power Lines Risk Evaluation against Vegetation

Michele Gazzea , *Student Member, IEEE* and Reza Arghandeh , *Senior Member, IEEE*

Abstract—Power lines traverse diverse terrains over vast distances to deliver electricity. Vegetation near power lines, especially during severe weather, can fall and disrupt the electrical network, causing power outages and considerable economic losses. Traditional monitoring procedures are time-consuming and costly, requiring on-the-ground teams and aerial surveys by helicopters. However, the decrease in satellite launch costs, the increasing satellite population, and advancements in technology have made satellite imagery more affordable. In our study, we introduce *Artificial Intelligence and Space-based Monitoring for Power Lines Risk Evaluation against Vegetation (ASPIRE-V)*, a framework that enables up-to-date assessment of vegetation-related risks to the power lines. It uses high-resolution satellite images and weather data to create 3D model of trees plus key tree characteristics such as height, species, and strength against wind within the power lines right-of-way (ROW) to identify susceptible trees that can collide with the power lines automatically. The proposed framework is implemented and validated on an actual distribution grid in Western Norway. Our findings, corroborated by LiDAR data and other in-situ ground truths, show a strong capability to monitor tree conditions. This method enhances the toolkit available to vegetation management teams within electrical utilities, contributing to a more reliable and secure power supply.

Index Terms—Risk Assessment, Remote Sensing, Satellite Imagery, Power Line Monitoring

I. INTRODUCTION

POWER transmission and distribution networks are vital for many societal activities and services but are susceptible to extreme weather like heavy snow, hail, and strong winds. Trees near these lines, aggravated by harsh weather, are major contributors to power outages [1]. In Norway, over 80% of outages are due to vegetation and wind issues [2]. Trees falling on lines can cause disruptions, outages, and in dry areas, even lead to wildfires [3]. Therefore, continuous vegetation monitoring and management are crucial for electric utilities, which invest significant financial resources to maintain them.

Typically, utility operators conduct visual inspections by sending ground crews to drive along power lines, identifying and documenting areas at risk and trees encroaching on the right-of-ways (ROWS). Another method involves aerial surveys using helicopters or drones equipped with cameras or LiDAR technology to scan the lines [4]. Nonetheless, these traditional approaches are labor-intensive and highly expensive. The costs escalate further due to the extensive reach of power line networks, which can stretch for hundreds of kilometers. In countries like Norway, the challenge is compounded by power lines that traverse through remote and difficult terrains

like mountains and fjords. Therefore, vegetation management remains an ample item in electric companies' operation and maintenance costs.

Current literature features a few vegetation monitoring tools like ForestGALES [5] and TREFALL [6], designed primarily for forestry and arboriculture to assess risks from wind-induced forest damage and identify trees posing threats to infrastructure. These models require pre-gathered tree data, including location, species, and physical characteristics, typically obtained through field surveys or ground inspections. However, due to the high costs of monitoring extensive infrastructure networks, data collection is often sparse, conducted over multi-year periods and on a fixed schedule. This leads to infrequent updates of information, causing a disconnect between the management of vegetation tasks and the swift emergence of certain risks like vegetation overgrowth.

The decrease in satellite launch costs and the introduction of advanced sensor-equipped satellites have substantially lowered the price of satellite imagery. Commercial providers now offer high-resolution images with regular updates and global reach. This technology has been successfully applied in infrastructure monitoring post-natural disasters [7] and pre-disaster vulnerability assessments [8], [9]. This progress presents an opportunity to combine large-scale monitoring with frequent updates and cost-effectiveness, bridging the observability gap in traditional cycle-based monitoring. It improves situational awareness around power lines, facilitating proactive measures.

Vegetation detection and mapping have been extensively studied in forestry works [10], [11]. However, unlike forestry tasks, high-resolution imaging is crucial for power line monitoring, providing the sub-meter accuracy required to discern critical distances. Even a small 1 to 2-meter discrepancy can be significant in this context.

This paper presents "ASPIRE-V," a novel framework aimed at improving vegetation management for transmission and distribution companies. It facilitates monitoring and risk assessment of vegetation near power lines by integrating remote sensing data, machine learning, and mechanistic models. This approach estimates key tree parameters such as height, proximity to power lines, and species type from high-resolution satellite images, offering a cost-effective alternative to traditional field surveys and incorporating real-time weather data for risk assessment. The framework produces two types of risk maps: a static map identifying trees that could fall onto power lines, and a dynamic map using wind data to evaluate the risk of trees breaking and affecting the lines. These maps enhance proactive

1 vegetation management and situational awareness, improving
 2 the power grid's reliability and resilience. By integrating
 3 this framework into existing vegetation management systems,
 4 utilities can gain deeper insights into vegetation conditions,
 5 ultimately enhancing management and operational efficiency.

6 Our contributions are as follows:

- 7 • we offer in-depth characterization of trees along power
 8 lines using satellite imagery
- 9 • we compute multi-level risk assessments for power lines,
 10 incorporating collision and weather-related factors.
- 11 • we have applied this solution in a real-world setting
 12 and present insights on practical implications for electric
 13 utility companies.

14 II. STUDY AREA AND DATA USED

15 The research was conducted in collaboration with a power
 16 distribution system operator (DSO) in Askvoll, Western Nor-
 17 way, covering an area of approximately 20 square kilometers.
 18 This area includes a rural 26-kilometer-long 22kV distribution
 19 network characterized by fields, scattered and dense forests,
 20 and waterways. The monitored corridor for the power lines
 21 extends 10 meters on either side, creating a 20-meter-wide
 22 strip. It is important to note that the width of the monitoring
 23 corridor can be adjusted by the electric operator according to
 24 local or national requirements, and this choice does not restrict
 25 the applicability of the methodology described in the study.
 26 For the specified region, a high-resolution satellite image from
 27 Maxar's WorldView-2, captured in mid-May, was acquired.
 28 The image has a resolution of 0.5 m/pixel, ortho-rectified, and
 29 pan-sharpened [12] by the provider. This satellite image is
 30 distinguished by its eight unique spectral bands, which include
 31 the standard red, green, and blue bands and several infrared
 32 wavelengths.

33 We used the study region's LiDAR point cloud data obtained
 34 through airborne laser scanning (ALS) to train and validate the
 35 deep learning models. This LiDAR data is made accessible
 36 through a Norwegian national program [13], offering nation-
 37 wide point cloud coverage for public use. The point clouds are
 38 characterized by a density of 25 points per square meter, with
 39 each point in the point cloud representing a specific height
 40 above sea level.

41 The reference dataset for tree species was supplied by the
 42 Norwegian Institute of Bioeconomy Research, detailed in [14].
 43 This dataset offers extensive data on forest distribution nation-
 44 wide, categorizing forest stands by the dominant tree species
 45 present. It explicitly identifies stands of Norway spruces, Scots
 46 pines, and various deciduous trees, mainly birches, aspens, and
 47 rowan. For more intricate details on the creation and validation
 48 of this dataset, one can refer to the cited study by Astrup et
 49 al., [15]. The collected data for the study area is summarized
 50 in Figure 1 in the paper.

51 Lastly, historical wind data relative to wind direction, speed,
 52 and gust is obtained from [16].

53 III. METHODOLOGY

54 The overall pipeline of ASPIRE-V is shown in Fig. 2, and
 55 each block is described in detail in the following subsections.

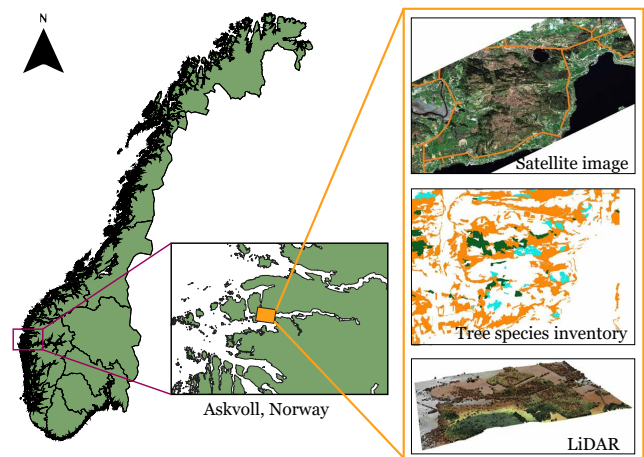


Fig. 1: The study area for this study is a 26-kilometer-long distribution network (shown as orange lines in the top figure) in western Norway. A WorldView-2 satellite image has been acquired for the region. Additionally, national tree species inventory and LiDAR data are acquired.

56 A. Input Data and pre-processing

57 A pre-processing procedure for multi-spectral satellite im-
 58 agery is used to facilitate machine learning training. Initially,
 59 pixel values in each spectral band are scaled and contrast-
 60 enhanced by adjusting the minimum and maximum values to
 61 the 2nd and 98th percentiles of pixel distribution, respectively,
 62 and normalizing each channel to the (0, 1) interval.

63 The Normalized Difference Vegetation Index (NDVI) is
 64 calculated from the satellite image red and infrared band to
 65 detect vegetation, using the formula $NDVI = \frac{NIR-RED}{NIR+RED}$
 66 [17]. NDVI values, ranging from -1 to 1, help differentiate
 67 between non-vegetated areas (low NDVI, 0.1 or less), sparse
 68 vegetation (moderate NDVI, around 0.2 to 0.5), and dense
 69 vegetation or peak growth crops (high NDVI, 0.5-1).

70 LiDAR point clouds are used to create a Digital Surface
 71 Model (DSM) and a Digital Terrain Model (DTM), the latter
 72 representing the Earth's surface without vegetation or build-
 73 ings. Heights in the DSM are normalized relative to the ground
 74 surface, creating a normalized Digital Surface Model (nDSM).
 75 A tree reference map \mathcal{M}_{trees} (ground truth) is generated
 76 using thresholds 1.3 meters and 0.1 on the nDSM and NDVI,
 77 respectively, differentiating trees from other green areas and
 78 filtering out non-vegetative or man-made structures. The tree
 79 map is then refined using morphological image processing
 80 techniques like erosion and dilation to eliminate artifacts and
 81 isolated points.

82 B. Tree Inventory Generation

83 Trees pose a substantial threat as they can be susceptible
 84 to falling onto power lines during strong wind events. When
 85 evaluating the risk to nearby infrastructure lines, it is crucial
 86 to consider various factors related to the trees, including their
 87 locations, proximity to the power lines, species, size, and
 88 height. For example, in [18], the authors show that Norway
 89 spruces are more vulnerable overall than Scots pines and
 90 birches are the least vulnerable. In our framework, we use a

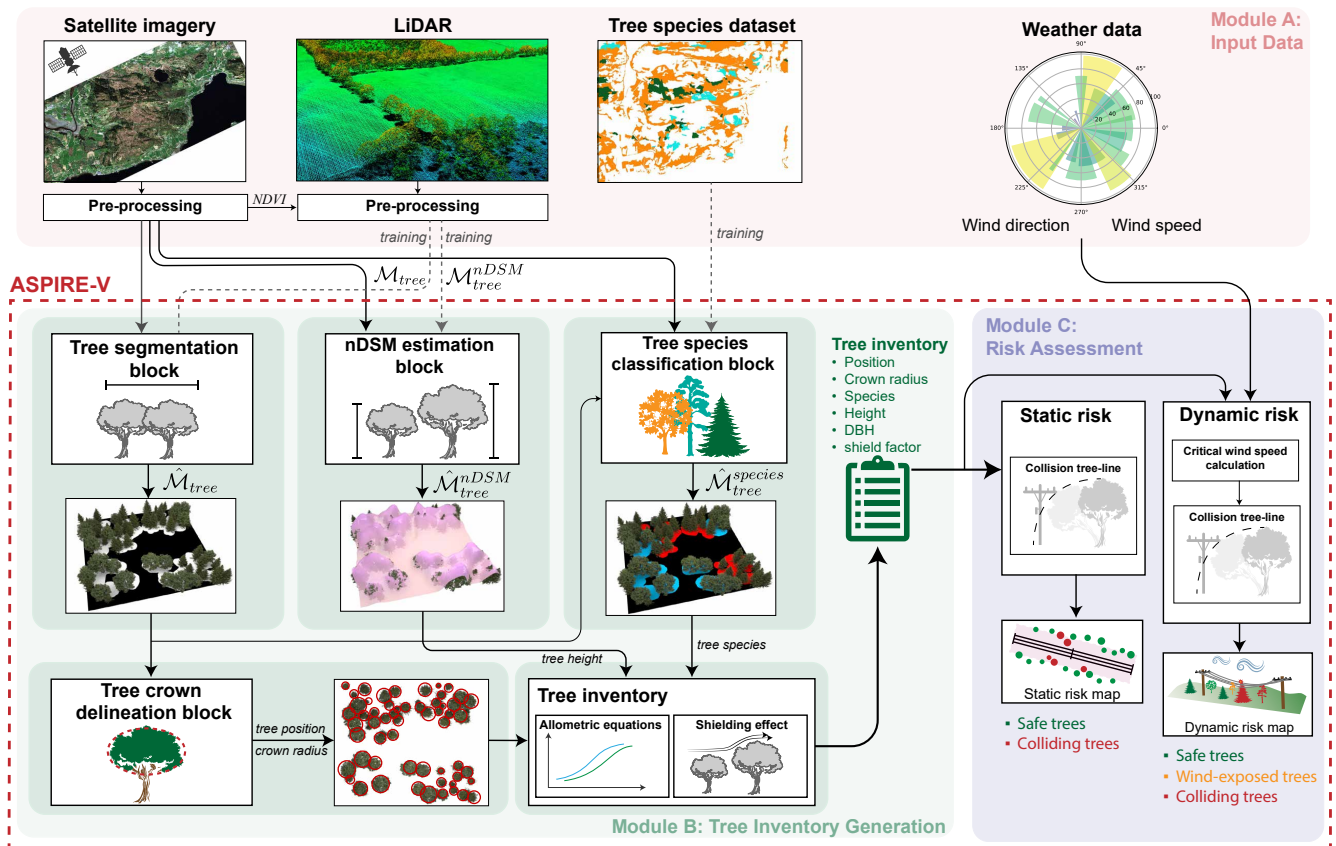


Fig. 2: Graphical overview of the ASPIRE-V framework. (1-Input data): The framework starts with the acquisition of satellite imagery for the designated region. It also utilizes LiDAR point cloud data and tree species inventory for the initial training of the machine learning models, although these inputs are not required once the models are developed. (2-Tree inventory generation): Different models are developed to segment trees, estimate their height, classify their species, and extract their crowns. Information regarding the tree's position, crown radius, species, and height is collected to create a tree catalog. Allometric equations are utilized to estimate the tree diameters at breast height (DBH) as well as the shielding effects of the trees. (3-Risk): All the information is integrated to determine the critical wind speed required for each tree to break. A comparison between the calculated critical wind speed and the actual wind data is performed to assess the vulnerability of each tree. This information is used to generate a dynamic risk map that indicates the potential risk to nearby infrastructure lines caused by trees in various weather conditions.

1 satellite image to estimate these tree parameters and generate
2 a tree inventory.

3 1) *Tree segmentation block:* We initiate our methodology
4 by developing a tree segmentation model that processes an
5 input image to produce a pixel-wise mask, denoted by \hat{M}_{tree} ,
6 which assigns a probability to each pixel indicating whether
7 it is part of a tree.

8 For the segmentation model, we chose an encoder-decoder
9 architecture with a Unet backbone [19]. This architecture
10 consists of a series of convolutional blocks with sizes
11 [16, 32, 64, 128], each followed by Max Pooling layers. Each
12 block contains two convolutional filters, a batch normalization
13 layer, an *elu* activation function, and a dropout layer for
14 regularization. In the decoder section, an attention mechanism
15 is utilized to merge features at different scales using the
16 attention mechanism proposed by [20]. Binary cross-entropy
17 serves as the loss function during network training, fitting for
18 a scenario with binary labels, where '0' signifies 'no-trees'
19 and '1' indicates 'trees'. The model is trained with the ground
20 truth provided by M_{trees} , generated in the data pre-processing
21 step.

2) *nDSM estimation block:* The second block of our frame-
work is focused on estimating tree height, a challenging task
when working with single optical images due to the inher-
ent lack of height information. There are well-documented
ambiguities in translating color measurements into height
values, making this task inherently ill-posed (as noted in
[21]). Typically, 3D height models are created using stereo
imagery [22], multi-angular photogrammetry [23], Synthetic-
aperture radar (SAR) interferometry [24], and LiDAR [25].
However, recent research has investigated machine learning's
potential in 3D reconstruction from single optical images [26].
The fundamental concept is to use both satellite imagery and
LiDAR data to train a model to discern the relationships
between contextual information (such as texture, color, and
shading) and elevation to estimate a Digital Surface Model
(DSM) [27]. We use the same architecture presented in III-B1,
modified to perform regression tasks. Therefore, the final layer
of the decoder is activated by a linear activation function, and
we use the mean squared error as a loss function. The deep
learning model is shown in Figure 3. The upper branch is
used for binary segmentation, and the lower branch is used
for height regression.

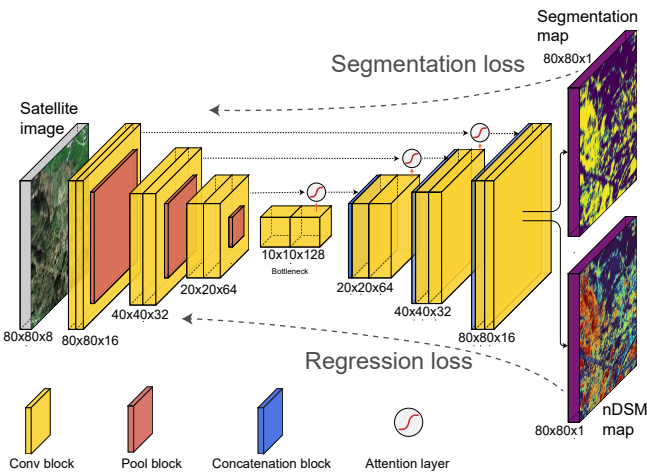


Fig. 3: Deep learning model architecture used to segment vegetation from a satellite image (upper branch) and estimate height (lower branch). Convolutional block (orange), pooling layers (red), up-sampling layers (blue), and classifier (purple).

3) *Tree species classification block*: In this block, we carry out a tree species multi-class segmentation task. Similarly to the segmentation block in III-B1, we take an input image and generate a pixel-wise mask denoted as $\hat{\mathcal{M}}_{tree}^{species}$. Each pixel in this mask contains the probability of belonging to one of the primary tree species categories, which, as outlined in Section II, include spruces, pines, and deciduous trees.

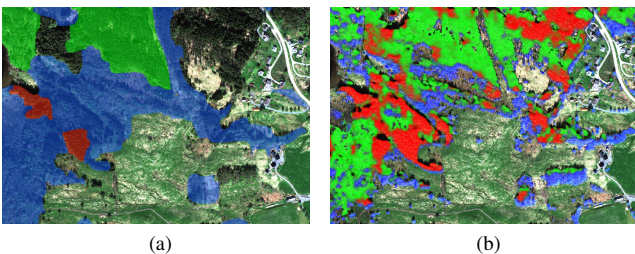


Fig. 4: (a): Typical tree species reference datasets may have certain limitations, such as incomplete coverage where some tree species are not included and imprecise demarcations where the boundaries between different regions or stands are not clearly defined. (b): Refined tree species mask using our approach. Legend: spruces (red), pines (green), deciduous (blue).

In a recent work presented in [28], we introduced an innovative approach that enables the model to identify different tree species at a level of detail close to the individual tree. This approach is designed to handle the inherent noise and low-resolution issues in the tree species dataset, greatly enhancing the quality of the available forest inventories (Figure. 4). We encourage interested readers to refer to the corresponding published paper for more in-depth information on this methodology.

4) *Tree crown delineation block*: The segmentation model presented in III-B1, produces a binary mask $\hat{\mathcal{M}}_{tree}$, that differentiates areas with and without trees. This mask indicates the presence of trees but does not specify individual tree locations or counts.

To address this, we integrate the tree crown delineation approach outlined in [29] with our binary tree mask $\hat{\mathcal{M}}_{tree}$ to enhance its robustness in areas that may contain both trees and non-tree elements. A step-by-step graphical representation of the crown extraction is shown in Figure 5.

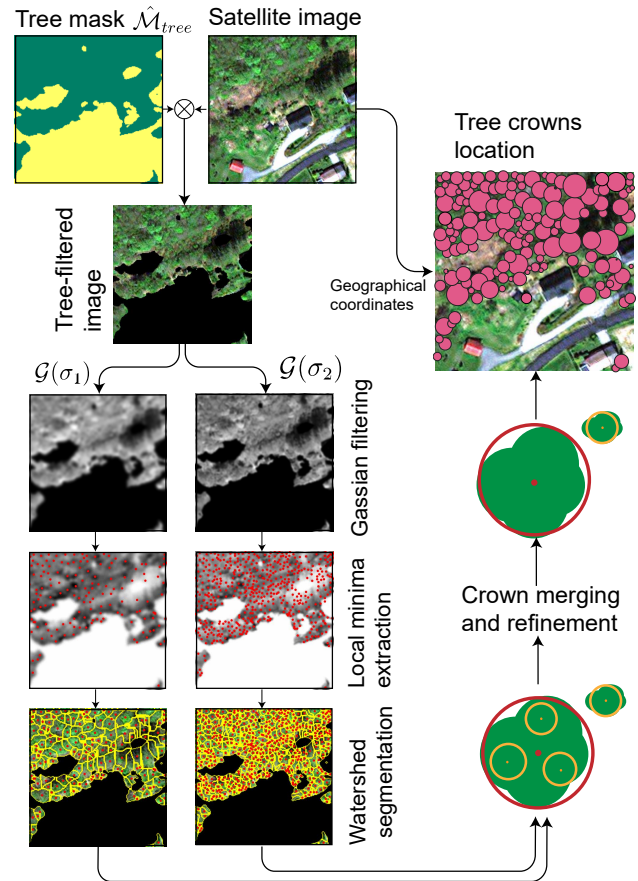


Fig. 5: A step-by-step graphical representation of the crown extraction.

The input satellite image is multiplied by the tree mask $\hat{\mathcal{M}}_{tree}$ to extract the tree areas. The resulting image is converted to grayscale and smoothed using two 2D Gaussian filters \mathcal{G} with standard deviation, σ_1 and σ_2 . When such a Gaussian filter is applied to the image, tree crowns with a similar shape and size to the filter are enhanced, and smaller objects are suppressed. The strength of each Gaussian filter σ is set to $0.3d$, as explained in [29], with $d = 1, 2$ meters, which is the typical size of tree crowns in the area. The smoothed image is inverted, and local minima in the image are identified, which serve as markers for watershed segmentation [30]. Each segmented region is converted into a circle, encompassing the same area. The tree crowns extracted at each scale are then merged together. This integration removes smaller crowns located within or having significant overlap (more than 80%) with larger crowns. Additionally, any tree crown with a center close to another tree crown (less than two meters) is removed. The geographical information associated with the input satellite image is utilized to project the extracted tree crowns into a real-world coordinate system to complete the process. This step ensures that the delineated tree crowns are

1 accurately positioned within the geographical context of the
2 area covered by the image.

3 5) *Tree inventory*: After extracting the tree crowns, the
4 position of each tree, specifically the centroid of each crown,
5 becomes readily available. Leveraging the information obtained
6 from $\mathcal{M}_{tree}^{nDSM}$ for tree height and $\mathcal{M}_{tree}^{species}$ for tree
7 species, we can integrate such information into each identified
8 tree. This process enables the creation of a tree inventory fully
9 derived from satellite remote sensing techniques, where each tree
10 entry encompasses information about its geographical
11 position on the map, tree height, crown size, and species.

12 a) *DBH estimation*: The diameter at breast height (DBH)
13 is a standard measurement for tree trunk diameter at about 1.3
14 meters high. It is crucial for assessing a tree's susceptibility
15 to wind but can't be directly measured from satellite images.
16 Instead, allometric equations are used to correlate DBH with
17 measurable parameters like tree height and generally expressed
18 as $H = (\frac{DBH}{b_1 + b_2 DBH})^3 + c$, with b_1, b_2, c species-specific
19 coefficient. However, these equations can vary by geographic
20 region and tree species. In Norway, specific non-linear height-
21 DBH models have been developed for major tree species [31].
22 Notably, these allometric functions are invertible, allowing
23 DBH estimation from tree height data in the inventory.

24 b) *Shielding effect*: Evaluating a tree's vulnerability to
25 wind involves considering the shielding effect of nearby trees.
26 For each tree within the designated corridor, the surrounding
27 360-degree space is divided into eight sectors aligning with the
28 main wind directions (e.g., North, North-East, East, etc.). For
29 each direction, the presence of surrounding trees is assessed.
30 A shielding factor is assigned based on these observations: 1
31 if there are at least two trees in that sector, or 0.2 if fewer.
32 These values are based on research suggesting that multiple
33 trees significantly reduce the wind's bending force on a tree
34 by a factor of approximately 5 [32]. The presence of multiple
35 nearby trees can significantly reduce the wind-induced bending
36 moment. To accurately calculate the shield factor for all trees,
37 even those on the corridor's edge, trees in an extended area
38 beyond the corridor need to be detected. Figure 6 graphically
39 shows the shielding factor calculation.

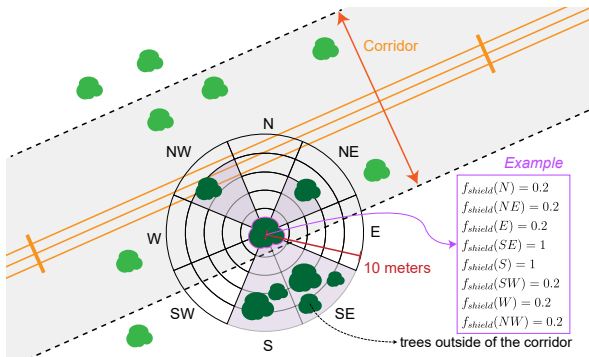


Fig. 6: Tree Shielding Factor Calculation: For each tree within the corridor, the 360-degree space is divided into eight sectors representing the main wind directions. Surrounding trees within a 10-meter radius are considered for each sector. A shield factor of 1 is assigned if there are more than two trees within the sector and a factor of 0.2 if not.

C. Risk Assessment

A tree inventory has been generated at this stage, as described in Section III-B. Each tree within this inventory is characterized by the following properties: position, crown radius, species, height, diameter at breast height (DBH), and shield factor. This information serves as the foundation for generating two distinct types of risk assessments: static risk and dynamic risk.

1) *Static risk*: The static risk assessment considers the positions and heights of the trees relative to the power lines. A trigonometric collision calculation is used to evaluate whether a tree has the potential to fall onto or disrupt the power line. Specifically, denoting with d the distance of a tree from the power line, h the power line height, and with H the tree height, we mark a tree as potentially dangerous if $H + \Delta \geq \sqrt{d^2 + h^2}$ (see Figure 7). A safety margin Δ is introduced to accommodate inaccuracies from the height estimation model and consider the bending catenary curvature of power lines wires.

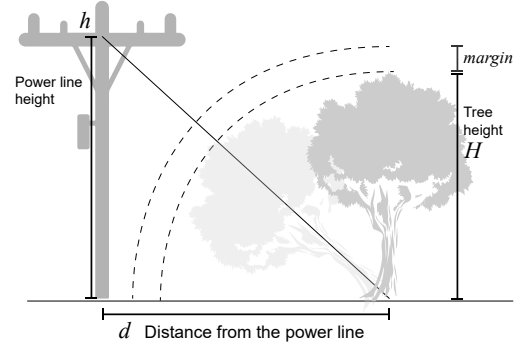


Fig. 7: A trigonometric collision calculation is performed to determine whether a tree has the potential to fall onto the power line. This calculation considers the tree's distance from the power line d , the height of the tree H , the height of the power line h , and a safety margin. Trees that can potentially collide with the overhead lines are flagged as potentially dangerous in the risk assessment.

The outcome of this static risk assessment is a risk map, which highlights trees encroaching too closely into the right-of-way. This map helps identify areas of concern where vegetation management actions may be needed to mitigate potential risks to the power lines or to investigate further.

2) *Dynamic risk map*: In the dynamic risk assessment, weather data is also considered, and the focus shifts to how trees can withstand wind and extreme weather conditions. This assessment aims to evaluate the resilience of trees to wind-induced forces during adverse weather events. The dynamic risk assessment involves the utilization of various parameters and models, as described in previous sections, to estimate each tree's ability to withstand wind. It incorporates factors like tree height, species, diameter at breast height (DBH), shield factor, and local wind conditions.

The study conducted by [33] demonstrated that, across a range of stand and soil conditions and for different tree species, there exists a conservative relationship between the maximum turning moment M_{max} and the square of the hourly wind speed at the top of the tree canopy ω^2 . Specifically, for well-acclimated trees the authors found that $M_{max} = \omega^2 \cdot T_c$, where

1 T_c is a turning moment coefficient. This coefficient depends
 2 on tree's physical properties and, as a first approximation,
 3 results in $T_c = 117.3 \cdot DBH^2 \cdot h$, where DBH is the
 4 diameter at breast height, and h is the tree height. The critical
 5 bending moment at which stem breakage occurs was defined
 6 by [34] as: $M_{crit} = \frac{\pi}{32} \cdot MoR \cdot DBH^3$ where MoR, or
 7 Modulus of Rupture, is a material property, measured in
 8 Pascal, used to describe the stress within a material just before
 9 it yields or fractures in a flexure test. Importantly, the MoR can
 10 vary among different tree species because the specific wood
 11 properties of each species influence it. The modulus of rupture
 12 per each wood can be found in wood property databases such
 13 as [35]. Finally, combining the previous equations, the critical
 14 wind speed for breakage for a particular wind direction is
 15 derived as:

$$\omega_{kr}^{breakage}(dir) = \sqrt{\frac{MoR \cdot DBH^3 \cdot f_{shield}(dir) \cdot \pi}{32 \cdot T_c \cdot f_{CW}}} \quad (1)$$

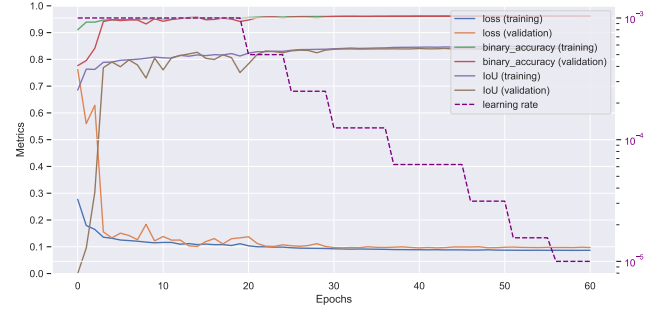
16 where f_{CW} is the additional moment multiplier provided by
 17 the overhanging displaced mass of the canopy, set to 1.25, and
 18 dir is the wind direction used as input data. A comprehensive
 19 explanation of the calculations and the underlying details
 20 can be found at [36]. To account for the fact that trees can
 21 be shielded from both the trees behind and in front of the
 22 oncoming wind, the parameter $f_{shield}(dir)$ is calculated as the
 23 mean of f_{shield} in the direction of the wind and the opposite
 24 direction of the wind. f_{shield} acts as a multiplier, modifying
 25 the critical breakage speed when trees are isolated

26 The critical wind speed for breakage is individually calcu-
 27 lated for each tree within the power line's corridor using
 28 Equation (1), considering the wind direction (dir) provided
 29 as input. Each tree's critical wind speed $\omega_{kr}^{breakage}(dir)$ is
 30 compared to actual wind gust speeds $\omega(dir)$. If $\omega(dir) \geq$
 31 $\omega_{kr}^{breakage}(dir)$, the tree is expected to break due to wind.
 32 Additionally, a collision calculation determines if a wind-
 33 damaged tree could collide with power lines. This method
 34 combines assessments of wind vulnerability and collision
 35 potential, offering a comprehensive dynamic risk evaluation
 36 for each tree in relation to wind conditions and their impact
 37 on power lines.

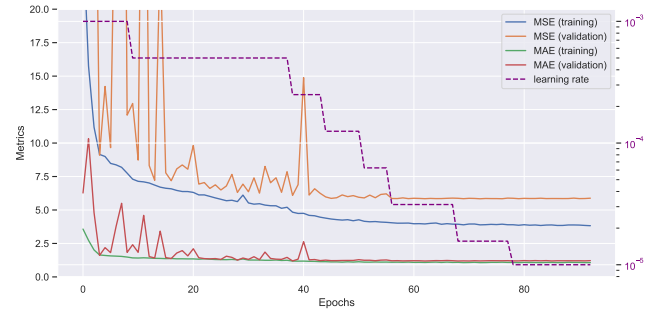
38 IV. RESULTS

39 The framework was developed in Python, with the deep
 40 learning modules implemented using the TensorFlow library.
 41 Geographical visualization of the data was performed using
 42 QGIS. For the development of the machine learning models,
 43 the study area is divided into two non-overlapping parts, each
 44 with a similar distribution of land use, including forests, fields,
 45 water basins, and more. The training part of the study area
 46 encompassed 10 square kilometers, while the testing part
 47 covered 4.7 square kilometers. Within the training part, a
 48 dataset is created by randomly extracting 20,000 patches, each
 49 measuring 80x80 pixels (equivalent to 40x40 meters given the
 50 image resolution). This dataset is split into 75% for the actual
 51 training and 25% for validation. During the training process,
 52 the model is trained with the training patches and fine-tuned

for each batch using the validation patches. To prevent over-
 fitting, an early stopping callback monitored the validation
 loss, and a learning rate adjustment callback is implemented
 to reduce the learning rate when the loss function reached a
 plateau. The Adam optimizer is used with an initial learning
 rate of 10^{-3} . Figure 8a displays the training history plot for
 the tree segmentation, while Figure 8b presents the training
 history plot for the height estimation.



(a)



(b)

Fig. 8: (a) Segmentation training history. The model stabilizes approximately after 25 epochs, reaching an accuracy of 0.96 and an Intersection over Union of 0.84. (b) Height estimation training history. The model stabilizes approximately after 40 epochs, reaching a Mean Absolute Error of 1.21 meters.

Once the trained models are applied to the testing area, they generate a tree segmentation map, a normalized Digital Surface Model (nDSM) map, and a tree species map. It's important to note that the model has not been exposed to the testing area during training. Because the testing image is too big to fit into the model, it is divided into overlapping 80×80 tiles. Predictions are made on each tile, and the resulting predicted tiles are then smoothly combined to reconstruct the entire area [37].

The evaluation metrics for the tree segmentation map in the testing area are shown in Table I. Each task is evaluated using specific metrics such as F1-score, Intersection over Union (IoU), ROC-Area under Curve (ROC-AUC), Mean Absolute Error (MAE), and Coefficient of Determination (R^2), depending on the specific task (binary classification, multi-class classification and regression).

These metrics indicate the accuracy and effectiveness of the model in segmenting trees in a previously unseen region. The evaluation metrics for height estimation in the testing area show a Mean Absolute Error (MAE) of 2.10 and an R-squared

TABLE I: PERFORMANCE METRICS FOR THE TREE SEGMENTATION, TREE SPECIES CLASSIFICATION AND HEIGHT ESTIMATION TASKS OVER THE TESTING AREA.

Model	Tree segmentation			Tree species classification			Tree height estimation	
Test metrics	F1-score	AoU	ROC-AUC	F1-score spruces:	F1-score: pines	F1-score: deciduous	MAE	R^2
Performance	0.88	0.80	0.92	0.88	0.65	0.76	2.10	0.74

(R^2) value of 0.74. The MAE indicates that 2.10 meters is the average absolute difference between the predicted heights and the actual heights of the trees. The R-squared value of 0.74 measures the goodness of fit of the model, with a value closer to 1 indicating a better fit. In this case, an R^2 value of 0.74 suggests that the model explains a significant portion of the variance in tree heights. For the tree species model, an accurate analysis of the results is presented in [28].

Figure 9 shows visually the output of the three models, namely the tree segmentation map $\hat{\mathcal{M}}_{tree}$, the estimated nDSM $\hat{\mathcal{M}}_{tree}^{nDSM}$ and the tree species map $\hat{\mathcal{M}}_{tree}^{species}$.

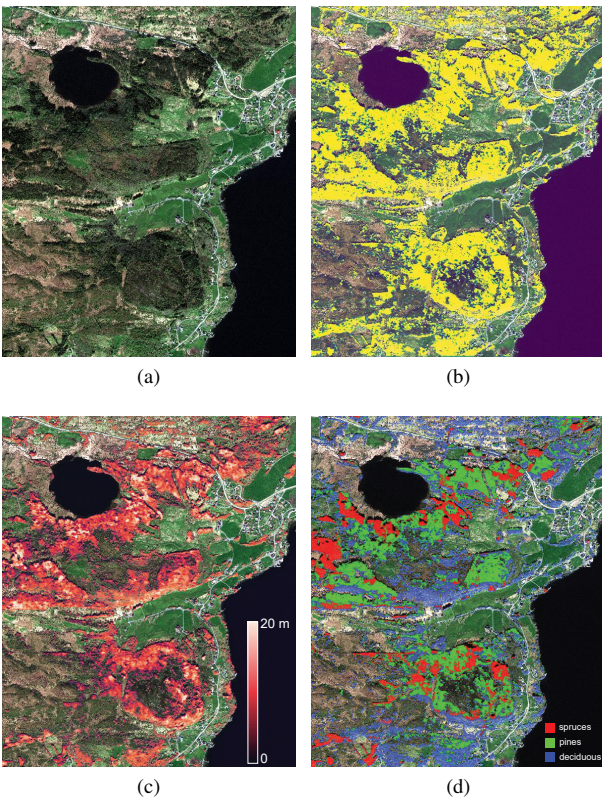


Fig. 9: Testing area. (a) satellite image, (b) tree segmentation map, (c) nDSM estimation map, and (d) tree species map.

The tree crowns are extracted along the power line's corridor, and the tree inventory is generated using the information of height derived by $\hat{\mathcal{M}}_{tree}^{nDSM}$, the tree species from $\hat{\mathcal{M}}_{tree}^{species}$, as well as the estimated DBH from the available allometric equation and the shielding effect, as described in III-B (Figure 11b).

From the generated tree inventory, the static risk map and dynamic risk map are calculated according to III-C1 and III-C2. In the study area, the heights of the 22kV overhead lines have an average height of 10.8 meters, as reported by [38]. Considering the estimated height error in the model, a

safety margin of 2 meters is added. The collision simulation is used to identify trees that have the potential to fall onto the power line. For the dynamic risk map, we compute statistics for the historical weather data in the region over the last four years. Results are shown in Figure 10.

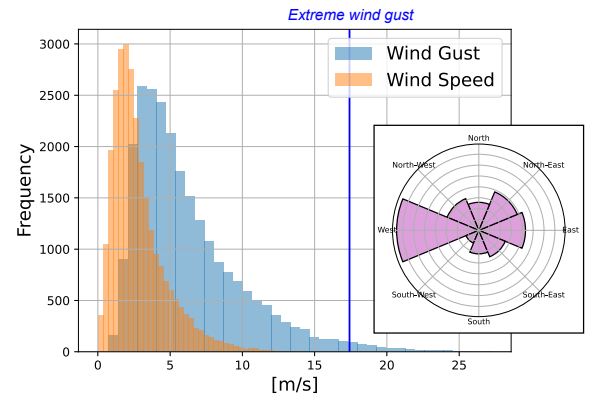


Fig. 10: Histogram of the historical data over the last four years (wind speed, gust, and direction) for the study area. We define an extreme weather event based on a wind gust threshold set at three times the standard deviation of the wind speed distribution (blue vertical line).

The analysis indicates that the most common wind direction in the region is from East to West. Typical wind speeds range from 0 to 5 meters per second, with occasional peaks reaching up to 10 meters per second. However, there are instances of wind gusts reaching speeds of up to 25 meters per second. To define an extreme weather event, a wind gust threshold is set at three times the standard deviation of the wind speed distribution, which corresponds to 17.4 meters per second in this case. This threshold aligns with the Beaufort scale [39], an empirical measure that associates wind speed with observed conditions at sea or on land. Wind speeds of 17.4 m/s fall within Category 8 on the Beaufort scale, where trees are known to begin breaking. Therefore, we simulate the dynamic risk map using a wind gust speed of 17.4 meters per second and from East to West as wind direction. Figures 11c and 11d show an example of the static and dynamic risk map for a portion of the grid, respectively.

In the static risk map, trees are flagged whether they can disrupt the power line due to their proximity and height to the overhead wires. In the dynamic risk map, the analysis compares the critical wind speed for breakage for every tree with the wind gust speed. A collision assessment is performed if a tree is found to be vulnerable to the wind. Trees are flagged on the dynamic risk map if they are susceptible to falling against the prevailing wind and potentially hitting the power line. This map considers the proximity of trees to the power line and their vulnerability during extreme weather conditions. The dynamic risk map provides a two-fold advantage: it can utilize historical or synthetic weather data and conduct

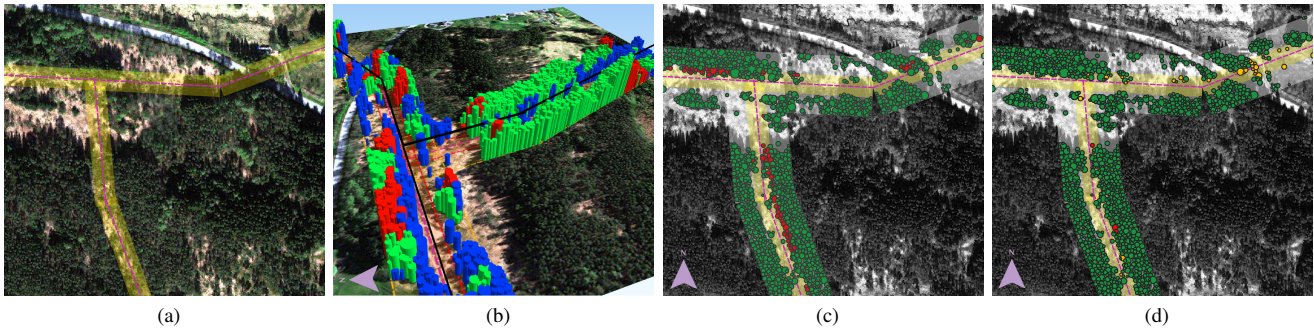


Fig. 11: (a): Satellite image for a portion of the power line. (b) The tree inventory is created by combining information from the binary tree segmentation map (\mathcal{M}_{tree}), the extracted crowns, the estimated height map ($\mathcal{M}_{tree}^{nDSM}$), and the tree species map ($\mathcal{M}_{tree}^{species}$), along the power line corridor. Each tree is visualized as a cylinder with height derived from $\mathcal{M}_{tree}^{nDSM}$ and color-coded by the species derived by $\mathcal{M}_{tree}^{species}$ (red: spruce, green: pine, blue: deciduous). (c-d): Example of the risk map along the power line corridor. The purple dashed line is the power line. The power line is denoted by the purple dashed line, with a 10-meter corridor on each side marked in yellow and a 30-meter corridor on each side in white. While the risk assessment maps are specifically computed for trees within the small corridor, it's essential to detect trees in the larger corridor as well to account for the shielding effect, as explained in section III-C2. (b) Static risk map: trees color-coded in red have the potential to hit the power line due to their proximity or height. (c) Dynamic risk map: trees color-coded in orange are exposed to incoming wind (in this case, from East to West) and can fall. However, they cannot collide with the power lines if they fall. Trees color-coded in red are exposed to incoming wind and can fall. Additionally, they can collide with the power lines. Visualizations made in QGIS.

1 simulations using weather forecast data to predict potential
 2 tree collisions with power lines. This approach enhances
 3 the ability to anticipate and mitigate risks associated with
 4 extreme weather events and their potential impact on power
 5 line vegetation management.

6 V. PRACTICAL CONSIDERATIONS FOR SATELLITE-BASED 7 VEGETATION MANAGEMENT IN ELECTRIC POWER 8 COMPANIES

9 This study, conducted from 2019 to 2023 under the
 10 GridEyeS project [40], represents a collaborative effort with a
 11 Norwegian electric company, two international weather intelli-
 12 gence and asset management companies, and Western Norway
 13 University. The Electric company's asset management and
 14 vegetation management teams provided continuous feedback,
 15 while the two service companies offered partial insights and
 16 guidelines for the development, implementation, and valida-
 17 tion of the proposed ASPIRE-V framework. The GridEyeS
 18 project, funded by the European Space Agency, has influenced
 19 the utilization of satellite imagery for power line surveillance,
 20 as evidenced by its contribution to the 2023 European Space
 21 Agency (ESA) market report [41].

22 A. Cost Effectiveness

23 In Europe and the US, vegetation management constitutes
 24 approximately 35% of total operational expenditures for utili-
 25 ties, amounting to a cost ranging from 100 to 1500 Euros per
 26 kilometer of power line per year, contingent on technological
 27 factors, geographic location, and the extent of the grid terri-
 28 tory [42], [43]. Comparative analysis indicates that satellite
 29 imagery for a specific region is up to 60% more cost-effective
 30 than helicopter and drone images [44]. Commercial high-
 31 resolution optical satellite images, priced between 7 and 40
 32 Euros per square kilometer, supplement the cost-effectiveness
 33 of free low-resolution satellite images, such as those from the
 34 Sentinel-2 constellation under the Copernicus program by the

European Space Agency. A study conducted by the Norwegian
 1 Transmission System Operator (TSO), Statnett, affirms that
 2 satellite imagery significantly reduces the cost of power line
 3 monitoring per kilometer of line per year [45].

4 The market for satellite imagery applications is projected
 5 to experience substantial growth until 2030, according to
 6 a recent study by the European Space Agency [41]. This
 7 expansion, coupled with anticipated advancements in reduced
 8 costs and enhanced image quality, underscores the increasing
 9 attractiveness of high-resolution satellite monitoring as a
 10 viable solution for vegetation management in power distribu-
 11 tion and transmission companies, particularly when integrated
 12 with traditional power line monitoring approaches.

14 B. Situational Awareness Enhancement

15 The elevated cost of power line vegetation monitoring and
 16 the expansive service territories necessitate utilities to conduct
 17 periodic assessments of their entire service area, spanning from
 18 two to ten years [46]. Satellite-based monitoring addresses
 19 this challenge by providing frequent revisits to a given area.
 20 Commercial satellites from various constellations offer multi-
 21 ple high-resolution images (25-50 cm) per day for any location
 22 globally [47], [48]. The broad perspective afforded by satellite
 23 imagery facilitates a comprehensive understanding of power
 24 lines' right-of-way (ROW), encompassing factors such as land
 25 cover, elevation, and the condition of objects and vegetation,
 26 within a condensed timeframe.

27 C. Enhancing Decision Support for Vegetation Management 28 Teams

29 Figure 12 illustrates a sample vegetation risk map for
 30 power lines generated by the proposed ASPIRE-V. This map,
 31 highlighting trees near power lines with color-coded risk
 32 indicators, can be seamlessly integrated into legacy notification
 33 dashboards for utilities. This integration enables a focused
 34

1 approach to high-risk zones, optimizing inspection costs and
 2 efforts. The utilization of risk maps holds the potential to
 3 significantly reduce overall ROW inspection time and cost,
 4 offering more updated situational awareness.

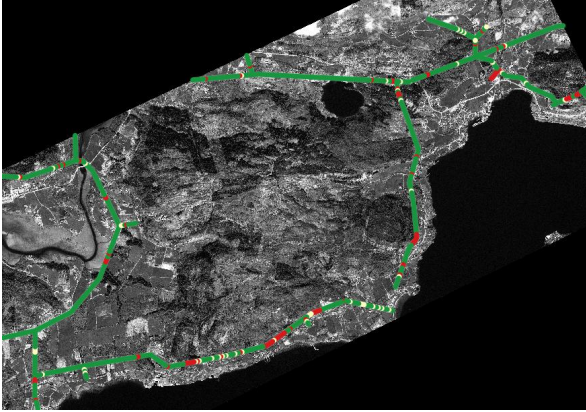


Fig. 12: Points are extracted along the power lines, and trees within 10 meters that could potentially fall onto the power lines are counted. The color-coding system is as follows: green is used if there are no trees posing a collision risk to the power line, yellow is employed if there are between one and three trees, and red is indicated if there are more than three trees.

5 D. Challenges of Using Satellite Images

6 Despite the advantages of satellite-based monitoring, certain
 7 limitations merit consideration. Establishing a 3D vegetation
 8 model and estimating vegetation risk for power lines involves
 9 complex tasks dependent on various parameters with varying
 10 degrees of stochasticity in vegetation and weather behavior.

11 Modern satellite imagery, while of high quality, has a
 12 maximum resolution of 15 cm based on current technology
 13 in the market [49]. This limitation may impede the detection
 14 of vegetation health conditions. Achieving enhanced perfor-
 15 mance in tree health assessment may necessitate additional
 16 in-situ data or synchronizing image acquisition timing with
 17 the phenological cycle of the relevant species [28].

18 Furthermore, estimating tree height from satellite images
 19 poses a challenge due to the absence of direct height infor-
 20 mation. Similar to other studies in the literature, our model
 21 is trained to establish a relationship between optical images
 22 and tree height using LiDAR data. It is important to note
 23 that model retraining may be required when deploying the
 24 framework in a different geographical area with significant
 25 changes in vegetation coverage and type.

26 The tree characterization presented in this work relies on a
 27 combination of mechanistic models and information obtained
 28 from remote sensing technologies. While the framework pro-
 29 vides valuable insights and risk assessments, predicting the
 30 future behavior of trees in response to weather conditions
 31 remains inherently challenging due to the stochastic nature
 32 of weather data and the variability in tree properties.

33 Notwithstanding the inherent uncertainties, our tree detec-
 34 tion and characterization methods have demonstrated effec-
 35 tiveness. The proposed risk maps serve as valuable tools
 36 for electric utilities, enhancing their awareness of vegetation
 37 near power lines. However, these maps are not universally

applicable, and utilities may adapt the risk assessment param-
 2 eters based on their on-field requirements, regulations, and
 3 expertise.

4 VI. CONCLUSIONS

5 This paper introduces an innovative framework for moni-
 6 toring trees along power lines using high-resolution satellite
 7 imagery. The framework leverages computer vision techniques
 8 to detect and characterize trees. It has been deployed in
 9 an existing power network in Norway and validated against
 10 LiDAR data and national databases, demonstrating high per-
 11 formance in assessing tree status. A collision simulation is then
 12 performed to identify trees along the corridor that can hit and
 13 disrupt the power lines. Additionally, tree mechanistic models
 14 are employed to assess each tree's resilience against incoming
 15 winds. By incorporating wind data, the framework can simu-
 16 late which trees are more susceptible to falling due to wind
 17 and colliding with the power lines. This comprehensive approach
 18 has the potential to significantly assist operators of power-line
 19 infrastructure in vegetation asset management transmission
 20 and distribution companies, providing an additional decision-
 21 making tool, ultimately improving the reliability and safety of
 22 the power supply.

23 VII. ACKNOWLEDGMENTS

24 This work is funded partly by the European Space Agency
 25 (ESA) under the GridEyeS project [40]. We thank StormGeo
 26 and Linja companies for providing feedback and insights into
 27 the work done. We intend to make the code openly accessible
 28 on GitHub ([50]) following the publication, to foster its
 29 adoption, further enhancement, and development by the wider
 30 community.

31 REFERENCES

- 32 [1] Howard Gugel, Svetlana Ekisheva, Mark Lauby, and Farzaneh Tafreshi.
 33 Vegetation-related outages on transmission lines in north america. In
 34 *2018 IEEE Power and Energy Society General Meeting (PESGM)*, 2018.
- 35 [2] Statnett Norway. Årsrapporter fra Feilanalyse. <https://www.statnett.no/for-aktorer-i-kraftbransjen/systemansvaret/arsrapporter-fra-feilanalyse/>.
- 36 [3] BBC News. PG&E to stand trial over deadly California wildfire . <https://www.bbc.com/news/world-us-canada-64505596>, 2020.
- 37 [4] Leena Matikainen, M. Lehtomäki, E. Ahokas, J. Hyypä, M. Karjalainen, A. Jaakkola, A. Kukko, and T. Heinonen. Remote sensing
 38 methods for power line corridor surveys. *Isprs Journal of Photogram-*
 39 *metry and Remote Sensing*, 119:10–31, 2016.
- 40 [5] Forestry Commission and Forest Research. ForestGALES. <https://www.forestryresearch.gov.uk/tools-and-resources/fthr/forestgales/>.
- 41 [6] D. Gullick, G.A. Blackburn, J.D. Whyatt, P. Vopenka, J. Murray, and
 42 J. Abbatt. Tree risk evaluation environment for failure and limb loss
 43 (treefall): An integrated model for quantifying the risk of tree failure
 44 from local to regional scales. *Computers, Environment and Urban*
 45 *Systems*, 75:217–228, 2019.
- 46 [7] Michele Gazzea, Alican Karaer, Mahyar Ghorbanzadeh, Nozhan Bal-
 47 afkan, Tarek Abichou, Eren Erman Ozguven, and Reza Arghandeh.
 48 Automated satellite-based assessment of hurricane impacts on roadways.
 49 *IEEE Transactions on Industrial Informatics*, 18(3):2110–2119, 2022.
- 50 [8] Michele Gazzea, Alican Karaer, Mahyar Ghorbanzadeh, Eren Erman
 51 Ozguven, and Reza Arghandeh. Roadway vulnerability assessment
 52 against hurricanes using satellite images. *Transportation Research*
 53 *Record*, 2677(3):1453–1464, 2023.
- 54 [9] Michele Gazzea, Amir Miraki, Onur Alisan, Monique M. Kuglitsch,
 55 Ivanka Pelivan, Eren Erman Ozguven, and Reza Arghandeh. Traffic
 56 monitoring system design considering multi-hazard disaster risks. *Sci-*
 57 *entific Reports*, 13:2045–2322, 2023.

- [10] Bireda Alemayehu, Juan Suarez-Minguez, Jacqueline Rosette, and Saeed A. Khan. Vegetation trend detection using time series satellite data as ecosystem condition indicators for analysis in the northwestern highlands of ethiopia. *Remote Sensing*, 15(20):5032, October 2023.
- [11] Takuro Furusawa, Takuya Koera, Rikson Siburian, Agung Wicaksono, Kazunari Matsudaira, and Yoshinori Ishioka. Time-series analysis of satellite imagery for detecting vegetation cover changes in indonesia. *Scientific Reports*, 13:8437, 2023.
- [12] Kidiyo Kpalma, Miloud Chikr El Mezouar, and Nasreddine Taleb. Recent trends in satellite image pan- sharpening techniques. 1st International Conference on Electrical, Electronic and Computing Engineering, pages 1–10, Vrnica Banja, Serbia, 2014.
- [13] Kartverket. Nasjonal detaljert høydemodell . <https://hoydedata.no/LaserInnsyn2/>, 2023.
- [14] Norwegian Institute of Bioeconomy Research (NIBIO). https://kilden.nibio.no/?lang=nb&topic=arealinformasjon&X=7195706.12&Y=284337.75&zoom=0.050089679614182224&bgLayer=graatone_cache. Online.
- [15] Rasmus Astrup, Johannes Rahlf, Knut Bjørkelo, Misganu Debella-Gilo, A. K. Gjertsen, and Johannes Breidenbach. Forest information at multiple scales: development, evaluation and application of the norwegian forest resources map sr16. *Scandinavian Journal of Forest Research*, 34:484 – 496, 2019.
- [16] European Weather Centre. Meteorological Model (MEPS). <https://data.europa.eu/data/datasets/d7568ec4-d9e0-4f8f-bf01-e9f672a79198?locale=en>.
- [17] John Wilson Rouse, Robert H. Haas, John A. Schell, and D. W. Deering. Monitoring vegetation systems in the great plains with erts. 1973.
- [18] Hongcheng Zeng, Heli Peltola, Ari Talkkari, Ari Venäläinen, Harri Strandman, Seppo Kellomäki, and Kaiyun Wang. Influence of clear-cutting on the risk of wind damage at forest edges. *Forest Ecology and Management*, 203(1):77–88, 2004.
- [19] O. Ronneberger, P. Fischer, and T. Brox. U-net: Convolutional networks for biomedical image segmentation. *ArXiv*, abs/1505.04597, 2015.
- [20] Jo Schlemper, Ozan Oktay, Michiel Schaap, Mattias Heinrich, Bernhard Kainz, Ben Glocker, and Daniel Rueckert. Attention gated networks: Learning to leverage salient regions in medical images. *Medical Image Analysis*, 53:197–207, 2019.
- [21] Chao-Jung Liu, Vladimir A. Krylov, Paul Kane, Geraldine Kavanagh, and Rozenn Dahyot. Im2Elevation: Building height estimation from single-view aerial imagery. *Remote Sensing*, 12(17):2719, Aug 2020.
- [22] C. Xiao, R. Qin, X. Huang, and J. Li. Individual tree detection from multi-view satellite images. In *IGARSS 2018 - 2018 IEEE International Geoscience and Remote Sensing Symposium*, pages 3967–3970, 2018.
- [23] H. Raggam. Surface mapping using image triplets: Case studies and benefit assessment in comparison to stereo image processing. *Photogrammetric Engineering and Remote Sensing*, 72:551–563, 2006.
- [24] Henrik Persson, Håkan Olsson, M.J. Soja, L.M.H. Ulander, and Johan Fransson. Experiences from large-scale forest mapping of sweden using tandem-x data. *Remote Sensing*, 9:1253, 12 2017.
- [25] A. Corte, F. E. Rex, D. Almeida, C. R. Sanquetta, C. A. Silva, Marks M. Moura, Ben Wilkinson, A. M. A. Zambrano, Ernandes M. da Cunha Neto, Hudson F. P. Veras, A. D. Moraes, Carine Klauberg, Midhun Mohan, A. Cardil, and E. N. Broadbent. Measuring individual tree diameter and height using gatereye high-density uav-lidar in an integrated crop-livestock-forest system. *Remote. Sens.*, 12:863, 2020.
- [26] Pedram Ghamisi and Naoto Yokoya. Img2dsm: Height simulation from single imagery using conditional generative adversarial net. *IEEE Geoscience and Remote Sensing Letters*, 15(5):794–798, 2018.
- [27] Michele Gazzea, Sindre Aalhus, Lars Michael Kristensen, Eren Erman Ozguven, and Reza Arghandeh. Automated 3d vegetation detection along power lines using monocular satellite imagery and deep learning. In *2021 IEEE International Geoscience and Remote Sensing Symposium IGARSS*, pages 3721–3724, 2021.
- [28] Michele Gazzea, Lars Michael Kristensen, Francesco Pirotti, Eren Erman Ozguven, and Reza Arghandeh. Tree species classification using high-resolution satellite imagery and weakly-supervised learning. *IEEE Transactions on Geoscience and Remote Sensing*, pages 1–1, 2022.
- [29] Linhai Jing, Baoxin Hu, Thomas Noland, and Jili Li. An individual tree crown delineation method based on multi-scale segmentation of imagery. *ISPRS Journal of Photogrammetry and Remote Sensing*, 70:88–98, 2012.
- [30] Jun Zhou, Yue Yin, and Shuai Wang. Image segmentation based on watershed algorithm. In *2021 International Conference on Intelligent Computing, Automation and Applications (ICAA)*, pages 10–13, 2021.
- [31] Ram P. Sharma and Johannes Breidenbach. Modeling height-diameter relationships for norway spruce, scots pine, and downy birch using norwegian national forest inventory data. *Forest Science and Technology*, 11(1):44–53, 2015.
- [32] Kenneth Earl Byrne. *Mechanistic modelling of windthrow in spatially complex mixed species stands in British Columbia*. PhD thesis, University of British Columbia, 2011.
- [33] Sophie E. Hale, Barry A. Gardiner, Axel Wellpott, Bruce C. Nicoll, and Alexis Achim. Wind loading of trees: influence of tree size and competition. *European Journal of Forest Research*, 131:203–217, 2012.
- [34] Barry Gardiner, Heli Peltola, and Seppo Kellomäki. Comparison of two models for predicting the critical wind speeds required to damage coniferous trees. *Ecological Modelling*, 129(1):1–23, 2000.
- [35] Eric Meier. The Wood Database. <https://www.wood-database.com/>.
- [36] Rupert Seidl, Werner Rammer, and Kristina Blennow. Simulating wind disturbance impacts on forest landscapes: Tree-level heterogeneity matters. *Environmental Modelling & Software*, 51:1–11, 2014.
- [37] Bohao Huang, Daniel Reichman, Leslie M. Collins, Kyle Bradbury, and Jordan M. Malof. Tiling and stitching segmentation output for remote sensing: Basic challenges and recommendations. *arXiv: Computer Vision and Pattern Recognition*, 2018.
- [38] <https://www.lysenett.no/byggeoggrave/og-arbeide-nar/trefelling-og-beskjaring/>.
- [39] Dilip K. Barua. *Beaufort Wind Scale*, pages 315–317. Springer International Publishing, Cham, 2019.
- [40] European Space Agency (ESA). Grideyes project. <https://business.esa.int/projects/grideyes>.
- [41] European Space Agency (ESA). Transmission and distribution of electrical power - market trends. <https://commercialisation.esa.int/2023/08/transmission-and-distribution-of-electrical-power/>.
- [42] Thomas Allen Short. *Electric Power Distribution Handbook*. CRC Press, 2014. Chapter 3. Overhead Line Performance.
- [43] Michele Gazzea, Michael Pacevicius, Dyrre Oliver Dammann, Alla Saponova, Torleif Markussen Lunde, and Reza Arghandeh. Automated power lines vegetation monitoring using high-resolution satellite imagery. *IEEE Transactions on Power Delivery*, 37(1):308–316, 2022.
- [44] Hans Ole Ørka and M. Hauglin. Use of remote sensing for mapping of non-native conifer species. <https://www.miljodirektoratet.no/globalassets/publikasjoner/m490/m490.pdf>, 2016. [Online].
- [45] Statnett. SAFES Project. <https://www.statnett.no/contentassets/525e71910628494db2e4c627eb00dddc/satellite-technologies-feasibility-study-for-power-lines.pdf>. Online.
- [46] B. Sacks. Ai improves resilience of vegetation management. <https://www.tdworld.com/vegetation-management/article/21131079/ai-improves-resilience-of-vegetation-management>. 2020-05-11.
- [47] A definitive guide to buying and using satellite imagery · up42. <https://up42.com/blog/a-definitive-guide-to-buying-and-using-satellite-imagery>.
- [48] Planet, imaging the entire earth, every day. <https://nbremer.github.io/planet-globe/>.
- [49] Introducing 15 cm HD: The Highest Clarity From Commercial Satellite. <https://blog.maxar.com/earth-intelligence/2020/introducing-15-cm-hd-the-highest-clarity-from-commercial-satellite-imagery/>.
- [50] Michele Gazzea. VIRASS (Vegetation and Infrastructures Risk Assessment through Satellite Scanning) . https://github.com/Ci2Lab/Michele_VIRASS, 2023.

AUTOMATED SATELLITE-BASED ASSESSMENT OF HURRICANE IMPACTS ON ROADWAYS

Gazzea M., Karaer A., Ghorbanzadeh M., Balafkan N., Abichou T., Ozguven E.E., and Arghandeh R.

in IEEE Transactions on Industrial Informatics, vol. 18, no. 3, pp. 2110-2119, 2022,
[doi:10.1109/TII.2021.3082906](https://doi.org/10.1109/TII.2021.3082906)

©2024 IEEE. Reprinted, with permission, from [68]

Automated Satellite-based Assessment of Hurricane Impacts on Roadways

Michele Gazzea , *Member, IEEE*, Alican Karaer , Mahyar Ghorbanzadeh , Nozhan Balafkan ,
Tarek Abichou, Eren Erman Ozguven  and Reza Arghandeh , *Senior Member, IEEE*

Abstract—During extreme weather events like hurricanes, trees can cause significant challenges for the local communities with roadway closures or power outages. Local responders must act quickly with information regarding the extent and severity of hurricane damage to better manage recovery procedures following natural disasters. This paper proposes an approach to automatically identify fallen trees on roadways using high-resolution satellite imagery before and after a hurricane. The approach detects fallen trees on roadways via a co-voting strategy of three different algorithms and tailored dissimilarity scores. The proposed method does not rely on the large manually labeled satellite image data, making it more practical than existing approaches. Our solution has been implemented and validated on an actual roadway closure dataset from Hurricane Michael in Tallahassee, Florida, in October 2018.

Index Terms—Remote Sensing, Satellite Imagery, Tree Debris Detection, Post-Hurricane Assessment, Deep-learning

I. INTRODUCTION

DAMAGE assessment is essential after catastrophic events like hurricanes, earthquakes, or tsunamis. Hurricanes, in particular, cause significant damages in the US, which is among the five countries most hit by natural disasters with an estimated cost of \$1.75 trillion for damages from 1980 to 2019 [1].

Aerial images are a valuable source of data for hurricane damage assessment [2]. However, flying helicopters and drones over damaged areas are highly prone to weather conditions. Moreover, their high operating costs are a burden on large-scale applications. In recent years, the dramatic drop in satellites' launching cost and the growing number of satellites in orbit significantly reduced the cost of high-resolution satellite imagery [3]. Commercial satellite providers can offer high-resolution images (0.3 to 0.5 pixels/meter) with a daily and sub-daily revisiting frequency for most parts of the globe.

The combination of coverage, frequency, and cost-efficiency of satellite imagery in addition to advancements in machine learning (ML) creates a paradigm shift for enhancing situational awareness in infrastructure networks [4], [5]. In

the recent literature, there are examples of using machine learning for assessing impacts of tsunamis [6], earthquakes [7], and floods [8] on infrastructure networks. In the event of hurricanes, fallen trees are one of the most common causes of damage to roadways, buildings, and electric lines. A major body of literature on hurricane-induced tree failures is focused on estimating tree failure probability concerning wind data ([9], [10]). Although such models are useful for better assessing fallen trees' consequences, few works have been done to automatically detect fallen trees using satellite images and machine learning.

Recently, supervised learning methods have been proposed to detect roadway closures using satellite images, typically by using Convolutional Neural Networks (CNNs) [11], [12], [13]. The major drawback of supervised models is that they rely highly on scant and expensive manually labeled data. It is also crucial to have clean and noise-free labels to train such models. Furthermore, supervised models, in general, are less scalable, and they need to be often retrained if we want to deploy them in another area, [14].

Unsupervised methods usually are more viable options in real-world remote sensing applications [15]. In unsupervised ML image processing approaches, features are extracted automatically for image segmentation or change analysis [16], [17]. Autoencoders (AEs) are one of the most efficient algorithms for images feature extraction. They represent data in a latent (usually smaller than the original) space preserving as much relevant information as possible.

In this paper, we focus on detecting fallen trees that cause roadway closures after hurricanes. We use high-resolution satellite images taken before and after a hurricane to perform change detection analysis and automatically locate areas where trees have landed on the roadways.

The main contributions of this paper are listed as follows:

- From the **application** point of view, our proposed approach needs limited labeled satellite images for trees in normal condition and it does not need any labeled data regarding fallen trees. In practice, our approach is unsupervised in relation to fallen trees. This increases the robustness of the approach against noisy or faulty labels, which are often acquired in satellite images and remote sensing applications. Our algorithm is also more scalable since it does not rely on an extensive training data set. Moreover, it has a lightweight open-loop architecture for fast computing time.
- From the **methodology** point of view, we propose a framework consisting of three different and powerful

M. Gazzea and R. Arghandeh are with the Department of Computer Science and Electrical Engineering at the Western Norway University of Applied Sciences, Bergen 5063, Norway. E-mail: (michele.gazzea@hvl.no, reza.arghandeh@hvl.no).

Alican Karaer, Mahyar Ghorbanzadeh, Tarek Abichou and Eren Erman Ozguven are with the Department of Civil & Environmental Engineering at the Florida State University, Tallahassee, Florida. E-mail: {akaraer, mghorbantzadeh, tabichou, eozen}@fsu.edu

Nozhan Balafkan is with StormGeo AS, Bergen, Norway. E-mail: nozhan.balafkan@stormgeo.com

algorithms, i.e. a segmentation model, a spectral vegetation index and Variational Autoencoders. We adapted and combined them to work together to overcome the shortage of each one of these methods to detect the fallen trees. This is done using tailored dissimilarity scores for changes in satellite images and a heuristic approach for thresholding.

II. STUDY AREA

Hurricane Michael was one of the strongest storms hitting the Southeast coast of the United States. It made landfall as an unprecedented Category 5 hurricane in the Florida Panhandle region with maximum sustained wind speeds of 140 knots (161 mph) bringing catastrophic storm surge to the Florida State and Big Bend areas (especially Mexico Beach and Panama City) [18]. It hit the City of Tallahassee between October 10th and 11th 2018, leaving 1.2 million electricity customers without power in several east coasts and southern states. Estimated damage from Michael throughout the United States reached \$25 billion [19]. Hurricane Michael hit the City of Tallahassee, Florida’s capital, on October 10th 2018. As a medium-sized city, Tallahassee has a population of 193,551 as of the year 2018 [20]. We acquired two high-resolution satellite images on a large portion of Tallahassee (Fig. 1) before and after Hurricane Michael. Images are provided by WorldView satellites, as described in Table I.

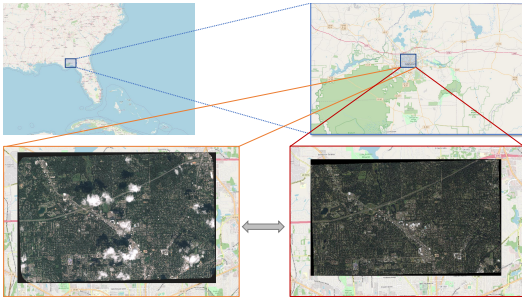


Fig. 1: Study area in Tallahassee (Florida) where satellite images before and after Hurricane Michael are acquired.

TABLE I: Satellite images used in this paper

	Date	Channels	Resolution
Pre-event image	September 14 2018	RGB-NIR	0.5m/pixel
Post-event image	October 13 2018	RGB-NIR	0.3m/pixel

For validation purposes, we use the dataset related to tree debris locations acquired from the contractual company hired by the City of Tallahassee to remove the debris.

III. METHODOLOGY

In this paper, our goal is to automatically detect fallen trees along roadways. Our method works with very limited training data and doesn’t need explicit training to recognize tree debris. To do so, our major assumption is that a fallen tree will exhibit a change that is possible to detect between satellite images from the same area taken before and after a hurricane. In literature, autoencoders have been used to extract and compare important features from images and perform change detection

[21]. The fundamental challenge with autoencoders is the lack of control over where the features are mapped and this is challenging in satellite images where feature vectors shall be compared. Therefore, we used Variational Convolutional Autoencoders (VAEs) [22] to overcome this issue. Relying solely on either autoencoders or variational autoencoders can be problematic due to the lack of semantic information about the changes. For example a passing vehicle or other environmental artifacts can be detected as changes but erroneously marked as tree debris. To solve the issue, we assume that a fallen tree should lead also to a change in the vegetation characteristics (coverage, chlorophyll index) in a particular location. Therefore we add semantic vegetation-related information. Given these considerations, from a practical point of view, we detect tree debris along roadways in satellite images using three different algorithms with their own limitations which we aim to overcome using them in a collaborative framework. Our selected methods are:

- **AEs/VAEs**: They are powerful feature extractors, and it is possible to compare the generated features in the latent space by analyzing satellite images before and after a hurricane. On the other hand, they are unsupervised, and they do not have semantic knowledge of the objects in satellite images.
- **NDVI**: It is one of the most common indexes for detecting vegetation in remote sensing applications. It uses the infrared band for evaluating chlorophyll-rich vegetation. However, it can’t properly distinguish grown trees from other types of vegetation, for example, grass or bushes.
- **Unet**: It is a modern segmentation method that is possible to specifically train to recognize trees in images. However, it is susceptible to shadows and occlusions.

We extract several patches, both from the image before the hurricane (I_{bfr}) and from the image after the hurricane (I_{aft}) to cover the whole roadways in the area. Based on the assumptions above, we develop three sub-models (called hereafter blocks), each computing a tailored, customized dissimilarity score as shown in Fig. 2. We threshold the dissimilarity score histograms to flag the presence of a potential fallen tree. We combine the three blocks together using a co-voting strategy to overcome each block’s inherent limitations and increase performances. The following subsections explain each block of our proposed algorithm.

A. Tree Segmentation Block

The first block is a tree segmentation algorithm. Given an RGB image I as input, the corresponding output M^{tree} is a single-channel image where trees are detected. The Tree Segmentation Block is the only supervised component of our proposed framework. To perform the tree segmentation task, we created a labeled dataset to train the model. However, it is worthwhile mentioning that the training task for tree segmentation in a given area can be done just once using a satellite image in normal conditions before the hurricane. From a practical point of view, it saves the effort and time for labeling images of fallen trees after hurricanes which would be required for traditional supervised methods.

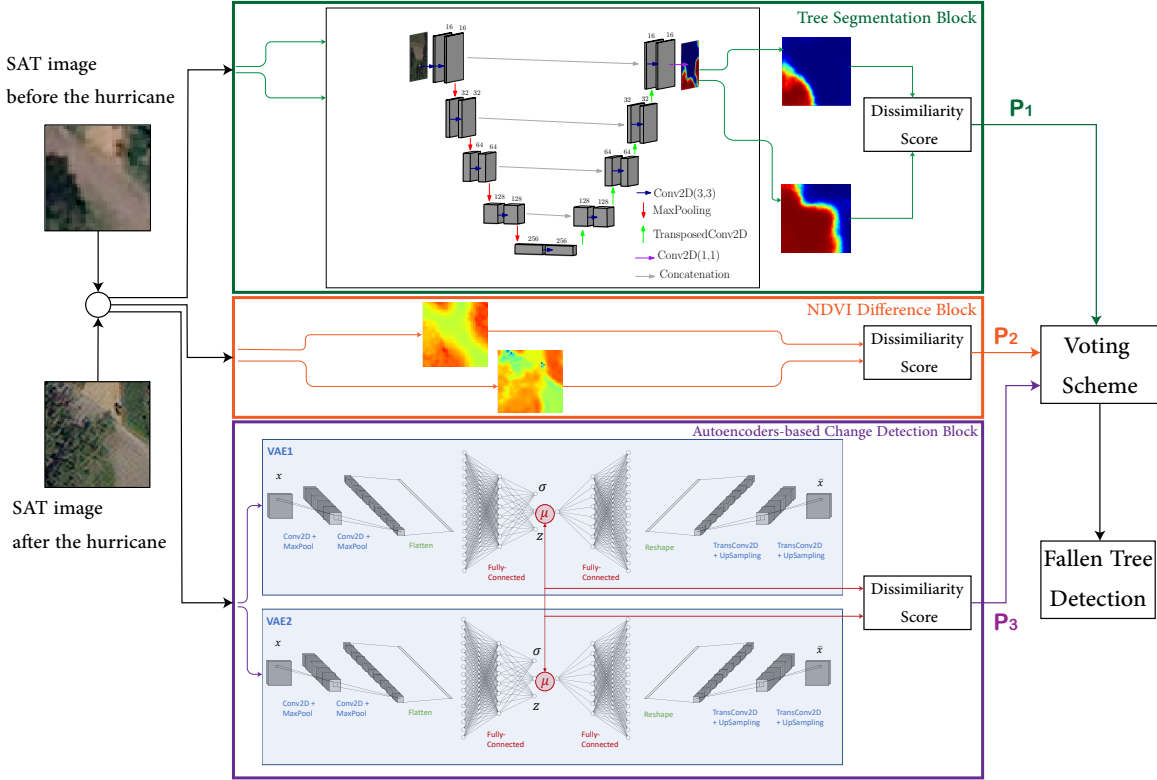


Fig. 2: Overview of the proposed approach for tree debris detection. Each of the three blocks computes a tailored, customized dissimilarity score from patches extracted before and after the hurricane. It does this using tree semantic segmentation (first block), vegetation index comparison (second block) and features comparison (third block).

We use a U-net architecture [23] which is a very popular segmentation model. Initially developed to segment biomedical images, it was successfully applied to a wide range of applications. The architecture is composed by a cascade of [16, 32, 64, 128, 256] convolutional layers activated by an Exponential Linear Unit (Elu) function, followed by a batch normalization layer and a Max Polling layer, as shown in Fig. 2. During the up-sampling procedure, concatenations layer have been used to ensure better spatial localization. We use the U-net to segment each patch I_{bfr} and I_{aft} separately. Finally, to quantify a dissimilarity between the two predicted segmentation maps, a dissimilarity score \mathcal{D}_{tree} is computed as the integral over the patch P of the pixel-wise difference between the segmentation map after the hurricane (M_{aft}^{tree}) and the segmentation map before the hurricane (M_{bfr}^{tree}). Such difference is then multiplied by a Gaussian kernel K centered at the center of the window (Equation 1).

$$\mathcal{D}_{tree} = \iint_{Patch} \left(M_{aft}^{tree} - M_{bfr}^{tree} \right) \otimes K \quad (1)$$

The Gaussian kernel is a function centered at the center of the acquired patch. It has larger values in the middle and decaying values as we move towards the edges of the patch. Since the patch is acquired at the center of the roadway, such weighting function is introduced so that differences in pixel values close to the center of the patch are weighted more than differences near the edges as we are more interested in assessing the condition at the center of the window. From Equation (1) we

note that the more M_{bfr} and M_{aft} are similar, the lower the value of \mathcal{D}_{tree} is.

B. NDVI Difference Block

The second block takes advantage of the multi-spectral data coming from satellites to compute the Normalized Difference Vegetation Index to recognize vegetation. NDVI is a popular index in remote sensing for vegetation detection and it is defined as:

$$NDVI = \frac{\rho_{nir} - \rho_{red}}{\rho_{nir} + \rho_{red}} \quad (2)$$

where ρ_{red} and ρ_{nir} stand for the spectral reflectance measurements acquired in the red (visible) and near-infrared regions, respectively. The reflectance measurements come directly with the optical images and are provided by the satellite operator as a bundle product. Green living plants look brighter in the near-infrared band due to chlorophyll near-infrared high reflectance. Similar to the previous block, we define a dissimilarity score \mathcal{D}_{NDVI} as the integral over the patch of the difference between $NDVI$ computed after the hurricane ($NDVI_{aft}$) and the $NDVI$ computed before ($NDVI_{bfr}$), with a multiplication with a Gaussian kernel K :

$$\mathcal{D}_{NDVI} = \iint_{Patch} \left(NDVI_{aft} - NDVI_{bfr} \right) \otimes K \quad (3)$$

C. Variational Autoencoders-based Change Detection Block

The third block is an unsupervised change detector that computes a dissimilarity value between images before and

after to detect whether a significant changes occurred. A direct pixel-wise comparison in the images is not optimal due to possibly different illumination and noise. Therefore, we use VAEs as deep feature extractors with a Siamese configuration [24]. The use of convolutional autoencoders has been motivated by the strong capabilities of deep learning methods to learn useful features in a low-dimensionality space. Variational autoencoders are also used to assure a well-defined topology of the latent space in which images are projected. This can be extremely irregular using standard autoencoders.

A variational autoencoder learns to map an input x into a distribution $p(z|x)$. It is composed by an encoder q_θ , a decoder p_ϕ , a sampler and a loss function. Since the encoder and the decoder are implemented as neural networks, θ and ϕ are all the trainable parameters of such networks. Mathematically it can be formulated as:

$$\text{Encoder: } x \rightarrow q_\sigma(z|x) \quad \text{Feature space} \quad (4)$$

$$\text{Sampler: } z \sim p(z|x) \quad (5)$$

$$\text{Decoder: } z \rightarrow p_\phi(x|z) = \tilde{x} \quad (6)$$

Since the distribution $P(z|x)$ is not known, Bayesian variational inference is used. We assume that the latent space, whose dimension K is chosen as hyper-parameter, follows a prior distribution which is assumed to be Gaussian in our study: $z \sim P(z) \sim N(\mu_k, \sigma_k)$, with $k = 1, \dots, K$. We use as a loss function the sum of a reconstruction term (typical of standard autoencoders) with a regularization term calculated as the Kullback-Leibler divergence between the latent space distribution and the prior distribution as follows:

$$L(\theta, \phi) = \underbrace{\text{MSE}(x, \tilde{x})}_{\text{Reconstruction loss term}} + \underbrace{\mathcal{KL}(q_\theta(z|x)||p(z))}_{\text{Regularization term}} \quad (7)$$

The first term is the reconstruction loss defined as Mean Squared Error (MSE) between the original input and the reconstructed one, this term encourages the decoder to learn to reconstruct the data well from the feature space. The second term is the Kullback-Leibler (KL) divergence between the distribution of the latent space retrieved by the encoder $q_\theta(z|x)$ and the prior distribution $p(z)$. The Gaussian prior distribution $p(z)$ keeps the representations z of each input sufficiently diverse and allows a closed-form expression for the KL divergence [22]. Using the loss function in Eq. (7), one autoencoder (VAE_1) is trained to learn features from the images *before* while the other one (VAE_2) is trained with the images *after* (see the last block of Fig. 2). Features are then extracted from the bottleneck layer. The two autoencoders, VAE_1 and VAE_2 , have been trained with the architecture described in Table II. We use the same idea as the previous block to calculate a dissimilarity score \mathcal{D}_{VAE} between the two images (before and after the hurricane). Hence, we compute the difference between features extracted from VAE_1 and VAE_2 which is then evaluated using an *Isolation Forest* algorithm [25]. Isolation forest is a tree-structure based unsupervised learning algorithm for anomaly detection, enabling isolating anomalous points in a dataset.

From Table II, each input image is encoded into a vector $\mu \in \mathbb{R}^K$ where $K = 128$ is the dimension of latent space.

TABLE II: Autoencoder architecture

Encoder	Decoder
$Input(80,80,3)$	Dense($20*20*64$)
Conv2D (3,3,32) + Relu	Reshape(20,20,64)
MaxPooling(2)	TransConv2D (3,3,64) + Relu
Conv2D (3,3,64) + Relu	UpSampling(2)
MaxPooling(2)	TransConv2D (3,3,32) + Relu
Flatten($20*20*64$)	UpSampling(2)
Dense(1024)	TransConv2D (3,3,3) + Sigmoid
Dense($dim(z) = 128$)	$Output(80,80,3)$

The 3-layers architecture of our deep learning, composed by *Conv-Relu-BatchNormalization*, with a number of filters increasing by the power of 2 is a popular choice when building Convolutional Networks for computer vision tasks. On the other hand, the parameter K , which is the dimension of the latent space, is chosen empirically. The parameter K sets the amount of ‘‘compression’’ we are expecting from the autoencoder. A value too large does not provide a good feature representation in the latent space. On the other hand, a value too small will destroy most of the information during the encoding step. Section IV will justify our choice of the latent space dimension K .

D. Fallen Tree Detection

Our proposed framework includes three blocks, including tree segmentation, NDVI, and deep features comparison as presented in subsections III-A, III-B, and III-C. Each block computes a dissimilarity score between a pair of patches from two satellite images captured before and after a hurricane.

We extract N patches from the images before and after a hurricane to cover the roadways area. Then, we calculate the dissimilarity values per each patch location $i = 1, \dots, N$ along the roadways for each block of the algorithm. Then, the block’s outcome (a vector with N component) is represented in a histogram. We expect the histogram to be an unimodal distribution where one set (clear, debris-free locations) dominates the histogram with respect to the secondary set (obstructed locations). We used the maximum deviation method [26], especially designed for unimodal histograms, to compute a threshold and to divide the histogram in two parts. The threshold Th is selected at the point of the histogram furthest from the straight line connecting the histogram peak and the tail (Fig. 3).

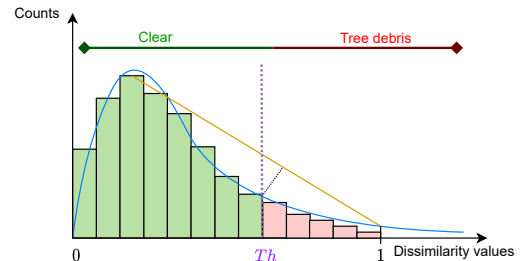


Fig. 3: Histogram of the dissimilarity values computed for each block from extracted patches. We say that there is a tree debris in a location if the corresponding dissimilarity score is greater than the threshold Th .

We also use a piece-wise linear mapping to map each dissimilarity score, computed at location $i = 1, \dots, N$ to create

a probabilistic value of having a tree debris $P_{debris} \in (0, 1)$ in a location. The threshold Th calculated in the previous subsection corresponds to $P_{debris} = 0.5$ as shown in Fig. 4

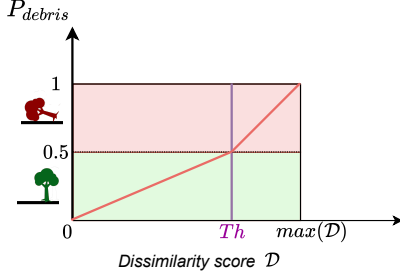


Fig. 4: Map from the dissimilarity score to the probability of tree debris P_{debris} .

Locations with $P_{debris} > 0.5$ will be flagged as fallen tree or tree debris, and clear otherwise.

E. Co-Voting Scheme

Since each block's output is independent from the other blocks, a combination strategy can possibly increase the performances. We call $P_i, i = 1, 2, 3$ the tree debris probability coming from block 1, 2 and 3 respectively. The P_{debris} is the overall tree debris probability. Here we present three possible combinations:

- *Combination 1 - Aggressive:* a location is marked as *tree debris* if at least one of the three blocks has $P_i > 0.5$.

$$P_{debris} = (P_1 > 0.5) \vee (P_2 > 0.5) \vee (P_3 > 0.5)$$

- *Combination 2 - Moderate:* a location is marked as *tree debris* if at least two of the three blocks has $P_i > 0.5$.

$$P_{debris} = (P_1 > 0.5 \wedge P_2 > 0.5) \vee (P_1 > 0.5 \wedge P_3 > 0.5) \vee (P_2 > 0.5 \wedge P_3 > 0.5)$$

- *Combination 3 - Conservative:* a location is marked as *tree debris* if all the three blocks has $P_i > 0.5$.

$$P_{debris} = (P_1 > 0.5) \wedge (P_2 > 0.5) \wedge (P_3 > 0.5)$$

Furthermore, we can combine probabilities P_1, P_2, P_3 together using weights $\kappa_1, \kappa_2, \kappa_3$ as follows:

$$P_{debris} = \kappa_1 P_1 + \kappa_2 P_2 + \kappa_3 P_3 \quad (8)$$

where $\sum_i \kappa_i = 1$ In this way it is possible to estimate the contribution of the three blocks to the overall detection performance, and determine the weight of each block for an optimal combined decision.

IV. RESULTS & DISCUSSIONS

For validation purposes, two satellite images have been acquired for a portion of the City of Tallahassee (Florida), as described in Section II. We use a 24×24 meters sliding window (corresponding to 80×80 pixels given the satellite resolution) along the roadway's path to extract patches from

the two different satellite images before and after the hurricane. Patches are spatially spaced no more than 10 meters along the road center lines. In this way, $N = 5116$ single patches are extracted, covering the whole roadway network in the study area. Due to the different resolution, the patches extracted before the hurricane have been up-sampled to match with the number of pixels of the same patches extracted after the hurricane. The three blocks have been implemented as described in subsections III-A, III-B and III-C.

The code has been implemented in Python using the sklearn library for machine learning and Tensorflow/Keras for the deep learning part. The testing platform is a computer equipped with a 10th Gen i7 CPU, 32GB of RAM and an NVIDIA GeForce RTX 2080 Super as GPU. The images are encoded in GeoTiff format, so all pixels can be geo-referenced and precisely located in real-world coordinates. We use QGIS to integrate and visualize all the data.

To train the tree segmentation block (see section III-A), we created a labeled dataset from a part of the study area not overlapping with the locations along the roadways where we implemented and tested our algorithm. This training dataset is made of 1200 images of 160x160 pixels. The segmentation model is trained using the training dataset. The Adam optimizer has been used with a learning rate of 0.001 and exponential decays factor of 0.9. The model, with 1,944,049 trainable parameters, has been trained using binary cross-entropy as loss function. Once the model is trained to effectively recognize trees, it is used to segment trees along the 5116 patches extracted along the roadways to compute the dissimilarity scores. It is worthwhile mentioning that the model has not seen those 5116 patches during the training phase.

The variational autoencoder has been trained using the same optimizer as the tree segmentation model. The loss function is defined in Eq. 7. The encoder has 26,497,216 trainable parameters while the decoder has 3,358,659. Since variational autoencoders are unsupervised models, the usual training/validation split is not necessary.

In Table III we show the computation time needed to train each single block and compute the corresponding dissimilarity scores for all the locations along the roadways.

TABLE III: Computation time per block for training ($T_{training}$) and for the calculation of dissimilarity scores ($T_{\mathcal{D}}$) for the entire study area.

Subroutine	$T_{training}$ (sec.)	$T_{\mathcal{D}}$ (sec.)
1: Tree Segmentation (Supervised)	135	4.2
2: NDVI (no-learning)	<i>not applicable</i>	1.6
3: VAE (Unsupervised)	113	2.1
Patches extraction along roadways		1.73

We note that the most computationally-intensive operations are the training process for the tree segmentation block and the variational autoencoders block. Despite that, the entire framework is able to scan and locate fallen trees across the entire study area, which is $\approx 6K m^2$, in less than 5 minutes.

Fig. 5 shows visually an example of a hurricane-induced vegetation change. Note that the NDVI difference and the tree segmentation difference (Fig. 5e and 5h respectively) clearly illustrate such changes.

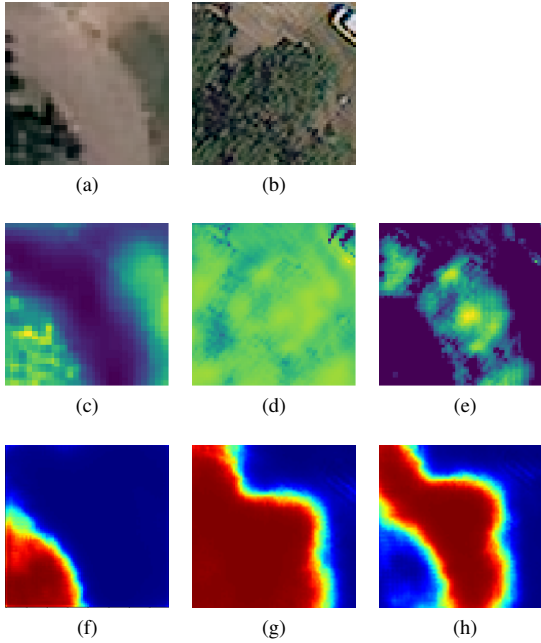


Fig. 5: An example to show a Hurricane-induced vegetation change in a patch: (a) RGB image sample acquired before the hurricane; (b) RGB image sample acquired after the hurricane; (c) NDVI of the image before the hurricane; (d) NDVI of the image after the hurricane; (e) NDVI difference; (f) tree segmentation of the image before the hurricane; (g) tree segmentation of the image after the hurricane; (h) Tree segmentation difference.

Fig. 6 shows an example of a reconstructed patch. With the proposed variational autoencoder architecture, the raw input RGB image ($3 \times 80 \times 80 = 19200$ pixels) is encoded into only 128-values vector (dimension of the latent space), thus achieving a high compression rate. Nevertheless, it is possible to decode the patch back without losing many details, as shown in Fig. 6, therefore such features catch the relevant patterns in the initial images.

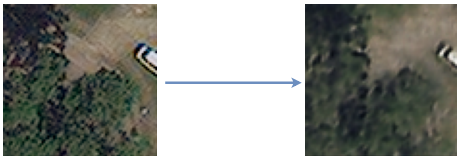


Fig. 6: Example of reconstructed patch: (left) original patch extracted after the hurricane, (right) reconstructed patch.

For each patch, dissimilarity scores \mathcal{D}_{tree} , \mathcal{D}_{NDVI} and \mathcal{D}_{VAE} are calculated and normalized into the interval $(0, 1)$. To validate the algorithm, we use the geo-location of stacked piles of tree debris provided by the City of Tallahassee municipality to us, as described in Section II. The debris piles location on the map are not accurate in some cases. It can also be more than one report referring to the same fallen tree. To solve these issues, we spatially cluster the reported trees locations (using MeanShift algorithm). We introduce a distance threshold of $d = 40$ meters between the points reported by the City and the points detected by our algorithm from satellite images. The accuracy scores, True Positive (TP),

False Positive (FP), and False Negative (FN), are calculated as follows and as sketched in Fig. 7.

- *True Positives*: Number of debris detected by the algorithm (red points) close to the ground-truth debris (stars)
- *False Positives*: Number of debris detected by the algorithm (red points) not close to the ground-truth debris (stars)
- *False Negative*: Number of ground-truth debris (stars) not close to debris detected by the algorithm (red points)

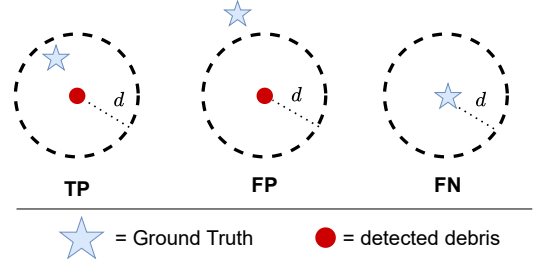


Fig. 7: Calculation of True Positive (TP), False Positive (FP) and False Negative (FN).

Then, we calculate the recall, precision and F1-score (harmonic mean of recall and precision) of the model compared with the ground truth as follows:

$$\begin{aligned} Recall &= \frac{TP}{TP + FN}, & Precision &= \frac{TP}{TP + FP} \\ F1 &= \frac{2(Recall \cdot Precision)}{Recall + Precision} \end{aligned} \quad (9)$$

Since in our application both recall and precision are important measurements, we used F1-score as a final metrics.

We first used Eqs. (9) to evaluate the performances of each block in our approach independently. To show the effectiveness of the proposed threshold Th , a sensitivity analysis is performed to evaluate the effect of the threshold on recall, precision and F1-score values. These scores are plotted as a function of the threshold in Fig. 8. We note that such an analysis is only possible when having the ground-truth. In other words, it is not possible to develop an algorithm to choose the optimal threshold that optimizes the performances in advance. We notice that the threshold we choose heuristically in the subsection III-D (vertical purple line) approximates closely the *argmax* of the F1-score. This shows the strength of our threshold choice in this case. Most importantly, it is evaluated a-priori based on the distribution of the dissimilarity scores.

Finally, we compare the different blocks as well as the different combinations proposed in Section III-E. The results are presented as bar plots in Fig. 9.

From the accuracy comparison we see that Combination 1 and 3 achieve the highest recall and precision respectively. However, Combination 1 results in an over-estimation of tree debris in the area, leading to low precision, because it merges the obstructed locations detected by all the three blocks. Combination 3 is too conservative and unable to detect most of the tree debris resulting in high number of false negatives (low recall). Combination 2 (moderate strategy) is the most balanced and achieves the highest F1-score among

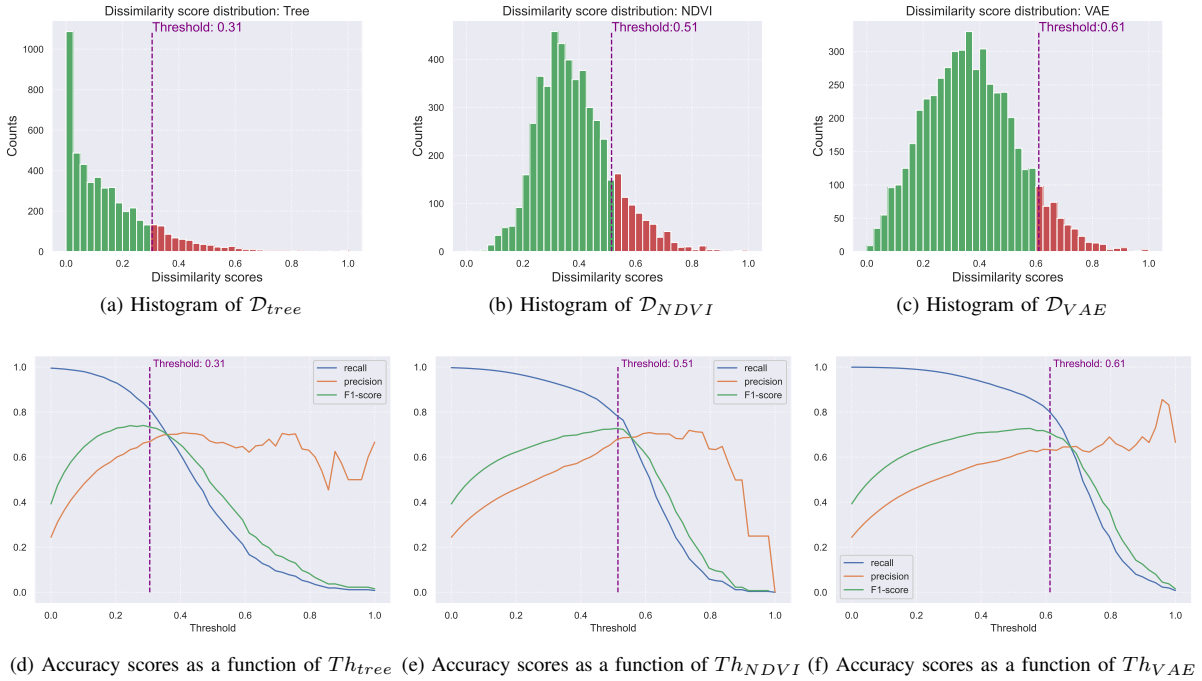


Fig. 8: Sensitivity Analysis: first column) Tree segmentation block, second column) NDVI block, third column) VAE block. Recall, precision and F1 curves are plotted in blue, orange, green respectively as function of the threshold. The purple vertical line shows the threshold value we heuristically selected using the procedure explained in subsection III-D

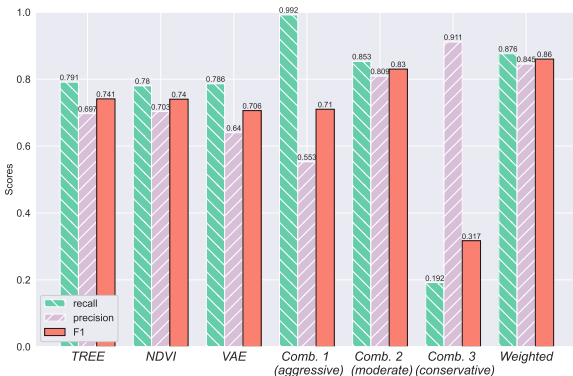


Fig. 9: Recall, precision and F1-score for each single block presented and the different combinations presented in subsection III-E.

the three combinations. Moreover, it is possible to estimate the contribution of the three blocks to the overall detection performance, and determine the weights $\kappa_1, \kappa_2, \kappa_3$ of each block for an optimal combined decision. The weighting shows that *TREE* and *NDVI* have a slightly better F1-score than *VAE*. Therefore, we assigned proportionally-derived values to κ_1, κ_2 than κ_3 as: $\kappa_1 = \kappa_2 = 0.35, \kappa_3 = 0.3$ using the F1-score as metrics. With such weighting combination, the performances are further improved by 3.6%.

We compared our best results, with other state-of-the-art machine learning algorithms. Table IV shows the comparison results.

We noted that our approach outperforms other state-of-the-art methods. Autoencoders-based algorithms are used for

TABLE IV: Comparison between our final approach and other deep-learning methods (Autoencoder-based, CNN-based) and machine learning methods (features descriptors + Support Vector Machines).

Algorithm	Recall	Precision	F1-score
Our approach	0.875	0.845	0.859
Sparse AEs [27]	0.708	0.587	0.642
Joint AEs [28]	0.841	0.668	0.744
CNN [13]	0.947	0.725	0.821
GLCM+SVM [29]	0.816	0.691	0.748
LBP+SVM [30]	0.828	0.698	0.757

change detection but they can't effectively recognize tree debris due to their fully unsupervised nature. Other machine learning-based methods exploit specific descriptions, specifically Gray-Level Co-Occurrence Matrix (GLCM) and Local Binary Patterns (LBP) to extract texture signature classified then using a Support Vector Machine (SVM). However, our approach outperform them by 13%. CNN achieves a higher recall accuracy than our method. Nevertheless, if we compare the F1-score, our model shows an improvement by 4%. It is noticeable that the CNN model is supervised, thus it has been trained directly with tree debris ground truth data to recognize them. However, the tree debris ground truth may not be available always in real-world application. Our approach shows comparable performance without relying on actual fallen trees data for training. Therefore it is more practical in areas where such labels might not be available.

Finally, the framework's output is used to automatically create a map showing all the detected fallen trees within the area, see Fig. 10. In case of a future hurricane, such a map can be generated quickly after the hurricane hits and used by the

city municipality or transportation authorities responsible for hurricane restoration to overview the most damaged areas. The satellite images provide wide area situational awareness after a hurricane with low cost and in a short time. Therefore, our proposed automated approach using satellite images is adding extra value to the emergency management teams on top of the information from traditional ground based inspections.

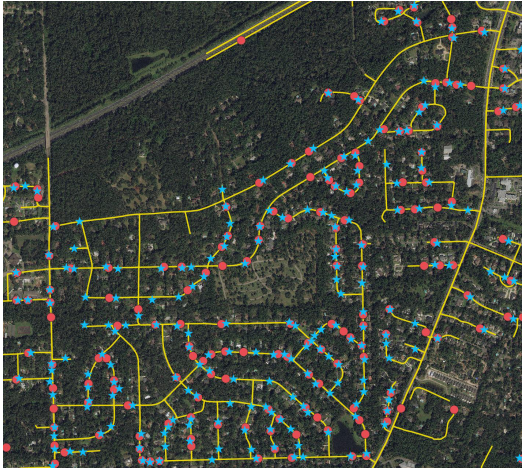


Fig. 10: Example of map showing all the detected anomalies within the area using Combination 2 in the study area. Blue stars are the reported debris locations. Red points are the debris detected by our algorithm. The yellow lines are the scanned roadways.

V. PRACTICAL CONSIDERATIONS FOR EMERGENCY MANAGEMENT TEAMS

Satellite data has a number of advantages compared to other infrastructure monitoring approaches such as post hurricane ground-based inspection, aerial inspection with helicopters or drones, and direct reports from citizens.

Our proposed satellite based framework can serve as a complementary source for emergency management teams in addition to the traditional roadway inspection approaches especially in rural areas, remote locations, and less populated regions. Depending on the extend of hurricane damages or the weather conditions, ground-based inspection of roadways may not be possible or it is limited by roadway closures. Helicopters and drones are also prone to weather conditions. Cities can get advantage of active participation of citizens through phone calls or recently mobile applications, called city dashboards, to receive report of damages or roadway closures. However, not all cities have mobile applications in operation or they face a low adoption rate among their citizens [31], [32]. Moreover, cellular networks and internet access aftermath a natural disaster may fail. Therefore, citizens can not provide critical information to the city government using mobile applications. Above all, the tremendous drop in satellites data costs in recent years made them more cost effective than aerial inspection methods, such as helicopters and drones especially for large areas [4].

It is worth while mentioning that are some practical limitations in using optical satellite images. The first is the cloud coverage. It is not always possible to acquire a cloud-free

image right after the event of hurricane. For example, in this study the first suitable image could be acquired two days after the hurricane hit.

Moreover, the accuracy of fallen tree detection depends on ecological aspects of the target area such as the tree coverage density. In our case, the city of Tallahassee in Florida is highly covered with large trees such as Tupelo (*Nyssa sylvatica*) and Red maple (*Acer rubrum*) with wide canopies that mostly make (beautiful and tourist attractive) canopy roads. In such canopy roads, it is challenging to distinguish fallen trees from standing ones. Canopy roads impose a geometric limitation for inferring fallen trees on the roads' pavement. The satellite's view from the top cannot always realize that a tree is on the pavement or if it is standing over the road. Fig 11 shows a view of a canopy road in Tallahassee. However, such tangled

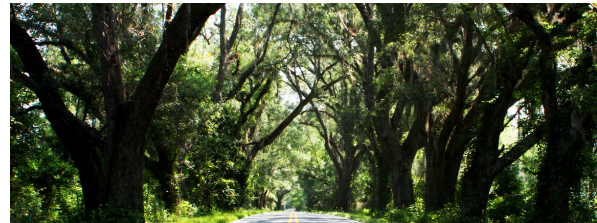


Fig. 11: A typical canopy road in Tallahassee. Photo courtesy of <https://leontrees.org/explore/>

canopy roads are limited, and their locations are already known in advance by the city municipality. They can rely more on ground-based inspections or residents' reports for such areas. In our study, most false negatives occurred in such roads that brought our accuracy to 86%. In other words, the classic ground-based inspection is more critical in specific geographical areas in each city where the remote sensing approaches have limitations.

In terms of satellite data storage requirements, commercial satellite image providers and data companies offer cloud-based solutions to access and analyze the images in archive or on demand. A typical high resolution satellite image can be up to few GigaBytes. If one does not use a cloud based service, the local workstations can usually handle such images for limited studies or proof-of-concepts. There are a number of standard formats for satellite images such as GeoTIFF, NetCDF, and HDF. In this study we used GeoTiff format. A GeoTiff image is a normal bitmap image that contains additional metadata about the geo-locations of the pixels. In this way it is possible to map each pixel into a real-world coordinate system.

Finally, the proposed satellite based approach for hurricane impact study on roadways can be extended to other infrastructure networks such as electricity lines, rail roads, and natural gas pipelines. Specifically, the electric grid has a similar topology to roadways in some parts of the world like the United States where overhead power lines are laid parallel to roadways. Fallen trees induce similar threats to power lines and can cause power outages after hurricanes. Our approach with some modification can be used for electric grid damage assessment.

VI. CONCLUSIONS

This paper proposes an automated framework to detect fallen trees on roadways after hurricanes. We use two satellite images for the City of Tallahassee in Florida, acquired before and after Hurricane Michael in October 2018. Our proposed satellite-based analytical framework relies on three different methods integrated into an automated setting. Despite the challenging task from the remote sensing perspective, our solution leads to 0.86% accuracy in detecting fallen trees. It is also more practical since it works with a limited training dataset and has a fast computing time. Our approach is complementary to the classic hurricane damage assessment practices. It provides the emergency management teams with a wide area of situational awareness at a lower cost and in a shorter time, which can be beneficial for stakeholders. This study focused only on the impact of Hurricane Michael on the City of Tallahassee. However, the proposed methodology can be successfully extended to other locations given the data availability on satellite imagery and hurricane-induced disruptions. This would especially be useful to cities when setting priorities in their disaster improvement programs and for regulating vegetation management through zoning. A similar methodology can be also used for other types of infrastructure networks rather than roadways. Therefore, our future work will be toward investigating different machine learning algorithms and expanding our platform to other applications such as electricity networks.

REFERENCES

- [1] National Oceanic and Atmospheric Administration (NOAA). Hurricane costs. <https://coast.noaa.gov/states/fast-facts/hurricane-costs.html>.
- [2] Martin Schaefer, Richard Teeuw, Simon Day, Dimitrios Zekkos, Paul Weber, Toby Meredith, and C.J. Westen. Low-cost uav surveys of hurricane damage in dominica: automated processing with co-registration of pre-hurricane imagery for change analysis. *Natural Hazards*, 101, 04 2020.
- [3] Lake Singh, William Whittecar, Marc DiPrinzio, Jonathan Herman, Matthew Ferring, and Patrick Reed. Low cost satellite constellations for nearly continuous global coverage. *Nature Communications*, 11, 01 2020.
- [4] H. Jones. The recent large reduction in space launch cost. In *48th International Conference on Environmental Systems ICES-2018-818-12 July 2018, Albuquerque, New Mexico*, 2018.
- [5] M. Gazzea, M. Pacevicius, D. O. Dammann, A. Sapronova, T. M. Lunde, and R. Arghandeh. Automated power lines vegetation monitoring using high-resolution satellite imagery. *IEEE Transactions on Power Delivery*, pages 1–1, 2021.
- [6] Akansha Mehrotra, Krishna Kant Singh, Madhav Ji Nigam, and Kirat Pal. Detection of tsunami-induced changes using generalized improved fuzzy radial basis function neural network. *Natural Hazards*, 77, 05 2015.
- [7] M. Ji, Lanfa Liu, Runlin Du, and M. Buchroithner. A comparative study of texture and convolutional neural network features for detecting collapsed buildings after earthquakes using pre- and post-event satellite imagery. *Remote Sens.*, 11:1202, 2019.
- [8] Bo Peng, Zonglin Meng, Qunying Huang, and Caixia Wang. Patch similarity convolutional neural network for urban flood extent mapping using bi-temporal satellite multispectral imagery. *Remote Sensing*, 11(21):2492, Oct 2019.
- [9] D. Gullick, A. Blackburn, D. Whyatt, and P. Vopenka. Tree risk evaluation environment for failure and limb loss (treefall) : Predicting tree failure within proximity of infrastructure on an individual tree scale. 2017.
- [10] A. Kocatepe, Mehmet Baran Ulak, Grzegorz Kakareko, E. Ozguven, Sungmoon Jung, and R. Arghandeh. Measuring the accessibility of critical facilities in the presence of hurricane-related roadway closures and an approach for predicting future roadway disruptions. *Natural Hazards*, 95:615–635, 2018.
- [11] Q. D. Cao and Youngjun Choe. Building damage annotation on post-hurricane satellite imagery based on convolutional neural networks. *Natural Hazards*, pages 1–20, 2020.
- [12] D. E. Kisllov and K. Korznikov. Automatic windthrow detection using very-high-resolution satellite imagery and deep learning. *Remote Sens.*, 12:1145, 2020.
- [13] Baolin Yang, S. Wang, Yi Zhou, Fu tao Wang, Q. Hu, Ying Chang, and Q. Zhao. Extraction of road blockage information for the jiuzaigou earthquake based on a convolution neural network and very-high-resolution satellite images. *Earth Science Informatics*, 13:115–127, 2019.
- [14] Francesco Nex, Diogo Duarte, Fabio Giulio Tonolo, and Norman Kerle. Structural building damage detection with deep learning: Assessment of a state-of-the-art cnn in operational conditions. *Remote Sensing*, 11(23):2765, Nov 2019.
- [15] Wenzhong Shi, Min Zhang, Rui Zhang, Shanxiong Chen, and Zhao Zhan. Change detection based on artificial intelligence: State-of-the-art and challenges. *Remote Sensing*, 12(10):1688, May 2020.
- [16] P. Zhang, M. Gong, H. Zhang, J. Liu, and Y. Ban. Unsupervised difference representation learning for detecting multiple types of changes in multitemporal remote sensing images. *IEEE Transactions on Geoscience and Remote Sensing*, 57(4):2277–2289, 2019.
- [17] E. Kalinicheva, J. Sublime, and M. Trocan. Neural network autoencoder for change detection in satellite image time series. In *2018 25th IEEE International Conference on Electronics, Circuits and Systems (ICECS)*, pages 641–642, 2018.
- [18] National Oceanic and Atmospheric Administration (NOAA). Catastrophic hurricane michael strikes florida panhandle. <https://www.weather.gov/tae/HurricaneMichael2018>.
- [19] National Oceanic and Atmospheric Administration (NOAA). Assessing the u.s. climate in 2018. <https://www.ncei.noaa.gov/news/national-climate-201812>.
- [20] Wikipedia contributors. Tallahassee, florida — Wikipedia, the free encyclopedia. https://en.wikipedia.org/w/index.php?title=Tallahassee,_Florida&oldid=1011330996, 2021.
- [21] Y. Zhan, K. Fu, M. Yan, X. Sun, H. Wang, and X. Qiu. Change detection based on deep siamese convolutional network for optical aerial images. *IEEE Geoscience and Remote Sensing Letters*, 14(10):1845–1849, 2017.
- [22] Diederik P. Kingma and Max Welling. An introduction to variational autoencoders. *CoRR*, abs/1906.02691, 2019.
- [23] O. Ronneberger, P. Fischer, and T. Brox. U-net: Convolutional networks for biomedical image segmentation. *ArXiv*, abs/1505.04597, 2015.
- [24] Kian Ahrabian and B. BabaAli. Usage of autoencoders and siamese networks for online handwritten signature verification. *Neural Computing and Applications*, 31:9321–9334, 2018.
- [25] F. T. Liu, K. M. Ting, and Z. Zhou. Isolation forest. In *2008 Eighth IEEE International Conference on Data Mining*, pages 413–422, 2008.
- [26] Paul L. Rosin. Unimodal thresholding. *Pattern Recognition*, 34(11):2083–2096, 2001.
- [27] E. Kalinicheva, J. Sublime, and M. Trocan. Neural network autoencoder for change detection in satellite image time series. In *2018 25th IEEE International Conference on Electronics, Circuits and Systems (ICECS)*, pages 641–642, 2018.
- [28] Jérémie Sublime and E. Kalinicheva. Automatic post-disaster damage mapping using deep-learning techniques for change detection: Case study of the tohoku tsunami. *Remote Sens.*, 11:1123, 2019.
- [29] H. Rastiveisi, E. Hosseini-Zirdoo, and F. Eslamizade. Automatic blocked roads assessment after earthquake using high resolution satellite imagery. *ISPRS - International Archives of the Photogrammetry, Remote Sensing and Spatial Information Sciences*, pages 601–605, 2015.
- [30] Idrissa Coulibaly, R. Lepage, and Michèle St-Jacques. Road damage detection from high resolution satellite images based on machine learning. In *IEEE, MultiTemp 2015*, 07 2015.
- [31] Jinghui (Jove) Hou, Laura Arpan, Yijie Wu, Richard Feiock, Eren Ozguven, and Reza Arghandeh. The road toward smart cities: A study of citizens’ acceptance of mobile applications for city services. *Energies*, 13(10):2496, May 2020.
- [32] Vaibhav S. Diwanji, Laura Arpan, Mehmet Baran Ulak, Jinghui (Jove) Hou, Eren Erman Ozguven, and Reza Arghandeh. Understanding citizens’ communication channel preferences during natural disasters: A synchronicity-based, mixed-methods exploration using survey and

geospatial analysis. *International Journal of Disaster Risk Reduction*, 47:101646, 2020.



Michele Gazzea, IEEE Student Member received his Bachelor's degree in Information Engineering and his Master's degree in Automation and Control Engineering, both from the University of Padova (Italy). He worked in Cielle.srl in Treviso (Italy) as an R&D engineer studying and designing diagnostic techniques on milling and engraving CNC machines. He worked as a researcher for Electrolux to perform model-based analysis of power consumption in washing machines until he started his new occupation as a Ph.D. student in Western Norway

University of Applied Sciences in Bergen (Norway). His research interests are in data analytics, machine and deep learning, computer vision, and remote sensing applications.



Alican Karaer, IEEE Student Member is a Ph.D. Candidate and in the Civil and Environmental Engineering Department of Florida A&M University – Florida State University College of Engineering (USA). He has received his Master of Science degree from University of North Florida and Bachelor's degree from Istanbul Technical University (Turkey) both from Civil Engineering Department emphasizing transportation engineering. He is the lead researcher in Florida Department of Transportation funded projects exploring the feasibility of drone

utilization and computer vision applications for automated road inventory and traffic data collection. His research interests are in the line of data analytics, deep learning, GIS, and remote sensing applications for transportation and infrastructure management.



Mahyar Ghorbanzadeh received the Bachelor of Science degree in civil engineering, in 2014, and the master's degree in highway and transportation engineering from University of Guilan, Iran, in 2017. He currently works as a graduate research assistant toward the Ph.D. degree at the Department of Civil & Environmental Engineering, Florida State University. His research interests include transportation accessibility, urban mobility, evacuations, disasters, and resilience.



Nozhan Balafkan received his first master degree in astrophysics from university of Leipzig and his second master degree in physics of climate from university of Tromsø. After this, he has experience as a research assistant in astrophysics in Canada at Saint Mary's University. He is currently working in StormGeo AS (Norway) as data scientist.



Tarek Abichou is a Professor in the Department of Civil and Environmental Engineering at the FAMU-FSU College of Engineering (USA). His research is on the environmental geotechnics, sustainable solid waste management systems and civil engineering applications. He has been recently involved in research on the resilience of coastal communities and barrier islands to rising sea levels and how to incorporate the use of livable shorelines to enhance coastal resiliency.



Eren Erman Ozguven, IEEE Member is an Associate Professor of Civil and Environmental Engineering and Director of the Resilient Infrastructure and Disaster Response (RIDER) Center at the FAMU-FSU College of Engineering (USA). Dr. Ozguven focuses on ever-growing mobility, safety, accessibility, and resiliency problems in the context of smart infrastructure and cities. His work examines the simultaneous and interdependent movements of populations—including the aging and other vulnerable groups, and the commodities and services that

meet their needs.



Reza Arghandeh, IEEE Senior Member is a Full Professor in the Department of Computing, Mathematics, and Physics and Department of Electrical Engineering at the Western Norway University of Applied Sciences (HVL), Norway. He is the Director of Collaborative Intelligent Infrastructure Lab (CI2). He is also a lead data scientist with StormGeo AS. He has been an Assistant Professor in ECE Dept, FSU, USA 2015-2018, and a postdoctoral scholar at EECS Dept, University of California, Berkeley 2013-2015. His research has been supported by U.S.

National Science Foundation, U.S. Department of Energy, the European Space Agency, and the European Commission.

ROADWAY VULNERABILITY ASSESSMENT AGAINST HURRICANES USING SATELLITE IMAGES

Gazzea, M., Karaer, A., Ghorbanzadeh, M., Ozguven, E. E., and Arghandeh, R

In Transportation Research Record, 2677(3), pp. 1453-1464, 2023, <https://doi.org/10.1177/03611981221124593>

Roadway Vulnerability Assessment against Hurricanes Using Satellite Images

Michele Gazzea¹ , Alican Karaer² , Mahyar Ghorbanzadeh² , Eren Erman Ozguven² , and Reza Arghandeh¹ 

Transportation Research Record
2023, Vol. 2677(3) 1453–1464
© National Academy of Sciences:
Transportation Research Board 2022



Article reuse guidelines:
sagepub.com/journals-permissions
DOI: 10.1177/03611981221124593
journals.sagepub.com/home/trr



Abstract

Infrastructures such as roadways, power lines, and communications networks play a critical role in our society. However, they are also susceptible to failures, especially those caused by extreme events, quickly affecting large geographical areas. Predicting where and when these failures will occur with high confidence is very difficult because of the stochastic nature of such events. Nevertheless, it is possible to know in advance which areas are more vulnerable and plan accordingly. This paper aims to use remote sensing techniques based on satellite images to detect roadways' vulnerabilities to hurricanes. Each road is assigned a vulnerability score based on the information retrieved from the satellite image and other geographic information system (GIS) data, which can be used to create a vulnerability map of the area. Both vegetation exposure along the roads and the consequences of the closures are considered in the vulnerability assessment. The study area has been selected in Tallahassee, Florida, U.S., where a high-resolution satellite image was acquired in September 2018, 2 weeks before Hurricane Michael. The findings of this work can help management teams and city responders to identify the most vulnerable regions at risk of disruption and organize resources before the event.

Keywords

data and data science, remote sensing, sustainability and resilience, transportation infrastructure protection and preparedness, vulnerability and threat assessment

Our modern society relies on critical infrastructures to support all its operations, functionalities, and enterprises. Such infrastructures are composed of public and private physical structures such as roads, railways, bridges, tunnels, water supply, sewers, electrical grids, and telecommunications networks (1). They are considered so vital because their incapacitation or destruction would have a debilitating effect on security, national economic security, national public health or safety, or any combination thereof (2). Such fundamental elements are often exposed to failures and disruptions, dramatically affecting citizens' lives and causing society stress. Thus, it is fundamental to understand and monitor the vulnerability of such infrastructures to ease or limit outages' consequences. Disruptions can be caused by various events, from technical failures (electric outages, traffic incidents) to natural disasters (floods, landslides, hurricanes, wildfires, earthquakes, etc.). While accidents and technical failures may have limited effects, disruptions caused by nature may cover large areas. Among the different

infrastructures, the road network is critical for transportation and all services' accessibility, and it is often severely affected by natural disasters like hurricanes.

Hurricanes and the damage they cause have gained attention recently, with disaster management analysis spanning two different directions. Post-disaster assessment deals with the consequences of a natural disaster, detecting and estimating damages, recovery optimization, resource allocations, and so forth. On the other hand, pre-disaster assessment copes with analyzing the area before the event for vulnerability analysis to achieve better prevention and resilience. Traditionally, such evaluations are performed by manual or visual inspection,

¹Department of Computer Science and Electrical Engineering, Western Norway University of Applied Sciences, Bergen, Norway

²Department of Civil and Environmental Engineering, FAMU–FSU College of Engineering, Tallahassee, FL

Corresponding Author:

Michele Gazzea, michele.gazzea@hvl.no

which is a time-consuming and risky operation, especially in the proximity of collapsed buildings or fallen trees. However, remote sensing technologies are growing in use. Aerial images are a valuable source of data for hurricane damage assessment (3). Still, the high operating costs of helicopters and limited coverage of drones are a limitation to large-scale applications. In recent years, the dramatic drop in the launching cost of satellites and the growing number of satellites in orbit has significantly reduced the cost of high-resolution satellite imagery (4). Commercial satellite providers can offer high-resolution images (0.3–0.5 m/pixel) with a high revisiting frequency for most parts of the globe. Furthermore, single snapshots can cover large areas at once. Therefore, the combination of coverage, frequency, and cost-efficiency of satellite imagery, in addition to advancements in machine learning, creates a paradigm change for cities enhancing situational awareness for infrastructure networks (5).

Concerning post-disaster assessment, recently, in two studies by Gazzea et al., the authors developed a framework to automatically detect fallen trees at roadway-level after a hurricane using high-resolution satellite images (6, 7). Similarly, in Kaur et al., a deep-learning technique for detecting damaged buildings in post-hurricane satellite images is proposed (8). In two studies by Karaer et al., the authors introduce a remote-sensing-based approach that can rapidly analyze the damage caused by catastrophic storms at a city scale (9, 10).

Concerning pre-disaster assessment, the current works are focused on statistical analyses to identify spatial patterns of outages and their relationship with demographic and socioeconomic variables, such as in two studies by Ghorbanzadeh et al. (11, 12). While these studies can provide valuable information for city officials to better prepare emergency policies for potential hurricanes, these analyses are done a posteriori. Furthermore, vegetation, one of the primary causes of roadway outages during extreme weather events, is often either not considered or not taken into account with simple metrics, for example, computing vegetation indexes like the Normalized Difference Vegetation Index (NDVI) (13).

Some studies, such as Gullick et al. and ÖiftÖi et al., tried to quantify single tree failure probability resulting from extreme weather events by proposing empirical mechanical models to estimate the possibility of trees failures (14, 15). Such works take into account tree characteristics (e.g., tree canopy, stem mass, tree mass, and diameter at breast height), soil strength, and wind-induced bending moment on each tree, and combine them with wind data (16). However, because of the complexity and limitations of measuring such characteristics, which are required information for mechanistic models, it is often impossible to obtain accurate estimations of the failure probability for trees. Statistical models are

another approach for predicting the probability of wind-related tree failure, as shown in Kabir et al. but they still require data from surveys and inventories (17).

In this paper, we propose a framework for rapid, scalable, and low-cost vulnerability assessment along roadways using high-resolution satellite images. We implemented our framework in a portion of the City of Tallahassee, the capital of Florida, U.S., in September 2018, before Hurricane Michael.

The contributions of our approach are as follows:

- We calculate the vegetation exposure of roadways based on tree parameters estimated via satellite imagery, such as height, distance to the roadway, health, and density.
- We propose a vulnerability index which combines the vegetation exposure with road importance, calculated based on the consequences that such closures have on the transportation network, such as mobility and number of buildings affected.

Study Area and Data Description

Hurricane Michael was one of the strongest storms that hit the U.S. southeast coast. It made landfall as a Category 5 hurricane in Florida's Panhandle region with maximum sustained wind speeds of 140 knots (161 mph), bringing a catastrophic storm surge to the State of Florida and Big Bend areas (especially Mexico Beach and Panama City) (18). It hit Florida on October 10, 2018, and the related power outages, at their greatest extent, affected nearly 400,000 electricity customers in Florida, representing about 4% of the state (19). Furthermore, damage to over 2.8 million acres (1.1 million hectares) of forested land caused an estimated \$1.29 billion in damage to the timber industry. The 12% of damaged forest area was classified as "catastrophic" by the Florida Forest Service (20). Estimated damage from Hurricane Michael throughout the U.S. reached \$25 billion (21).

To develop our framework, we acquired data from both satellite images and the municipality. Figure 1 summarizes the data used.

We acquired one high-resolution multi-spectral satellite image for a 6.5 km² (2.5 mi²) portion of Tallahassee, the capital of Florida. The image, provided by Maxar WorldView-2 satellite, is composed of four channels: red (R), green (G), blue (B), and near-infrared (NIR) with a spatial resolution of 0.5 m/pixel. The given resolution allows for recognizing trees, buildings, and other infrastructure. The image is encoded as a GeoTIFF file so that each pixel can be precisely located in a geographical reference system. The picture was taken in September

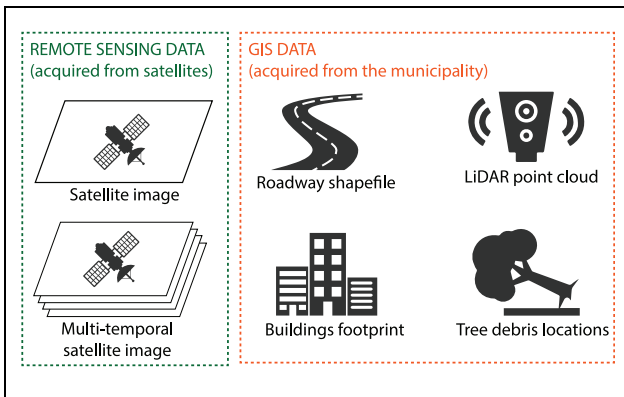


Figure 1. Summary of the data used for the study.

2018, two weeks before Hurricane Michael. In addition, to estimate tree health, we acquired multi-temporal satellite images spanning equal intervals within the period 2017–2018, from a five satellites constellation operated by Planet company with a resolution of 3 m/pixel and composed of four bands (RGB-NIR) (22).

We acquired the buildings' footprints and the locations of roads from publicly available databases of the municipality of Tallahassee. Laser imaging detection and ranging (LiDAR) point clouds, freely available from the city, have been used to train the height estimation algorithm and to extract building height. LiDAR is a reliable tool that maps an environment and provides the corresponding 3D point cloud representation. Still, it is also costly and generates a massive amount of data to be processed. The idea of our approach is to use available LiDAR data to train a suitable deep-learning model. Finally, we use the geo-locations of stacked piles of tree debris collected by the authorities after the hurricane and provided by the City of Tallahassee municipality to justify and discuss the proposed vegetation exposure scores.

Methodology

This paper aims to assess vulnerabilities along roadways using satellite images. In our study, we identify the vulnerability V_r of a road r as a combination of the vegetation exposure $\mathcal{V}\mathcal{E}_r$ in that road and the consequences \mathcal{I}_r of the closure on the road r , specifically based on road importance and amount of buildings (both private and public) along the road (23). Mathematically, we say that:

$$V = \underbrace{(\text{buildings; road importance})}_{\mathcal{I}} \otimes \underbrace{(\text{vegetation exposure})}_{\mathcal{V}\mathcal{E}} \quad (1)$$

Equation 1 claims that, even if a road has high vegetation exposure, the associated vulnerability can still be low if nobody lives in the surroundings or if the road is not critical for the mobility network, reinforcing what is also expected from common sense. Therefore, our framework is composed of two parts. The first part assesses the vegetation along roadways using satellite images, assigning each road a vegetation exposure score based on the quantity, health, and height of trees, and their distance to the road. The second part integrates data from the municipality, specifically the volume of buildings along the road and roadways locations. Topological analysis is also performed to detect more critical roads in relation to mobility. Finally, vegetation exposure, road importance, and building volume are combined into a vulnerability score per road. The output is a vulnerability map of the road network of the area. The overall pipeline is shown in Figure 2, and each part is further described.

Remote Sensing Module

The first module deals with vegetation, which is the main cause of roadway closures after hurricanes. Tall trees pose a significant threat, as strong winds can easily cause them to fall on the road corridor. Furthermore, locations with an increased number of trees are also dangerous as, from a probabilistic point of view, it is more likely that some of them may fall. Therefore, the density and height of trees, and distance from the road are essential factors to consider for vulnerability analysis. All the parameters above can be estimated using one satellite image.

Height Estimation. This module estimates the tree canopy height from the satellite image. Measuring tree canopy height accurately from single images is, in general, an ill-posed task because optical images taken from above clearly do not contain height information and there are intrinsic ambiguities in mapping a color measurement into a height value (24). Usually, the most common techniques for 3D generation include stereo images, multi-angular photogrammetry, synthetic-aperture radar (SAR) interferometry, and LiDAR (25–28). Nevertheless, some papers addressed the issue by resorting to machine learning for 3D reconstruction using single optical images. Fully convolutional-deconvolutional network architectures are a useful tool that has been proven to be capable of guiding the model through the process of learning this ambiguous mapping with considerable accuracy (29). The main idea is to use satellite images and LiDAR data to train a model to learn the complex relationship between contextual information (texture, color, shading, etc.) and height, to regress a digital surface model (DSM). Mathematically, we denote with y_i the true height of a pixel obtained from the

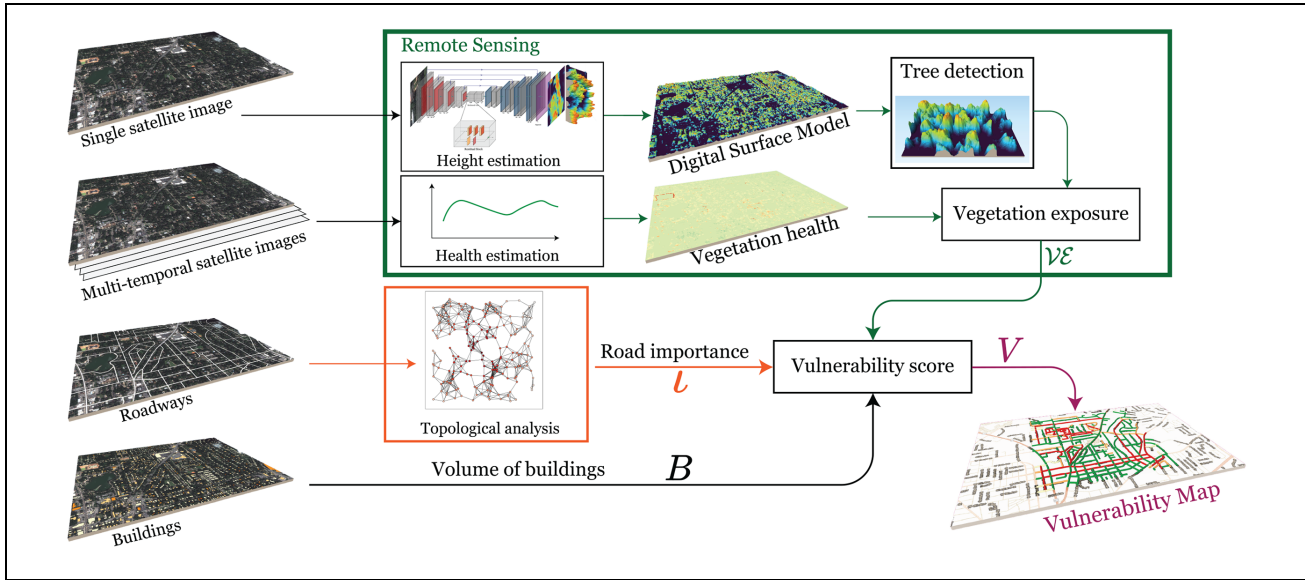


Figure 2. Overall pipeline of the approach.

Note: We use remote sensing data to get vegetation parameters and compute the vegetation exposure \mathcal{VE} of roads. Vegetation exposure is combined with the road importance ι , derived from a topological analysis of the network with the amount of buildings B to compute a vulnerability score V . The output is a score V for each road in the network.

ground-truth (LiDAR in our study) and $\hat{y}_i = f(x, \theta)$ the predicted height obtained from the model with parameters θ using the input image x . We formulate the task as a regression problem, and we define a loss function as the mean squared error between the true height and the predicted height:

$$\mathcal{L}(y, \theta, x) = \frac{1}{N} \sum_{i=1}^N (y_i - \hat{y}_i)^2 = \frac{1}{N} \sum_{i=1}^N (y_i - f(x_i, \theta))^2 \quad (2)$$

The model should minimize this loss function. Therefore, given a training dataset $\{x, y\}$, we aim to learn the weights of the model such that $\theta^* = \arg \min_{\theta} \mathcal{L}(y, \theta, x)$. In this paper, we use a neural-network-based model called Res-UNet (Figure 3), which has been found to perform better for such regression tasks (30). The model uses the popular U-net for semantic segmentation as a backbone where residual blocks have replaced the traditional convolutional blocks. The architecture is composed by a cascade of (16, 32, 64, 128, 256) residual blocks, consisting of convolutional layers, batch normalization, and *relu* activation. The final layer of the decoder is activated by a sigmoid function.

Tree Detection. The output of the height estimation model is a DSM, which represents the height of the pixel. Trees are then detected using a local maxima filter running on the predicted DSM to estimate the position of the tree stem. The filter finds the peaks on the image

corresponding to the highest values. A minimum distance between peaks is set to 6m, and the minimum intensity of peaks set to 4m to prevent oversampling the DSM with spurious peaks (caused by, for example, noise), (Figure 4).

Health Estimation. Furthermore, inspired by the work done in De Petris et al., we estimate the health of the vegetation in the considered area by analyzing the trend of vegetation index over the acquired multi-temporal images (31). An anomalous negative vegetation index trend can be caused by transitory problems, for example, insect attacks or gradual biomass decrease resulting from plant pathologies/tree aging. An unhealthy tree shows characteristics suggesting that rapid development in pathogenic wood-induced decay is ongoing and, consequently, its general propensity to fail is higher (32). We used the NDVI, defined as:

$$NDVI = \frac{\rho_{NIR} - \rho_{RED}}{\rho_{NIR} + \rho_{RED}} \quad (3)$$

where

ρ_{red} = the spectral reflectance measurements acquired in the red (visible) region, and

ρ_{nir} = the spectral reflectance measurements acquired in the NIR region.

Green living plants look brighter in the NIR band because of chlorophyll NIR high reflectance. We compute the NDVI value in the study area for each of the

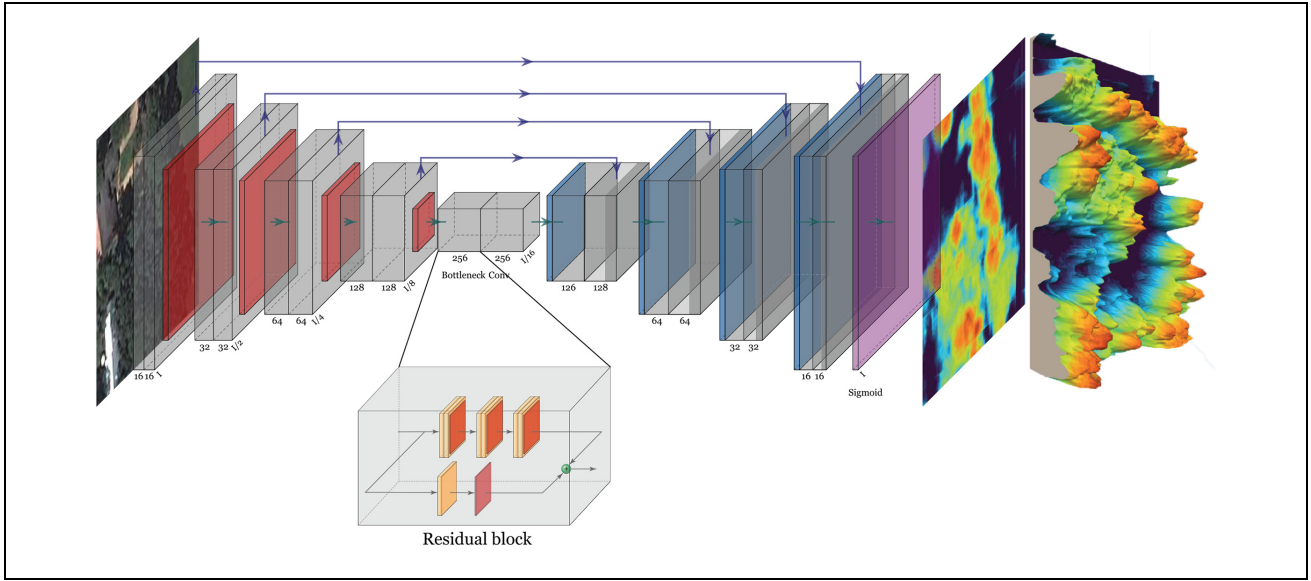


Figure 3. Deep-learning model architecture used to regress the digital surface model (DSM) from a single satellite image. Note: blue shading = up-sampling layers; grey shading = residual block; purple shading = regressor; red shading = pooling layers. Residual blocks add a shortcut between the input and the output to bypass standard cascade of two or more stacked convolutional layers.

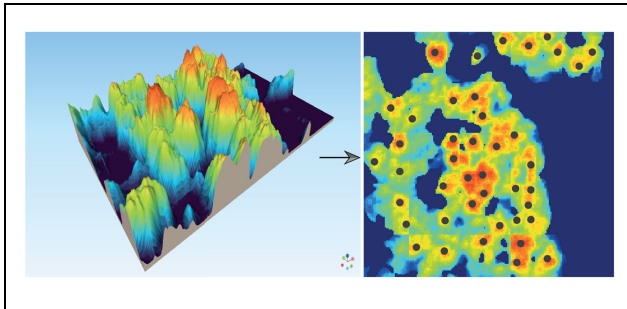


Figure 4. Digital surface model (DSM) represented as 3D surface.

Note: Local maxima filter is used to detect the peaks in the DSM, estimating the position of the trees.

five satellite images acquired during the years 2017 and 2018. To filter out spurious changes resulting from seasonality, we computed the average value of the index per each year and calculate the difference:

$$\Delta_{NDVI} = \mathbb{E}[NDVI]_{2018} - \mathbb{E}[NDVI]_{2017} \quad (4)$$

We assign the corresponding value from Δ_{NDVI} to each detected tree location. We expect the histogram of Δ_{NDVI} for all the trees in the city to follow a Gaussian-like distribution centered approximately at 0. Practically, it means that most of the trees have been neutral over the 2 years, while a minority of them experienced a positive Δ_{NDVI} (growth) and others a negative Δ_{NDVI} (decay) trend. To isolate the most significant negative trend in Δ_{NDVI} , we

set a threshold Th as $Th = \mu - \sigma$, where μ and σ are the mean and standard deviation of the distribution. We assign the trees with $\Delta_{NDVI} > Th$ the value “1” (healthy) and trees with $\Delta_{NDVI} < Th$ the value “0.5” (unhealthy). See Figure 5.

Vegetation Exposure. The previous part estimates trees’ height, location, and health status. The number and distance of trees from the roadway can be derived from their location using the Euclidean distance. All these parameters are essential factors to consider and should be combined to assess the vegetation exposure to hurricanes for a given road. We extract equally distributed points every 20m along the road. For each point, we compute the vegetation exposure \mathcal{VE}_{point} by taking into account the height, health, and distance from the roadway, and the number of all the trees within a certain radius R from the point, as described in Equation 5:

$$\mathcal{VE}_{point} = \sum_{i=1}^{N_{trees}} \left(\frac{H_i}{D_i \cdot He_i} \right) \quad (5)$$

where

H = the height of the tree,
 He = the health of the tree, and
 D = the distance of the tree.

Figure 6 illustrates the process graphically.

Finally, the vegetation exposure for the entire road is defined as the maximum value among all the vegetation exposure calculated at the different points, Equation 6:

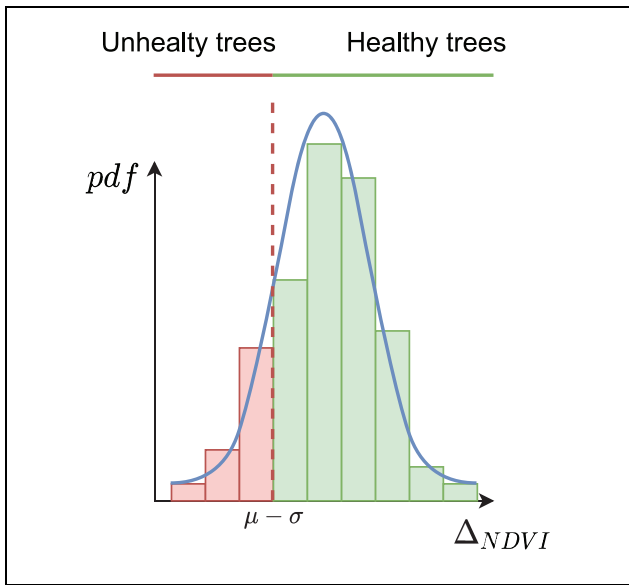


Figure 5. Based on the histogram of Δ_{NDVI} , we define a threshold to classify trees as healthy and unhealthy. Note: $\Delta_{NDVI} = \Delta_{NDVI}$ is the difference between the NDVI in the two time periods, 2018 and 2017; pdf = probability density function.

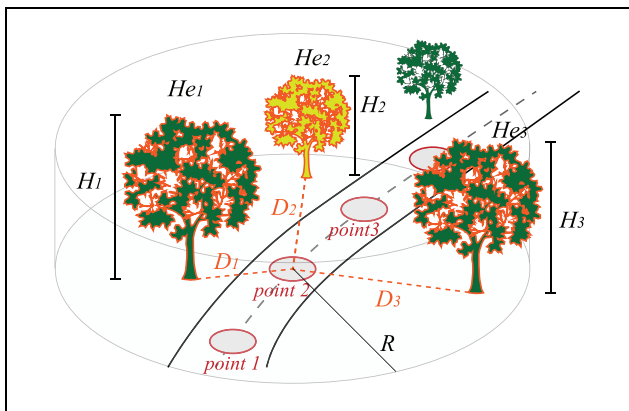


Figure 6. Vegetation exposure for a road. Note: The road is sampled into equally distributed points. For each point we take into account the number of trees, distance to roadway, height, and health for the calculation of the vegetation exposure.

$$\mathcal{V}\mathcal{E}_{road} = \max(\mathcal{V}\mathcal{E}_{point}) \quad \forall \text{point} \in \text{road} \quad (6)$$

Topological Analysis

The previous part computes a value related to how exposed a road is, based on vegetation. However, as presented in Equation 1, the consequences of the closure should also be considered. Specifically, some roads are more important than others if we consider how they are connected. For instance, if a road has many connections,

there exist several routes to bypass it in case of a blockage. On the other hand, a closure can potentially disconnect the network if the road has low redundancy. The set of all roads naturally forms a complex network that can be studied within graph theory. We first translate the roadway shape-file locations into a graph. We first remove the “dummy” nodes in the original file. Roads are usually composed of piece-wise linear segments and include nodes that exist only as points to help streets bend around curves, but they are not nodes in a topological sense. Topological nodes consist of all the intersections between roads. Figure 7 shows the process of converting the road shape-file into a graph structure visually. Note that we are only interested in the relation between nodes and edges in the graph analysis. Thus, the geographical shape of the road is irrelevant.

In this paper, we use the centrality indicator to rank the importance of edges in the graph network (33). In particular, we use the betweenness centrality of edges. Betweenness centrality measures the importance of an edge over the flow of information (i.e., traffic flow) between a pair of vertices in the graph under the assumption that information primarily flows over the shortest paths between them. From a transportation point of view, the betweenness centrality of a road (edge) is computed as the percentage of all shortest paths between two intersections (nodes) in the network that passes through the considered road (edge). Thus, a road with high betweenness centrality may have considerable influence over the information passing between other roads. So, they represent a critical part of the network, since removing them will disrupt the information flow in the network.

Betweenness centrality c_B of an edge e is calculated as:

$$c_B(e) = \sum_{s,t \in V} \frac{\sigma(s,t|e)}{\sigma(s,t)} \quad (7)$$

where

V = the set of nodes of the graph,

$\sigma(s,t)$ = the number of shortest path between s and t , and

$\sigma(s,t|e)$ = the number of those paths passing through edge e .

Furthermore, we further classify the roads into two different groups, assigning a multiplier of $l = 1$ or $l = 2$ if a road is a *Common* or *County/State* road, respectively. The reason is that usually County and State roads experience a larger traffic flow than common roads. Thus, this a priori information should be reflected in the road importance calculation. The road importance ι_r is calculated directly and proportionally to the centrality values, multiplied by corresponding road label as $\iota_r = c_B(r) \otimes l$.

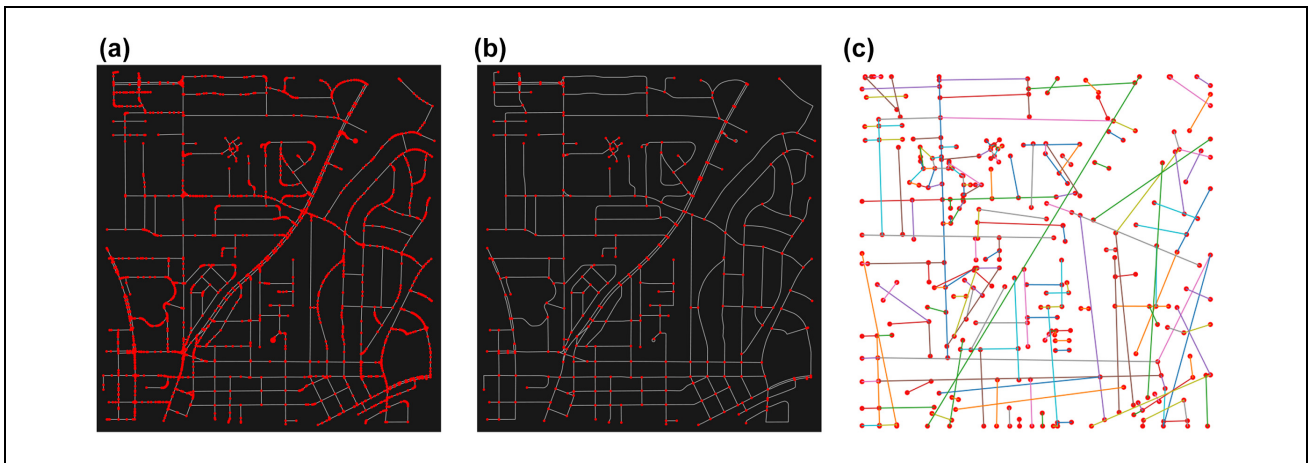


Figure 7. A roadway network shape-file (a) is converted into a graph structure (c) by removing the non-topological nodes (b): (a) Roadway network, (b) Roadway network where only the topological nodes are maintained, and (c) Roadway network as graph.

Vulnerability Score

Keeping in mind Equation 1, we calculate the vulnerability of a road r combining the vegetation exposure $\mathcal{V}\mathcal{E}_r$ calculated from Equation 6 with the road importance ι_r and the volume of buildings B_r along the entire road. Specifically, the volume of a building is calculated as the product of its footprint, derived from the building footprint dataset, and its average height, derived from the LiDAR point cloud. This calculation is performed for all the buildings within a specific buffer size (set to 50 m) along the road. Finally, we normalized each term within the range (0, 1) and multiply them together as:

$$V_r = (\mathcal{V}\mathcal{E}_r) \otimes (\iota_r) \otimes (B_r) \quad (8)$$

Results and Discussion

The framework has been developed in Python, using the *Tensorflow/Keras* libraries for the deep-learning modules, *scikit-image* for the image processing parts, and *networkx* library for the topology analysis (34–36). QGIS has been used to visualize and integrate all the different data (37). We first trained and tested the height estimator module. We trained the model described in Figure 3 using an Nvidia RTX 2080 Super as GPU. We used the Adam optimizer with a learning rate of 10^{-4} . A 1.5 km^2 (0.57 mi^2) area of the city has been selected as a training dataset. The model is then tested in the remaining 5 km^2 (1.93 mi^2). An early stopping callback monitors the validation loss, keeps track of the loss function, and eventually stops the training to avoid over-fitting. Trees are then detected using the local maxima filter on the surface output of the model.

We calculate the distribution of the absolute error between the ground truth (derived from LiDAR) and the

estimated height (from the model) as $e = |y - \hat{y}|$. The distribution of the error in Figure 8a shows a mean error of 1.4 m. Figure 8b shows the resulting distribution of Δ_{NDVI} . As presented in Figure 5, the selected threshold is computed as $\mu - \sigma = -0.03$. Therefore, we label the trees with $\Delta_{NDVI} < -0.03$ as unhealthy, and healthy otherwise.

Figure 9 shows a visual example of the estimated digital surface model (DSM) and the detected tree positions.

A tree catalog is built to store the information about each detected tree's position, height, and health, as estimated in the previous steps. Once the tree catalog has been created, we compute vegetation exposure for each road. First, we sample a road every 20 m and use Equation 5 to compute the vegetation exposure per each location. The radius R is set at 20 m. Equation 6 is then used to compute the vegetation exposure per road. It is worth mentioning that it is very challenging to validate the obtained vegetation exposure fully. However, we can use the tree debris dataset provided by the municipality to investigate the relation between vegetation exposure on the road and the a posteriori presence of fallen trees after the hurricane. We classify the roads into two groups. One group is composed of all the roads that had tree debris within a buffer zone of 20 m. The other group is composed of all the debris-clear roads after the hurricane. For each road, we compute the vegetation exposure level as described in Equation 6. We then plot the calculated vegetation exposure levels within the two groups. Results are shown in Figure 10.

We observe that roads that did not have tree debris in the proximity have, statistically, a lower vegetation exposure level. On the other hand, roads with tree debris have a higher vegetation exposure level. Nevertheless, because of the stochastic nature of the hurricane, there is a slight

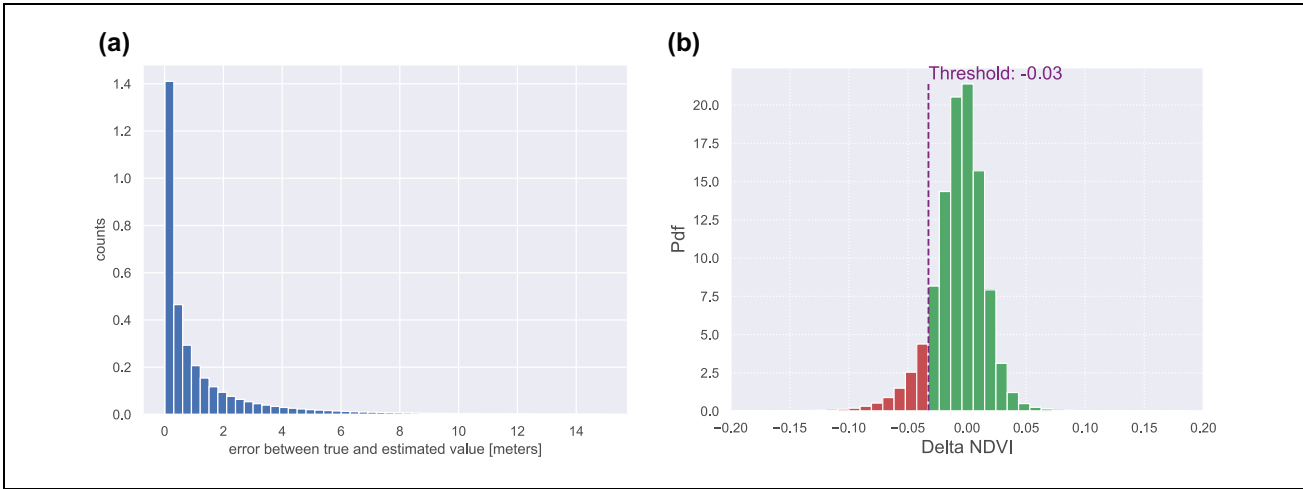


Figure 8. (a) Distribution of the height error between the estimated digital surface model (DSM) and the ground-truth, (b) Distribution of Δ_{NDVI} .

Note: $\Delta_{NDVI} = \Delta_{NDVI}$ is the difference between the NDVI in the two time periods, 2018 and 2017; pdf = probability density function.

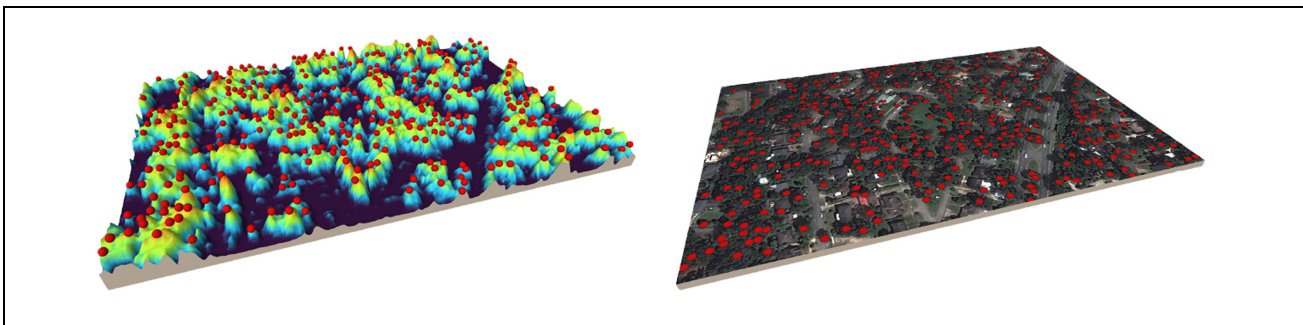


Figure 9. Digital surface model generated from the satellite image—trees are detected as the local maxima on the surface: (Left) Digital surface model generated from the satellite image, (Right) Trees are detected as the local maxima on the surface.

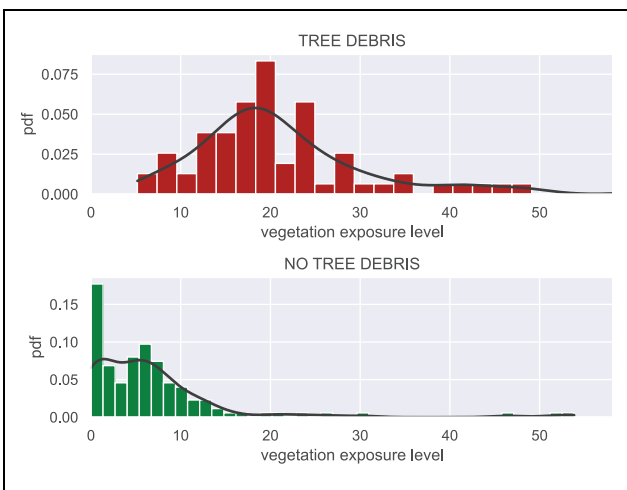


Figure 10. Vegetation exposure level for all the roads that had tree debris after the hurricane (top). Vegetation exposure level for all the roads that did not have tree debris after the hurricane (bottom).

Note: pdf = probability density function.

overlap between the two distributions. In other words, some roads with relatively significant vegetation exposure levels did not have fallen trees.

Before using Equation 8, we normalized the values within the range (0, 1) for each considered term in the vulnerability function (i.e., volume of buildings along the road B_r , importance of the road ι_r , and vegetation exposure of the road $\mathcal{V}\mathcal{E}_r$). Figure 11 shows the distributions of the values for each element.

Finally, we can use Equation 8 to assign a vulnerability score to each road. Figure 12 shows the vulnerability map geographically displayed over the study area.

It is possible to automatically highlight the most vulnerable locations at the city scale. This can help the management teams and city responders to organize and allocate resources at specific points in the city.

Practicalities

We trained a deep-learning model to regress the DSM using LiDAR data from the municipality in the proposed

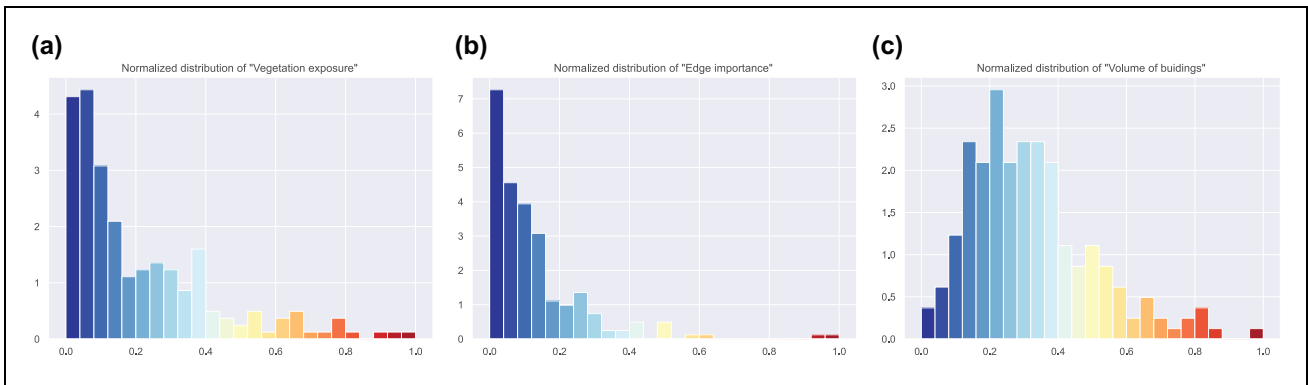


Figure 11. Normalized distributions for the three elements considered in Equation 2: (a) Normalized distribution of the vegetation exposure, (b) Normalized distribution of the road importance, (c) Normalized distribution of the buildings volume. Note: The histograms are colored according to the value: from 0 (low level, blue) to 1 (high level, red).



Figure 12. Vulnerability map of the study area generated using our remote sensing approach.

Note: Values have been visually clustered into three classes: green (low level), orange (medium level), and red (high level).

framework. However, it is not always possible to have a DSM training dataset for the specific study area, especially when the ground truth comes from expensive sources such as LiDAR or time-consuming surveys. If LiDAR data or any height information is not available, training a model using a manually created dataset is impossible. Nevertheless, the model shown in Figure 3 can still be used to segment vegetation. Although the height cannot be retrieved this way, the distance and the number of trees can still be estimated from the segmentation map. A similar vegetation exposure function can then be modified to remove the height from the calculation. The advantage is that training datasets are generally easier to acquire in segmentation tasks than complete 3D point clouds. For example, free data can be used to train a segmentation model. If a model has been properly trained, it can still achieve sub-optimal yet accurate results.

To illustrate this concept, we trained our model using both our data from Tallahassee and data from the

Potsdam dataset. The dataset, from a portion of the German city of Potsdam, is downloadable at the International Society for Photogrammetry and Remote Sensing (ISPRS) (38). The output of the model, in this case, is a binary map where “1” is if a pixel is part of a tree and “0” otherwise. Instead of the regression loss presented in Equation 2, binary cross-entropy \mathcal{L} should be used as loss function for training the network, since only two labels are considered (0 for *no-trees* and 1 for *trees*) (39). Such loss is often used in binary classification tasks, and it is defined as:

$$\mathcal{L} = -(y \log(p) + (1 - y) \log(1 - p)) \quad (9)$$

where

p = the predicted probability value, and

$y = \{0, 1\}$ = the true label.

The output of the model is a probability value between 0 and 1. Cross-entropy loss increases as the predicted probability diverges from the actual label.

Accuracy score metrics is defined as:

$$\text{Accuracy} = \frac{\text{Number of pixels correctly predicted}}{\text{Total number of pixels}} \quad (10)$$

and results are shown in Table 1.

Figure 13 shows an example of vegetation segmentation for a portion of the area using our model.

There is a drop in the performances when we use the model trained in a completely different area. However, this is not very limiting from a practical point of view as the model can be fine-tuned using the new area, with less data.

Finally, it is worth mentioning that the proposed vulnerability function (Equation 8) is not unique and local authorities might implement different functions. Furthermore, other data can be included, depending on

Table 1. Comparison Between the Tree Segmentation Model Using the Potsdam or Tallahassee Dataset as Training. The Testing Area is Tallahassee for Both Cases

Approach	Training set	Accuracy (%)
Tree segmentation	Potsdam	89.3
	Tallahassee	96.4

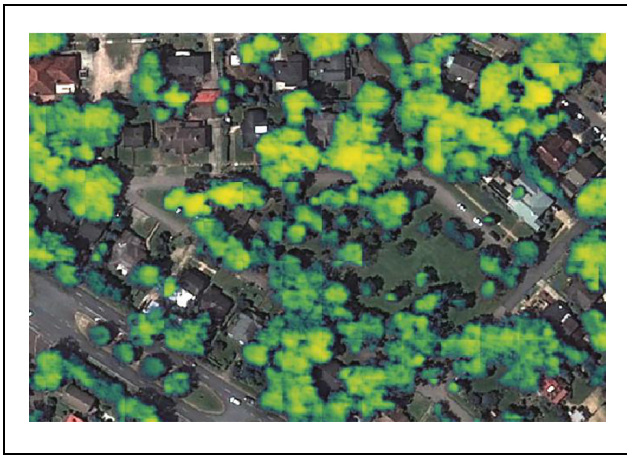


Figure 13. Output of the model in Figure 3, trained to perform vegetation segmentation instead of height regression.

Note: The output shows the pixels that are part of trees but information about the height is not available.

their availability. Nevertheless, in this paper, the scope is to show the capabilities of remote sensing to retrieve helpful information that can be used for vulnerability assessment.

Conclusions

This paper developed an automated framework to detect vulnerabilities at the roadway level using satellite imagery. We used high-resolution satellite images of a portion of Tallahassee (Florida) acquired before Hurricane Michael in September 2018. The framework calculates the vegetation exposure of roads based on tree parameters estimated from satellite images, such as height, health, proximity to roads, and density. Additionally, it integrates the vegetation exposure with the number of buildings and the road importance and assigns each road a vulnerability score. A vulnerability map can be generated road-wise for the whole roadway network. It can be quickly generated before the event and can improve the planning procedures conducted by city and state agencies. Compared with visual or manual surveys, it is also

cheap and practical to implement. The proposed methodology can be applied to other cities prone to hurricanes, given the data availability. Especially for small and medium coastal towns with limited resources prone to storms in Florida, the proposed approach can help quickly identify highly vulnerable locations on roadways without the need for sophisticated technology. Finally, local authorities could implement customized or adapted functions based on additional data and their prior knowledge and experience. We believe our method can serve as a complementary source to the other existing approaches (e.g., manual surveys, drones), providing a high potential for added satellite-based observability with minimal costs and high availability, and attaining traction as our industry becomes better at storing and sharing datasets.

Acknowledgments

Our involvement in the ITU/WMO/UNEP Focus Group on AI for Natural Disaster Management (FG-AI4NDM) activities and leading a use case on AI for hurricanes' impact inspired this paper (40). We greatly appreciate the FG-AI4NDM team and chair (Dr. Monique Kuglitsch) for creating a collaborative learning and knowledge exchange environment. Finally, the authors want to thank the City of Tallahassee for their support and for providing data.

Author Contributions

The authors confirm contribution to the paper as follows: study conception and design: M. Gazzea, A. Karaer, M. Ghorbanzadeh, E. E. Ozguven, R. Arghandeh; Data collection: M. Gazzea, A. Karaer, M. Ghorbanzadeh, E. E. Ozguven and R. Arghandeh; analysis and interpretation of results: M. Gazzea, A. Karaer, M. Ghorbanzadeh, R. Arghandeh; draft manuscript preparation: M. Gazzea, A. Karaer, M. Ghorbanzadeh, E. E. Ozguven, R. Arghandeh. All authors reviewed the results and approved the final version of the manuscript.


Declaration of Conflicting Interests


The author(s) declared no potential conflicts of interest with respect to the research, authorship, and/or publication of this article.


Funding


The author(s) received no financial support for the research, authorship, and/or publication of this article.


ORCID iDs

Michele Gazzea  <https://orcid.org/0000-0003-0759-4887>

Alican Karaer  <https://orcid.org/0000-0002-6704-0379>

Mahyar Ghorbanzadeh  <https://orcid.org/0000-0002-5651-7573>

Eren Erman Ozguven  <https://orcid.org/0000-0001-6006-7635>

Reza Arghandeh  <https://orcid.org/0000-0002-0691-5426>

References

- Jeffrey, E. F. What in the World is Infrastructure? <https://30kwelsi3or29z2y020bgbet-wpengine.netdna-ssl.com/wp-content/uploads/2018/03/what-in-the-world-is-infrastructure.pdf>, 2009. Accessed 11 August 2022
- US Department of Homeland Security (DHS). Infrastructure Security Sectors. <https://www.cisa.gov/infrastructure-security>. 2022. Accessed 11 August 2022
- Schaefer, M., R. Teeuw, S. Day, D. Zekkos, P. Weber, T. Meredith, and C. J. van Westen. Low-Cost UAV Surveys of Hurricane Damage in Dominica: Automated Processing with Co-Registration of Pre-Hurricane Imagery for Change Analysis. *Natural Hazards*, Vol. 101, 2020, pp. 755–784.
- Singh, L., W. Whittecar, M. DiPrinzio, J. Herman, M. Ferringer, and P. Reed. Low Cost Satellite Constellations for Nearly Continuous Global Coverage. *Nature Communications*, Vol. 11, 2020, p. 200.
- Gazzea, M., M. Pacevicius, D. O. Dammann, A. Saproнова, T. M. Lunde, and R. Arghandeh. Automated Power Lines Vegetation Monitoring Using High-Resolution Satellite Imagery. *IEEE Transactions on Power Delivery*, Vol. 37, No. 1, 2021, pp. 308–316.
- Gazzea, M., A. Karaer, N. Balafkan, E. E. Ozguven, and R. Arghandeh. Post-Hurricanes Roadway Closure Detection Using Satellite Imagery and Semi-Supervised Ensemble Learning. Presented at 100th Annual Meeting of the Transportation Research Board, Washington, D.C., 2021. Number TRBAM-21-00892. <https://trid.trb.org/view/1759300>
- Gazzea, M., A. Karaer, M. Ghorbanzadeh, N. Balafkan, T. Abichou, E. E. Ozguven, and R. Arghandeh. Automated Satellite-Based Assessment of Hurricane Impacts on Roadways. *IEEE Transactions on Industrial Informatics*, Vol. 18, No. 3, 2021, pp. 2110–2119.
- Kaur, S., S. Gupta, S. Singh, V. T. Hoang, S. Almakdi, T. Alelyani, and A. Shaikh. Transfer Learning-Based Automatic Hurricane Damage Detection Using Satellite Images. *Electronics*, Vol. 11, No. 9, 2022, p. 1448.
- Karaer, A., M. B. Ulak, T. Abichou, R. Arghandeh, and E. E. Ozguven. Post-Hurricane Vegetative Debris Assessment Using Spectral Indices Derived From Satellite Imagery. *Transportation Research Record: Journal of the Transportation Research Board*, 2021, 2675: 504–523.
- Karaer, A., M. Chen, M. Gazzea, M. Ghorbanzadeh, T. Abichou, R. Arghandeh, and E. E. Ozguven. Remote Sensing-Based Comparative Damage Assessment of Historical Storms and Hurricanes in Northwestern Florida. *International Journal of Disaster Risk Reduction*, Vol. 72, 2022, p. 102857.
- Ghorbanzadeh, M., M. Koloushani, M. B. Ulak, E. E. Ozguven, and R. A. Jouneghani. Statistical and Spatial Analysis of Hurricane-Induced Roadway Closures and Power Outages. *Energies*, Vol. 13, No. 5, 2020, p. 1098.
- Ghorbanzadeh, M., M. Koloushani, E. E. Ozguven, A. Vanli, and R. Arghandeh. City Transportation Network Vulnerability to Disasters: The Case of Hurricane Hermine in Florida. *Environmental Hazards*, Vol. 21, No. 3, 2021, pp. 199–217.
- Rouse, J. W., R. H. Haas, J. A. Schell, and D. W. Deering. *Monitoring Vegetation Systems in the Great Plains with ERTS*. NASA, Washington, D.C., 1973.
- Gullick, D., G. A. Blackburn, J. D. Whyatt, P. Vopenka, J. Murray, and J. Abbatt. Tree Risk Evaluation Environment for Failure and Limb Loss (Treefall): An Integrated Model for Quantifying the Risk of Tree Failure from Local to Regional Scales. *Computers, Environment and Urban Systems*, Vol. 75, 2019, pp. 217–228.
- Ciftçi, C., S. Arwade, B. Kane, and S. Brena. Analysis of the Probability of Failure for Open-Grown Trees During Wind Storms. *Probabilistic Engineering Mechanics*, Vol. 37, 2014, pp. 41–50.
- Wu, J. Developing General Equations for Urban Tree Biomass Estimation with High-Resolution Satellite Imagery. *Sustainability*, Vol. 11, No. 16, 2019, p. 4347.
- Kabir, E., S. Guikema, and B. Kane. Statistical Modeling of Tree Failures During Storms. *Reliability Engineering & System Safety*, Vol. 177, 2018, pp. 68–79.
- National Oceanic and Atmospheric Administration (NOAA). Catastrophic Hurricane Michael Strikes Florida Panhandle October 10, 2018. <https://www.weather.gov/tae/HurricaneMichael2018>. Accessed 11 August 2022
- U.S. Energy Information Administration. Hurricane Michael Caused 1.7 Million Electricity Outages in the Southeast United States. <https://www.eia.gov/todayinenergy/detail.php?id=37332>. 2018. Accessed 11 August 2022
- Florida Forest Service. Initial value estimate of altered, damaged or destroyed timber in Florida. <https://www.fdacs.gov/content/download/82204/file/HurricaneMichaelInitialTimberDamageEstimate1.pdf>. 2018. Accessed 11 August 2022
- National Center for Environmental Information. *Assessing the U.S. Climate in 2018*. National Center for Environmental Information, Asheville, NC, 2018.
- Planet Team. Planet Application Program Interface: In Space for Life on Earth. <https://api.planet.com>. 2017. Accessed 11 August 2022
- Jenelius, E., and L. Mattsson. Road Network Vulnerability Analysis: Conceptualization, Implementation and Application. *Computers, Environment and Urban Systems*, Vol. 49, 2015, pp. 136–147.
- Liu, C. J., V. A. Krylov, P. Kane, G. Kavanagh, and R. Dahyot. Im2elevation: Building Height Estimation from Single-View Aerial Imagery. *Remote Sensing*, Vol. 12, No. 17, 2020, p. 2719.
- Xiao, C., R. Qin, X. Huang, and J. Li. Individual Tree Detection from Multi-View Satellite Images. In *IGARSS 2018-2018 IEEE International Geoscience and Remote Sensing Symposium*, IEEE, Valencia, Spain, 2018, pp. 3967–3970.
- Raggam, H. Surface Mapping Using Image Triplets: Case Studies and Benefit Assessment in Comparison to Stereo Image Processing. *Photogrammetric Engineering and Remote Sensing*, Vol. 72, No. 5, 2006, pp. 551–563.
- Persson, H., H. Olsson, M. J. Soja, L. M. H. Ulander, and J. Fransson. Experiences From Large-Scale Forest Mapping of Sweden Using TanDEM-X Data. *Remote Sensing*, Vol. 9, No. 12, 2017, p. 1253.

28. Corte, A. P. D., F. E. Rex, D. Almeida, C. R. Sanquetta, C. A. Silva, M. M. Moura, B. Wilkinson, et al. Measuring Individual Tree Diameter and Height Using Gatoreye High-Density UAV-Lidar in an Integrated Crop-Livestockforest System. *Remote Sensing*, Vol. 12, No. 5, 2020, p. 863.
29. Ghamisi, P., and N. Yokoya. Img2dsm: Height Simulation from Single Imagery Using Conditional Generative Adversarial Net. *IEEE Geoscience and Remote Sensing Letters*, Vol. 15, No. 5, 2018, pp. 794–798.
30. Gazzea, M., S. Aalhus, L. M. Kristensen, E. E. Ozguven, and R. Arghandeh. Automated 3d Vegetation Detection Along Power Lines Using Monocular Satellite Imagery and Deep Learning. In 2021 IEEE International Geoscience and Remote Sensing Symposium IGARSS, IEEE, Brussels, Belgium, 2021, pp. 3721–3724.
31. De Petris, S., F. Sarvia, and E. Borgogno-Mondino. A New Index for Assessing Tree Vigour Decline Based on Sentinel-2 Multitemporal Data. Application to Tree Failure Risk Management. *Remote Sensing Letters*, Vol. 12, No. 1, 2020, pp. 58–67.
32. Develey-Rivière, M. P., and E. Galiana. Resistance to Pathogens and Host Developmental Stage: A Multifaceted Relationship Within the Plant Kingdom. *The New Phytologist*, Vol. 175, No. 3, 2007, pp. 405–416.
33. Saxena, A., and S. Iyengar. Centrality Measures in Complex Networks: A Survey. *arXiv*, abs/2011.07190, 2020.
34. Chollet, F. *Keras*. GitHub, 2015.
35. van der Walt, S., J. L. Schönberger, J. Nunez- Iglesias, F. Boulogne, J. D. Warner, N. Yager, E. Gouillart, et al. Scikit-Image: Image Processing in Python. *PeerJ*, Vol. 2, 2014, p. e453.
36. Hagberg, A. A., D. A. Schult, and P. J. Swart. Exploring network structure, dynamics, and function using networkx. In *Proc., 7th Python in Science Conference* (G. Varoquaux, Vaught, T., and J. Millman, eds.), Pasadena, CA USA, 2008, pp. 11–15.
37. QGIS Development Team. *QGIS Geographic Information System*. Open Source Geospatial Foundation, Beaverton, OR, 2009.
38. International Society for Photogrammetry and Remote Sensing (ISPRS). 2D Semantic Labeling Contest -Potsdam. <https://www2.isprs.org/commissions/comm2/wg4/benchmark/2d-sem-label-potsdam/>. Accessed 11 August 2022
39. Wang, Q., Y. Ma, K. Zhao, and Y. Tian. A Comprehensive Survey of Loss Functions in Machine Learning. *Annals of Data Science*, Vol. 9, 2022, pp. 187–212.
40. United Nations (UN). Focus Group on AI For Natural Disaster Management (FG-AI4NDM). <https://www.itu.int/en/ITU-T/focusgroups/ai4ndm/Pages/default.aspx>. Accessed 11 August 2022

The views expressed in this paper are of the authors and do not necessarily reflect the opinions or policies of the City of Tallahassee.